

Physical Properties of $\text{Al}_{1-x}\text{In}_x\text{N}/(\text{AlN})/\text{GaN}$ ($0.07 \leq x \leq 0.21$) Heterostructures and their Application for High Power Electronics

THÈSE N° 4586 (2011)

PRÉSENTÉE LE 27 SEPTEMBRE 2011

À LA FACULTÉ DES SCIENCES DE BASE

LABORATOIRE EN SEMICONDUCTEURS AVANCÉS POUR LA PHOTONIQUE ET L'ÉLECTRONIQUE

PROGRAMME DOCTORAL EN PHYSIQUE

ÉCOLE POLYTECHNIQUE FÉDÉRALE DE LAUSANNE

POUR L'OBTENTION DU GRADE DE DOCTEUR ÈS SCIENCES

PAR

Marcus GONSCHOREK

acceptée sur proposition du jury:

Prof. O. Schneider, président du jury

Prof. N. Grandjean, directeur de thèse

Dr Y. Cordier, rapporteur

Dr S. Delage, rapporteur

Prof. A. Fontcuberta i Morral, rapporteur



ÉCOLE POLYTECHNIQUE
FÉDÉRALE DE LAUSANNE

Suisse
2011

Abstract

AlInN is a material which is known to be difficult to be grown among the III-nitride ternary compounds. It attracted much attention only recently and starts to be studied intensively mainly for electronic applications. The aim of this work is manifold. Various structural, electrical and optical measurements are brought together to underline the outstanding quality of AlInN epi-layers grown by metalorganic vapor phase epitaxy (MOVPE).

Especially the electrons confined at the heterointerface of coherently grown AlInN on GaN buffer layers determine crucially the electronic properties. An appropriate model based on charge balance is proposed allowing the extraction of all significant electrical properties. An AlN interlayer has been introduced at the AlInN/GaN interface and was found to tremendously affect transport properties. This issue is studied intensively and results indicate that even slightest deviations from atomically perfect interfaces leads to the creation of huge piezoelectric fields disturbing carrier transport in the case of strongly mismatched epilayers. A similar debate was conducted concerning the localization of carriers in InGaN quantum wells.

High electron mobility transistors (HEMT) processed from these heterostructures exhibits excellent device performance exceeding 2 A/mm even on sapphire substrates. This are the highest currents ever reported for nitride heterostructures. The same structures grown on Si(111) substrates allow reaching cut-off frequency in excess of 100 GHz . However, results are puzzling and on at first sight striking since the device saturation currents of structures grown on SiC are similar to results on sapphire despite its much larger thermal diffusivity. Therefore we studied the temperature arising in the device under applied voltages using a micro-photoluminescence (μ PL) setup. To our knowledge this is the first study of this type. The main advantage is the use of the short wavelength for excitation in comparison with well-established Raman methods. However we find from this analysis a significant heat development up to 1200 K for devices with 5 μ m drain-source distance.

The heating can be understood in terms of excited optical phonons due to field accelerated electrons under applied voltages. The comparison of the available amount of phonons in the finite volume covered by the 2D electrons and the number of created phonons in the acceleration process allows formulating a simple relation for the saturation currents as a function of the transport properties. However, this mechanism also explains why the saturation currents are far below expected values from simple velocity saturated currents models and independent of the substrate. However, heat, *i.e.* the decomposition of local optical phonons into acoustical phonons with large group velocity, is dissipated differently depending on substrate influencing therefore mainly the reliability of the devices. Beside the

Abstract

electrical breakdown due to avalanche carriers a second thermally induced breakdown mechanisms is proposed.

Finally, the capability of those heterostructures for sensing is discussed. Especially the electrically response on external stimulus such as UV radiation and the exposition of the surface to polar liquids is investigated.

Keywords: Wide bandgap semiconductors, gallium nitride, aluminium indium nitride, electron gas, high electron mobility transistor

Zusammenfassung

Aluminium Indium Nitrid (AlInN) ist innerhalb der Gruppe der ternären Nitrid-Verbindungen aufgrund von thermodynamischen Aspekten das Material das am schwierigsten zu züchten ist. Deshalb gelang das erfolgreiche Wachstum von hochqualitativen epi-Schichten erst kürzlich. Das Ziel dieser Arbeit ist daher vielfältig. Verschiedene optische, elektrische und strukturelle Charakterisierungsmethoden unterstreichen die Qualität der Heterostrukturen. Das Wachstum der Schichten die hier diskutiert werden wurde ausschließlich mit metallorganischer Gasphasenepitaxie (engl: metalorganic vapor phase epitaxy (MOVPE)) realisiert.

Insbesondere wenn AlInN auf Galliumnitrid (GaN) aufgewachsen sammeln sich Elektronen an der Hetero-Schnittstelle die im wesentlichen sämtliche elektronischen Eigenschaften der Probe festlegen. Ein einfaches Model basierend auf einer Ladungsbilanzgleichung erlaubt die Extraktion aller wesentlichen Materialparameter wie Polarisationsladungen, dielektrische Konstante in Abhängigkeit vom ternären Indiumgehalt. Insbesondere das Einfügen einer Aluminiumnitrid (AlN) Zwischenschicht zwischen der verspannungsfreien AlInN Barriere und der GaN Schicht hat einen dramatischen Effekt auf die elektronischen Transporteigenschaften. Der Effekt der Verspannung der AlN Schicht (~2.4%) auf die GaN und AlInN Schicht wird im Detail behandelt. Insbesondere sehr geringe Abweichungen von atomistisch perfekten Schnittstellen in der Größenordnung von Monoschichten führt dabei zur Bildung signifikanter lokaler piezoelektrischer Felder und Verzerrung der lokalen Bandkante die die Elektronenbewegung signifikant beeinflussen.

Transistoren die auf Elektronen mit hohen Beweglichkeiten basieren (engl: High electron mobility transistor (HEMT)) die aus diesen Heterostrukturen prozessiert werden zeigen exzellente Charakteristika mit Stromdichten über 2 A/mm. Das ist der höchste Wert der auf diesem Materialsystem bisher gemessen wurde. Wenn diese Heterostrukturen auf Si(111) Substraten gewachsen zeigen die Transistoren eine cut-off Frequenz oberhalb von 100 GHz. Nichtsdestotrotz sind die Resultate widersprüchlich da Strukturen die auf SiC und Saphir gewachsen sind ähnliche Sättigungsströme zeigen trotz der dreimal höheren thermalen Diffusivität des SiC Substrats.

Deshalb wird im folgendem die Temperaturentwicklung in den HEMTs auf verschiedenen Substraten mittels Mikro-Photolumineszenz im elektronischen Nicht-Gleichgewicht untersucht. Der Hauptvorteil ist die Anregung mit kurzwelligem Licht (244 nm) im Vergleich zu der etablierten Raman-Methode, was eine bessere Fokussierung auf den Elektronenkanal erlaubt. Mit dieser Methode finden wir Temperaturen bis 1200 K in Transistoren mit einem Abstand der Emitter- und Kollektorkontakte von mit 5 µm.

Die hohen Temperaturen können als angeregte elementare Gitterschwingungen *i.e.* Phononen aufgefasst werden die durch Beschleunigung von Elektronen in den hohen lateralen elektrischen Feldern unter angelegten Spannungen erzeugt werden. Der Vergleich der verfügbaren Phononenanzahl in dem endlichen Volumen das von den lokalisierten 2D Elektronen eingenommen wird mit der Anzahl der in dem Beschleunigungsprozess angeregten Phononen erlaubt die Ableitung eines modifizierten Ausdrucks für die Sättigungsströme im Vergleich mit gängigen 3D Driftgeschwindigkeitssättigungsmodellen in Abhängigkeit von den lateralen Transporteigenschaften der 2D Elektronen. Dieses phononenbegrenzte Stromsättigungsmodell erklärt weiterhin die drastische Abweichung vom Driftgeschwindigkeitssättigungsmodell und die Unabhängigkeit von der Wahl des Substrats. Nichtsdestotrotz, Hitze, *i.e.* der Zerfall von lokalisierten optischen Phononen in akustische Phononen mit großer Gruppengeschwindigkeit, wird in Abhängigkeit vom Substrat unterschiedlich dissipiert was sich wiederum auf die Langlebigkeit und Reproduzierbarkeit der HEMTs auswirkt. Neben dem elektrischen Durchbruch für Elektronen die sich in bulk-artigem Material bewegen (3D) das durch die Erzeugung von Avalanche-Elektronen ausgelöst wird ein zweiter für die HEMT Operation relevanter thermisch induzierten Durchbruchmechanismus vorgeschlagen.

Am Ende der Arbeit wird die Einsatzmöglichkeit solcher Heterostrukturen für den Einsatz als Sensoren diskutiert. Insbesondere wird auf die elektrische Reaktion der 2D Elektronen in den AlInN/AlN/GaN Heterostrukturen auf externe Anregungen wie UV Strahlung, Hitze oder den Kontakt mit polaren Flüssigkeiten eingegangen.

Schlüsselbegriffe: Halbleiter mit großer Bandlücke, Galliumnitrid, Aluminiumindiumnitrid, Elektronengas, HEMT

Acronyms

2DE(H)G	2 dimensional electron (hole) gas
ACF	Autocorrelation function
AFM	Atomic force microscopy
BTE	Boltzmann transport equation
CV	Capacitance-voltage
ECV	Electrochemical capacitance-voltage
FWHM	Full width at half maximum
HEMT	High electron mobility transistor
HWHM	Half width at half maximum
LD	Laser diode
LED	Light emitting diode
LM	Lattice-matched
MBE	Molecular beam epitaxy
MD	Misfit dislocation
MFP	Mean free path
ML	Monolayer
MFS	Minimum feature size
μPL	Microphotoluminescence
MOVPE	Metalorganic vapor phase epitaxy
PL	Photoluminescence
PSD	Power spectral density
QW	Quantum well
RBS	Rutherford backscattering
RLP	Reciprocal lattice point
RMS	Root mean square
RPA	Random phase approximation
RT	Room temperature
SEM	Scanning electron microscopy
SNMS	Secondary neutral mass spectroscopy
TEM	Transmission electron microscopy
TLM	Transfer length method
XRD	X-ray diffraction

Content

Abstract	iii
Zusammenfassung	v
Acronyms	vii
Table of contents	ix
Introduction	1
Scientific research on III-nitride alloys	1
Objectives	2
Outline	2
Bibliography	4
1 Material Properties of III-V Nitride Semiconductors	7
1.1 Crystalline structure	7
1.2 A survey on bandstructure properties	8
1.3 Strain and stress	11
1.4 Spontaneous and piezoelectric polarization	14
1.5 Heterostructure engineering	16
Bibliography	19
2 Heteroepitaxy and characterization of GaN (0001)	21
2.1 Introduction.	21
2.2 Metal-organic vapor phase epitaxy	21
2.3 Substrate for GaN epitaxy (GaN, sapphire, SiC, Si).	23
2.4 Epitaxy of GaN	24
2.5 Characterization of GaN epilayers	26
2.5.1 X-ray diffraction	26
2.5.2 Photoluminescence.	28
2.5.3 Capacitance-voltage and Hall measurements	29
2.6 Conclusions	31
Bibliography	31

3 Heteroepitaxy and characterization of $\text{Al}_{1-x}\text{In}_x\text{N}/\text{AlN}/\text{GaN}$ (0001) ($0.03 \leq x \leq 0.23$)	33
3.1 Introduction.	33
3.2 AlInN epitaxial growth	33
3.3 Structural characterization	34
3.2.1 Determination of In content	36
3.2.2 Surface morphology	37
3.2.3 AlN interlayer	38
3.4 Conclusions	40
Bibliography	41
4 Electrical characterization of $\text{Al}_{1-x}\text{In}_x\text{N}/\text{AlN}/\text{GaN}$ (0001) ($0.03 \leq x \leq 0.23$)	43
4.1 Introduction.	43
4.2 2DEG fundamentals and balance equation.	43
4.3 Capacitance-voltage	46
4.4 Electrical properties of non-LM heterostructures	50
4.5 Graded AlInN	52
4.6 Conclusions	54
Transition: A survey on mobilities in AlInN/AlN/GaN heterostructures	54
Bibliography	57
5 Subband Structure and Transport	59
5.1 Introduction.	59
5.2 Subband structure	59
5.3 Interface morphology, autocorrelation function, and power spectral density	65
5.4 Roughness induced strain, deformation potential and piezoelectric fields	69
5.5 Scattering mechanisms in nitride heterostructures.	72
5.6 Application to $\text{Al}_{1-x}\text{In}_x\text{N}/\text{AlN}/\text{GaN}$ heterostructures.	76
5.7 Conclusions	79
Bibliography	79
6 Optical properties of $\text{Al}_{1-x}\text{In}_x\text{N}/\text{AlN}/\text{GaN}$ (0001) ($0.03 \leq x \leq 0.23$)	83
6.1 Introduction.	83
6.2 Absorption and luminescence, origin of the stokes shift.	83
6.3 Alloy broadening in nitrides – a survey	85
6.4 Field broadening in $\text{Al}_{1-x}\text{In}_x\text{N}/\text{AlN}/\text{GaN}$ (0001) heterostructures . . .	86
6.5 Spatial and thermal aspects of LM AlInN related luminescence . . .	88
6.6 Conclusions	89
Bibliography	90

7 Devices based on $\text{Al}_{1-x}\text{In}_x\text{N}/\text{AlN}/\text{GaN}$ (0001) heterostructures ($0.03 \leq x \leq 0.23$)	91
7.1 Introduction.	91
7.2 High electron mobility transistors	92
7.2.1 Principles of HEMT devices	92
7.2.2 A survey on $\text{AlInN}/\text{AlN}/\text{GaN}$ HEMT device characteristics	97
7.2.3 Spatially resolved temperature profiling in $\text{AlInN}/\text{AlN}/\text{GaN}$ HEMT devices using $\mu\text{Photoluminescence}$	102
7.2.4 Field <i>versus</i> phonon limited current saturation mechanisms	110
7.2.5 Modelling $\text{AlInN}/\text{AlN}/\text{GaN}$ HEMT devices using 2D Current-Poisson calculations	118
7.2.6 Advanced HEMT concepts	123
7.3 Chemical, thermal and UV sensing.	125
7.4 Conclusion	129
Bibliography	130
 Conclusion	 135
Summary of experimental results	135
Conclusion	136
Outlook	137
Bibliography	138
 Acknowledgements	 139
 Curriculum Vitae	 141
 Publications	 143

Introduction

III-nitrides The gallium nitride material was synthesized first in 1930 and then grown epitaxially by means of hydride phase vapour epitaxy (HVPE) in 1969 by Maruska *et al.* [1]. Two years later an important breakthrough was achieved with the realization of the growth *via* metal organic chemical vapor phase epitaxy (MOVPE) [2] and the first optical studies on high-quality GaN crystal [3]. Since then the scientific work done on this material system is exploding as depicted in Figure 1 according to *Web of Science* statistics [4]. In the 1980's the *p*-type doping was discovered leading to the first high-brightness light emitting diode (LED) [5]. This pushed forward the development of the InGaN ternary alloy and consequently the blue laser diode [6]. In the next decade the AlGaN ternary alloy was perceived as a candidate for high power electronics. More recently, AlInN has come to the attention of the nitride community as the last of the ternary alloys owing to the difficulties in growth. The interest for this peculiar alloy manifests in the steep increase in publication rate since 2000. Indeed, it is an attractive candidate for optical and electronic devices, with a bandgap covering an unprecedented spectral range from ultraviolet (UV) to infrared (IR).

One of the main drawbacks of III-nitrides is the fact that the binary compounds namely GaN, AlN and InN exhibit large lattice-mismatch (LM) with each other preventing arbitrary combinations of epitaxial layers and thicknesses for the growth of heterostructures. Along this, AlInN has the uniqueness of intermediating between the lattice-mismatches of AlN or InN grown on GaN templates and allowing therefore strain-free, LM heterostructures. This offers a new degree of freedom in designing nitride heterostructures for a wide range of applications. For instance, LM AlInN/GaN distributed Bragg reflectors (DBR) have been grown with reflectivity close to 100% [7] thanks to the high contrast in the indices of refraction ($\sim 7\%$). This is an important milestone towards vertical cavity surface emitting lasers (VCSELs). Another interesting feature is the possibility of transforming AlInN into an oxide by means of electrochemical selective etching [8].

On the other hand, Kuzmik [9] pointed out that the combination of strain-free AlInN epi-layers together with a high polarization discontinuity over the heterointerface would lead to superior device performance with respect to AlGaN/GaN heterostructures. Therefore, the LM AlInN/GaN system is an ideal candidate for high power electronics.

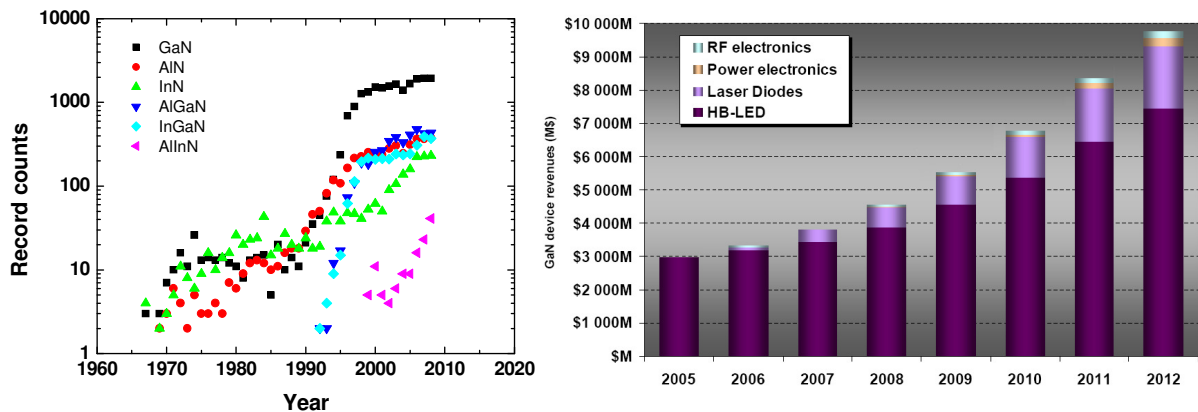


Figure 1 (a) Record counts containing the acronyms of the nitride compounds in the title *versus* year of publication according to Ref. [4]. (b) Nitride device market revenues and forecast. Values are taken from Ref. [10].

Introduction

State of the art At the beginning of this thesis, in 2005 there was only scarce information on the AlInN alloy properties as can be seen from Figure 1. The well established material system for high power devices was AlGaN/GaN. These structures exhibit typical 2D electron gas (2DEG) density confined at the heterointerface in the order $\sim 1.0 \times 10^{13} \text{ cm}^{-2}$. Especially, high electron mobility transistors (HEMTs) operating at GHz frequencies processed from these heterostructures already reached market maturity and are successfully commercialized [11] with a special interest in communication technologies such as “Worldwide Interoperability for Microwave Access” (WiMAX) [12].

On the other hand, it was found that AlInN/GaN heterostructures exhibit more than twice the amount of electrons confined at the heterointerface, *i.e.* in of the order of $2.6 \times 10^{13} \text{ cm}^{-2}$ and hence there is a serious interest for the next generation of high power electronics. Unfortunately these electrons forming the so-called 2DEG suffer from poor in-plane transport properties. It was thus one of the purposes of this thesis to improve the quality of this brand new heterostructures for next generation power devices.

Therefore, we used an approach also explored already with the AlGaN system, namely the insertion of an AlN interlayer. This helps to keep the electrons confined in the GaN and less scattered by alloy composition fluctuations. The variation of the interlayer thickness thereby results in a ‘high mobility window’ with a maximum of $1200 \text{ cm}^2/\text{Vs}$ at an interlayer thickness of $\sim 1 \text{ nm}$ and a 2DEG density of $\sim 2.6 \times 10^{13} \text{ cm}^{-2}$ at room temperature (RT) [13]. HEMTs processed from these heterostructures exhibit saturation currents up to 2 A/mm [14] and operate at frequencies up to 100 GHz [15]. Such devices typically exhibit maximum power densities up to 6.5 W/mm at 10 GHz .

Objectives The scope of this thesis is manifold. On one hand, there is a general aspect, *i.e.* to investigate general properties of the AlInN alloy ranging from structural, electronic, and optical properties. On the other hand, physical phenomena are discussed, which are closely related to the device operation such as transport properties and thermal effects on device characteristics. At the end of the thesis, other applications of such heterostructures will be briefly tackled.

Outline In **Chapter I** an overview over the most important structural, optical and electrical properties, which are (partially) unique to III-nitrides is given. Especially the role of the polarization discontinuity across heterojunctions grown on *c*-plane is pointed out.

Since the quality of the GaN buffer is crucial and can have a huge impact on device parameters, **Chapter II** is dedicated to growth techniques, substrate types, and common methods to characterize basic structural, electrical and optical properties.

In the following, growth and structural characterization of AlInN alloy grown on GaN are discussed (**Chapter III**). Special care is taken to determine the actual indium content. Along this, Rutherford backscattering (RBS) and x-ray reflection reciprocal space mappings (RSM) are brought together to measure indium content and strain state of the epilayers. It was found that the LM In composition is met at $\sim 17\%$. The exact composition also depends on the residual strain of the buffer [16-17]. Careful fitting procedures of x-ray rocking curves around the symmetric 002 reflexes were carried out. All the characterization methods suggest that AlInN epilayers exhibit high quality in terms of homogeneity and coherent strain state.

Chapter IV deals with the electrical characterization of AlInN/AlN/GaN heterostructures. A model based on charge balance in a one-subband approximation is proposed in order to describe the dependence of the 2DEG density on barrier and interlayer thicknesses. These findings are in good agreement with results found by potential mapping *via* electron holography [18]. Especially, it allows the extraction of important parameters such as polarization charge density across the interfaces, surface potential, critical thickness to form the 2DEG, and static dielectric constant of the alloy.

However, in heterostructures exhibiting such high 2DEG densities, the one-subband approximation is questionable. If the 2DEG density is higher than $1.0 \times 10^{13} \text{ cm}^{-2}$ the occupation of the second subband becomes probable, as found experimentally in AlN/GaN and AlGaN/AlN/GaN heterostructures [19-21] by Shubnikov-de-Haas (SdH) oscillations. Therefore, the subband occupation in such high 2DEG density AlInN/GaN heterostructures is discussed in detail as a function of barrier thickness at the beginning of **Chapter V**. As pointed out by a lot of authors, the morphology of the interface becomes crucial [22-23]. Therefore a detailed discussion on the GaN morphology is inserted. The monolayer (ML) steps appearing at the GaN buffer surface during growth are discussed in details. During the overgrowth with AlN, significant strain can build up around these ML steps with a range of a few nm and acting as scattering sources for 2D electrons. At the end of the Chapter these scattering mechanisms are brought together to calculate the mobility of the 2DEG in the framework of a two-subband transport model [24] as a function of the barrier thickness. It is found that for low densities, *i.e.* low barrier thickness, the mobility is limited by the uncompensated surface donors and by the dislocations while in the high density regime the interface roughness scattering (*i.e.* scattering at the in-plane potential fluctuation) and the scattering at the deformation potential and electric fields arising from the step fluctuations are the main limiting factors. Especially the second subband mobility is expected to be larger than that of the first subband due to its larger separation from the heterointerface. For high 2DEG density this can significantly influence the Hall coefficient and explains its strong decrease at low temperatures. This effect is not unique to AlInN/GaN but also appears in AlN/GaN [25].

Chapter VI is mainly dedicated to photoluminescence measurement results performed on AlInN/AlN/GaN heterostructures. It is found that the strong luminescence broadening with full width at half maximum in the order of $\sim 300 \text{ meV}$ originates from the strong non-linear behavior of the bandgap as function of the In composition [26]. Another important contribution to the broadening is the presence of strong electric field. Thicker layers exhibit therefore less broaden AlInN-related peak than thinner layers due to reduced built-in electric field. This dependence allows us to give an estimate of the effective electron mass in lattice-matched AlInN, which is as high as $\sim 0.3 m_0$. The strong Stokes shift up to 0.6 eV between absorption and luminescence measurements [27] might be explained in terms of strong hole localization [28-29].

Finally, we discuss in **Chapter VII** results from devices processed from the heterostructures discussed above. Their properties are briefly summarized and compared to common analytic models. Further we perform microphotoluminescence (μPL) measurements - to our knowledge - for the first time to probe the heat in such HEMT devices [30]. The advantage in comparison with common Raman methods is the extremely high depth resolution thanks to the excitation wavelength of 244 nm . The temperature found in these devices reaches 1200 K for drain-source distances d_{DS} of $\sim 5 \text{ }\mu\text{m}$ under drain-source voltages V_{DS} of 20 V for

heterostructures grown on sapphire. The saturation currents in nitride heterostructures can be understood in the framework of a two-piece model [31] taking into account a smooth transition between mobility limited and saturation velocity limited currents across the HEMT channel. This model is extended in the following by replacing the static room temperature mobility by the channel mobility obtained if channel heating *via* phonon excitation under applied drain-source voltages is taken into account. A general expression is derived giving access to the ultimate drain-source saturation currents in nitride HEMT heterostructures. At the end other potential applications of such heterostructures, namely UV detection and chemical sensing are briefly discussed.

Bibliography

- [1] H. P. Maruska, and J. J. Tietjen, *Preparation and Properties of Vapor-Deposited Single-Crystalline GaN*, Appl. Phys. Lett. **15**, 327 (1969).
- [2] H. M. Manasevi, F. M. Erdmann, and W. I. Simpson, *Use of Metalorganics in Preparation of Semiconductor Materials .4. Nitrides of Aluminum and Gallium*, J. Electrochem. Soc. **118**, 1864 (1971).
- [3] R. Dingle *et al.*, *Absorption, Reflectance, and Luminescence of GaN Epitaxial Layers*, Phys. Rev. B **4**, 1211 (1971).
- [4] *Web of Science published by THOMSON REUTERS: www.isiknowledge.com.*
- [5] S. Nakamura, M. Senoh, and T. Mukai, *Highly P-Typed Mg-Doped GaN Films Grown with GaN Buffer Layers*, Jpn. J. Appl. Phys. 2 **30**, L1708 (1991).
- [6] S. Nakamura, T. Mukai, and M. Senoh, *Candela-Class High-Brightness InGaN/AlGaIn Double-Heterostructure Blue-Light-Emitting Diodes*, Appl. Phys. Lett. **64**, 1687 (1994).
- [7] J. F. Carlin, and M. Ilegems, *High-quality AlInN for high index contrast Bragg mirrors lattice matched to GaN*, Appl. Phys. Lett. **83**, 668 (2003).
- [8] J. Dorsaz *et al.*, *Selective oxidation of AlInN layers for current confinement in III-nitride devices*, Appl Phys Lett **87**, 072102 (2005).
- [9] J. Kuzmik, *Power electronics on InAlN/(In)GaN: Prospect for a record performance*, IEEE Electron Device Lett. **22**, 510 (2001).
- [10] *YOLE DEVELOPPEMENT, Market Research and Strategy Consulting Company: <http://www.yole.fr>.*
- [11] *Cree, Inc.: www.cree.com.*
- [12] *WiMAX, Worldwide Interoperability for Microwave Access: <http://en.wikipedia.org/wiki/WiMAX>.*
- [13] M. Gonschorek *et al.*, *High electron mobility lattice-matched AlInN/GaN field-effect transistor heterostructures*, Appl. Phys. Lett. **89**, 062106 (2006).
- [14] F. Medjdoub *et al.*, *Small-signal characteristics of AlInN/GaN HEMTs*, Electron. Lett. **42**, 779 (2006).

-
- [15] H. F. Sun *et al.*, *102-GHz AlInN/GaN HEMTs on Silicon With 2.5-W/mm Output Power at 10 GHz*, IEEE Electron Device Lett. **30**, 796 (2009).
 - [16] V. Darakchieva *et al.*, *Effects of strain and composition on the lattice parameters and applicability of Vegard's rule in Al-rich $Al_{1-x}In_xN$ films grown on sapphire*, J. Appl. Phys. **103**, 103513 (2008).
 - [17] M. Gonschorek *et al.*, *Two-dimensional electron gas density in $Al_{1-x}In_xN/AlN/GaN$ heterostructures ($0.03 \leq x \leq 0.23$)*, J. Appl. Phys. **103**, 093714 (2008).
 - [18] L. Zhou *et al.*, *Polarization field mapping of $Al_{0.85}In_{0.15}N/AlN/GaN$ heterostructure*, Appl. Phys. Lett. **94**, 121909 (2009).
 - [19] C. P. Jiang *et al.*, *Subband electron properties of modulation-doped $Al_xGa_{1-x}N/GaN$ heterostructures with different barrier thicknesses*, Appl. Phys. Lett. **79**, 374 (2001).
 - [20] T. W. Kim *et al.*, *Magnetotransport, optical, and electronic subband properties in $Al_xGa_{1-x}N/AlN/GaN$ heterostructures*, Solid State Commun. **132**, 67 (2004).
 - [21] Y. Cao *et al.*, *Very low sheet resistance and Shubnikov-de-Haas oscillations in two-dimensional electron gases at ultrathin binary AlN/GaN heterojunctions*, Appl. Phys. Lett. **92**, 152112 (2008).
 - [22] M. N. Gurusinghe, S. K. Davidsson, and T. G. Andersson, *Two-dimensional electron mobility limitation mechanisms in $Al_xGa_{1-x}N/GaN$ heterostructures*, Phys. Rev. B **72**, 045316 (2005).
 - [23] D. N. Quang *et al.*, *Roughness-induced mechanisms for electron scattering in wurtzite group-III-nitride heterostructures*, Phys. Rev. B **72**, 245303 (2005).
 - [24] S. Mori, and T. Ando, *Intersubband Scattering Effect on the Mobility of a Si (100) Inversion Layer at Low-Temperatures*, Phys. Rev. B **19**, 6433 (1979).
 - [25] Y. Cao, and D. Jena, *High-mobility window for two-dimensional electron gases at ultrathin AlN/GaN heterojunctions*, Appl. Phys. Lett. **90**, 182112 (2007).
 - [26] E. Iliopoulos *et al.*, *Energy bandgap bowing of InAlN alloys studied by spectroscopic ellipsometry*, Appl. Phys. Lett. **92**, 191907 (2008).
 - [27] R. Butté *et al.*, *Current status of AlInN layers lattice-matched to GaN for photonics and electronics*, J. Phys. D: Appl. Phys. **40**, 6328 (2007).
 - [28] C. F. Klingshirn, *Semiconductor optics* (Springer, Berlin ; New York, 1997).
 - [29] L. W. Wang, *Calculations of carrier localization in $In_xGa_{1-x}N$* , Phys. Rev. B **63**, 245107 (2001).
 - [30] M. Gonschorek *et al.*, *Temperature mapping of $Al_{0.85}In_{0.15}N/AlN/GaN$ high electron mobility transistors through micro-photoluminescence studies*, Eur. Phys. J.-Appl. Phys. **47**, 30301 (2009).
 - [31] K. Lehovec, and R. Zuleeg, *Volgate-Current Characteristics of GaAs J-Fets in Hot Electron Range*, Solid State Electron. **13**, 1415 (1970).

Introduction

Material Properties of III-V Nitride Semiconductors

Chapter I aims to give a general introduction into structural, optical and electrical properties of III-V nitride semiconductors. Especially the presence of strong polarization effects, caused by the wurtzite structure in c -axis material, drastically change the optical and electrical properties of heterostructures in comparison to common III-V semiconductors. This allows for the so-called ‘polarization doping’ in single heterostructures or leads to the strong quantum confined stark effect (QCSE) in quantum well (QW) heterostructures.

1.1 Crystalline structure

GaN crystallizes preferentially in the hexagonal wurtzite structure. The zincblende phase is thermodynamically not stable. Figure 1.1 shows the wurtzite crystal structure of III-V nitrides. Yellow sphere depicts the nitrogen atom while grey sphere stands for the metallic Ga, Al or In atoms. In crystallography the wurtzite phase corresponds to a hexagonal lattice whose character of symmetry can be described with the space group $P6_3mc$. The unit cell can be described by the two lattice parameters a and c as indicated in Figure 1.1, which have for the case of GaN the values $a=0.3187$ nm and $c=0.5184$ nm, respectively.

As can be seen, the metallic and nitrogen atoms form sub-lattices perpendicular to the main axis (c -axis) which are hexagonal closely packed (hcp) in each plane. The planes consisting each of nitrogen or metallic atoms then take the form ABABAB along the main axis. Further the sub-lattices are displaced by an amount $3/8 c$ along the c -axis, *i.e.* there is a lack of inversion symmetry with respect to the c -axis. This is a key property since the absence of symmetry leads to two polarities, namely the Ga-face polarity in (0001) direction and N-face polarity in $(000\bar{1})$ direction. If the crystal is grown on a substrate with the orientation as depicted in Figure 1.1 it is also referred to as c -plane material. Beside the polar c -plane material there is a big effort to fabricate non-polar material with crystal orientations such as $(11\bar{2}0)$ or $(10\bar{1}0)$. The former is referred to as a -plane and the latter as m -plane. These both planes are oriented perpendicular to the c -plane. For the fabrication of a -plane GaN layers one uses *e.g.* $(1\bar{1}02)$ -oriented sapphire substrate [1] while for m -plane GaN layers *e.g.* γ -LiAlO₂ substrates are employed [2].

Every atom of either metallic or nitrogen nature is tetrahedrally surrounded by four atoms of the opposite kind. Ideally the bond lengths in the tetrahedron are equal for wurtzite structure. The bonding angle is 109.47° . However, GaN exhibits a mixed ionic-covalent bonding. The fraction of the ionic character is given as 0.5 using Pauling ionicity basing on the constituent electronegativities [3].

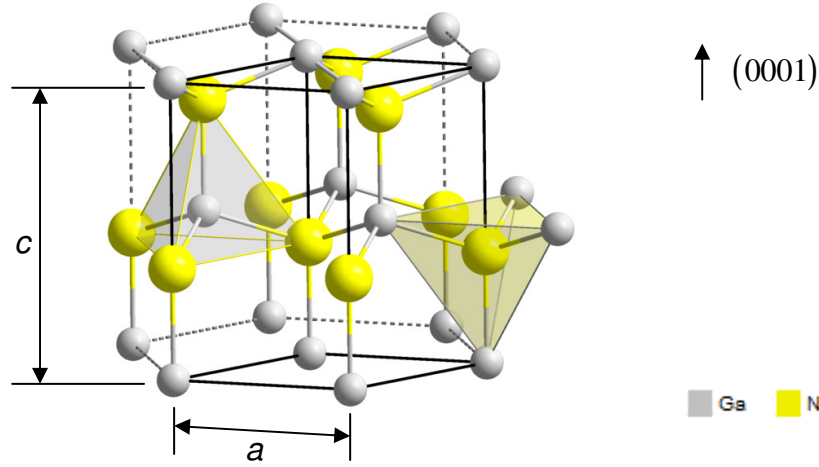


Figure 1.1 Wurtzite crystal structure of III-V nitrides. Yellow spheres depict the nitrogen atoms while grey spheres represent the metallic Ga, Al or In atoms. For GaN the dimensions of the unit cell are $a=0.318$ nm and $c=0.518$ nm, respectively. Picture is taken from Ref. [4].

1.2 A survey on bandstructure properties

Bandgaps Among the III-V semiconductor compounds the bandgaps of nitrides cover the widest range of energy from the near infrared (IR) to the deep ultraviolet (UV). The values of the bandgaps at room-temperature assuming relaxed bulk-like material are 6.2 eV, 3.42 eV, and 0.65 eV for AlN, GaN and InN, respectively [5]. In Figure (1.2) they are displayed together with the interpolations between binaries *versus* lattice parameters as orange lines. The relation between the bandgap value *versus* ternary alloy composition deviates for nitrides clearly from Vegard's law (linear interpolation) and is commonly approximated as

$$E_{g,A_xB_{1-x}N} = E_{g,AN}x + E_{g,BN}(1-x) - b_{A,B}x(1-x) \quad (1.1)$$

where $E_{g,AN}$ and $E_{g,BN}$ represents the bandgap values for the two binary compounds. The unambiguous determination of the bowing parameter $b_{A,B}$ requires a detailed knowledge on strain state, sample quality and exact composition. Since it is in general a difficult task to determine all these parameters exactly, various values for $b_{A,B}$ can be found in the literature. A well established value for the AlGaN alloy is $b_{AlGaN} \sim 0.7$ eV. Among the ternary alloys containing indium the scattering of the reported values for $b_{A,B}$ is even larger. This diversity was caused for a long time by the low material quality of high In content alloys and even the wrong estimate of the InN bandgap. In some more recent work the authors could establish consistent values for the bowing parameter: $b_{InGaN} \sim 1.4$ eV for InGaN alloy [6] and $b_{AlInN} \sim 5$ eV for the AlInN alloy. One nevertheless should keep in mind that Equation (1.1) is a phenomenological description. Recently, the bandgap of AlInN was successfully described with a composition dependent bowing parameter of the form $b_{AlInN}=15.3/(1+4.8 x)$ [7].

Temperature dependence The dependence of the bandgap energy *versus* temperature is commonly described by the semi-empirical Varshni relation [9]

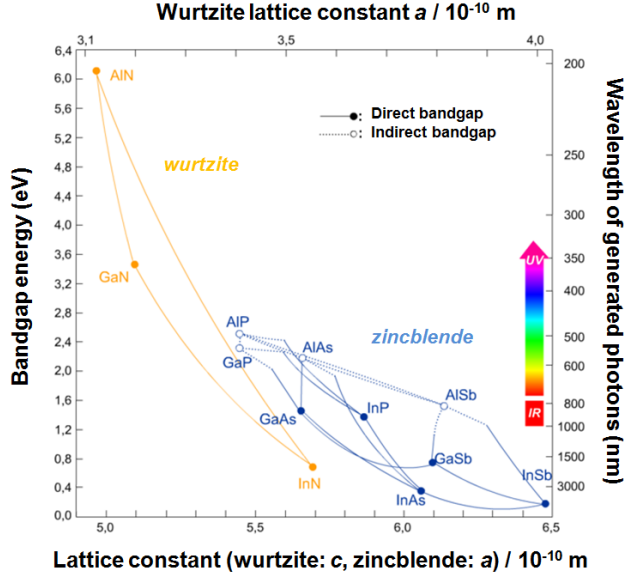


Figure 1.2 Bandgaps of common III-V semiconductor compounds *versus* their lattice constants. Picture taken from Ref. [8].

$$E_g(T) = E_g(0) - \frac{\alpha T^2}{T + \beta} \quad (1.2)$$

where α and β are material specific parameters whose units are (meV/K) and (K), respectively. Typical bulk values of these parameters for III-V nitride are given in Table (1.1). Note that these values should be regarded as benchmark or approximate values since actual values for epitaxially grown layers might differ for the following reason: due to the thermal expansion coefficient mismatch in heteroepitaxy the strain state of the epilayer grown on a specific substrate becomes temperature and substrate dependent. Consequently, α and β should carefully be determined for each specific sample.

Table 1.1 Varshni parameters α and β for wurtzite III-V nitride semiconductors [10].

Material	α (meV/K)	β (K)
GaN	0.94	780
AlN	1.8	1460
InN	0.25	624

Band structure GaN is a so-called direct bandgap semiconductor, *i.e.* the minimum of the conduction band and the maximum of the valance band are both located in the center of the Brillouin zone at the Γ point. The Brillouin zone including the Γ point and the two next higher (~ 2 eV) conduction band minima's labeled as A and M-L is shown in Figure 1.3 (a). Commonly the complete bandstructure, *i.e.* the particles energy *versus* its wavevector \mathbf{k} , is calculated in framework of the density-functional theory in the local density approximation (DFT-LDA). The result is shown in Figure 1.3 (b). Figure 1.3 (c) represents a magnification of the band structure around the Γ point. It reveals the fine structure of the valence band which split into three subbands known as heavy holes (HH), light holes (LH) and split-off holes (SO), respectively. In contrast to the conduction band which is unique with symmetry

1 Material Properties of III-V Nitride Semiconductors

Γ_7 the degeneracy of the valence band is lifted two times *via* the crystal field coupling Δ_{cr} and the spin-orbit coupling Δ_{SO} . For small values of \mathbf{k} near the center of the Brillouin zone (Γ) the dispersion relation of the bands can be approximated as

$$E_{e,h} = E_{e,h}(\mathbf{k}=0) \pm \frac{\hbar^2 k^2}{2m_{e,h}^*} \quad (1.3)$$

where m_e^* and m_h^* are the effective masses of the conduction (+ sign in Equation (1.3)) and valence band (- sign in Equation (1.3)), respectively. In general effective masses are anisotropic, but for simplicity averaged isotropic values are used. Typical averaged isotropic effective masses for HH and LH are shown in Table 1.2.

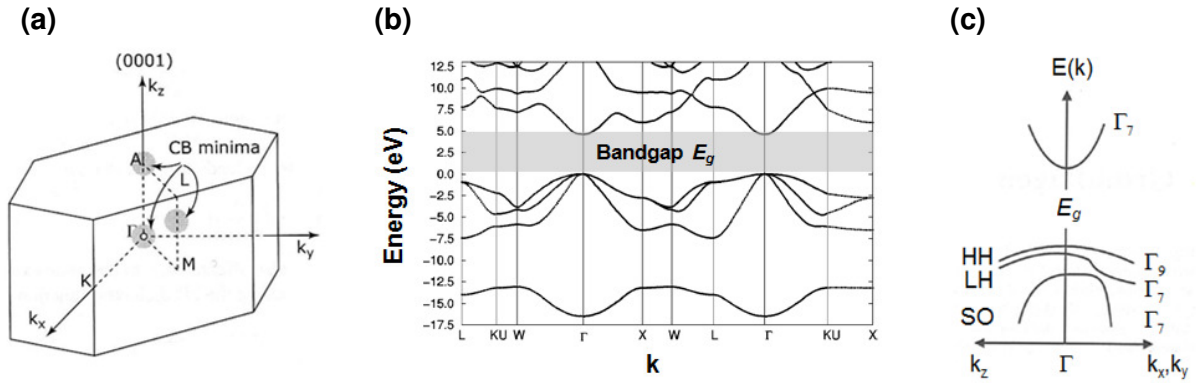


Figure 1.3 (a) Brillouin zone for wurtzite GaN according to Ref. [11]. (b) Computed band structure of wurtzite GaN within the framework of DFT-LDA according to Ref. [12] for important directions in the Brillouin zone. (c) Detail of the GaN band structure around $\mathbf{k} = 0$ according to Ref. [13].

Interestingly, HH and LH exhibit similar effective masses in the direction parallel to the growth axis. In contrast, there is a huge difference concerning their respective in-plane effective masses. Due to the equal parallel effective masses for the binary compounds one expects similar subband energies for HH and LH in quantum well (QW) heterostructures grown on *c*-plane material. Further leads the lift of the degeneracy of the valence band to three different excitonic transition energies labeled as E_A , E_B and E_C associated to HH, LH and split-off holes, respectively. The transitions can then be observed with spectroscopic methods [14]. Furthermore, the transition energies depend on the strain-state of the material.

Material	$m_e^*(\perp)$ $/m_0$	$m_e^*(\parallel)$ $/m_0$	$m_{HH}^*(\perp)$ $/m_0$	$m_{HH}^*(\parallel)$ $/m_0$	$m_{LH}^*(\perp)$ $/m_0$	$m_{LH}^*(\parallel)$ $/m_0$
GaN	0.2	0.2	1.6	1.1	0.15	1.1
AlN	0.4	0.4	10.42	3.53	0.24	3.53
InN	0.07	-	1.63	-	0.27	-

Table 1.2 Effectives masses for electrons (m_e^*/m_0), heavy (m_{HH}^*/m_0) and light (m_{LH}^*/m_0) hole parallel (\parallel) and perpendicular (\perp) to the polar [0001] axis in isotropic approximation around the Γ point. Values are taken from Ref. [15].

1.3 Strain and stress

Unfortunately, the different III-V nitride binary compounds GaN, AlN and InN exhibit equilibrium (bulk) lattice constants which differs significantly from each other. This imposes a lot of restrictions and problems to heterostructure engineering. In Table 1.3 the equilibrium bulk lattice constants for GaN, AlN and InN are shown as well as their biaxial strain occurring if the respective material is grown epitaxially on GaN. The biaxial strain in percent is defined as $\epsilon_{\parallel} = (a_{\text{GaN}} - a) / a$, where a is the lattice parameter of the epilayer. As it can be seen in the third column the strain can mount up to -10.2 % for the case of InN/GaN.

Now the question arises how the physical properties of the epilayer change in a realistic growth scenario. Then the epilayer takes over the in-plane (a) lattice parameter of the layer underneath. This is referred to as pseudomorphic growth. If the a lattice parameter is fixed the crystal has to compensate this by finding a new equilibrium value for the c lattice constant depending on the elastic properties of the material. Then the volume of the unit cell is not longer conserved, which affects a lot of crucial physical properties of the (strained) epilayer, *e.g.* band gaps, band offsets, polarization charges, dielectric constants.

Material	a (Å)	c (Å)	$\epsilon_{\parallel} = (a_{\text{GaN}} - a) / a$ (%)
GaN	3.187	5.184	0
AlN	3.112	4.982	+2.4
InN	3.548	5.760	-10.2

Table 1.3 Lattice parameters of III-V binary nitrides and biaxial strain if the material is epitaxially grown on GaN.

Strain and stress are connected *via* Hook's law. In its most general form (tensor notation) it can be written as

$$\boldsymbol{\sigma} = \mathbf{C} : \boldsymbol{\epsilon} \quad (1.4)$$

Here $\boldsymbol{\sigma}$ is the stress tensor, $\boldsymbol{\epsilon}$ the strain tensor and \mathbf{C} the elasticity tensor. Since we have a transversely isotropic material which exhibits a symmetry with respect to a symmetry axis (c -axis) the elasticity tensor can be expressed as [16]

$$\mathbf{C} = \begin{pmatrix} C_{11} & C_{12} & C_{13} & 0 & 0 & 0 \\ C_{12} & C_{11} & C_{13} & 0 & 0 & 0 \\ C_{13} & C_{13} & C_{33} & 0 & 0 & 0 \\ 0 & 0 & 0 & C_{44} & 0 & 0 \\ 0 & 0 & 0 & 0 & C_{44} & 0 \\ 0 & 0 & 0 & 0 & 0 & \frac{C_{11} - C_{22}}{2} \end{pmatrix} \quad (1.5)$$

1 Material Properties of III-V Nitride Semiconductors

Equation (1.4) can then be written using the Voigt notation (reduction of the 3×3 strain and stress tensors to vectors containing 6 elements, respectively) and the identities $\epsilon_{\parallel} = \epsilon_{xx} = \epsilon_{yy} = (a - a_0) / a_0$ and $\epsilon_{\perp} = \epsilon_{zz} = (c - c_0) / c_0$, where the index “0” refers to the unstrained equilibrium lattice constants. Then Equation (1.4) can be simplified to

$$\begin{pmatrix} \sigma_{\parallel} \\ \sigma_{\perp} \end{pmatrix} = \begin{pmatrix} C_{11} + C_{12} & C_{13} \\ 2C_{13} & C_{33} \end{pmatrix} \begin{pmatrix} \epsilon_{\parallel} \\ \epsilon_{\perp} \end{pmatrix} \quad (1.6)$$

During growth the surface is free so that $\sigma_{\perp} = \sigma_{zz} = 0$ and Equation (1.6) further reduces to

$$\epsilon_{\perp} = -2 \frac{C_{13}}{C_{33}} \epsilon_{\parallel} \quad (1.7)$$

This relation finally gives the deformation of the epitaxial layer in z -direction as a function of the in-plane strain and elastic coefficients. The elastic constants are given in Table 1.4.

Material	C_{11} (GPa)	C_{12} (GPa)	C_{13} (GPa)	C_{33} (GPa)	C_{13}/C_{33}
GaN	390	145	106	398	0.266
AlN	396	137	108	373	0.290
InN	223	115	92	224	0.411

Table 1.4 Elastic constants for III-V nitrides taken from Refs. [6, 17].

As an example one could take an AlN layer which is grown pseudomorphically on relaxed GaN. Then the AlN a -lattice constant adopts the GaN a -lattice constant leading to an in-plane expansion of the AlN unit cell (tensile strain). ϵ_{\parallel} takes a value of +2.4%. According to Equation (1.7) the unit cell shrinks in growth direction (compressive strain) by an amount $\epsilon_{\perp} = -1.4\%$.

Strain dependence of the band structure As was demonstrated above strain effects play an important role in III-V nitride heteroepitaxy as well as in the growth of nanostructures. The distortion of the crystal lattice from the equilibrium positions induces changes in the electronic orbitals overlap. The bandgap change can be described within the deformation potential theory and an extensive study of the problem in GaN can be found in the literature [18, 19]. To obtain the excitonic energies E_A (HH), E_B (LH) and E_C (SO) one has to solve the eigenvalue problem using an appropriate Hamiltonian which couples the conduction and the different valence bands respecting their energy dependence for the different components according to the crystal symmetry while energetic shifts result from the strain connected *via* the deformation potentials. This Hamiltonian for wurtzite crystal symmetry was first setup by Pikus and Bir [20] and solved for GaN under biaxial strain using cubic approximation by Shikanai *et al.* [21]. The excitonic resonance energy E_A reads therefore as

$$E_A^1 = E_A^0 + \left(D_1 - \frac{C_{33}}{C_{13}} D_2 \right) \epsilon_{zz} + \left(D_3 - \frac{C_{33}}{C_{13}} D_4 \right) \epsilon_{zz} \quad (1.8)$$

where D_i are the components of the deformation potential and E_A^0 is a constant connected to the crystal-field and spin-orbit coupling. This linear behavior with respect to ϵ_{zz} is in agreement with empirical relation obtained by fitting the experimental data yielding $E_A = 3.478 + 15.4 \epsilon_{zz}$ eV. Experimental data as well as the theoretical dependence are shown for E_A , E_B and E_C as a function of ϵ_{zz} in Figure 1.4. As usual for direct bandgap semiconductors, the compressive (out-of-plane) strain tends to increase the bandgap, and consequently the energy of the excitonic transitions, while the tensile tends to reduce it. Therefore optical spectroscopy, *i.e.* the measurements of the excitonic transitions allows to draw reliable conclusion on the strain state of the respective layer. A recent overview and discussion concerning deformation potentials in III-V nitrides can be found in Ref. [22].

Since excitonic transitions occur at the Γ point, *i.e.* at $\mathbf{k}=0$ one might be also interested in the complete dispersion relations under the influence of strain. This problem was discussed in Ref. [23] using $k \cdot p$ theory. The valence band structure of GaN under compressive strain is shown in comparison with the unstrained case in Figure 1.4 (b). One observes that the compressive strain shifts the HH (A) and LH bands (B) by a similar amount while the split off band (C) is lowered by ~ 50 meV with respect to the valence band edge. Further, it can be seen that the compressive strain does not change significantly the curvature of the dispersion relations and hence the effective masses. Consequently, the HH and LH effective masses along the [0001] direction remain similar and the in-plane effective masses preserve their large difference.

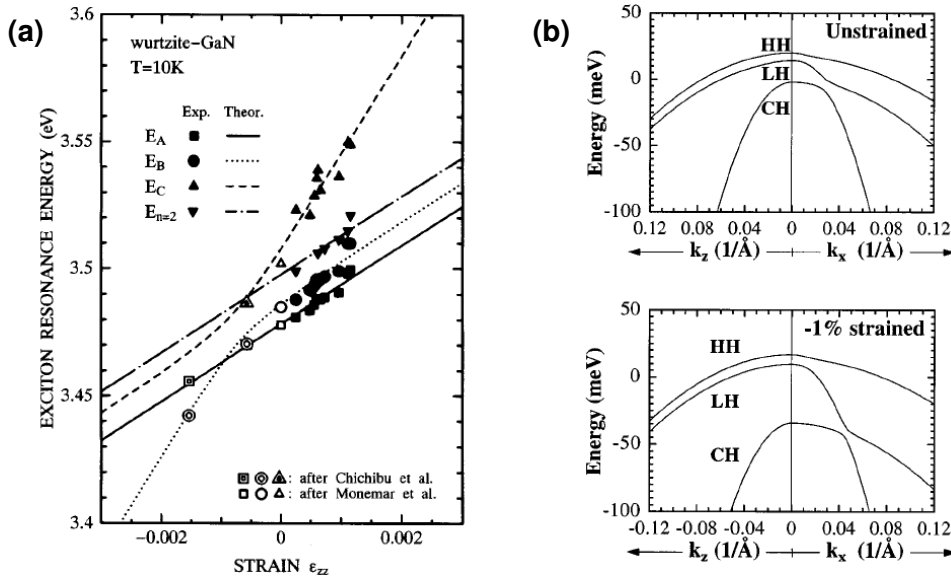


Figure 1.4 (a) Experimental data and theoretical model for the excitonic resonance energies E_A , E_B and E_C versus out-of-plane strain in GaN after Ref. [21]. (b) Valence-band dispersion relations for unstrained and -1% compressively strained wurtzite GaN after Ref. [23]. The horizontal axis is split to display dispersion along transverse k_x and longitudinal k_z direction.

1.4 Spontaneous and piezoelectric polarization

Spontaneous polarization Polarization is a phenomenon which occurs mainly on the atomic/molecular scale. Classically, polarizations is the formation of dipole moments as direct response due to an applied external electric field, *e.g.* the electronic polarization can be understood as the displacement of the electron cloud of the atom with respect to the nucleus in the presence of an electric field.

There is a class of materials exhibiting polarization without the presence of an external electric field. In so-called ferroelectrics, polarization is formed *spontaneously* if the temperature falls below a critical temperature T_C . On an atomic scale the crystal undergoes a phase transition from a (nonpolar) cubic structure to a polar structure. A typical example of ferroelectrics is BaTiO_3 . The polar structure is characterized by a spatial separation of positively and negatively charge centroids (Ba^{2+} and Ti^{4+} ions) resulting in a permanent dipole moment.

In III-V nitrides the spontaneous polarization is permanent and independent of the temperature due to their polar wurtzite structure. It is present in the ideal wurtzite structure and even reinforced due to non-ideality. Assessment of this deviation is the internal parameter u , which represents the cation-anion bond length along the c -axis normalized to c , and the ratio of the lattice parameters c/a . For the ideal wurtzite structure u takes the value $3/8=0.375$ while $c/a = \sqrt{8/3} = 1.633$. Taking the values from Table 1.3 the ratios c/a for GaN, AlN and InN amounts to 1.627, 1.601 and 1.623, respectively. Therefore the deviation from ideal wurtzite structure is biggest for AlN among the III-V nitrides. Results are summarized in Table 1.5. The polarization P is defined as the dipole moment per unit volume whose unit is consequently C/m^2 . The results are listed in the last column of Tab. 1.5. The spontaneous polarization P_{sp} follows the trend that for a stronger deviation from the ideal wurtzite structure its amount increases. Bernardini *et al.* [24] showed for AlN that if an ideal wurtzite structure is assumed the amount of P_{sp} is strongly reduced to approximately 30% of the actual value.

Material	c/a	c/a	u	$P_{\text{sp}}(\text{C/m}^2)$
GaN	1.627	1.634	0.376	-0.029
AlN	1.601	1.619	0.380	-0.081
InN	1.623	1.627	0.377	-0.032
Ref.	Tab. 1.1	[24]	[24]	[24]

Table 1.5 Unit cell parameters and spontaneous polarization of wurtzite group-III nitride semiconductors.

It is worth to underline this important property of III-V nitrides. Such high values of P_{sp} are not found in conventional strain-free III-V semiconductors. It is therefore more instructive to compare the III-V nitrides to ferroelectric materials. Typical representatives such as BaTiO_3 or LiNbO_3 exhibit P_{sp} of $\sim 0.3 \text{ C/m}^2$ and $\sim 3.0 \text{ C/m}^2$, respectively, *i.e.* P_{sp} in AlN is approximately 4 times smaller than in BaTiO_3 and 40 times smaller than in LiNbO_3 .

Piezoelectric polarization If layers are strained a second component adds to the spontaneous polarization P_{sp} , namely the piezoelectric polarization P_{pz} . The piezoelectric polarization for a wurtzite structure can then be expressed as [25]

$$\mathbf{P}_{pz} = \mathbf{e} : \boldsymbol{\epsilon} = \begin{pmatrix} 0 & 0 & 0 & 0 & e_{15} & 0 \\ 0 & 0 & 0 & e_{15} & 0 & 0 \\ e_{31} & e_{31} & e_{33} & 0 & 0 & 0 \end{pmatrix} : \boldsymbol{\epsilon} \quad (1.9)$$

where \mathbf{P}_{pz} couples to the strain vector (Voigt notation) *via* the piezoelectric tensor \mathbf{e} . The third rank tensor \mathbf{e} has $3^3=27$ independent elements which can further be reduced due to the crystal symmetry. In the case of a triclinic crystal (lowest symmetry) it reduces to 18 independent elements, in the case of wurtzite (high symmetry) there are only 3 independent elements, namely e_{31} , e_{33} and e_{15} as can be seen from Equation (1.9). The piezoelectric polarization which builds up in the (0001) direction couples to the e_{31} and e_{33} element while the e_{15} element couples to the shear strains. Considering only the polarization in (0001) direction, Equation (1.9) reduces to

$$P_{pz} = 2 e_{31} \epsilon_{\parallel} + e_{33} \epsilon_{\perp} \quad (1.10)$$

where the components of $\boldsymbol{\epsilon}$ are replaced by the in-plane and out-of-plane strains ϵ_{\parallel} and ϵ_{\perp} , respectively. The values of e_{31} , e_{33} and e_{15} are listed in Table 1.6 as obtained by Bernardini *et al.* [24]. There are some remarkable peculiarities. Firstly, the absolute values of e_{31} and e_{33} are approximately ten times larger than in conventional III-V or II-VI semiconductors. Secondly, the signs of e_{31} and e_{33} are the same as in II-VI semiconductors and opposite to III-V semiconductors. And thirdly, the magnitude of e_{31} and e_{33} increases if one moves upward within period V (from Sb to N) since the ionic contribution will dominate over the electronic contribution to the bond if the anion becomes lighter [24].

To choose an example we go back to the coherently strained AlN epilayer grown on strain-free GaN. With $\epsilon_{\parallel} = +2.4\%$ and $\epsilon_{\perp} = -1.4\%$ and the piezoelectric constants for AlN according to Table 1.6 P_{pz} in Equation (1.10) evaluates to -0.049 C/m^2 while the spontaneous polarization P_{sp} within the AlN is -0.081 C/m^2 , *i.e.* both P_{pz} and P_{sp} are in the same order of magnitude.

Material	$e_{33} \text{ (C/m}^2\text{)}$	$e_{31} \text{ (C/m}^2\text{)}$	$e_{15} \text{ (C/m}^2\text{)}$
GaN	0.73	-0.49	-0.30
AlN	1.46	-0.60	-0.48
InN	0.97	-0.57	-

Table 1.6 Piezoelectric constants of wurtzite group-III nitrides [24].

1.5 Heterostructure engineering

Band offsets and strain effects on band offsets The reliable determination of band offsets in nitride heterostructures is a difficult task. Relying on x-ray photoelectron spectroscopy (XPS) requires sophisticated correction methods due to the presence the strong polarization fields and localized carriers [26]. If heterostructures are lattice-mismatched the strain acting on the unit cells shifts the valence band offset (VBO) ΔE_V and band gap ΔE_g , resulting even in forward-backward asymmetries of band offsets [27]. For pseudomorph AlN/GaN the values amounts to $\Delta E_{V,AlN/GaN} = 0.3$ eV [26, 27] and $E_{g,AlN\text{ strained}} = 5.5$ eV resulting in a conduction band offset (CBO) of $\Delta E_{C,AlN/GaN} = 1.7$ eV. For InN/GaN XPS measurements give a value of $\Delta E_{V,InN/GaN} = 0.6$ eV, resulting with $E_{g,InN} = 0.64$ eV in a CBO of $\Delta E_{C,InN/GaN} = 2.2$ eV.

The trends in band alignments in (relaxed) III-V nitride binaries are sketched in Figure 1.5. To fix the energy scale the GaN valence band is set to 0 eV. Additionally, the case of AlN bandgap reduction (due to tensile in-plane strain) and shift of respective CBO and VBO if AlN is grown coherently on relaxed GaN is depicted as dashed column. Similar experimental data for InN are not yet available due to the extreme small critical thickness for plastic relaxation. The indicated strained case is an estimation based on the latest results on InN deformation potentials by Gil and coworkers.

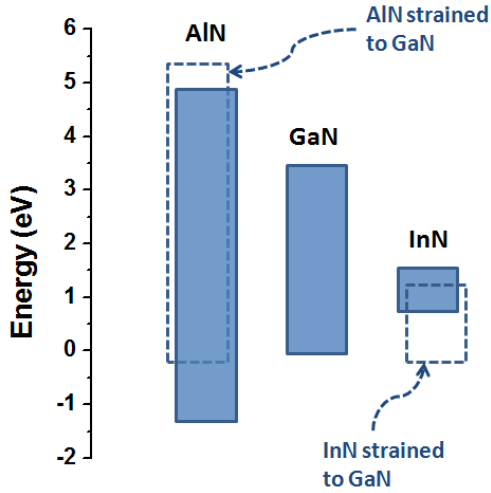


Figure 1.5 Band alignments of (relaxed) III-V nitride binaries shown as full columns. To fix the energy scale the GaN valence band is set to 0 eV. Additionally, the case of AlN bandgap reduction and shift of respective CBO and VBO is depicted (dashed column) if AlN is grown coherently on relaxed GaN. Similar experimental data for InN is not yet available due to the extreme small critical thickness of ~ 1 nm. Values are estimated with the latest results on InN deformation potentials by Gil *et al.*.

Electric fields and Quantum confined stark effect As already indicated throughout Chapter I, the presence of polarization has tremendous effects in the band diagrams of heterostructures. The total polarization discontinuity σ across a heterointerface if a nitride layer B is grown onto a layer A and with crystal orientation along (0001) is given as

$$\sigma = n \cdot (P_A - P_B) = n \cdot ((P_{sp,A} + P_{pz,A}) - (P_{sp,B} + P_{pz,B})) \quad (1.11)$$

where n is the unitary vector of the (0001) plane. To come back to the example of the strained AlN/GaN layer with GaN equal to layer A and AlN equal to layer B Equation (1.11) evaluates to $((-0.029 \text{ C/m}^2 + 0 \text{ C/m}^2) - (-0.081 \text{ C/m}^2 + (-0.049 \text{ C/m}^2))) = +0.101 \text{ C/m}^2$ or in units of a charge density σ/e , with the elementary charge e , the result correspond to $+6.4 \times 10^{17} \text{ m}^{-2}$. Note that the sign is positive but would be opposite if the order of the stack would be

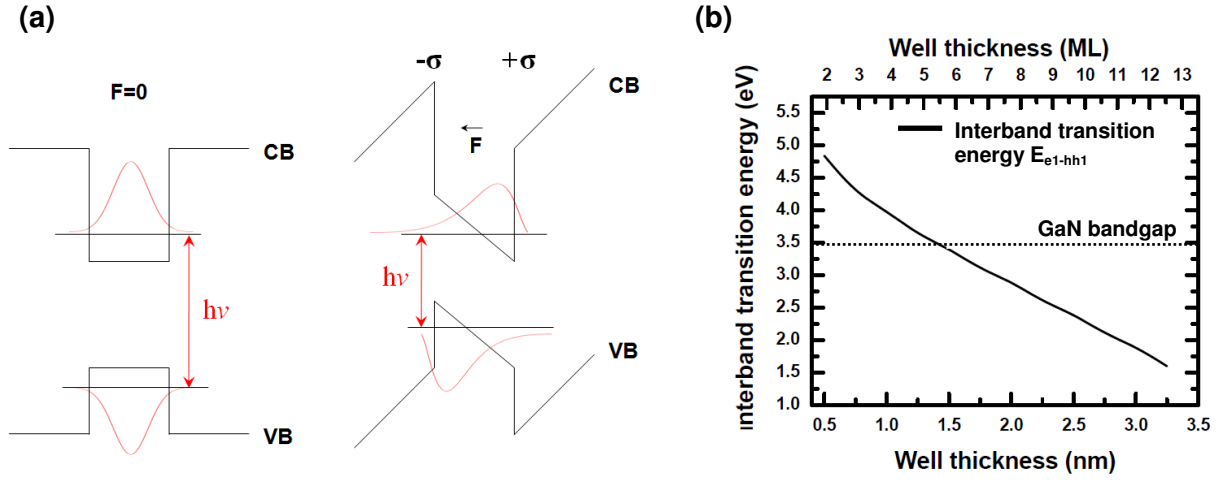


Figure 1.6 (a) CB and VB wavefunctions in an AlN/GaN/AlN QW in the presence and absence (flat-band case) of polarization charge density. (b) Interband transition energy in an AlN/GaN single quantum well (SQW) after Ref. [28].

inverted while keeping the strain conditions, *i.e.* a GaN/AlN heterointerface. If the heterointerface lies within the sample, *i.e.* is far from surface where boundary conditions become crucial and the polarization charge density is not compensated by mobile carriers the electric fields $F_{A/B}$ are directly given by

$$F_A = -\frac{\sigma}{\epsilon_0 \epsilon_A} \quad F_B = \frac{\sigma}{\epsilon_0 \epsilon_B} \quad (1.12)$$

which yields in the case of AlN/GaN with $\sigma = +0.101 \text{ C/m}^2$ a field of $\sim 10 \text{ MV/cm}$. It is clear that such extremely high fields have tremendous effects on optical properties. In Figure 1.6 (a) the band diagrams of a GaN QW which is embedded between two AlN layers is sketched schematically in the presence and absence of polarization charges. The presence of the piezoelectric charges alters the flat-band situation in the QW on the left side into an triangular shape on the right side. The wavefunctions calculated on such a band diagram are consequently located closer to the interface reducing strongly their overlap. Further the transition energy $E_{e_1-hh_1}$ for the emission of photons is strongly reduced. This is a crucial aspect to consider in designing optoelectronic devices. The transition energy can be expressed as

$$E_{e_1-hh_1} = e_1 + hh_1 + E_g - E_X - eF_w t_w \quad (1.13)$$

where e_1 and hh_1 represent the electron and hole confinement energies, E_g the bandgap of the QW material and E_X the exciton binding energy. The term $-eF_w t_w$, where F_w and t_w refer to the electric field and the thickness of the QW, is responsible for the so called *Stark effect*, which leads to a situation where the transition energy $E_{e_1-hh_1}$ can be significantly lower than the bulk bandgap value E_g of the QW material. In Figure 1.6 (b) the transition energies in an AlN/GaN single quantum well (SQW) are shown as a function of the QW thickness t_w after

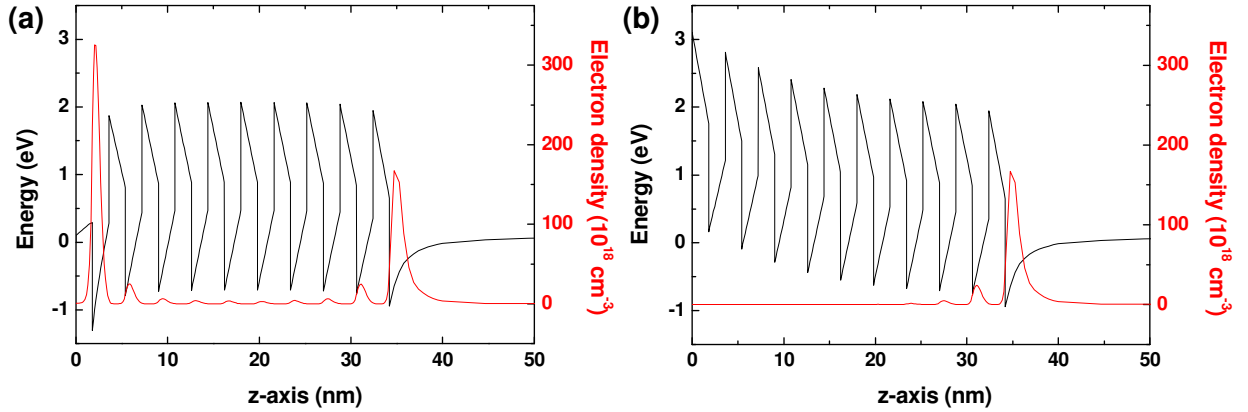


Figure 1.7 Band diagram of an AlN/GaN multi quantum well (MQW) grown on GaN for a pinned surface potential of (a) 0 eV and (b) 3 eV at $z=0$ nm together with the resulting electron distribution.

Ref. [28]. The horizontal line represents the GaN bandgap energy. If the QW thickness is lower than 1.5 nm the confinement terms e_1 and hh_1 dominates in Equation (1.13), while for QW thicknesses >1.5 nm the term $-eF_w t_w$ dominates. However it is clear that if the QW is much thicker than a few nm the field inside the QW weakens also and the transition energy $E_{e_1-hh_1}$ recovers the bulk bandgap value of the QW material. This is due to the screening of F_w by free carriers. For $\text{In}_{0.13}\text{Ga}_{0.87}\text{N}/\text{GaN}$ QW *e.g.* this occurs at a thickness of ~ 20 nm [17]. A plot of $E_{e_1-hh_1}$ versus t_w (in the linear regime) allows therefore estimating F_w , as it was done *e.g.* in Ref. [29] for lattice-matched $\text{Al}_{0.85}\text{In}_{0.15}\text{N}/\text{GaN}$ QW heterostructures.

Surface states and Fermi level pinning So far no surface effects in nitride heterostructures were discussed. At nitride surfaces unoccupied cation dangling bonds and metallic cation adlayers pin the Fermi level within the bandgap [30]. On the same time the surface atomic sheet density is $1/a^2 \sim 10^{15} \text{ cm}^{-2}$, *i.e.* ~ 100 times the polarization sheet charge density of an AlN/GaN heterostructure with $\sigma_{\text{AlN/GaN}}/e = +6.4 \times 10^{13} \text{ cm}^{-2}$. The surface with its distorted bonds provides therefore a huge reservoir of electrons. They are accumulated at the heterointerface between AlN/GaN forming a so-called two dimensional electron gas (2DEG) and compensating at the same time the piezoelectric charge density bound to the heterointerface. If the heterostructure is free of dopants, the maximum 2DEG density of $6.4 \times 10^{13} \text{ cm}^{-2}$ is recovered in the limit of an infinitely thick AlN epilayer. This will be practically prevented by the onset of plastic relaxation of the AlN epilayer at a certain critical thickness (typically a few nm) and will consequently lead the loss of the piezoelectric contribution to the total polarization charge density. Taking another instructive example of an AlN/GaN multi-quantum well (MQW) grown on a GaN substrate, as illustrated in Figure 1.7, to demonstrate the tremendous effect of Fermi level pinning on heterostructure design. Left panel show the theoretical profile of a surface potential (energy difference between CB and Fermi level at $z=0$) close to zero while right panel displays the more realistic case of a surface potential of half the AlN bandgap. The calculation was done self-consistently according to the framework described in Chapter 5. As it can be seen the carrier distribution is drastically changed since the electrons tend to locate close to the interface with the GaN substrate while additionally only three QWs are slightly occupied. A further discussion of these heterostructures can be found in Ref. [28].

Bibliography

- [1] M. Craven *et al.*, *Structural characterization of nonpolar (1120) a-plane GaN thin films grown on (1102) r-plane sapphire*, Appl. Phys. Lett **81**, 469 (2002).
- [2] Y. Sun *et al.*, *Impact of nucleation conditions on the structural and optical properties of m-plane GaN (1100) grown on γ -LiAlO₂*, J. Appl. Phys. **92**, 5714 (2002).
- [3] S. Adachi, *properties of group-IV, III-V and II-VI semiconductors* (Wiley, 2005).
- [4] http://en.wikipedia.org/wiki/Gallium_nitride.
- [5] J. Wu *et al.*, *Unusual properties of the fundamental band gap of InN*, Appl. Phys. Lett. **80**, 3967 (2002).
- [6] I. Vurgaftman, and J. R. Meyer, *Band parameters for nitrogen-containing semiconductors*, J. Appl. Phys. **94**, 3675 (2003).
- [7] E. Iliopoulos *et al.*, *Energy bandgap bowing of InAlN alloys studied by spectroscopic ellipsometry*, Appl. Phys. Lett. **92**, 191907 (2008).
- [8] <http://de.wikipedia.org/wiki/III-V-Verbindungshalbleiter>.
- [9] Y. P. Varshni, *Temperature Dependence of Energy Gap in Semiconductors*, Physica **34**, 149 (1967).
- [10] <http://www.ioffe.rssi.ru/SVA/NSM/Semicond/>.
- [11] D. Jena, *Polarization effects in semiconductors : from ab initio theory to device application* (Springer, New York, 2007).
- [12] I. N. Remediakis, and E. Kaxiras, *Band-structure calculations for semiconductors within generalized-density-functional theory*, Phys. Rev. B **59**, 5536 (1999).
- [13] <http://www.ioffe.rssi.ru/SVA/NSM/Semicond/GaN/index.html>.
- [14] R. Dingle *et al.*, *Absorption, Reflectance, and Luminescence of GaN Epitaxial Layers*, Phys. Rev. B **4**, 1211 (1971).
- [15] F. Bechstedt, U. Grossner, and J. Furthmuller, *Dynamics and polarization of group-III nitride lattices: A first-principles study*, Phys. Rev. B **62**, 8003 (2000).
- [16] W. Slaughter, and B. Verlag, *The linearized theory of elasticity*, CURRENT SCIENCE **84**, 232 (2003).
- [17] O. Ambacher, and V. Cimalla, *Polarization effects in semiconductors : from ab initio theory to device application* (Springer, New York, 2007).
- [18] B. Gil, and O. Briot, *Internal structure and oscillator strengths of excitons in strained α -GaN*, Phys. Rev. B **55**, 2530 (1997).
- [19] B. Gil, O. Briot, and R. L. Aulombard, *Valence-band physics and the optical properties of GaN epilayers grown onto sapphire with wurtzite symmetry*, Phys. Rev. B **52**, 17028 (1995).
- [20] G. L. Bir, *Symmetry and strain-induced effects in semiconductors [by] G. L. Bir and G. E. Pikus. With foreword by J. C. Hensel. Translated from Russian by P. Shelnitz. Translation edited by D. Louvish* (Wiley, New York, 1974).

1 Material Properties of III-V Nitride Semiconductors

- [21] A. Shikanai *et al.*, *Biaxial strain dependence of exciton resonance energies in wurtzite GaN*, J. Appl. Phys. **81**, 417 (1997).
- [22] Q. Yan *et al.*, *Strain effects in group-III nitrides: Deformation potentials for AlN, GaN, and InN*, Appl. Phys. Lett. **95**, 121111 (2009).
- [23] S. L. Chuang, and C. S. Chang, *k-p method for strained wurtzite semiconductors*, Phys. Rev. B **54**, 2491 (1996).
- [24] F. Bernardini, V. Fiorentini, and D. Vanderbilt, *Spontaneous polarization and piezoelectric constants of III-V nitrides*, Phys. Rev. B **56**, 10024 (1997).
- [25] H. Morkoç, and J. Leach, *Polarization effects in semiconductors : from ab initio theory to device application* (Springer, New York, 2007).
- [26] X. Q. Xu *et al.*, *Influence of band bending and polarization on the valence band offset measured by x-ray photoelectron spectroscopy*, J. Appl. Phys. **107** (2010).
- [27] F. Bernardini, and V. Fiorentini, *Macroscopic polarization and band offsets at nitride heterojunctions*, Phys. Rev. B **57**, R9427 (1998).
- [28] S. Nicolay, *Physics and applications of intersubband transitions in nitride based heterostructures*, Thesis EPFL, no. 4106, Dir.: N. Grandjean (2008).
- [29] R. Butté *et al.*, *Current status of AlInN layers lattice-matched to GaN for photonics and electronics*, J. Phys. D Appl. Phys. **40**, 6328 (2007).
- [30] D. Segev, and C. G. V. d. Walle, *Origins of Fermi-level pinning on GaN and InN polar and nonpolar surfaces*, EPL (Europhysics Letters) **76**, 305 (2006).

Heteroepitaxy and characterization of GaN (0001)

2.1 Introduction

Since the quality of the buffer layer is of crucial importance for device performance this chapter is dedicated to the growth and characterization of GaN, which act as channel material in the final HEMT device. Especially the growth on different substrates, their advantages and drawbacks are discussed. For example growth on sapphire allows for a low-cost mass production while a growth on silicon-carbide (SiC) offers high thermal conductivity, which is crucial for performance and long-time device reliability. However, the epitaxy of GaN on SiC and silicon (Si) substrates cannot be performed directly due to wetting issues leading to 3D growth. Therefore the introduction of an AlN seed interlayer is required. The growth on Si is especially interesting for hybrid structures allowing on-chip combination of GaN and Si technologies and circuits. Further Si can easily and cost-efficiently be chemically etched which provides a low-cost substrate removal. In the following, structural and electrically properties of epitaxially grown GaN films on these different substrates will be discussed.

2.2 Metal-organic vapor phase epitaxy (MOVPE)

Metal-organic vapor phase epitaxy (MOVPE) is a growth technique that is carried out at moderate pressures (2-100 kPa), contrarily to growth techniques such as molecular beam epitaxy (MBE) which takes place under vacuum conditions. Since the metal atoms (*i.e.* Ga, Al, In) cannot be brought in the gas phase in their elementary form, these reactants are provided as metal-organic precursors, namely as trimethylgallium (TMGa), triethylgallium (TEGa), trimethylaluminium (TMAI) and trimethylindium (TMIn). The metal-organic precursors are stocked in so-called 'bubblers' where they form a saturated vapour with a pressure P_{vap} above the liquid. The 'bubblers' are surrounded by a thermostatic bath to adjust a defined vapour pressure. Then a carrier gas (typically H_2 or N_2) is flowing through the 'bubblers' taking an amount of molecules along. This amount arrives as metal-organic flow in the growth chamber.

The typical MOVPE growth process can be summarized by the following stages: transport of the reactants near to the substrate surface, chemical reaction and adsorption, surface kinetics and growth, desorption and removal of reaction by-products. For the growth of III-V nitrides the nitrogen is provided to the reaction chamber by means of ammonia (NH_3). Then the reaction can be written as $(\text{CH}_3)_3\text{Ga} + \text{NH}_3 \rightarrow \text{GaN}_{(\text{solid})} + 3\text{CH}_{4(\text{gas})}$. Note that this is only a very simplified picture of the real reactions which involve also pre-reactions and additional reaction products. Ammonia exhibits only a very low decomposition rate (typically 10%), consequently a large amount of ammonia has to be introduced into the growth chamber (V/III ratio ~600 for GaN). MOVPE is a technique where only the substrate is heated, not the chamber in total. Therefore the surface growth kinetics depends crucially on

2 Heteroepitaxy and characterization of GaN

the substrate or growth temperature. It is desired to adjust the growth temperature in order that the growth process is only limited by the diffusion rate of reactants to the substrate surface (diffusion controlled regime) which depends only weakly on temperature. If the growth temperature is on the other hand too low (kinetic regime) the growth process is blocked by a decreased rate of desorbed reaction by-products. Choosing the growth temperature too high will result in a decomposition of the reactants before they arrive at the substrate surface (desorption regime). Despite a high quality of the precursors it is inevitable in MOVPE growth to incorporate impurity atoms such as C, O or H in the crystal.

Samples discussed in this work have been grown using an Aixtron 200/4 RF-S low pressure MOVPE reactor. A sketch of such a MOVPE reactor is shown in Figure 2.1. This reactor is limited to 2-inch substrates while growth temperatures can be raised up to 1200° C. To prevent pre-reactions of metal-organics with NH₃ the reactor is provided with a separation plate and individual feeds for metal-organics and ammonia. Ammonia as well as silane (SiH₄), which is conventionally used for *n*-doping, are stored in pressurized gas bottles and are separately introduced into the growth chamber *via* the lower feed. The metal-organic flow ($flow_{MO}$) arriving in the reactor chamber, depending on the carrier gas flow ($flow_{source}$) and the source pressure (P_{source}) is given by the following relation

$$flow_{MO} = flow_{source} \frac{P_{vap}}{P_{source} - P_{vap}} \approx flow_{source} \frac{P_{vap}}{P_{source}} \quad (2.1)$$

During the growth, the thickness of the epilayer and hence the growth rate can be measured precisely by means of an *in situ* reflectivity setup consisting of a laser with the wavelength $\lambda=950$ nm, which is placed above the rotating substrate holder plate. The thickness d of the growing layer can be obtained from the number of Fabry-Perot interference fringes where one oscillation period corresponds to a thickness of

$$d = \frac{\lambda}{2n_{GaN}} = 206 \text{ nm} \quad (2.2)$$

where the refractive index n of GaN is ~ 2.3 .

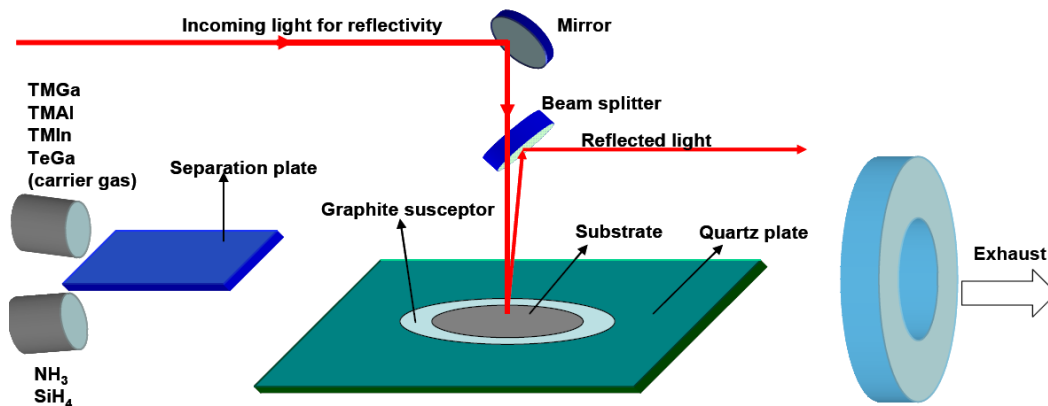


Figure 2.1 Schematic sketch of a MOVPE reactor with *in situ* reflectivity measurement setup.

2.3 Substrate for GaN epitaxy (GaN, sapphire, SiC, Si)

The most desirable substrate for the growth of GaN is of course **GaN (0001)** itself enabling homoepitaxy. During the last decades several methods were developed in order to provide high-crystalline quality and large-size GaN substrates. The most successful and commercial available method is based on hydride vapour phase epitaxy (HVPE), which allows growth rates larger than 100 $\mu\text{m/h}$ thanks to the use of GaCl as precursor instead of metal organics. With such a high growth rate thick layers of several mm can be grown up to 6-inch wafers. Interestingly it has been demonstrated that the dislocation density decreases toward the surface with increasing thickness [1], lying typically around $\sim 10^{4-5} \text{ cm}^{-2}$. Then GaN layer can be lifted-off from the foreign substrate by a decomposition of the GaN at the heterointerface induced by a laser pulse through the transparent substrate [2] or by means of a self-separation process [3]. Once obtained the bulk-like GaN, also referred to as *boule*, it is possible to saw it perpendicular to the *c*-plane growth axis in order to obtain single wafers with a thickness typically around 400 μm . Since the manufacturing method is quite expensive the price for a single free-standing (FS) GaN wafer lies between 2000-9000 \$ per 2-inch wafer, depending on the dislocation density. However, these high-quality substrates are required to improve the performance of laser diodes. It is obvious once having a layer with a few mm thickness to cut slices parallel to the growth axis to fabricate *m*-plane substrate. There is a big interest in this orientation since it allows to get rid of polarization effects [4] and it has been proven that LED grown onto these substrates exhibit superior efficiency [5]. Both types of substrates are commercially available [6, 7], but the size is limited to $5 \times 15 \text{ mm}^2$.

A much cheaper alternative is for the moment the growth on foreign substrates. The most common substrates for GaN growth are Si(111), SiC, and Al_2O_3 (sapphire), which have each specific advantages and drawbacks. Optimized GaN layers grown on those substrates are also commercially available as templates. Especially GaN grown on sapphire and Si are a low-cost alternative with respect to FS GaN. However, there is the drawback of higher dislocation density (typically $10^8 - 10^{10} \text{ cm}^{-2}$), *i.e.* a marginal quality. This can be improved *via* epitaxial lateral overgrowth (ELO) to reduce further defect densities [8].

Beside established MOVPE and HVPE growth methods, recently another technique becomes competitive, the so-called ammonothermal growth [9, 10]. The outstanding material quality is accompanied by very low dislocation densities $\sim 10^3 \text{ cm}^{-2}$ and therefore ultra-low broadening of the x-ray rocking curve ($\sim 16 \text{ arcsec}$). At the present stage *c*-plane GaN seeds up to 2-inch in diameter can be manufactured with this technique [11].

As pointed out as foreign substrates there are mainly three interesting candidates, namely Si(111), SiC, and **Al_2O_3 (sapphire)**. The latter one has the advantage of high material strength with a high Young's modulus E . It is now expected from simple models [12] that wafer bowing is proportional to $\sim E_{\text{GaN}}/E_{\text{Substrate}} \cdot (\alpha_{\text{Substrate}} - \alpha_{\text{GaN}})$, with the thermal expansion coefficient α . Consequently bowing effects for GaN/sapphire are expected to be much lower than GaN/Si(111) despite similar α mismatches. Another advantage is its availability up to 6-inch wafers and its low price, *e.g.* ~ 50 \$ for a 2-inch wafer. On the other hand, the main drawbacks are its poor thermal conductivity and insulating.

Contrarily, the most desirable substrate for high power electronics would certainly be **SiC** due to its superior thermal conductivity κ which is even three times higher than for GaN. Together with its low *a*-lattice parameter mismatch of $\sim 3\%$ it is certainly the substrate of choice for this type of application. Unfortunately with ~ 1000 - 2000 \$ per 2 inch-6H-SiC-high resistivity wafer it is still very expensive. Doped substrates are available at lower prices.

2 Heteroepitaxy and characterization of GaN

A trade-off between sapphire and SiC would certainly be **Si(111)**. Since it combines high κ with a relatively low price around 70 \$ per 2-inch wafer. Furthermore it is desirable to combine the advantages of Si and GaN in electrical circuits on one chip [13]. Si offers additionally the possibility of easy substrate removing by wet etching. The main drawbacks are the large lattice mismatch and the thermal expansion coefficient mismatch which leads to large wafer bowing effects and cracking of the epilayers. From the device point of view main drawbacks of the Si substrate are a reduced breakdown voltage and potential RF losses.

The physical properties of the different substrates for GaN epitaxy as discussed above are summarized in Table 2.1.

Substrate	GaN (0001)	Al ₂ O ₃ (0001)	6H-SiC	Si (111)
a (Å)	3.187	4.759	3.073	3.840
$\epsilon_{\parallel, \text{GaN}}$ (%)	0	+49	-3.6	+20.5
E (GPa)	150	470	700	160
κ (W cm ⁻¹ K ⁻¹)	1.3	0.23	4.9	1.3
α (10 ⁻⁶ K ⁻¹)	5.6	6.7	4.3	2.6

Table 2.1 Properties of different substrates. Here a , ϵ_{\parallel} , E , κ and α are in-plane equilibrium lattice constant, the (hypothetical) biaxial strain of a GaN layer pseudomorphically grown on the respective substrate, the Young's modulus, the thermal conductivity and thermal expansion coefficient, respectively. Young's modulus is an indication for physical hardness and strength of wafer bowing effects. Values are taken from Ref. [14].

2.4 Epitaxy of GaN

GaN/Al₂O₃ GaN layers grown directly on sapphire substrates usually exhibit rough surfaces with high density of dislocations $> 10^{10}$ cm⁻². This is due to the large lattice-mismatch between GaN and sapphire and to a co-existence of grains having various orientations. However, the growth of high-quality GaN epitaxial layers with smooth surface morphology and low dislocation density ($\leq 10^9$ cm⁻² range) became possible by growing a thin AlN or GaN layer at low-temperature around $T_g=500^\circ\text{C}$ (LT-buffer) on the sapphire surface prior to the high-temperature growth ($T_g>1000^\circ\text{C}$) of the main GaN layer (HT-GaN). This method was developed by Amano *et al.* and Nakamura *et al.*, and is called as “2-step growth” [15, 16]. The widely accepted model of the conventional 2-step growth method with a GaN buffer is as follows. The growth of the LT-buffer forms high-density GaN islands with different crystal types (cubic and hexagonal) and different crystal orientations on the sapphire surface. However, islands are transformed into low surface density (0001) Ga-faced hexagonal crystals during the temperature ramping process after the LT-buffer growth. Then, the growth of HT-GaN induces an epitaxial lateral overgrowth (ELO)-like growth of the initial islands at first, leading to the increase of their lateral sizes. Further growth of the HT-GaN induces island coalescence, resulting in (0001) Ga-faced smooth GaN surface. The dislocations are formed within the initial GaN islands due to the lattice-mismatch and at the coalescence boundaries due to island misorientation. However, most of the dislocations generated at the initial stage of the buffer layer deposition are bend during the ELO-like growth process. This results in a dislocation density down to mid 10^8 cm⁻² after a few GaN μm growth.

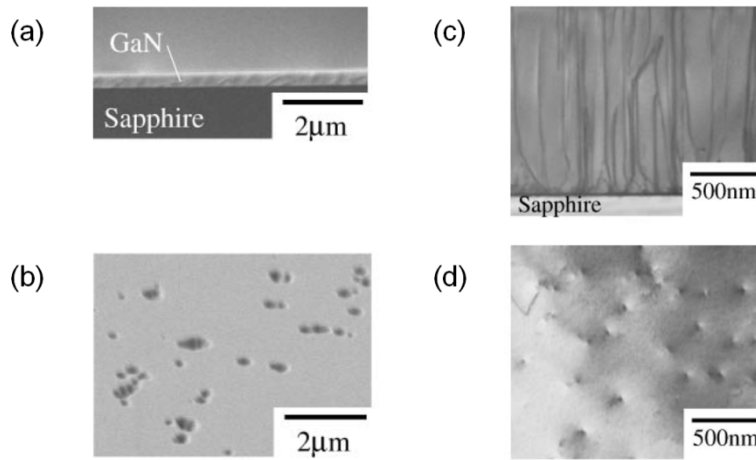


Figure 2.2 (a) and (b) cross-sectional and plan-view SEM images of the 2-step growth sample whose growth was interrupted at the initial stage (300 nm) of the HT-GaN growth. (c) and (d) [1120] cross-sectional and plan-view bright-field TEM images for the 2 μm thick GaN/sapphire wafer grown using the 2-step growth. At the end of the HT growth the pits from subfigure (b) are vanished and the GaN exhibits a smooth surface (subfigure (d)). Pictures are taken from Ref. [17].

GaN/(AlN)/SiC and GaN/(AlN)/Si SiC possess a 10 times higher thermal conductivity than sapphire and even Si exceeds that of sapphire by a factor three. Therefore these are the substrates of choice for high power application. The former has the advantage of high epilayer quality while the latter is interesting for low-cost devices. The main drawback for the growth on both substrates is the high difference of thermal expansion coefficients between GaN and the substrate. In addition to that, GaN does not wet SiC or Si surfaces, which leads to 3D growth with poor material quality and surface morphology. A common approach is therefore the introduction of an AlN nucleation layer.

The role of the AlN nucleation layer was studied intensively *in situ* by Waltereit *et al.* for GaN/(AlN)/6H-SiC grown by molecular beam epitaxy (MBE) [18]. Deposition of GaN directly on SiC results in a 3D growth front where the GaN layer is already fully relaxed. This result is not unexpected because of the large lattice mismatch $\sim 3.4\%$ between GaN and SiC and from the difference in surface free energy. However, the situation is different for the case of AlN nucleation layers. In agreement with reported values of critical thicknesses of the 1% mismatched AlN/6H-SiC (0001) interface, a 5 nm AlN layer grows coherently on SiC, exhibiting a quite flat surface. Note, however, that the lattice mismatch between GaN and this strained AlN layer is the same as that between GaN and SiC. Nevertheless, GaN exhibits 2D growth on the AlN layer and roughens only after 40 nm of deposition.

Similar to MBE, GaN deposited *via* MOVPE directly on 6H-SiC substrates at 900 °C exhibits columnar-like grains, faceted surfaces, and high net carrier concentrations ($n_D - n_A > 1 \times 10^{19} \text{ cm}^{-3}$) [19]. In contrast, both the HT-AlN buffer layers and the subsequently grown GaN films deposited on similar SiC substrates are monocrystalline with low misorientation and low-angle grain boundaries as shown in Figure 2.3 (a). On the contrary, the growth of the AlN nucleation layer on Si(111) is not coherent and forms domains and even amorphous AlN/Si interface [20]. GaN epilayers exhibit flat surface with a root mean square (rms) roughness of $\sim 0.3 \text{ nm}$ and dislocation density of $\sim 1 \times 10^{10} \text{ cm}^{-2}$.

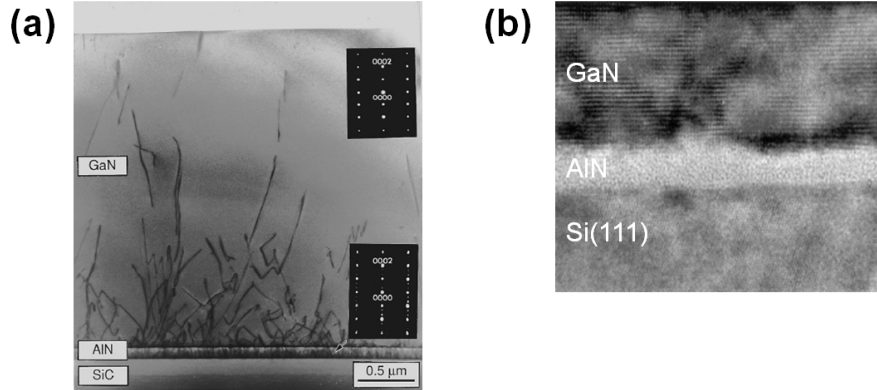


Figure 2.3 (a) Cross-sectional TEM micrograph of a 2.7 μm GaN(0001) film deposited at 950 $^{\circ}\text{C}$ *via* MOVPE on a high-temperature (1100 $^{\circ}\text{C}$) monocrystalline AlN buffer layer predeposited on a vicinal 6H-SiC(0001) substrate. Image is taken from Ref. [19]. (b) TEM image of 500 nm GaN film grown on a 1200 $^{\circ}\text{C}$ AlN buffer layer predeposited on a Si(111) substrate. The image reveals an amorphous layer at Si/AlN interface. Image is taken from Ref. [20].

2.5 Characterization of GaN epilayers

After introducing general aspects and citing state-of-the art work done in this field of GaN epitaxial growth we refer in the following to the characterization of samples grown in our group. Various techniques are brought together to investigate the structural, optical and electrical properties of the GaN templates. Especially, the insertion of an annealing phase between the growth of the LT-GaN and the HT-GaN with a temperature of 1160 $^{\circ}\text{C}$, *i.e.* ~ 100 K above the HT-GaN growth temperature, leads to a significant improvement in the GaN template resistivity.

2.5.1 X-ray diffraction (XRD)

XRD is a very important tool for a non-destructive structural characterization of semiconductor bulk crystals or heterostructures. It gives various information about crystalline quality, lattice parameters, wafer bowing effects, dislocation density, thicknesses of epilayers, interface morphology or alloy composition.

To measure the Bragg diffraction angle θ_B so-called ω - 2θ scans are recorded, which refers to a situation where the sample rotates around the angle ω , while the detector rotates with twice this velocity around the angle 2θ . If the Bragg condition $\lambda = 2d_{hkl} \sin \theta_B$ for a given lattice spacing d_{hkl} of the crystal is met at a certain scan angle, constructive interference will lead to a peak maximum of the reflected intensity. In Bragg's law hkl refers to the Miller index and λ to the wavelength of the x-ray source. Here the Cu $K\alpha_1$ radiation with a wavelength of 1.540562 \AA is used.

In Figure 2.4 (a) high-resolution ω - 2θ scans around the symmetric (002) and the asymmetric (105) reflections are shown for GaN (0001) layers grown on sapphire. The peak at $\sim 17.27^{\circ}$ correspond to the GaN (002) reflection as can be expected from Bragg's law. Furthermore, if previously a calibration procedure is carried out, the measured Bragg angle can be used to determine the lattice parameters c (symmetric) and a (asymmetric).

Wurtzite GaN [0001] exhibits a significant amount of dislocations as can be seen from Figure 2.2. In general screw, edge and mixed-type dislocations can occur within GaN, where the following Burgers vectors can be assigned: $\mathbf{b} = [0001]$, $\mathbf{b} = [1120]$, and $\mathbf{b} = 1/3 [1123]$, respectively [21]. Screw dislocations lead to a local distortion of the c -plane distances (tilt) and have consequently an impact on symmetric XRD scans. Edge dislocations cause a local in-plane deviation from the hexagonal configuration but do not distort the distances between planes perpendicular to the [0001] direction (twist) so that symmetric scans are not suitable to detect this type of dislocation. Consequently, asymmetric XRD scans are required to measure the influence of edge dislocations. Indeed, the dislocation density can be related to the full width at half maximum (FWHM) $\Delta\omega$ of the symmetric (002) and asymmetric (105) scans if wafer bowing effects are neglected. For our GaN (0001) layers grown on sapphire according to Fig. 2.4 (a) these linewidths amounts to 43 arcsec and 119 arcsec, respectively. The larger $\Delta\omega$ for asymmetric scans is obvious since it comprise broadening due to edge and screw dislocations. Comparing these $\Delta\omega$ with literature values, the edge and screw dislocation density should be lower than $1 \times 10^{-10} \text{ cm}^{-2}$ and $1 \times 10^{-7} \text{ cm}^{-2}$, respectively [22].

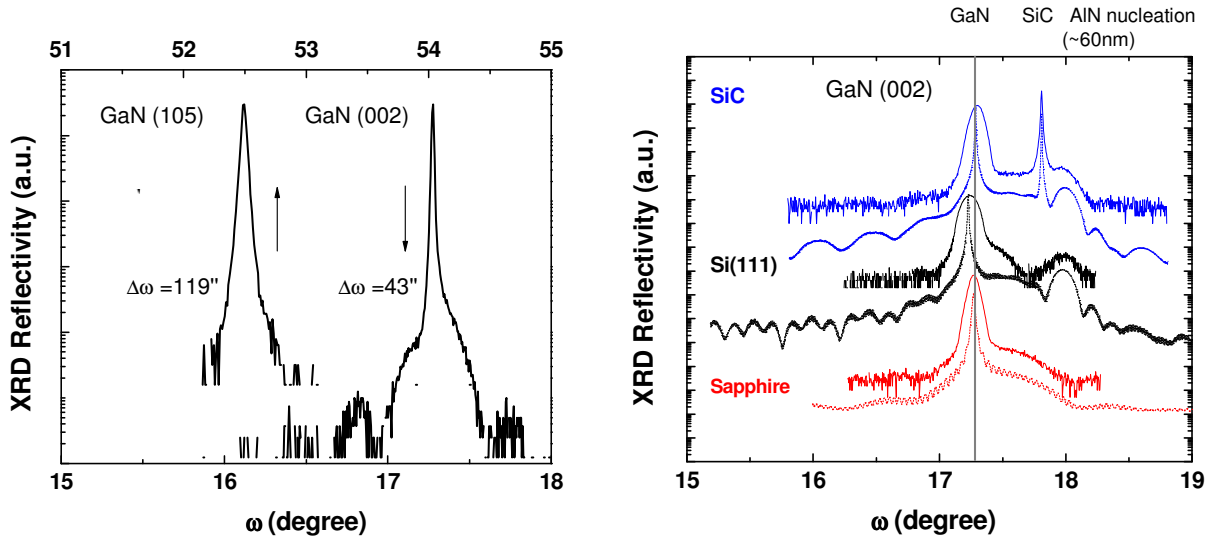


Figure 2.4 (a) Symmetric and asymmetric x-ray diffraction ω -scans around the (002) and the (105) reflex, respectively for a GaN film grown on sapphire. (b) ω -scans around the (002) reflex for GaN/sapphire (red), GaN/(AlN)/Si(111) (black) and GaN/(AlN)/SiC (blue) together with simulated scans.

Figure 2.4 (b) shows ω -scans around the (002) reflex for GaN/sapphire (red), GaN/(AlN)/Si(111) (black) and GaN/(AlN)/SiC (blue) together with simulated curves. The simulation of these curves is a highly non-trivial task. For a further reading the attention is drawn to Ref. [23]. GaN films grown on sapphire are slightly under compressive strain, therefore the GaN related peak is slightly shifted to lower angles with respect to the completely relaxed GaN indicated by the vertical line at 17.279° . Especially, for structures grown on SiC the substrate peak is visible. From the angular difference of $\sim 0.206^\circ$ between substrate and the AlN nucleation layer ($\sim 60 \text{ nm}$) related peak it can be concluded that the nucleation layer is completely relaxed. Nevertheless, GaN is under slight tensile strain ($\sim 0.06\%$). If the same assumption of a relaxed 60 nm AlN nucleation layer is made for films grown on Si(111) then one can deduce from the simulation a slight compressive strain, *i.e.* similar to films grown on sapphire ($\sim 0.2\%$). However, recent intense studies were published where always a slight residual tensile strain was found [24] likely due to the difference in thermal expansion coefficients.

2 Heteroepitaxy and characterization of GaN

2.5.2 Photoluminescence (PL)

The photoluminescence (PL) is carried out under weak excitation power density using the 244 nm line of a continuous wave Ar^+ laser frequency doubling unit. For GaN, the luminescence is excitonic. PL emission spectra are shown in Figure 2.5 for GaN(0001) films grown on sapphire (left) and (AlN)/SiC (right) at 8 K (black) and 300 K (grey). Visible at 8 K are the free excitons (FX_A , FX_B , FX_C), a bound exciton (I_2) and the 1st LO phonon replica of FX_A [25, 26]. At 300 K spectra are broadened due to phonon interactions [27]. Scale bars, which refer to the strain-free GaN FX_A free exciton energy indicates that the GaN on sapphire is under compressive strain while films grown on (AlN)/SiC are nearly completely relaxed or slightly under tensile strain at 8K. Table 2.2 summarizes the exciton energies and (002) XRD reflections allowing to conclude that layers grown on sapphire are under slight compressive strain while GaN/(AlN)/SiC layer are nearly completely relaxed.

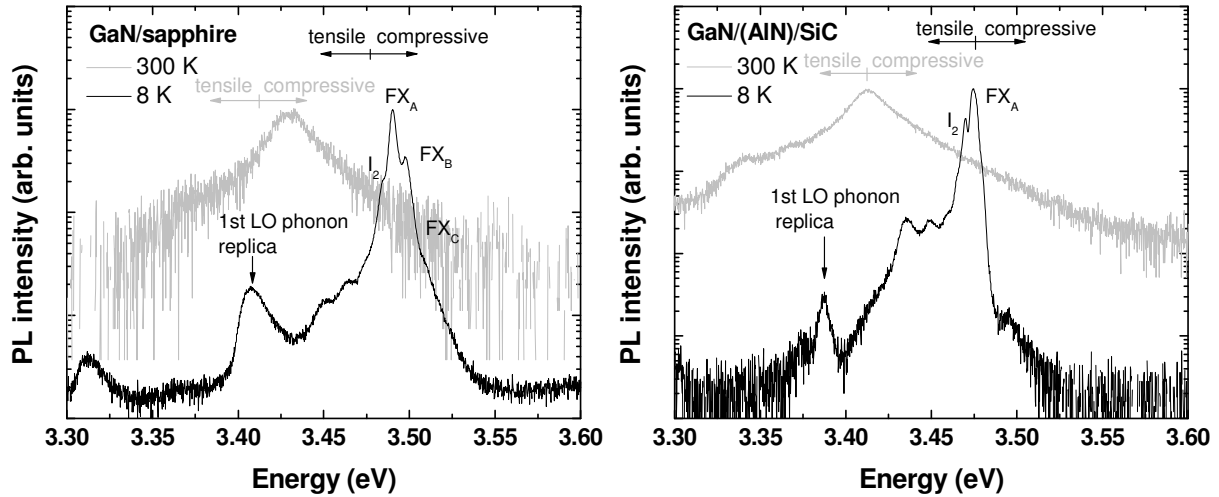


Figure 2.5 PL spectra for GaN(0001) film grown on sapphire (left) and (AlN)/SiC (right) at 8 K (black) and 300 K (grey). Visible at 8 K are the free exciton (FX_A), a bound exciton (I_2) and the 1st LO phonon replica. At 300 K spectra are broadened due to the phonon interactions. Scale bars for strain-free GaN indicates that the GaN on sapphire is under compressive strain while films grown on (AlN)/SiC are nearly completely relaxed.

Substrate	GaN/sapphire	GaN/GaN	GaN/(AlN)/SiC	GaN/(AlN)/Si
$\theta_{(0002)}$ (°)	17.269	17.279	17.298	17.240
E_{8K} (eV)	3.490	3.476	3.474	-
E_{300K} (eV)	3.429	3.413	3.413	3.417
$(a-a_0)/a_0$	$\sim -0.2\%$	0	$\sim +0.06\%$	$\sim -0.15\%$

Table 2.2 FX_A exciton energy (8 K and 300 K) and maximum of the (002) XRD reflection for GaN/sapphire and GaN/SiC layers in comparison with strain-free values indicating that GaN/sapphire films are under slight compressive strain while GaN/SiC layers are nearly completely relaxed.

Differences on the result obtained by XRD and luminescence might partially be due to different depth resolution, *i.e.* due to the absorption coefficient of GaN at the 244 nm excitation wavelength the carriers are mainly excited at the surface while XRD probes the whole sample and averages therefore also strain gradients over the whole GaN thickness. These issues are *e.g.* discussed in Refs. [28, 29]

2.5.3 Capacitance-voltage and Hall measurements

High resistive GaN buffer The standard procedure to grow GaN buffer templates on sapphire was according to section 2.4 the following: i) high temperature (1200°C) cleaning of the substrate in H₂ ii) growth of the LT-GaN layer at 535°C iii) ramping of the growth temperature to 1065°C to grow the HT-GaN layer (see Figure 2.6).

The resulting buffer layer exhibits a sheet resistivity of a few kΩ/□ (sample A744), too low for HEMT applications since the presence of high amount of donors reduces the breakdown voltage drastically and reduces therefore the device performance. Capacitance-voltage (C-V) profiling reveals a high concentration of electrons at the sapphire/GaN interface, presumably due to oxygen which can be incorporated directly from the Al₂O₃ substrate. According to the literature there are two major approaches to overcome this issue i) compensation of the donors due to formation of acceptor states *via* intentional doping with transition metals such as Fe or Cr, or by ii) tuning the growth conditions in order to self-compensate the material through higher dislocation density or defects [30]. Especially the second approach points out the critical importance of the high-temperature annealing of the nucleating layer. Contrarily to Hubbard *et al.* in Ref. [30], we explore the effect of annealing at temperatures above the main growth temperature of 1065°C.

The results are summarized in Table 2.3, which displays that an annealing at 1160°C gives rise to a high sheet resistivity (A765, A769). Note that the Hall setup is limit to the range 1 μΩ cm - 10 MΩ cm for a 1 μm thick layer. The increase in the annealing temperature up to 1160°C decreases the sheet carrier concentration by almost four orders of magnitudes. By C-V profiling, it is confirmed that there is no accumulation of electrons at the GaN/sapphire interface. Unfortunately, the increase of resistivity is accompanied by an increase of the dislocation density, typically from 9×10⁸ cm⁻² to 2.5×10⁹ cm⁻² as revealed by atomic force microscopy (AFM) (Figure 2.6). The morphology of the surface also tends to degrade at high annealing temperatures, thus a short annealing time (5 min, A769) is preformed in the new 3-step growth procedure. An attempt (A768) to carry out a “rapid thermal annealing” by ramping at 1165°C and immediately cooling at 1065°C in 5 min did not provide a high-resistive buffer.

Sample	Growth conditions	R _s (Ω/□)	R _{H, 300 K} (cm ²)	μ _{300 K} (cm ² /Vs)
A744	60 min at 1065°C	3×10 ³	2×10 ¹³	98
A760	30 min at 1100°C/30 min at 1065°C	1×10 ⁴	8×10 ¹²	78
A762	12 min at 1130°C/48 min at 1065°C	6×10 ⁴	3×10 ¹²	30
A765	12 min at 1160°C/48 min at 1065°C	>10 ⁷	-	-
A768	Rising/cooling to 1165°C within 6 min/55 min at 1065°C	8×10 ³	2×10 ¹³	38
A769	5 min at 1160°C/55 min at 1065°C	3×10 ⁷	3×10 ⁹	66

Table 2.3 Sheet resistivity (R_s), Hall coefficient (R_H) and Hall mobility (μ) for 2.2 μm thick GaN epi-layers grown on sapphire substrate for various growth conditions measured at RT in a standard Hall setup in Van der Pauw geometry.

2 Heteroepitaxy and characterization of GaN

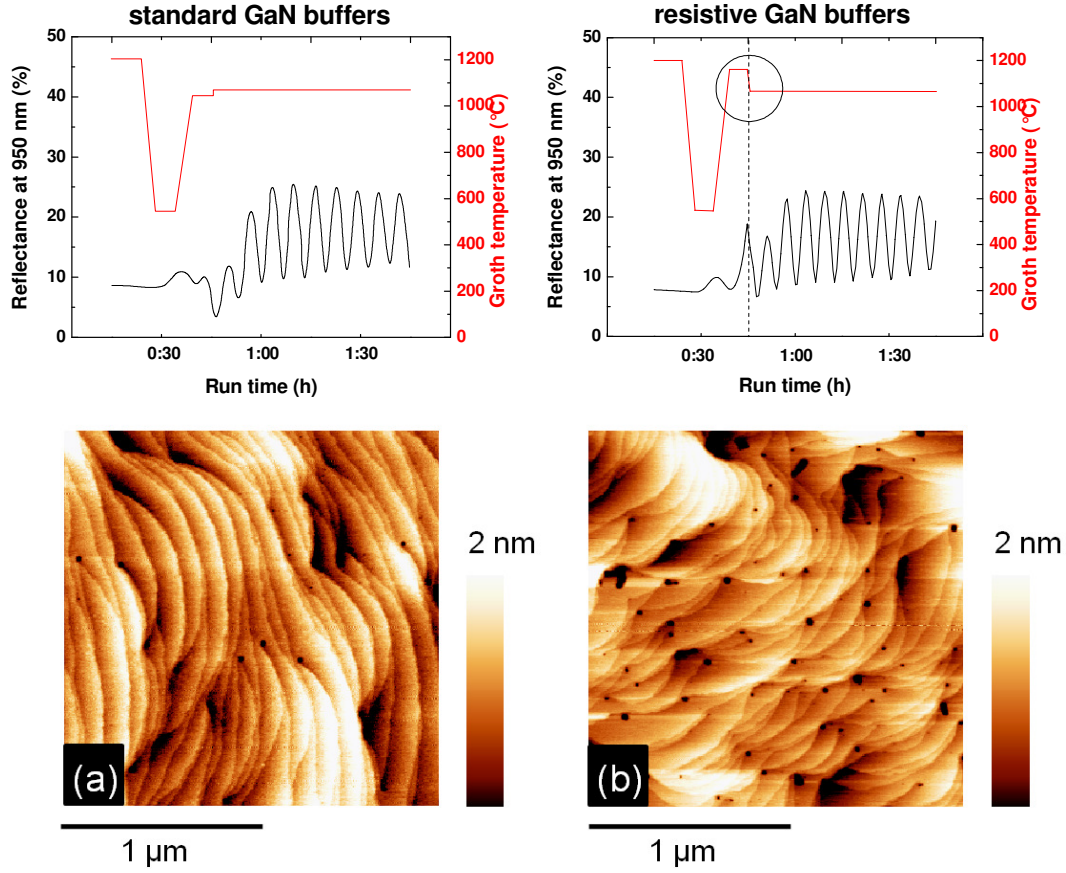


Figure 2.6 *In situ* reflectance and growth temperature for a standard GaN buffer (a) and the high resistive GaN buffer (b). Additionally, the surface morphology revealed from AFM is given. RMS roughness of the GaN films is for both surface ~ 0.45 nm. The dislocation density is $9 \times 10^8 \text{ cm}^{-2}$ for (a) and $2.5 \times 10^9 \text{ cm}^{-2}$ for (b).

Residual doping An important issue for the device performance is the breakdown voltage. The critical voltage where avalanche breakdown occurs is given according to Ref. [31] as

$$V_B = 23.6 E_g^4 [eV] \times (N_D [cm^{-3}] / 10^{16})^{-0.75} \quad (2.3)$$

Therefore, the influence on the residual doping N_D on device properties is crucial. Figure 2.7 shows the apparent carrier density profile deduced from CV measurements for GaN films grown on sapphire, (AlN)/SiC and (AlN)/Si substrates. Vertical lines indicate the interfaces with the substrates, respectively. Obviously, films grown on (AlN)/SiC exhibit the lowest residual electron concentration dropping below $\sim 10^{14} \text{ cm}^{-3}$ below the interface with the substrate. On the other hand, for films grown on sapphire there might remain a residual electron accumulation close to the substrate interface. Films grown on (AlN)/Si(111) might be further optimized to achieve a lower $N_D - N_A$.

Evaluation expression 2.3 for the found residual donor concentrations $\leq 10^{15} \text{ cm}^{-3}$ yields however V_B beyond 10^4 V . Additionally, currents were measured in lateral contact geometry according to the inset in Figure 2.7 (b) with a contact distance of $5 \mu\text{m}$ for a GaN buffer on sapphire and SiC. Especially, currents for GaN epilayers on SiC are extremely low. IVDS curves for the GaN epilayer on sapphire are several orders of magnitudes larger than those on SiC. This is in agreement with results from CV.

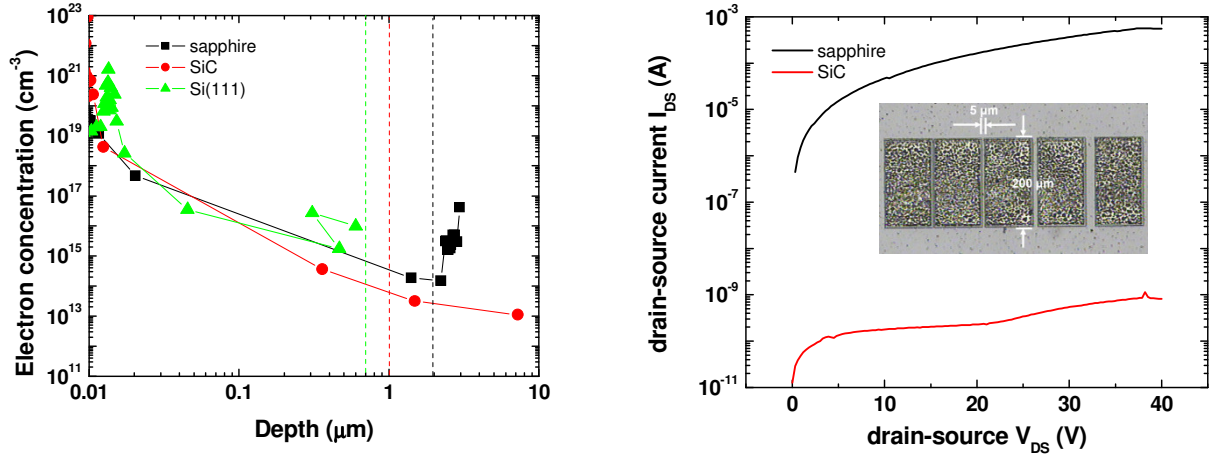


Figure 2.7 (a) Apparent carrier density profile deduced from electrochemical CV measurement for GaN films grown on sapphire, (AlN)/SiC and (AlN)/Si substrates. Vertical lines indicate the interfaces with the substrates and hence the GaN thicknesses, respectively. Films grown on (AlN)/SiC exhibit the lowest residual electron concentration throughout the GaN buffer. (b) IV characteristics for a lateral contact geometry according to the figure in the inset with a contact distance of 5 μm for a GaN epilayer on sapphire and SiC.

2.6 Conclusions

We achieved high resistive GaN buffers grown on sapphire by using a HT-GaN layer grown at 1160°C which result in typical residual donor concentrations ($N_D - N_A$) of $\sim 1 \times 10^{14} \text{ cm}^{-3}$. This is extremely low compared with the two-dimensional electron gas which builds up at the heterointerface between the AlInN barrier and the buffer ($\sim 0.001\%$). The surface rms roughness value is $\sim 0.45 \text{ nm}$ and the dislocation density is as low as $\sim 2.5 \times 10^9 \text{ cm}^{-2}$. The GaN buffer exhibits a slight residual compressive strain of $\sim -0.2\%$. Furthermore, GaN buffer were successfully grown on Si(111) and SiC using an AlN ($\sim 60 \text{ nm}$) seed layer. The AlN seed is found to be completely relaxed from XRD measurements. Especially the GaN grown on SiC is nearly completely relaxed and only a very low residual tensile strain of $\sim +0.06\%$ is found at RT. Experimentally, GaN thicknesses of 700 nm on Si(111) are achieved before cracking occurs due to the high thermal expansion coefficient mismatch. Furthermore the GaN grown on Si(111) exhibits the largest XRD FWHM, likely due to higher dislocation density and additional curvature of the sample.

Bibliography

- [1] R. P. Vaudo *et al.*, *GaN Boule Growth: A Pathway to GaN Wafers with Improved Material Quality*, *physica status solidi (a)* **194**, 494 (2002).
- [2] M. Kelly *et al.*, *Large Free-Standing GaN Substrates by Hydride Vapor Phase Epitaxy and Laser-Induced Liftoff*, *Jpn. J. Appl. Phys.* **38**, 217 (1999).
- [3] C. Hennig *et al.*, *Self-separation of thick 2-inch GaN layers grown by HVPE on Al_2O_3 using ELO with masks containing tungsten*, *physica status solidi (c)* **4**, 2638 (2007).
- [4] P. Waltereit *et al.*, *Nitride semiconductors free of electrostatic fields for efficient white light-emitting diodes*, *Nature* **406**, 865 (2000).
- [5] U. T. Schwarz, and M. Kneissl, *Nitride emitters go nonpolar*, *physica status solidi (RRL) – Rapid Research Letters* **1**, A44 (2007).

2 Heteroepitaxy and characterization of GaN

- [6] Cree, Inc., www.cree.com.
- [7] Mitsubishi Chemical, www.m-kagaku.co.jp.
- [8] D. Gogova *et al.*, *Large-area free-standing GaN substrate grown by hydride vapor phase epitaxy on ELO GaN template*, *Physica B: Condensed Matter* **371**, 133 (2006).
- [9] R. Dwilinski *et al.*, *Bulk ammonothermal GaN*, *J. Cryst. Growth* **311**, 3015 (2009).
- [10] R. Dwilinski *et al.*, *Homoepitaxy on bulk ammonothermal GaN*, *J. Cryst. Growth* **311**, 3058 (2009).
- [11] R. D. R. Dwilinski, and M. Zajac, *Bulk GaN: Ammonothermal Trumps HVPE*, *Compound Semiconductor* **16** (2010).
- [12] S. Pearton, C. Abernathy, and F. Ren, *Topics in growth and device processing of III-V semiconductors* (World Scientific Pub Co Inc, 1996).
- [13] J. W. Chung *et al.*, *Seamless On-Wafer Integration of Si(100) MOSFETs and GaN HEMTs*, *IEEE Electron Device Lett.* **30**, 1015 (2009).
- [14] <http://www.ioffe.rssi.ru/SVA/NSM/Semicond/>.
- [15] H. Amano *et al.*, *Metalorganic Vapor-Phase Epitaxial-Growth of a High-Quality GaN Film Using an AlN Buffer Layer*, *Appl. Phys. Lett.* **48**, 353 (1986).
- [16] S. Nakamura, *GaN Growth Using GaN Buffer*, *Jpn. J. Appl. Phys.* **30**, L1705 (1991).
- [17] H. Fujikura *et al.*, *Realization of low dislocation GaN/Al₂O₃ wafers by 3-step MOVPE growth with island induced dislocation control*, *Jpn. J. Appl. Phys.* **42**, 2767 (2003).
- [18] P. Waltereit *et al.*, *Influence of AlN nucleation layers on growth mode and strain relief of GaN grown on 6H-SiC(0001)*, *Appl. Phys. Lett.* **74**, 3660 (1999).
- [19] T. W. Weeks *et al.*, *GaN Thin-Films Deposited Via Organometallic Vapor-Phase Epitaxy on α (6H)-SiC(0001) Using High-Temperature Monocrystalline AlN Buffer Layers*, *Appl. Phys. Lett.* **67**, 401 (1995).
- [20] H. Lahreche *et al.*, *Optimisation of AlN and GaN growth by metalorganic vapour-phase epitaxy (MOVPE) on Si(111)*, *J. Cryst. Growth* **217**, 13 (2000).
- [21] M. Moram *et al.*, *X-ray diffraction of III-nitrides*, *Rep. Prog. Phys.* **72**, 036502 (2009).
- [22] H. Heinke *et al.*, *X-ray diffraction analysis of the defect structure in epitaxial GaN*, *Appl. Phys. Lett.* **77**, 2145 (2000).
- [23] O. Brandt, P. Waltereit, and K. H. Ploog, *Determination of strain state and composition of highly mismatched group-III nitride heterostructures by x-ray diffraction*, *J. Phys. D Appl. Phys.* **35**, 577 (2002).
- [24] A. Le Louarn *et al.*, *AlN buffer layer growth for GaN epitaxy on (111) Si: Al or N first?*, *J. Cryst. Growth* **311**, 3278 (2009).
- [25] R. Dingle *et al.*, *Absorption, Reflectance, and Luminescence of GaN Epitaxial Layers*, *Phys. Rev. B* **4**, 1211 (1971).
- [26] I. H. Lee *et al.*, *Evolution of stress relaxation and yellow luminescence in GaN/sapphire by Si incorporation*, *Appl. Phys. Lett.* **71**, 1359 (1997).
- [27] W. Liu *et al.*, *Phonon-assisted photoluminescence in wurtzite GaN epilayer*, *Semicond. Sci. Tech.* **13**, 769 (1998).
- [28] A. Hoffmann *et al.*, *Spatially resolved investigations of the excitonic luminescence in GaN*, *Mat. Sci. Eng. B-Solid* **50**, 192 (1997).
- [29] T. Paskova *et al.*, *HVPE GaN thick films for quasi-substrate applications: Strain distribution and wafer bending*, *J. Electron. Mater.* **33**, 389 (2004).
- [30] S. M. Hubbard *et al.*, *High-resistivity GaN buffer templates and their optimization for GaN-based HFETs*, *J. Cryst. Growth* **284**, 297 (2005).
- [31] O. Ambacher, and V. Cimalla, *Polarization effects in semiconductors : from ab initio theory to device application* (Springer, New York, 2007).

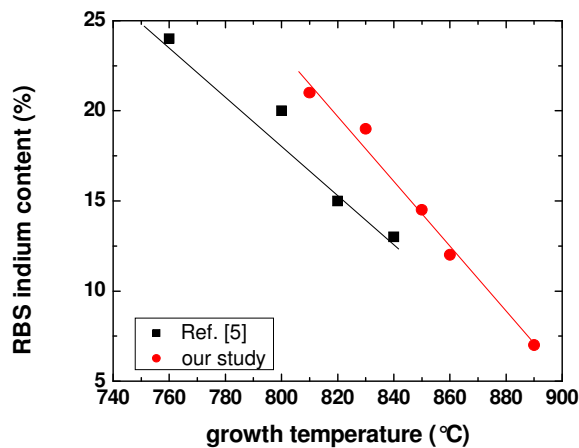
Heteroepitaxy and structural characterization of $\text{Al}_{1-x}\text{In}_x\text{N}$ (0001) ($0.07 \leq x \leq 0.21$)

3.1 Introduction

This chapter aims to give an insight into the growth and structural properties of AlInN grown around the lattice matched (LM) composition. To examine the quality of the material a lot of different techniques such as XRD, Rutherford backscattering (RBS), secondary neutral mass spectroscopy (SNMS) are brought together revealing indeed a high crystalline quality in terms of compositional homogeneity and epitaxial properties.

3.2 AlInN epitaxial growth

The growth of the AlInN material is a difficult task due to the large difference existing between InN and AlN covalent bonds, which may lead to phase separation and strong composition inhomogeneities. Additionally, the large difference in optimum growth temperature (T_g) between InN ($\sim 600^\circ\text{C}$) and AlN ($\sim 1100^\circ\text{C}$) for layers grown by MOVPE does not facilitate the incorporation of indium in the AlN matrix for Al-rich AlInN layers. Therefore only a few groups worldwide have achieved a reliable material quality [1-6]. The incorporated indium fraction depends therefore on multiple parameters: growth temperature, III/V ratio, substrate lattice parameter, etc. Even for the same growth temperature reported in the literature one may obtain different composition using a different substrate or reactor (Figure 3.1). Another source of confusion arises from the method used to estimate the indium content. As will be demonstrated later on, XRD can only be a reliable tool if the interplay of thickness, strain state and composition is fully understood. As an example, Figure 3.1 shows



the indium content obtained *via* Rutherford back-scattering (RBS) *versus* growth temperature of our samples discussed in this work and for sake of comparison data from Ref. [5].

Figure 3.1 Indium percentage estimated by Rutherford backscattering in the $\text{Al}_{1-x}\text{In}_x\text{N}$ alloy *versus* growth temperature for our 15 nm thick samples and for 120 nm thick samples from Ref. [5]. Lines are guides to the eyes. Both set of samples are grown on GaN/sapphire. Differences in the indium composition for the same growth temperature arise from different strain state of the GaN buffer or differences in the reactor chambers, *e.g.* flow rates.

Despite the same growth temperature, the indium content varies up to 5%. This is related to the specific geometry and parameters of the individual growth reactor *e.g.* flow rates and to the strain state of the GaN template. One may also question the accuracy of the temperature, as it is always tricky to determine the actual surface temperature during growth.

3.3 Structural characterization

Critical thickness The generation of misfit dislocations (MDs) is a well-known phenomenon in heteroepitaxy, in which a thin film is grown on a substrate with a significantly different lattice parameter. Below a certain film thickness, called the critical thickness t_{cr} , a heteroepitaxial film may be grown pseudomorphically on a substrate, while a relaxation of misfit strain *via* plastic deformation occurs for thicker films $t > t_{cr}$. In this sense, the most common mechanism of plastic relaxation is through the formation of MDs.

Several theoretical models for calculating the critical thickness in isotropic materials have been published over the years [7-9]. Although these account reasonably well for the strain relaxation processes occurring in cubic systems such as SiGe/Si and InGaAs/GaAs, there has been only one report attempting to estimate the effect of hexagonal symmetry on the t_{cr} values [10]. Nevertheless, the model of Fischer *et al.* [7] provides a simple estimate for the critical thickness, namely $t_{cr} \sim b_e/2\epsilon_{||}$, with $b_e=0.31825$ nm the length of the Burgers vector. Figure 3.2 shows t_{cr} expected for the onset of plastic relaxation *via* the formation of MDs for the $\text{Al}_{1-x}\text{In}_x\text{N}$ alloy grown on GaN with $a=0.31825$ nm. The lattice matched condition is met at $x=0.175$, where epilayers could potentially be grown infinitely thick. Experimentally, layer thicknesses of ~ 500 nm were achieved. In practice t_{cr} drops rapidly below 100 nm within a $\pm 1\%$ range beside the LM condition. In the limits of the binary compounds, *i.e.* AlN and InN grown on *c*-plane GaN, the estimate yields $t_{cr} \sim 6.5$ nm for AlN/GaN, in very good agreement with experimentally results [11]. For InN/GaN the experimental t_{cr} is found to be ~ 1 monolayer (ML), *i.e.* t_{cr} is slightly overestimated in Figure 3.2 [12].

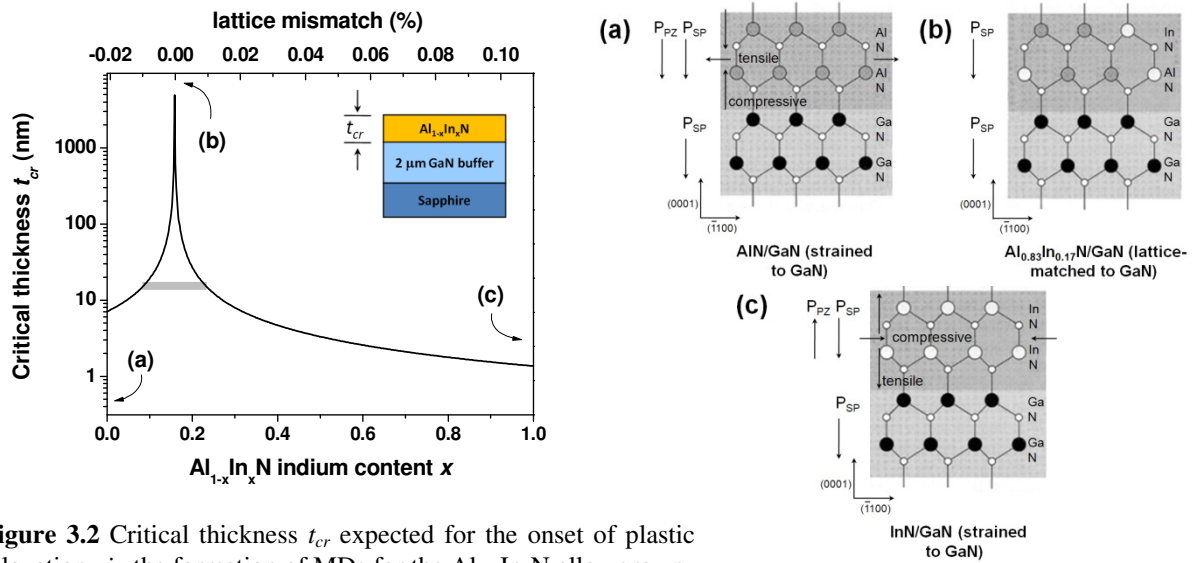


Figure 3.2 Critical thickness t_{cr} expected for the onset of plastic relaxation *via* the formation of MDs for the $\text{Al}_{1-x}\text{In}_x\text{N}$ alloy grown on GaN with $a=0.3182$ nm. The lattice matched condition is met at $x=0.175$, where epilayers could potentially be grown infinitely thick. In practice t_{cr} drops rapidly below 100 nm within a $\pm 1\%$ range from the LM condition. On the right side of the figure, the three cases of interest, namely AlN/GaN, LM AlInN/GaN and InN/GaN are depicted together with the direction of the polarization. Adapted from Ref. [13].

3 Heteroepitaxy and structural characterization of $\text{Al}_{1-x}\text{In}_x\text{N}$ (0001) ($0.07 \leq x \leq 0.21$)

The model proposed by Holec *et al.* [10] is thus expected to match better for the high indium content regime taking into account the hexagonal symmetry. Here, we want to point out the importance of determining exactly the strain state of the epilayers, since it influences most of optical and electrical properties. Throughout the literature there is often a careless handling of these issues. On the other hand, the extreme low critical thicknesses for the binary compounds grown on *c*-plane GaN make it difficult to apply routine measurement techniques such as absorption, luminescence, XRD, deep level transient spectroscopy, residual donor concentration *via* CV experiments.

Lattice parameters A widely employed method to extract composition of ternary alloys is based on the application of Vegard's rule, *i.e.*, assuming that the relaxed lattice parameters of the ternary alloy can be calculated from a linear interpolation between the relaxed lattice parameters of the respective binary compounds. The applicability of this rule to the $\text{Al}_{1-x}\text{In}_x\text{N}$ system is, however, disputable owing to the large difference in ionic sizes and ionicity of the binaries. Recent first-principle calculations [14] infer deviations from Vegard's rule for wurtzite $\text{Al}_{1-x}\text{In}_x\text{N}$ alloys of 0.063 and -0.16 Å for the *a* and *c* lattice parameters, respectively. Figures 3.3 show asymmetric reciprocal space maps (RSMs) around the GaN 1015 reciprocal lattice point (rlp) for 14 nm thick $\text{Al}_{1-x}\text{In}_x\text{N}$ layers. The lattice parameters *a* and *c* can be read out from the RSM for an asymmetric reflection using the relations $a = 2\pi / q_x \cdot \sqrt{4/3(h^2 + k^2 + hk)}$ and $c = 2\pi / q_z \cdot l$ with q_x and q_z the lateral and transverse scattering vectors, respectively, and *l* is the Miller index in (*hkl*) notation. Results are summarized in Table 3.1. It is seen from Figure 3.3 that the diffractions from the $\text{Al}_{1-x}\text{In}_x\text{N}$ and GaN layers have the same lateral position, evidencing a pseudomorphic growth of the thin $\text{Al}_{1-x}\text{In}_x\text{N}$ layers. The relatively large transverse broadening of the RSMs associated with the $\text{Al}_{1-x}\text{In}_x\text{N}$ layers is related to the limited film thickness. In contrast the asymmetric RSMs of 100 nm thick $\text{Al}_{1-x}\text{In}_x\text{N}$ layers [15] are much narrower in the transverse direction.

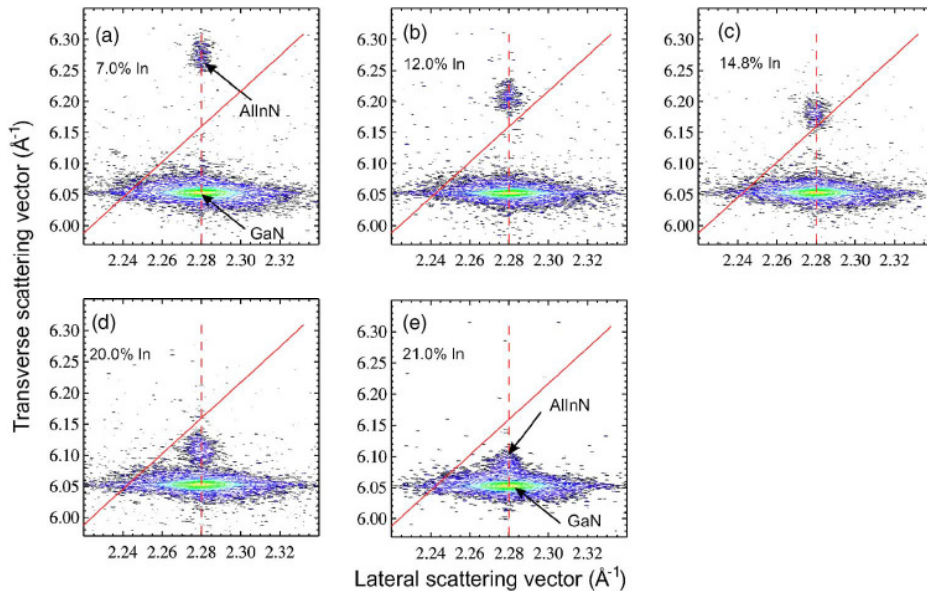


Figure 3.3 Reciprocal space maps around the GaN 105 reciprocal lattice point from ~14 nm thick $\text{Al}_{1-x}\text{In}_x\text{N}$ layers with nominal In contents of $x=0.07$ (a), $x=0.120$ (b), $x=0.148$ (c), $x=0.20$ (d), and $x=0.210$ (e). The RSMs are normalized to the maximum intensity and the same contour levels (from 0.0001 to 1) equidistant in log scale are used in (a)–(e). The positions of fully relaxed and pseudomorphic growth of $\text{Al}_{1-x}\text{In}_x\text{N}$ are given by solid and dashed lines, respectively. (XRD measurements performed in collaboration with Linköping University.)

3 Heteroepitaxy and structural characterization of $\text{Al}_{1-x}\text{In}_x\text{N}$ (0001) ($0.07 \leq x \leq 0.21$)

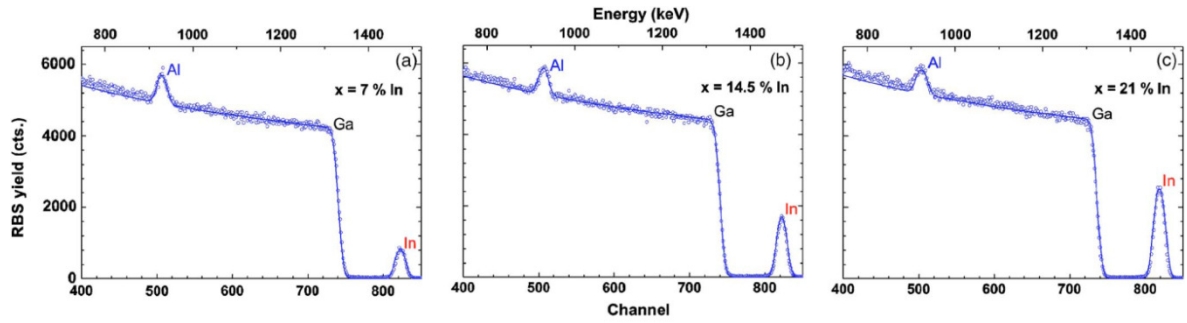


Figure 3.4 Random and simulated RBS spectra for ~14 nm thick $\text{Al}_{1-x}\text{In}_x\text{N}$ layers with In contents $x=0.07$ (a), $x=14.8$ (b), and $x=0.21$ (c). (RBS measurements performed in collaboration with Linköping University.)

The maximum full widths at half maximum of symmetric and asymmetric rocking curves from 100 nm thick $\text{Al}_{1-x}\text{In}_x\text{N}$ layers do not exceed 190 and 170 arcsec, respectively, indicating state-of-the-art material in terms of defect density and crystal quality of the alloys. The asymmetric RSMs from the 100 nm thick $\text{Al}_{1-x}\text{In}_x\text{N}$ layers reveal that none of them are fully coherent to the GaN buffer layer (not shown here see Ref. [15]). The $\text{Al}_{1-x}\text{In}_x\text{N}$ layers with In contents between 0.128 and 0.158 show deviation from the coherent growth towards smaller in-plane lattice parameters, indicating tensile strain relaxation, whereas films with higher In content show deviation from the coherent growth towards larger in-plane lattice parameters, indicating compressive strain relaxation. This is in agreement with the expectation for t_{cr} from the previous subsection which is around ~20 nm for those In contents.

Determination of indium content As already mentioned, to estimate the In content from the lattice parameters one has to make an assumption for the unknown strain-free lattice parameters, which are usually interpolated according to Vegard's law. The results are given in Table 3.1. Recently, Lorenz *et al.* [6] clarified the deviation observed between the indium composition determined by XRD analysis from the actual indium composition obtained by RBS using non-zero lattice constant bowing parameters equal to -0.010 \AA and -0.075 \AA for the a and c lattice constants, respectively. This led to LM condition for AlInN on fully relaxed GaN layer corresponding to an indium composition of 17.1%.

To verify the In content we determined on the above set of samples, we performed also RBS measurements using a 1.7 MeV $^4\text{He}^+$ beam at a grazing incidence angle of 60° and a scattering angle of 170° . Results are presented in Figure 3.4. For further details on the setup see Ref. [15, 16]. The In contents we measured this way are listed in Table 3.1. They range

Sample	FX_A energy (eV)	a_{GaN} (Å)	c_{GaN} (Å)	a_{AlInN} (Å)	c_{AlInN} (Å)	Indium content (Vegard's law)	Indium content for $b_a=-0.010\text{ \AA}$ $b_c=-0.075\text{ \AA}$	Indium content RBS
A	3.4895	3.1821	5.1892	3.1821	5.0008	7.8%	7.2%	7%
B	3.4896	3.1821	5.1892	3.1821	5.0588	13.1%	12.2%	12%
C	3.4906	3.1817	5.1895	3.1817	5.0835	15.3%	14.3%	14.5%
D	3.4865	3.1831	5.1883	3.1839	5.1369	19.8%	18.7%	19.5%
E	3.4835	3.1842	5.1875	3.1863	5.1615	21.8%	20.6%	21%

Table 3.1 Main structural parameters of 14 nm thick AlInN samples: LT GaN FX_A energy, GaN lattice constants, AlInN lattice constants, indium composition deduced from Vegard's law and using the bowing parameters $b_a=-0.010\text{ \AA}$ and $b_c=-0.075\text{ \AA}$ given in Ref. 6 and indium content deduced from RBS experiments.

3 Heteroepitaxy and structural characterization of $\text{Al}_{1-x}\text{In}_x\text{N}$ (0001) ($0.07 \leq x \leq 0.21$)

from 7% up to 21% for the 14 nm thick $\text{Al}_{1-x}\text{In}_x\text{N}$ layers. Note that RBS indium content are in very good agreement with results deduced from XRD if the lattice bowing parameter determined by Lorenz *et al.* is used. Since the GaN buffer is additionally under slight compressive strain the LM should be met at 16.5%. Furthermore, it should be mentioned that some grading of In composition along the growth axis is in very likely. According to elastic recoil detection analysis the impurity levels of O, H, C, and Ga in the $\text{Al}_{1-x}\text{In}_x\text{N}$ films are below the detection limit of one atomic percent.

Surface morphology The samples under discussion have also been studied by means of AFM. Results for $\text{Al}_{1-x}\text{In}_x\text{N}/\text{AlN}(1\text{nm})/\text{GaN}$ grown on sapphire are shown in Figure 3.5 for three different compositions, namely $x=7\%$, 15% and 21% . Indicated are the rms roughness values for $10\mu\text{m} \times 10\mu\text{m}$ and $2\mu\text{m} \times 2\mu\text{m}$ scans. In Chapter 5 a more detailed description of 2D surfaces will be given and the term root mean square roughness will be defined. The lower is the rms value the smoother is the surface. Note that for certain types of surface morphologies the rms value can depend on scan size, independent of the fact that other features such as pits might appear at a large scale [17]. Especially the heterostructures, which are grown close to the LM condition, are locally very smooth with rms of ~ 0.2 nm *i.e.* one ML. Non-LM barriers exhibit larger rms values on the $10\mu\text{m} \times 10\mu\text{m}$ and as well on the $2\mu\text{m} \times 2\mu\text{m}$ scan range. But on a local scale *i.e.* $2\mu\text{m} \times 2\mu\text{m}$ they exhibit rms values of ~ 1 nm. Especially the 7% sample shows some bump like feature while the 21% sample shows some anisotropic wave-like features on the larger scan range. Figure 3.6 displays AFM images of LM barriers grown on different substrates. The heterostructures grown on SiC are even smoother than those grown on sapphire. In case of Si(111), a larger rms value of ~ 0.26 nm on the $2\mu\text{m} \times 2\mu\text{m}$ scan is observed. In a future work it would be interesting to compare the rms of the GaN buffer before the growth of the barrier with the values from Figure 3.6. But from literature [18, 19] it can be assumed that these values correlate. Therefore the rms of the GaN buffer has a crucial impact on transport properties. Especially the morphology of GaN buffer grown on Si(111) is strongly influenced by the growth conditions of the AlN seed layer [19].

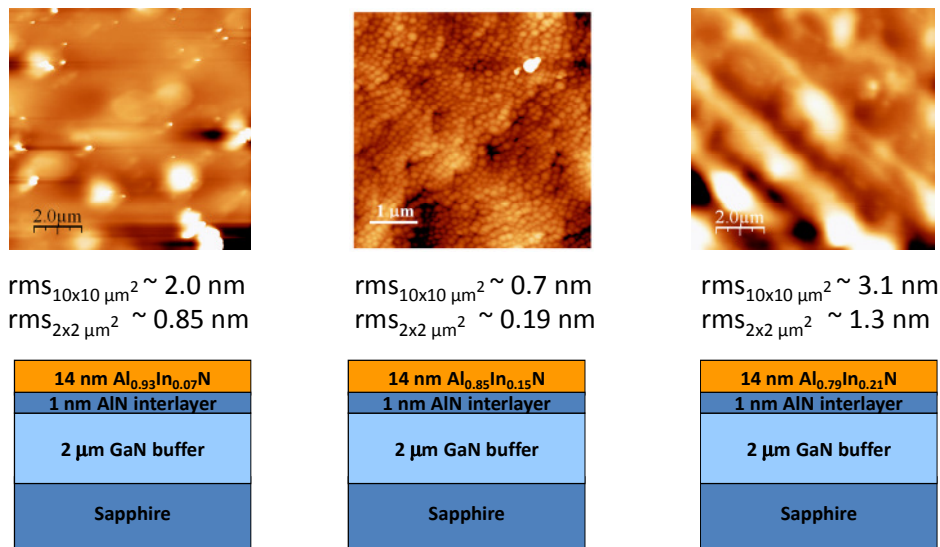


Figure 3.5 AFM images for $\text{Al}_{1-x}\text{In}_x\text{N}/\text{AlN}(1\text{nm})/\text{GaN}$ heterostructures grown on sapphire for $x=7\%$, 15% and 21% . Indicated are the rms roughness values for $10\mu\text{m} \times 10\mu\text{m}$ and $2\mu\text{m} \times 2\mu\text{m}$ scans.

3 Heteroepitaxy and structural characterization of $\text{Al}_{1-x}\text{In}_x\text{N}$ (0001) ($0.07 \leq x \leq 0.21$)

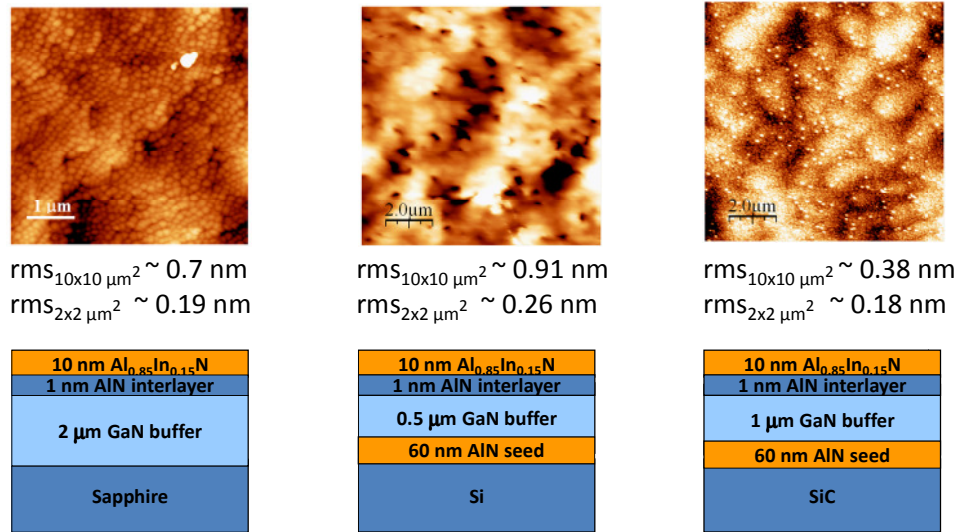


Figure 3.6 AFM images of $\text{Al}_{0.85}\text{In}_{0.15}\text{N}/\text{AlN}(1\text{nm})/\text{GaN}$ heterostructures grown on sapphire, Si(111) and SiC, with corresponding rms roughness values for 10 $\mu\text{m} \times 10 \mu\text{m}$ and 2 $\mu\text{m} \times 2 \mu\text{m}$ scans.

AlN interlayer Since we are mainly interested in heterostructures with good lateral transport properties a thin AlN interlayer was introduced between the AlInN barrier and the GaN buffer to reduce alloy scattering and increase the separation of the 2DEG wavefunction from the heterointerface. A similar attempt was made in conventional $\text{AlGaInN}/\text{GaN}$ heterostructures leading to high HEMT device performance and outstanding transport properties [20]. In our case, the introduction of such an AlN interlayer with a thickness of ~ 1 nm between the 13 nm thick LM AlInN and the GaN buffer allowed us to report a record mobility of $\sim 1200 \text{ cm}^2/\text{Vs}$ [21]. For slightly larger and smaller AlN interlayer thicknesses the mobility drops quickly down. The exact origin of this sharp ‘high mobility window’ will be the subject of further discussion in the next chapters (4 and 5). Since this interlayer plays a crucial role we want to discuss briefly how this ultrathin layer affects the XRD reflectivity scans.

To underline the outstanding crystalline quality of our materials, Figure 3.7 displays a typical TEM picture of such an $\text{Al}_{0.85}\text{In}_{0.15}\text{N}(13\text{nm})/\text{AlN}(1\text{nm})/\text{GaN}$ heterostructure. This measurement was carried by Zhou *et al.* and the image is taken from Ref. [22].

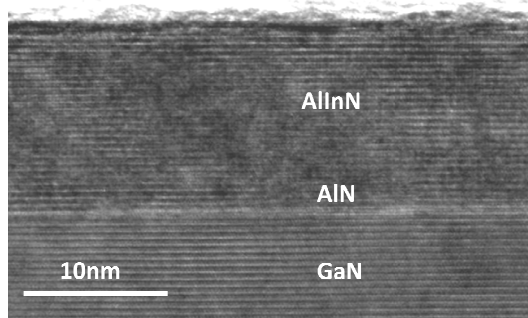


Figure 3.7 Cross-sectional high-resolution TEM image taken under [1120] zone axis of an $\text{Al}_{0.85}\text{In}_{0.15}\text{N}(13\text{nm})/\text{AlN}(1\text{nm})/\text{GaN}$ heterostructure. AlInN/AlN and AlN/GaN interfaces are well-defined. Image is taken from Ref. [22].

As demonstrated above by means of reciprocal space mapping, the epi-layers are completely pseudomorphic. We are now turning back to the ω - 2θ scans around the GaN (002) reflection, which are usually used for routine measurements. Results are depicted in Figure 3.8. We focus first on the subfigure (b) where the AlN interlayer was kept constant at 1.1 nm and the $\text{Al}_{0.85}\text{In}_{0.15}\text{N}$ barrier thickness was varied. We see that the angle at which the maximum of the AlInN related reflectivity appears depends strongly on the barrier thickness. This effect is caused by the fact that the layer thickness is of the same order as the absorption length of the material at the energy of the Cu $K\alpha_1$ radiation ($\lambda = 1.540\,562\text{ \AA}$), which is $\sim 55\text{ \AA}$ for AlN. Decreasing the barrier thickness down to this length causes strong deviations from the Bragg condition (see inset in subfigure (b)). For further details see the work of Tapfer and coworkers [23]. These effects are included in the theoretical simulations indicated as red curves, which are calculated with an algorithm described in Ref. [24]. Keeping the $\text{Al}_{0.85}\text{In}_{0.15}\text{N}$ constant at 13 nm and varying the AlN interlayer thickness has also a significant effect on the angular separation of the AlInN related peak (inset in subfigure (a)). Note that the simulations are in excellent agreement with the experimental results indicating also the overall good material quality in terms of homogeneous incorporation of indium and layer thicknesses.

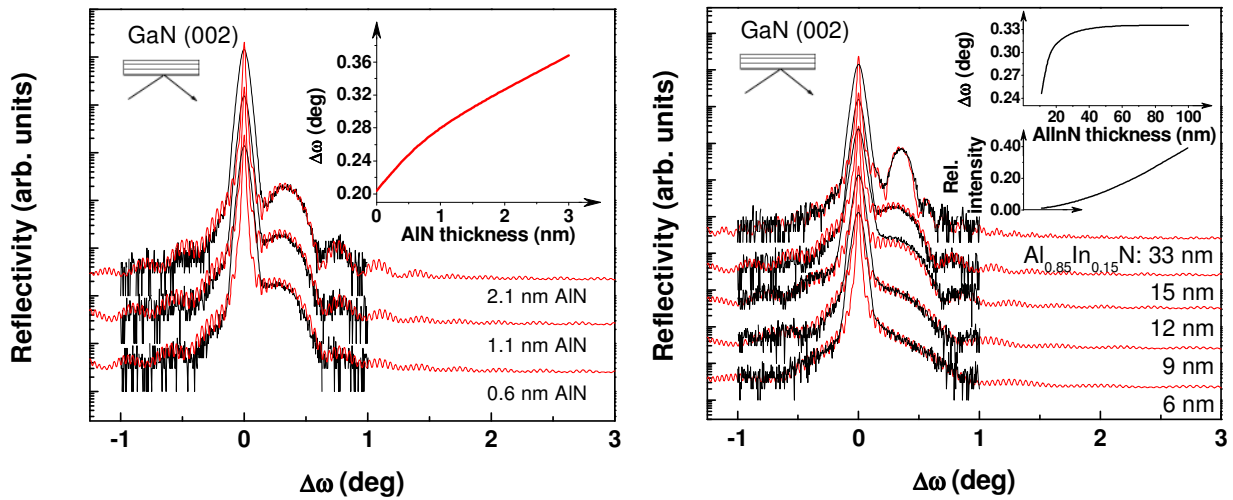


Figure 3.8 (a) Measured and simulated XRD ω - 2θ scans around the GaN (002) reflection for a 13 nm thick $\text{Al}_{0.85}\text{In}_{0.15}\text{N}$ barrier grown on 2 μm GaN/sapphire for varying AlN interlayer thicknesses. Inset shows the shift of the AlInN related peak due to the interlayer insertion. (b) Similar measurements as in (a) but the interlayer thickness was kept at 1.1 nm and the $\text{Al}_{0.85}\text{In}_{0.15}\text{N}$ barrier thickness was varied. Inset shows the AlInN related peak shift due to the barrier thickness increase and the intensity of the AlInN related reflection relative to the GaN.

Atomic structure From the literature it is known that very often, when it is intended to grow the AlInN alloy on GaN template, Ga is unintentionally incorporated into the barrier. Therefore, secondary neutral mass spectroscopy (SNMS) was performed to analyze the layer and buffer composition. The advantage of SNMS compared to secondary ion mass spectroscopy (SIMS) is that $\sim 90\%$ of sputtered material reaches the mass spectrometer reducing thereby matrix effects. A drawback is the strong variance of ionization probabilities for different atoms. Figure 3.9 shows a SNMS sputtering profile of an $\text{Al}_{0.85}\text{In}_{0.15}\text{N}$ (13 nm)/AlN(1 nm)/GaN/sapphire sample. The AlN interlayer manifests itself as a sharp peak in the Al concentration profile for sputtering times between 160 and 170 s (inset). The detected

3 Heteroepitaxy and structural characterization of $\text{Al}_{1-x}\text{In}_x\text{N}$ (0001) ($0.07 \leq x \leq 0.21$)

intensities of Ga, Al, and In species between 0 and 160 s sputtering times confirm that the barrier only consists of the AlInN alloy. Note that the exponential decay of the intensities does not allow drawing strong conclusions on diffusion or concentration gradients since they even appear for layers with constant homogeneous compositions and are hence inherent to this method [25]. However, we can firmly state from SNMS analysis that there is no or at least only a negligible Ga diffusion into the AlInN barrier. The concentrations were calculated from simple stoichiometry assumptions and considering the volume density of Ga and N in the wurtzite unit cell. Note that in the GaN buffer, residual concentrations of In and O are incorporated (In is within the detection limit).

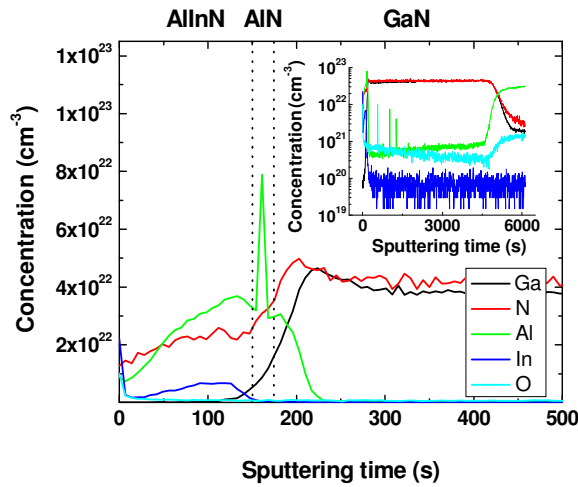


Figure 3.9 Secondary neutral mass spectroscopy (SNMS) sputtering profile of an $\text{Al}_{0.85}\text{In}_{0.15}/\text{AlN}/\text{GaN}$ heterostructure grown on sapphire. The GaN buffer is reached after 180 s sputtering and the sapphire after 5000 s. Sputtering intensities are scaled to atomic concentrations according to their stoichiometry. Outset shows the first seconds where the $\text{Al}_{0.85}\text{In}_{0.15}$ barrier is sputtered. Clearly, no Ga is incorporated in the barrier and the AlN interlayer manifests itself as an Al concentration peak at ~170 s. The residual oxygen concentration throughout the GaN buffer is $\sim 5 \cdot 10^{20} \text{ cm}^{-3}$.

3.4 Conclusions

It was demonstrated that high quality pseudomorphic $\text{Al}_{1-x}\text{In}_x\text{N}$ layers can be grown on GaN templates previously deposited on different substrates at least in a composition range $0.07 \leq x \leq 0.21$ for 15 nm epilayers. Experimentally, AlInN layers up to 500 nm can be grown if the LM composition is perfectly matched. However, for the estimate of the indium content from XRD rocking curves it is crucial to take into account the finite thickness of the barrier otherwise it will lead to a wrong interpretation of the results. Taking into account the slight residual strain in the GaN/sapphire heterostructures, the LM composition should be met at $x \sim 16.5\%$. SNMS measurement confirms that the barriers consist only of Al, In and N, *i.e.* no gallium diffusion into the barrier. Furthermore, the insertion of an ultrathin AlN interlayer between barrier and buffer has already a significant effect on XRD rocking curves and has to be considered carefully in the analysis. AFM measurements reveal the outstanding low rms roughness value ($\sim 0.19 \text{ nm}$) of the barrier grown with $x \sim 14.5\%$ on sapphire and SiC. The rms value found for the $\text{Al}_{0.85}\text{In}_{0.15}\text{N}/(13\text{nm})/\text{AlN}(1\text{nm})/\text{GaN}/\text{Si}(111)$ heterostructure is $\sim 30\%$ higher. Interestingly, this correlates well with the transport properties (Figure 7.9), suggesting a close relation between surface/interface morphology and transport. For $\text{Al}_{1-x}\text{In}_x\text{N}$ layers away from the LM condition (*i.e.* $x=7\%$ or 21%), the surfaces roughen and are accompanied by hillock/spike-like features in the tensile regime and a wavy-like feature in the compressive regime, respectively.

Bibliography

- [1] R. Butté *et al.*, *Current status of AlInN layers lattice-matched to GaN for photonics and electronics*, J. Phys. D Appl. Phys. **40**, 6328 (2007).
- [2] J. F. Carlin, and M. Ilegems, *High-quality AlInN for high index contrast Bragg mirrors lattice matched to GaN*, Appl. Phys. Lett. **83**, 668 (2003).
- [3] C. Hums *et al.*, *Metal-organic vapor phase epitaxy and properties of AlInN in the whole compositional range* (vol 90, art no 022105, 2007), Appl. Phys. Lett. **91**, 139901 (2007).
- [4] C. Hums *et al.*, *Metal-organic vapor phase epitaxy and properties of AlInN in the whole compositional range*, Appl. Phys. Lett. **90**, 022105 (2007).
- [5] K. Lorenz *et al.*, *Relaxation of compressively strained AlInN on GaN*, J. Cryst. Growth **310**, 4058 (2008).
- [6] K. Lorenz *et al.*, *Anomalous ion channeling in AlInN/GaN bilayers: Determination of the strain state*, Phys. Rev. Lett. **97**, 085501 (2006).
- [7] A. Fischer, H. Kuhne, and H. Richter, *New Approach in Equilibrium-Theory for Strained-Layer Relaxation*, Phys. Rev. Lett. **73**, 2712 (1994).
- [8] J. W. Matthews, and A. E. Blakeslee, *Defects in Epitaxial Multilayers .1. Misfit Dislocations*, J. Cryst. Growth **27**, 118 (1974).
- [9] R. People, and J. C. Bean, *Calculation of Critical Layer Thickness Versus Lattice Mismatch for $\text{Ge}_x\text{Si}_{1-x}/\text{Si}$ Strained-Layer Heterostructures*, Appl. Phys. Lett. **47**, 322 (1985).
- [10] D. Holec *et al.*, *Critical thickness calculations for InGaN/GaN*, J. Cryst. Growth **303**, 314 (2007).
- [11] Y. Cao, and D. Jena, *High-mobility window for two-dimensional electron gases at ultrathin AlN/GaN heterojunctions*, Appl. Phys. Lett. **90**, 182112 (2007).
- [12] A. Yoshikawa *et al.*, *Fabrication and characterization of novel monolayer InN quantum wells in a GaN matrix*, J. Vac. Sci. Technol. B **26**, 1551 (2008).
- [13] D. Jena, *Polarization effects in semiconductors : from ab initio theory to device application* (Springer, New York, 2007).
- [14] B. T. Liou, S. H. Yen, and Y. K. Kuo, *Vegard's law deviation in band gap and bowing parameter of $\text{Al}_x\text{In}_{1-x}\text{N}$* , Appl. Phys. A-Mater. **81**, 651 (2005).
- [15] V. Darakchieva *et al.*, *Effects of strain and composition on the lattice parameters and applicability of Vegard's rule in Al-rich $\text{Al}_{1-x}\text{In}_x\text{N}$ films grown on sapphire*, J. Appl. Phys. **103**, 103513 (2008).
- [16] http://en.wikipedia.org/wiki/Rutherford_backscattering_spectrometry.
- [17] Y. Zhao, G. C. Wang, and T. M. Lu, *Characterization of amorphous and crystalline rough surface : principles and application* (Academic Press, San Diego, 2001).

3 Heteroepitaxy and structural characterization of $\text{Al}_{1-x}\text{In}_x\text{N}$ (0001) ($0.07 \leq x \leq 0.21$)

- [18] S. Keller *et al.*, *Metalorganic chemical vapor deposition of high mobility AlGaIn/GaN heterostructures*, J. Appl. Phys. **86**, 5850 (1999).
- [19] H. Lahreche *et al.*, *Optimisation of AlN and GaN growth by metalorganic vapour-phase epitaxy (MOVPE) on Si(111)*, J. Cryst. Growth **217**, 13 (2000).
- [20] L. Shen *et al.*, *AlGaIn/AlN/GaN high-power microwave HEMT*, IEEE Electron Device Lett. **22**, 457 (2001).
- [21] M. Gonschorek *et al.*, *High electron mobility lattice-matched AlInN/GaN field-effect transistor heterostructures*, Appl. Phys. Lett. **89**, 062106 (2006).
- [22] L. Zhou *et al.*, *Polarization field mapping of $\text{Al}_{0.85}\text{In}_{0.15}\text{N}/\text{AlN}/\text{GaN}$ heterostructure*, Appl. Phys. Lett. **94**, 121909 (2009).
- [23] L. Tapfer *et al.*, *Improved model for the determination of strain fields and chemical composition of semiconductor heterostructures by high-resolution x-ray diffractometry*, Solid State Commun. **98**, 599 (1996).
- [24] O. Brandt, P. Waltereit, and K. H. Ploog, *Determination of strain state and composition of highly mismatched group-III nitride heterostructures by x-ray diffraction*, J. Phys. D Appl. Phys. **35**, 577 (2002).
- [25] S. Hofmann, and J. Schubert, *Determination and application of the depth resolution function in sputter profiling with secondary ion mass spectroscopy and Auger electron spectroscopy*, J. Vac. Sci. Technol. A **16**, 1096 (1998).

Electrical characterization of $\text{Al}_{1-x}\text{In}_x\text{N}$ (0001) ($0.07 \leq x \leq 0.21$)

4.1 Introduction

In this chapter, we will mainly discuss the electrical properties of the $\text{Al}_{1-x}\text{In}_x\text{N}/\text{AlN}/\text{GaN}$ heterostructures. A simple balance equation model, which allows extracting important parameters such as polarization charges, dielectric constant and surface potential, is developed. Besides, the fact that the electric properties behave in agreement with this model indicates also the good quality of the films. In the compressive regime ($x > 0.165$), properties however deviate from the expectations for a homogeneous random alloy. Effects of a compositional gradient are then discussed. The chapter is wrapped with a section giving a survey on transport properties in such heterostructures aiming to build a bridge to Chapter 5 where the transport properties on a microscopic scale are discussed.

4.2 2DEG fundamentals and balance equation

Origin and fundamentals of the 2DEG As already pointed out in chapter I, even for simple nitride heterostructures the optical and electrical properties can be rather complex. If one has a two-layer heterostructure with a positive/negative polarization charge building up at the heterointerface, electrons/holes originating from the sample tend to compensate these charges forming a 2DEG/2DHG with mobile carriers near the heterointerface. Manipulating the amount of the polarization charges can also be seen as “polarization doping”. The polarization is continuous inside a layer. The abrupt change of the polarization across the heterointerface can be regarded as a fixed charge located at the heterointerface where the net polarization is the difference of the polarization of both layers or expressed mathematically

$$\frac{\partial [\sigma_A \Theta(-z) + \sigma_B \Theta(z)]}{\partial z} = (\sigma_B - \sigma_A) \delta(z) \quad (4.1)$$

where $\sigma_{A/B}$ is the polarization in the A and B layer, δ is the Dirac function and Θ the Heaviside function, and the interface is located at $z=0$. Figure 4.1 shows the polarization charge bound at the heterointerface for all possible nitride barriers grown pseudomorphically on GaN. Conventional AlGaN HEMTs use the low Al content range (right side of the figure). This work aims to explore the region closed to the LM condition for the AlInN alloy.

In the following model we completely neglect the influence of donors. To significantly have an impact the buffer carrier concentration has to be at least $\sim 10\%$ of the 2DEG density, *i.e.* $n_{3D,\text{GaN}} \geq 0.1 \cdot n_{2\text{DEG}} / d_{\text{GaN}} \approx 10^{16} \text{ cm}^{-3}$. Since we measure $n_{3D,\text{GaN}}$ which are two orders of magnitude lower we confidently can neglect these effects. For our typical barrier thicknesses of $\sim 20 \text{ nm}$ AlInN this threshold mounts up to $n_{3D,\text{AlInN}} \geq 10^{18} \text{ cm}^{-3}$. If found

4 Electrical characterization of $\text{Al}_{1-x}\text{In}_x\text{N}$ (0001) ($0.07 \leq x \leq 0.21$)

donor concentrations would have been significantly higher for the barrier and the buffer, effects such as screening of electric field or thermal activation of electrons from donors have to be considered.

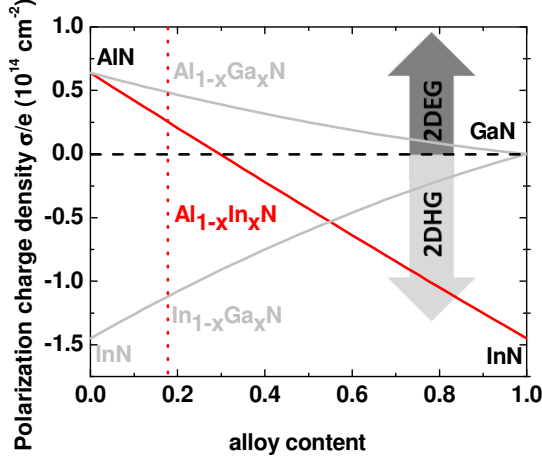


Figure 4.1 Polarization charge density bound at the heterointerface of the ABN/GaN heterostructure grown on Ga-face GaN [1]. Positive sign indicates the presence of a 2DEG while for negative polarization charges a 2DHG is expected. Note that the common notation is $\text{Al}_x\text{Ga}_{1-x}\text{N}$ and $\text{In}_x\text{Ga}_{1-x}\text{N}$, which was here because the focus is on the AlInN alloy.

Electrostatics of $\text{AlInN}/\text{AlN}/\text{GaN}$ heterostructures: a balance equation model In the following we are aiming to extract important parameters such as surface potential, polarization charges and dielectric constant from our heterostructures. The ground state energy of the triangular quantum well located at the heterointerface is given by the variational solution as [2]

$$E_0(n_s) \approx \left(\frac{9\pi\hbar e^2 n_{2d}}{8\epsilon_0\epsilon_b(x)\sqrt{8m^*}} \right)^{2/3} \quad (4.2)$$

where \hbar is the reduced Planck's constant, e is the electron charge, n_{2d} is the 2DEG sheet density, ϵ_0 the permittivity of the free space, $\epsilon_b(x)$ the relative dielectric constant and m^* the electron effective mass.

According to the band diagram Figure 4.2 (a) of a simple heterostructure, which can be applied also for $\text{AlGaInN}/\text{GaN}$ heterostructures, it follows that

$$e\Phi_s(x) - E \times d_b - \Delta E_C(x) + E_0 + (E_F - E_0) = 0 \quad (4.3)$$

Where $E = e(\sigma(x) - n_{2d})/(\epsilon_0\epsilon(x))$ is the electric field in the barrier pointing in growth direction. The difference between the Fermi level E_F and the ground state energy E_0 is given under the assumption that only one subband is filled as

$$E_F - E_0 = \frac{\pi\hbar^2}{m^*} n_{2d} \quad (4.4)$$

Interestingly, the above relation (4.3) gives then directly two limiting cases for $n_{2d}=0$, *i.e.* the situation where the 2DEG is fully depleted *via* the built-in surface potential when the so-called critical thickness is reached or an additional applied voltage is applied. In the first case

$$t_{depl} = \left(e\Phi_s(x) - \Delta E_C(x) \right) \frac{\epsilon_0\epsilon(x)}{e\sigma(x)} \quad (4.5)$$

This critical thickness is hence the thickness of the barrier where the built-in surface potential completely depletes the 2DEG. Below this thickness no electrons are accumulated at the heterointerface. For the second case, a fixed barrier thickness gives the voltage which has to be added to the surface potential to fully deplete the 2DEG. It is given by

$$V_{depl} = \left(e\Phi_s(x) - \frac{e\sigma(x)}{\epsilon_0\epsilon(x)} \times d_b - \Delta E_C(x) \right) \quad (4.6)$$

Hence the slope of depletion voltage *versus* barrier thickness gives directly $\sigma(x)/\epsilon(x)$ and the offset at $t_b=0$ the difference $e\Phi_s - \Delta E_C(x)$. Note that from the above equations all unknown parameters can be deduced from CV measurements as function of barrier thickness.

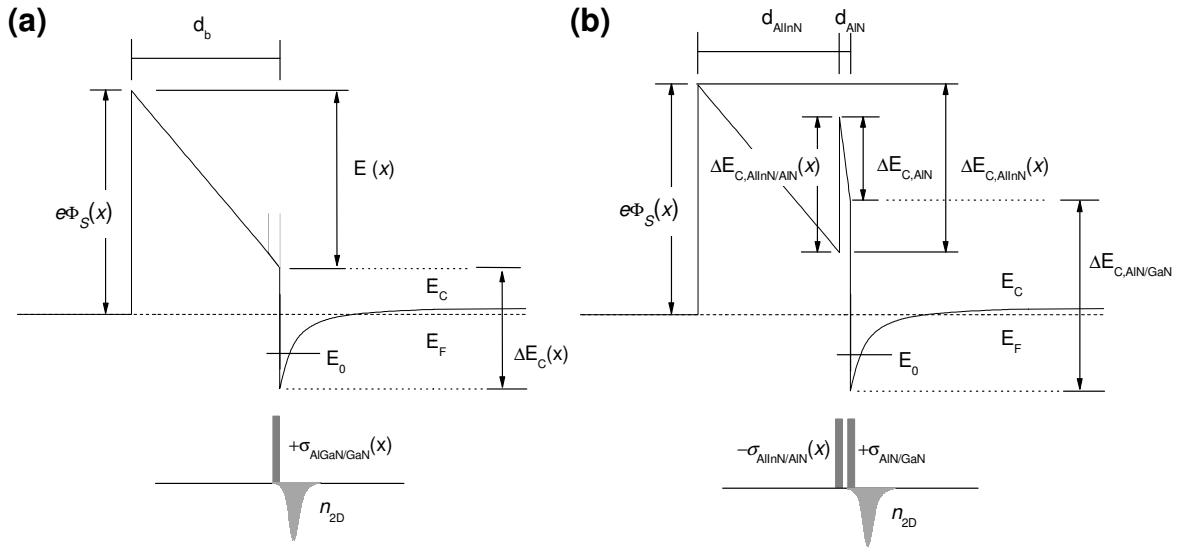


Figure 4.2 Band diagram for the balance equation model of an (a) AlGaIn/GaN and an (b) AlInN/AlN/GaN heterostructure. Note the signs of the polarization across both heterointerfaces, which have crucial importance.

Now we are turning to the case of an additional interlayer, namely a higher band gap material is inserted into the barrier and the bulk material. In the following we are referring to the concrete material, namely AlInN for the barrier, AlN for the interlayer, and GaN for the bulk. The band diagram is sketched in Figure 4.2 (b). Then the balance equation can be written as

$$e\Phi_s(x) - E_{C,AlInN} \times d_{AlInN} + \Delta E_{C,AlInN/AlN} - E_{C,AlN} \times d_{AlN} - \Delta E_{C,AlN/GaN}(x) + E_0 + (E_F - E_0) = 0 \quad (4.7)$$

Note that in this case $E_{C,AlN} = e(\sigma_{AlN/GaN} - n_{2d})/(\epsilon_0\epsilon_{AlN})$ is the field across the AlN interlayer and $E_{C,AlInN} = e(\sigma_{AlInN/AlN}(x) + \sigma_{AlN/GaN} - n_{2d})/(\epsilon_0\epsilon_{AlInN}(x))$ the field across the AlInN barrier. The latter is thus determined by the total polarization charge across the AlN interlayer. As for the single barrier heterostructure, setting $n_{2d}=0$ allows determining the critical thickness at a given interlayer thickness, such as

$$t_{depl} = d_{AlN} + \left(e\Phi_s(x) + \Delta E_{C,AlInN/AlN} - \frac{e\sigma_{AlN/GaN}}{\epsilon_0\epsilon_{AlN}} \times d_{AlN} - \Delta E_{C,AlN/GaN}(x) \right) \frac{\epsilon_0\epsilon_{AlInN}(x)}{e\sigma_{AlInN/GaN}(x)} \quad (4.8)$$

4 Electrical characterization of Al_{1-x}In_xN (0001) (0.07 ≤ x ≤ 0.21)

and for the depletion voltage:

$$V_{depl} = \left(e\Phi_s(x) - \frac{e\sigma_{AlInN/GaN}(x)}{\epsilon_0\epsilon_{AlInN}(x)} \times d_{AlInN} + \Delta E_{C,AlInN/AlN} - \frac{e\sigma_{AlN/GaN}}{\epsilon_0\epsilon_{AlN}} \times d_{AlN} - \Delta E_{C,AlN/GaN}(x) \right) \quad (4.9)$$

For a fixed interlayer thickness d_{AlN} the slope of the depletion voltage for a given AlInN composition *versus* AlInN barrier thickness gives directly $\sigma_{AlInN/GaN}(x)/\epsilon_{AlInN}(x)$. The offset at $d_{AlInN}=0$ yields then

$$V_{d_{AlInN}=0} = \left(e\Phi_s(x) + \Delta E_{C,AlInN/AlN} - e\sigma_{AlN/GaN} / \epsilon_0\epsilon_{AlN} \times d_{AlN} - \Delta E_{C,AlN/GaN}(x) \right) \quad (4.10)$$

Since $\epsilon_{AlInN}(x)$ is not known *a priori* they could be separated as follows. From the experience, lattice matched AlInN/AlN/GaN heterostructures exhibit 2DEG densities between 1 and $3 \times 10^{13} \text{ cm}^{-2}$ for barrier thicknesses between 6 and 30 nm. In this interval, Equation (4.2) might be approximated as being linear and can be expanded in terms of a Taylor development

$$(a \cdot n)^{(2/3)} \approx (a \cdot n_0)^{(2/3)} + \frac{2(a \cdot n_0)^{(2/3)}}{3n_0} (n - n_0) - O((n - n_0)^2) \quad (4.11)$$

Inserting this in Equation (4.7) and solving for the barrier thickness gives the dependence of the 2DEG density as function of the barrier thickness as a simple rational polynomial of the form

$$n(d_{AlInN}) = \frac{c_1 \cdot \sigma_{AlInN/GaN}(x) \times d_{AlInN} + c_2}{c_1 \times d_{AlInN} + c_3} \quad (4.12)$$

which gives in the infinite barrier thickness limit directly the value of $\sigma_{AlInN/GaN}(x)$. This means physically that all piezoelectric and spontaneous charges bound at heterointerface are compensated by 2D electrons. This is especially important since it is in most of the cases not possible to grow thick layers without strain relaxation for which the polarization charges would be altered.

Capacitance voltage Usually 2DEG densities are measured using capacitance voltage technique. However, this requires the fabrication of Schottky diodes, which is a time consuming and tricky task for nitride heterostructures contrary to arsenides. A way to overcome this problem is the use of electrochemical CV (ECV), where the Schottky contact is formed by an electrolyte/semiconductor interface. A suitable electrolyte for nitrides is H_3PO_4 . For a given reverse bias point the capacitance can then be probed by applying a small AC voltage. The advantage of ECV is now that the frequency of the AC voltage is a few kHz while in conventional CV the frequency is in the MHz regime. The former is clearly an advantage since large frequencies together with additional diode resistance r_s can distort seriously measured CV curves. A good introduction in CV and ECV techniques can be found in Refs. [3-4].

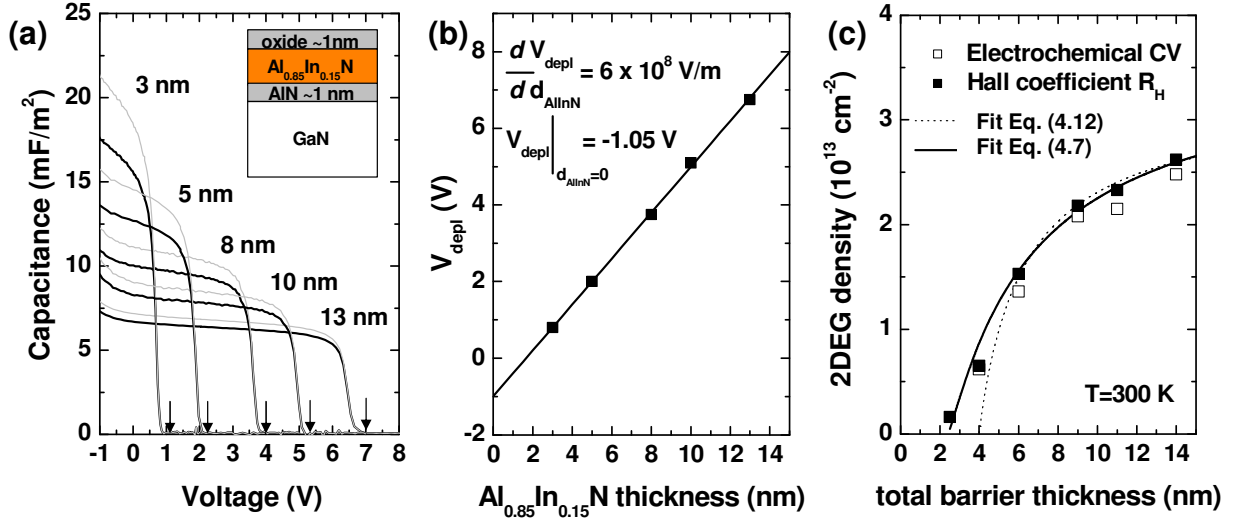


Figure 4.3 (a) Electrochemical CV of an $\text{Al}_{0.85}\text{In}_{0.15}\text{N}/\text{AlN}/\text{GaN}$ heterostructure. The AlN interlayer thickness is 1.1 nm for all subfigures. During the measurement a ~ 1 nm thin layer at the AlInN surface is transformed into an oxide. Black curves are as measured and grey ones true CV considering the oxide. The vertical arrows indicate the depletion voltage V_{depl} , which is defined as $n_{2D}=0$. (b) Depletion voltages V_{depl} as a function of AlInN thickness. Slope and offset are indicated. (c) 2DEG density as a function of the total barrier thickness $d_{\text{AlInN}}+d_{\text{AlN}}$: obtained by RT Hall measurement (R_H) and integrated from the CV-curves in subfigure (a). Full line corresponds to Equation (4.7) while dashed line stands for the approximated Equation (4.12).

Usually, the serial capacitance is independent of the resistance r_s . If a voltage is applied to the electrolyte the current flow induces an oxidation of the AlInN surface with a thickness of ~ 1 nm. The capacitance for an oxide dielectric layer is given as

$$C_{ox} = \frac{\epsilon \epsilon_r}{d} \quad (4.13)$$

Assuming that AlInN is transformed into Al_2O_3 with $\epsilon \sim 12$ then C is $\sim 0.1 \text{ F/m}^2$. The total measured capacitance is then simply the capacitance of two capacitors in series according to

$$C_{tot} = \frac{C \cdot C_{ox}}{C + C_{ox}} \quad (4.14)$$

where C is the true capacitance of the semiconductor heterostructure. In Figure 4.3 (a) the CV curves for $\text{Al}_{0.85}\text{In}_{0.15}\text{N}/\text{AlN}/\text{GaN}$ heterostructures are reported. Black lines indicate the *as measured* curves while grey curves indicate the corrected curves assuming 1 nm oxide layer. The capacitance for an arbitrary semiconductor heterostructure is given as

$$C(V_a) = e \frac{dQ}{dV} = e \frac{1}{dV} \left(\int [\rho(z, V_a) - \rho(z, V_a + dV)] dz \right) \quad (4.15)$$

with the space charge density ρ as a function of the z -position and the applied voltage V . The plateau-like structure results from the fact that the 2DEG is depleted approximately linearly with increasing applied voltage (an exact linear dependence would result in a Heaviside-step like behaviour which is not true and will be discussed in chapter 5). However, an integration of the CV curve from 0 V to the depletion voltage gives therefore according to Equation (4.15) the exact 2DEG density stored in the capacitor.

4 Electrical characterization of $\text{Al}_{1-x}\text{In}_x\text{N}$ (0001) ($0.07 \leq x \leq 0.21$)

Thus the thin oxide layer leads therefore to a slight underestimation of the true 2DEG density, as can be seen from Figure 4.3 (a). On the other hand, the depletion voltage is not significantly shifted. However, it might be possible that the electrolyte with a pH value of ~ 3 also influences the surface potential in the specific situation of electrolyte/AlInN surface in contrast to the free surface. This would then result in a shift of the integration range.

In Figure 4.3 (b) the depletion voltage *versus* AlInN barrier thickness is shown and gives, as can be expected from Equation (4.9), a linear behaviour. The slope $dV_{\text{depl}}/dd_{\text{AlInN}} = e \cdot \sigma_{\text{AlInN/GaN}}(0.15)/\epsilon_0\epsilon_{\text{AlInN}}(0.15)$ is $\sim 6 \times 10^8$ V/m, or expressed in terms of $\sigma_{\text{AlInN/GaN}}(0.15)/\epsilon_{\text{AlInN}}(0.15) \sim 0.332 \times 10^{17} \text{ m}^{-2}$. The offset at $d_{\text{AlInN}}=0$ is ~ -1.05 V. However, as it can be seen from Equation (4.9) this value is non-zero and determined by the other four non-vanishing expressions in Equation (4.9). Figure 4.3 (c) shows the integrated 2DEG densities from the uncorrected CV curves together with the Hall coefficients R_H at RT. Not considering the oxide films in CV analysis leads therefore to an underestimate of the correct 2DEG density. Note that R_H and CV results are in a very good agreement if the 1 nm oxide layer is considered.

We can now benefit from the information $\sigma_{\text{AlInN/GaN}}(0.15)/\epsilon_0\epsilon_{\text{AlInN}}(0.15) = 6 \times 10^8$ V/m and solve it for the unknown dielectric constant of the AlInN and plug the result back in Equation (4.7). Now there are 4 unknown parameters namely the surface potential $e\Phi_s(x)$, polarization charge across the AlInN/AlN interface $\sigma_{\text{AlInN/AlN}}(x)$, the dielectric constant of the alloy $\epsilon_{\text{AlInN}}(x)$, and the critical thickness t_{cr} . For the other parameters it is assumed

$$\begin{aligned} d_{\text{AlN}} &= 1.1 \text{ nm} & \Delta E_{C, \text{AlInN/AlN}}(0.15) &= 1.1 \text{ eV} & \sigma_{\text{AlN/GaN}} &= 6.5 \times 10^{17} \text{ m}^{-2} \\ \epsilon_{\text{AlN}} &= 10.3 & \Delta E_{C, \text{AlN/GaN}} &= 1.7 \text{ eV} \end{aligned} \quad (4.16)$$

Then the unknown parameters can be extracted by fitting data in Figure 4.3 (c) with Equation (4.7.) solved for the 2DEG densities yielding

$$\begin{aligned} e\Phi_s(0.15) &= 2.9 \text{ eV} \\ \sigma_{\text{AlInN/AlN}}(0.15) &= -2.8 \times 10^{17} \text{ m}^{-2} \quad \rightarrow \quad \sigma_{\text{AlInN/GaN}}(0.15) = 3.7 \times 10^{17} \text{ m}^{-2} \\ \epsilon_{\text{AlInN}}(0.15) &= 11.3 \\ t_{\text{depl}} &= 2.3 \text{ nm} \end{aligned} \quad (4.17)$$

With the parameters we deduced the model well reproduces the experimental data in the whole thickness range. Additionally the approximation from Equation (4.12) is shown as dotted line, which fits well only in a certain density regime, suggesting that no simple analytic expression is available. Then Equation (4.1) must be fully taken into account.

Figure 4.4 displays the CV curves for an $\text{Al}_{0.85}\text{In}_{0.15}\text{N}/\text{AlN}/\text{GaN}$ heterostructure with a fixed AlInN thickness of ~ 12.5 nm and various AlN interlayer thicknesses from 0.6 to 2.1 nm. The inset shows the depletion voltage for different interlayer thicknesses. The behaviour is not linear as in Figure 4.3 (b) and predicted by Equation (4.9). The local slope for the thicker interlayers 1.7 nm – 2.1 nm gives approximately the value expected for an AlN layer, namely $dV_{\text{depl}}/dd_{\text{AlN}} = e \cdot \sigma_{\text{AlN/GaN}}/\epsilon_0\epsilon_{\text{AlN}}$ is $\sim 11 \times 10^8$ V/m, or expressed in terms of $\sigma_{\text{AlN/GaN}}/\epsilon_{\text{AlN}} \sim 0.609 \times 10^{17} \text{ m}^{-2}$. On the other hand for a vanishing interlayer $d_{\text{AlN}}=0$ one should make the transition from 3-layer model Equation (4.7) to the 2-layer model Equation (4.3). A fit of depletion voltages for simple AlInN/GaN heterostructures (not shown here) yields again a slope $dV_{\text{depl}}/dd_{\text{AlInN}} = e \cdot \sigma_{\text{AlInN/GaN}}(0.15)/\epsilon_0\epsilon_{\text{AlInN}}(0.15)$ is $\sim 6 \times 10^8$ V/m but with a slightly different offset of ~ -0.85 V. Assuming a conduction band offset at the single

4 Electrical characterization of $\text{Al}_{1-x}\text{In}_x\text{N}$ (0001) ($0.07 \leq x \leq 0.21$)

$\text{Al}_{0.85}\text{In}_{0.15}\text{N}/\text{GaN}$ heterojunction of ~ 0.5 eV then the surface potential $e\Phi_s$ is according to $V_{\text{depl}}|_{d_{\text{AlInN}}=0} = e\Phi_s - \Delta E_C(x)$ approximately 1.35 eV, *i.e.* is only half the value found in heterostructures with thicker interlayers. This implicit dependence of the surface potential and conduction band offset is not considered in Equation (4.7).

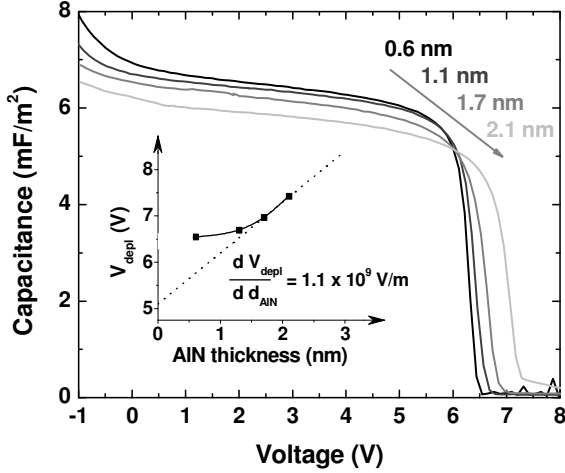


Figure 4.4 CV curves for an $\text{Al}_{0.85}\text{In}_{0.15}\text{N}/\text{AlN}/\text{GaN}$ heterostructure with a fixed AlInN thickness of ~ 12.5 nm and various AlN interlayer thicknesses. Inset shows the depletion voltage for the respective interlayer thicknesses. The behaviour is not linear as in Figure 4.3 (b). This is caused by thickness dependence of the surface potential and possibly due to a change in the static dielectric constant for these ultrathin layers. Local slope for thicker interlayers give approximately the value expected for an AlN layer.

Electron holography Zhou *et al.* performed electron holography measurements on the sample with 1.1 nm AlN interlayer and 13 nm $\text{Al}_{0.85}\text{In}_{0.15}\text{N}$ thickness [5]. When a TEM sample is not in strongly diffracting conditions, and has uniform potential through its projected thickness, then the relationship between the holographic phase shift Φ and electrostatic potential V is linear such as $\Phi = c_E V t$, where c_E is an energy-dependent constant and t is the sample thickness. Details are given in Ref. [5]. For these measurements it is necessary to thin the samples to ~ 200 nm *via* mechanical wedge-polishing and chemical etching in KOH solution. Figure 4.5 shows the electrostatic potential and the electron accumulation near the GaN/AlN interface calculated via Poisson's equation $n(z) = -\epsilon_0 \epsilon_r \partial^2 V(z) / \partial z^2$. Note that Zhou *et al.* estimated from this relation a 2DEG density of around $\sim 2.15 \times 10^{17} \text{ m}^{-2}$, *i.e.* somewhat lower compared to the electrical characterization in Figure 4.3. The deviation can have several origins: specific dielectric constant of the GaN buffer, penetration of 2DEG into the AlN not considered, averaging over a large region therefore interface morphology becomes important, and strain relaxation due to the small sample size. The field across the AlN layer is found to be 6.9 MV/cm. However, knowing the electric field for a specific thickness allows separating the expression $\sigma_{\text{AlN}/\text{GaN}}/\epsilon_{\text{AlN}}$ *via* solving

$$E_{C,\text{AlN}} = e(\sigma_{\text{AlN}/\text{GaN}} - 2.5 \times 10^{17} \text{ m}^{-2}) / (\epsilon_0 \epsilon_{\text{AlN}}) = 6.9 \times 10^8 \text{ V/m}$$

$$\frac{\partial V_{\text{depl}}}{\partial d_{\text{AlN}}} = e \cdot \sigma_{\text{AlN}/\text{GaN}} / \epsilon_0 \epsilon_{\text{AlN}} = 1.1 \times 10^8 \text{ V/m} \quad (4.18)$$

for the static dielectric constant and the total polarization charge leads to $\sigma_{\text{AlN}/\text{GaN}} \sim 6.5 \times 10^{17} \text{ m}^{-2}$ and $\epsilon_{\text{AlN}} \sim 10.2$. The same can be performed for the AlInN layer and leads to $\sigma_{\text{AlInN}/\text{GaN}}(0.15) \sim 3.6 \times 10^{17} \text{ m}^{-2}$ and $\epsilon_{\text{AlInN}}(0.15) \sim 11$, *i.e.* in a very good agreement with the assumptions made in Equations (4.16) for the former case of the AlN interlayer and the parameters obtained from the balance equation model Equation (4.17) for the latter case of the AlInN barrier.

4 Electrical characterization of $\text{Al}_{1-x}\text{In}_x\text{N}$ (0001) ($0.07 \leq x \leq 0.21$)

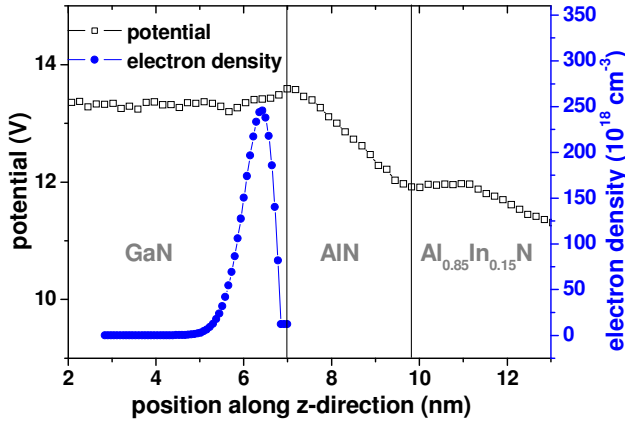


Figure 4.5 Electrostatic potential of an $\text{Al}_{0.85}\text{In}_{0.15}\text{N}/\text{AlN}/\text{GaN}$ heterostructure with 13 nm barrier thickness and 1 nm AlN interlayer thickness obtained by TEM electron holography. The field across the AlN interlayer reaches 6.9 MV/cm. Image is taken from Ref. [5].

2DEG densities in $\text{Al}_{1-x}\text{In}_x\text{N}/\text{AlN}/\text{GaN}$ heterostructures As we saw in the previous discussion from the simple balance equation we can extract the relevant electrostatic properties such as surface potential, dielectric constant and polarization charges. Now we apply this tool to get the parameters for heterostructures with indium composition in the range $0.07 \leq x \leq 0.21$. In Figure 4.6, the depletion voltages V_{depl} for 6 and 14 nm thick barriers as a function of $\text{Al}_{1-x}\text{In}_x\text{N}$ thickness for several compositions are shown. Black lines and grey lines indicate tensile and compressive regime, respectively. In subfigure 4.6 (b) the 2DEG densities (integrated from CV curve) at RT for 6, 9, 14 and 33 nm thick $\text{Al}_{1-x}\text{In}_x\text{N}$ barriers on GaN epilayers (black squares) are depicted. Blue lines correspond to a fit using Equation (4.7). A full line turning into a dashed line indicates that the critical thickness t_{cr} , beyond which pseudomorphic AlInN layers are expected to relax, is reached for the respective composition. Especially, the 14 nm barriers in the compressive regime exhibit similar 2DEG densities as the LM heterostructures causing similar depletion voltages. The electrostatic parameters are summarized in Table 4.1.

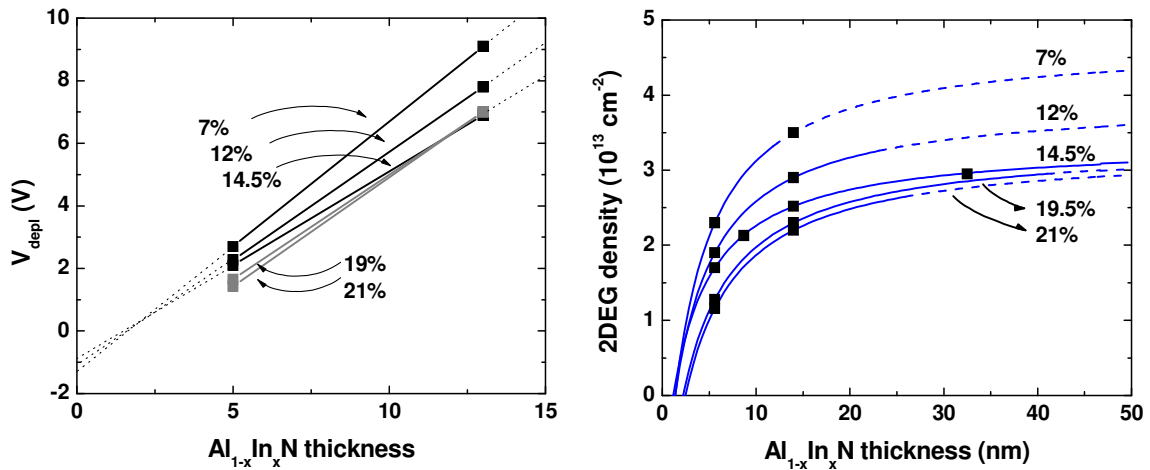


Figure 4.6 (a) Depletion voltages V_{depl} for 6 and 14 nm thick barriers as a function of the $\text{Al}_{1-x}\text{In}_x\text{N}$ thickness for several compositions. Black and grey lines stand for the tensile and compressive regime, respectively. (b) 2DEG density (integrated from CV curve) at RT for 6, 9, 14 and 33 nm thick $\text{Al}_{1-x}\text{In}_x\text{N}$ barriers on GaN epilayers (black squares). Blue lines correspond to fits using Equation (4.7). A full line turning into a dashed line indicates that the critical thickness t_{cr} , beyond which pseudomorphic AlInN layers are expected to relax, is reached for the respective composition.

4 Electrical characterization of $\text{Al}_{1-x}\text{In}_x\text{N}$ (0001) ($0.07 \leq x \leq 0.21$)

Indium content	t_{cr} of $\text{Al}_{1-x}\text{In}_x\text{N}$ (nm)	2DEG density (10^{13} cm^{-2})		$\Delta E_{C, \text{AlInN}/\text{AlN}}$ (eV)	$e\Phi_b(x)$ (eV)	$\sigma(x)/e$ (10^{13} cm^{-2})	$\epsilon_{\text{AlInN}}(x)$
		6 nm	14 nm				
7%	12.4	2.0	4.0	0.5	4.4	5.4	10.8
12%	24.9	1.6	2.9	1.0	3.4	4.2	10.9
14.5%	52.1	1.5	2.6	1.2	3.0	3.7	11.2
19.5%	44.6	1.28	2.3	1.5	2.6	3.3	~11.8
21%	28.0	1.16	2.2	1.6	2.6	3.2	~11.8

Table 4.1 Critical thickness t_{cr} for plastic relaxation, 2DEG densities deduced from C-V measurements for 6 and 14 nm thick barriers, band offset at the AlInN/AlN interface, surface potential and bound interface sheet density for 5 different compositions in the nearly LM regime between 7-21%.

Since band offset in nitride heterostructures can only be hardly measured we make the following assumption for the AlInN/AlN interface: it has been demonstrated that the valence band offset of coherently strained InN(2nm)/AlN (0001) is $\Delta E_{V, \text{InN}/\text{AlN}} \sim 3.1 \text{ eV}$ [6]. Furthermore it has been shown that the valence band offset of $\text{Al}_{1-x}\text{In}_x\text{N}/\text{GaN}$ heterostructures scales linearly between the binary compositions [7]. Therefore, the band offset is estimated as $\Delta E_{C, \text{AlInN}/\text{AlN}} = E_{g, \text{AlN}} - E_{g, \text{AlInN}(x)} - x \cdot \Delta E_{V, \text{InN}/\text{AlN}}$, where the bandgap dependence of the AlInN alloy is taken from Ref. [8]. Note that even in the case that the band offset of $\text{Al}_{0.0}\text{In}_{1.0}\text{N}/\text{AlN}(1\text{nm})/\text{GaN}$ behaves more as the band alignment of an InN/GaN heterostructure [9], *i.e.* negligible influence of the 1 nm AlN interlayer, the error in the low indium regime of the alloy on the band offset is minor since $\Delta E_{V, \text{AlN}/\text{GaN}} + \Delta E_{V, \text{InN}/\text{GaN}} \sim 1.5 \text{ eV}$.

Figure 4.7 (a) shows the 2DEG densities *versus* indium composition for 6 and 14 nm thick AlInN barriers and the extrapolated total bound sheet density $\sigma(x)/e$ obtained using Equation (4.7). Error bars indicate an uncertainty of $\pm 0.3 \times 10^{13} \text{ cm}^{-2}$ for the extrapolated $\sigma(x)/e$. Additionally, the spontaneous $P_{sp}(x)$ and the piezoelectric $P_{pz}(x)$ polarizations and their sum is shown based on the calculations of the macroscopic polarization for the AlInN alloy for two different atomic structures as given by Bernardini *et al.* [10]. Indeed, these authors pointed out a strong nonlinear behavior for $P_{sp}(x)$ and $P_{pz}(x)$ depending on the atomic structure. Calculations were performed for a random alloy, *i.e.* a random distribution of group-III elements on the wurtzite cation sites, while anion sites are occupied by nitrogen leading to a P_{sp} bowing parameter $b_{\text{random}} \sim -0.065 \text{ C/m}^2$ (black lines in Figure 4.7 (a)). On the other hand, ordering effects in the AlInN alloy can lead to a significant change in $P_{sp}(x)$. Thus for a CuPt-like structure, *i.e.* Al (or In) atomic planes alternating with Ga planes along the [0001] direction, b_{CuPt} is predicted to be $\sim -0.337 \text{ C/m}^2$ (grey lines in Figure 4.7 (a)). For the tensile strain regime, extrapolated $\sigma(x)/e$ values agree fairly well with the trend expected for pseudomorphic layers, *i.e.* a contribution from $P_{pz}(x)$ is present. On the other hand, the uncertainties on the extrapolation do not allow drawing a conclusion for the atomic structure of AlInN. In the compressive regime (samples 19.5% and 21%), the $\sigma(x)/e$ values are much higher than expected for a pseudomorphic random alloy. Even the 2DEG densities for the 14 nm thick AlInN barriers exceed the polarization limit given by the black full line despite only a minor onset of relaxation of $\sim 10\%$. The exact mechanism responsible for this behavior is

4 Electrical characterization of $\text{Al}_{1-x}\text{In}_x\text{N}$ (0001) ($0.07 \leq x \leq 0.21$)

not known at the present stage. Elastic energy release through AlInN phase segregation could be invoked, ordering effects or roughness induced polarization charges [11-12] could also play a role. In the next subsection the possibility of an Indium gradient is discussed.

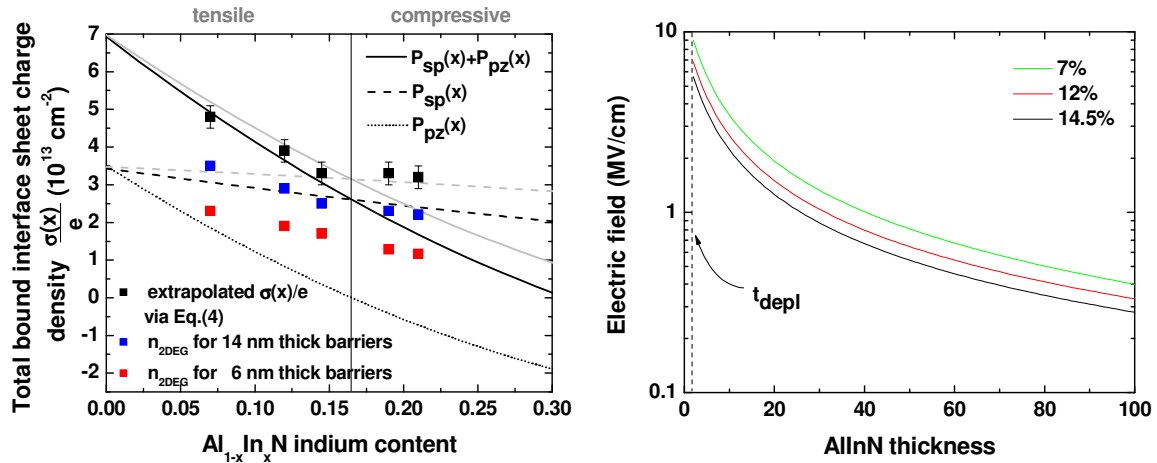


Figure 4.7 (a) Lines correspond to spontaneous (---) and piezoelectric (---) polarization charges and the sum of both (—) at RT. Black lines indicate the behavior of a random alloy while light grey lines correspond to a CuPt-like structure for the AlInN alloy. 2DEG densities for 6 nm thick (red squares), 14 nm thick (blue squares) AlInN barriers and the extrapolated total bound. (b) Electric field across the AlInN barrier for 7%, 12% and 14.5% indium calculated from the Equation (4.7) and Equation (4.18) using the parameters from Table 4.1.

The dielectric constant of AlN ~ 10.3 is close to the prediction of Wagner *et al.* for a strained AlN layer [13]. For the AlInN alloy the behavior seems to be non-linear. This is consistent with the findings for bowing parameters of longitudinal optical phonon frequencies [14] and of refractive indices [15].

If the dependence of the 2DEG density on barrier thickness and polarization charge is known for a specific composition, the electric field across the AlInN barrier as a function of the barrier thickness can easily be calculated using Equations (4.7) and (4.18) and the parameters from Table 4.1. The resulting field dependence is displayed in Figure 4.7 (b). Especially the optical properties depend sensitively on this electric field as discussed in Chapter 6. Note that only for thicknesses below t_{depl} , i.e. for fully depleted 2DEG, the field is given exactly by $e \cdot \sigma_{\text{AlInN/GaN}}(x) / \epsilon_0 \epsilon_{\text{AlInN}}(x)$.

Graded AlInN We demonstrated the overall very good agreement and consistency of electronic properties in the tensile regime. Now, it will be demonstrated that the assumption of an AlInN composition gradient in the compressive regime leads to a very good agreement with the observed behaviour. Indeed, Lorentz and co-workers [16-17] showed that compressively grown AlInN relaxes favourably by building up a compositional gradient starting from the composition higher than the LM composition and arriving at the LM composition close to the surface.

In Figure 4.8 (a) the experimental XRD ω -scans around the GaN (002) reflection for an $\text{Al}_{0.79}\text{In}_{0.21}\text{N}/\text{AlN}(1\text{nm})/\text{GaN}$ heterostructure is shown together with the simulated spectra for a constant concentration of 21% In, which is the content estimated by RBS. As it can be seen it does not match very precisely the shoulder at larger angles with respect to the GaN peak. We now verify the possibility of a gradient in the composition throughout the barrier and assuming a linear compositional gradient starting from $\sim 26\%$ near the AlInN/AlN interface and decreasing down to 16.5% at the sample surface (red). Note that in this case the

4 Electrical characterization of $\text{Al}_{1-x}\text{In}_x\text{N}$ (0001) ($0.07 \leq x \leq 0.21$)

mean indium composition is conserved ($26\% + 16.5\%$) / 2 $\sim 21\%$. As it can be seen the curve with gradient better matches the experimental data.

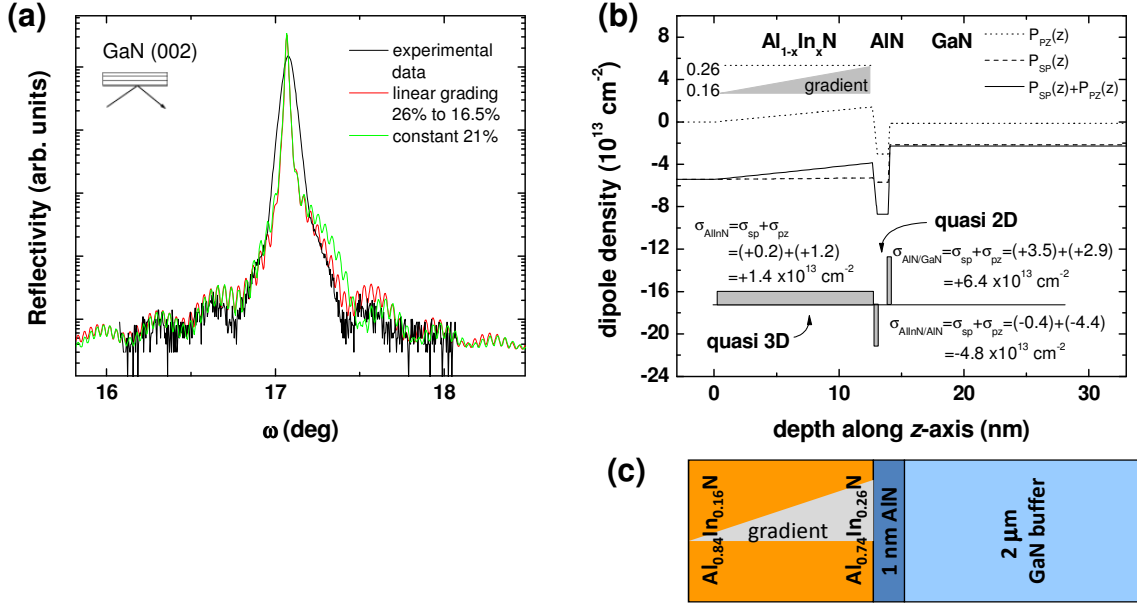


Figure 4.8 (a) Experimental data for an $\text{Al}_{0.79}\text{In}_{0.21}\text{N}/\text{AlN}(1\text{nm})/\text{GaN}$ heterostructure together with the simulated spectra for a constant In concentration of 21% throughout the barrier (green) and a linear compositional gradient starting from $\sim 26\%$ near the AlInN/AlN interface and decreasing down to 16.5% at the sample surface (red). (b) $P_{sp}(z)$ and $P_{pz}(z)$ and the sum of both across an $\text{Al}_{1-x}\text{In}_x\text{N}(13\text{nm})/\text{AlN}(1\text{nm})/\text{GaN}$ heterostructure with a composition gradient in the AlInN barrier according to the sketch in subfigure (c).

As shown in Figure 4.7, for high indium contents (*e.g.* $x \sim 21\%$) the 2DEG densities for the 14 nm thick barriers exceed the polarization charge density calculated for a homogeneous pseudomorphic alloy. Now we want to verify the effect of a gradient on the polarization charge across such a heterostructure. The results are depicted in Figure 4.7 (b). Shown are the $P_{sp}(z)$ and the $P_{pz}(z)$ and the sum of both. The gradient of $P_{sp}(z) + P_{pz}(z)$ across the AlN/GaN heterointerface gives according to Equation (4.1) the quasi 2D bound sheet charge of $\sim \sigma_{\text{AlN/GaN}} \sim 6.4 \times 10^{17} \text{ m}^{-2}$. The main difference compared to a homogenous barrier is the non-vanishing contribution from gradient of the polarization within the AlInN . This results in a quasi 3D behaviour of polarization in the AlInN besides the fixed polarization charges at the AlInN/AlN heterointerface. If the gradient is linear then according to Equation (4.1) the polarization gradient yields a constant “background” polarization in the barrier. Integrating this 3D “background” polarization $\sigma_{3D, \text{graded AlInN}} \sim 1.1 \times 10^{19} \text{ cm}^{-3}$ over the barrier thickness yields a significant quasi 2D like contribution of $\sigma_{2D, \text{graded AlInN}} \sim 1.4 \times 10^{17} \text{ m}^{-2}$. This significantly can increase the total amount of polarization charges in the vicinity of the 2DEG channel, assuming $\sigma_{\text{total}} = \sigma_{2D, \text{graded AlInN}} + \sigma_{\text{AlInN/AlN}} + \sigma_{\text{AlN/GaN}} \sim (1.4 + 4.8 + 6.4) \sim 3 \times 10^{17} \text{ m}^{-2}$. Then the presence of the quasi 3D background doping can indeed increase the total amount of polarization charges that will be compensated by the 2DEG electrons. Similar discussions have been published for the grading of AlGaIn alloy [2].

4.5 Conclusions

It was demonstrated that a simple charge balance model can describe adequately the experimental electrical properties. Especially for LM $\text{Al}_{0.85}\text{In}_{0.15}\text{N}/\text{AlN}(1\text{nm})/\text{GaN}$, the polarization charge were found to be as high as $\sigma_{\text{AlInN/GaN}}(0.15) \sim 3.7 \times 10^{17} \text{ m}^{-2}$, and with the dielectric constant $\epsilon_{\text{AlInN}}(0.15) \sim 11.2$, the surface potential $e\Phi_s \sim 3 \text{ eV}$ and the critical thickness for the formation of the 2DEG $t_{\text{depl}} = 2.3 \text{ nm}$. The latter is especially important for normally-off HEMT devices, *i.e.* devices where a voltage has to be applied in order to have carriers in the channel [18]. These results were confirmed with potential mapping measurements *via* electron holography. This model can also be applied to the non-LM heterostructures where resulting parameters are summarized in Table 4.1. In the tensile regime, the polarization charges correspond to theoretical expectation for a homogeneous random alloy. In the compressive regime, the 2DEG density is too high compared with the theoretical calculation. It has been shown in the literature that compressive AlInN relaxes favourably by building up a compositional gradient ending with the LM composition at the surface. We calculated the polarization charge in such a heterostructure and it was found that any deviation from the homogenous case gives an additional background polarization to the polarization discontinuities at the heterointerfaces. This would indeed lead to an increase of total polarization and consequently in an increase of the 2DEG density. The parameters of Table 4.1 can also be used to calculate the electric field throughout the heterostructure as a function of the thickness. This is important for careful device design optimization.

Transition: A survey on mobilities in AlInN/AlN/GaN heterostructures

At this point a short excursion will be given in order to give an overview of general transport properties in nitride heterostructures. A detailed discussion of transport mechanisms will be given in the next chapter. By confining electrons at heterointerfaces, so that they can be regarded as quasi 2D sheet charges (although they possess an extension in the z -direction), usually lead to higher mobilities in comparison to a situation where the electrons have to travel in a 3D bulk layer. The higher mobility in the 2D case is mainly achieved by eluding the intentional doping and therefore the scattering on ionized impurities. Assuming a width of the 3D channel of $\sim 50 \text{ nm}$ than one requires a donor density of $N_D \sim 1 \times 10^{19} \text{ cm}^{-3}$ (and additionally fully ionized) to achieve the same amount of sheet charge as found in the 2DEG by ‘polarization doping’. Using the Brooks-Herring formula for scattering at ionized impurity in 3D with a $n_{II} = N_D \sim 1 \times 10^{19} \text{ cm}^{-3}$ at RT yields a mobility of $\sim 200 \text{ cm}^2/\text{Vs}$ [19]. The mobility drops even faster for higher impurity densities. On the other hand the confined 2D electrons form a natural channel within a few nm which can be used easily by controlling the currents *via* metallic contacts. In general one requires for high power applications both: high mobility and high 2DEG densities.

As demonstrated above, AlInN heterostructures have the capability to confine a high amount of electrons at the heterointerface. For a good in-plane transport we inserted an AlN interlayer. As can be seen in Figure 4.9 (a) by varying the AlN thickness a ‘high mobility

‘window’ is formed reaching a value of up to $1200 \text{ cm}^2/\text{Vs}$ at thicknesses of 1.1 nm [20]. The high mobility window originates from the fact that the 2DEG electrons penetrate into the alloy for $d_{\text{AlN}} = 0$. For $d_{\text{AlN}} > 1.7 \text{ nm}$ the strain induced by the interlayer in the GaN buffer is too large and decreases the channel interface quality, accompanied by an increase in the surface rms roughness value. This behaviour is also found in binary AlN/GaN heterostructures [21].

In Figure 4.9 (b) the iso-contours of sheet resistivity together with the $\mu(n_{2D})$ for different types of nitride heterostructures at 300 K are shown. Different 2DEG densities are mainly obtained by changing barrier thickness or composition. AlN/GaN can cover the whole range of densities up to $6 \times 10^{13} \text{ cm}^{-2}$ owing to the high “polarization doping” [21]. On the other hand AlGaN/GaN heterostructures can go to higher mobilities but thanks to only low 2DEG densities [22]. Strain-free AlInN heterostructures mediate between those two extrema yielding low sheet resistivity in the order of $\sim 200 \Omega/\square$ for $d_{\text{AlN}} = 1.1 \text{ nm}$. Similar as for AlInN heterostructures, the insertion of an AlN interlayer increases also the mobility in AlGaN/AlN/GaN heterostructures as indicated by the blue triangle [23].

On the other hand, an interesting behaviour of the mobility can be observed for the $\text{Al}_{0.85}\text{In}_{0.15}\text{N}/\text{AlN}(1\text{nm})/\text{GaN}$ heterostructure as a function of the AlInN barrier thickness (Figure 4.10 (a)). In general, the mobility at RT is reduced compared to low temperatures due to LO phonon scattering, while the mobility at low temperatures is limited only by structural properties, and is therefore, as we will see, a measure for the interface quality in terms of smoothness and atomistic perfection. In the limit of large barriers and consequently high 2DEG densities $\geq 2 \times 10^{13} \text{ cm}^{-2}$, the assumption of only one occupied subband is questionable. Thus the next chapter will be dedicated to the origin of the ‘high mobility windows’ while varying AlN interlayer or barrier layer thicknesses.

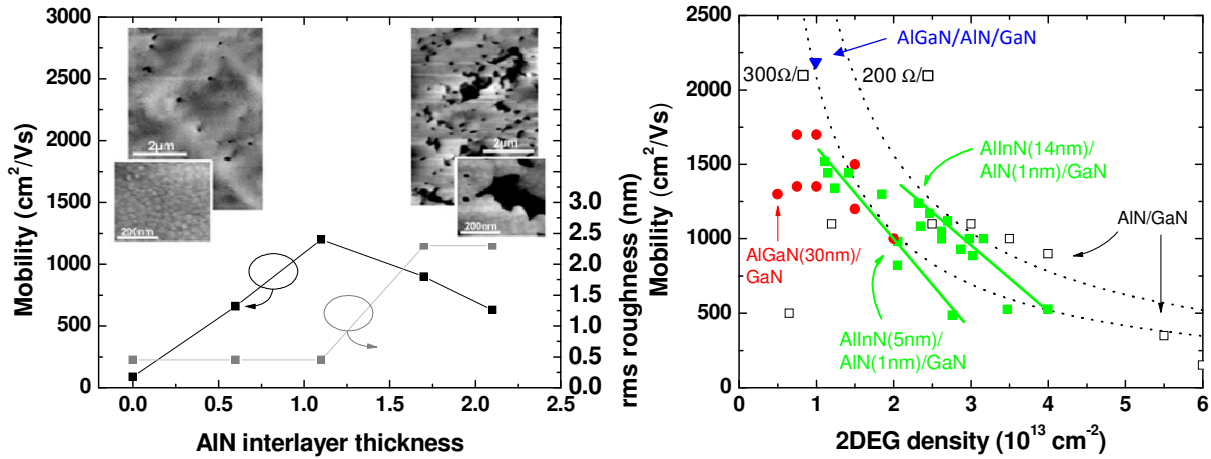


Figure 4.9 (a) ‘High mobility window’ in LM AlInN/AlN/GaN heterostructures as a function of the AlN interlayer thickness. For interlayer thicknesses $>1.7 \text{ nm}$ significant strain is induced in the 2DEG channel decreasing mobility. This is accompanied by surface morphology change and rms roughness value increase. (b) iso-contours of sheet resistance for different types of nitride heterostructures at 300 K. Different 2DEG densities are mainly induced by changing barrier thickness or composition. AlN/GaN system can cover the whole range of densities up to $6 \times 10^{13} \text{ cm}^{-2}$. AlGaN/GaN heterostructures can go to higher mobilities but for only low 2DEG densities. Strain-free AlInN heterostructures mediate between those two extrema yielding low sheet resistances in the order of $\sim 200 \Omega/\square$.

4 Electrical characterization of $\text{Al}_{1-x}\text{In}_x\text{N}$ (0001) ($0.07 \leq x \leq 0.21$)

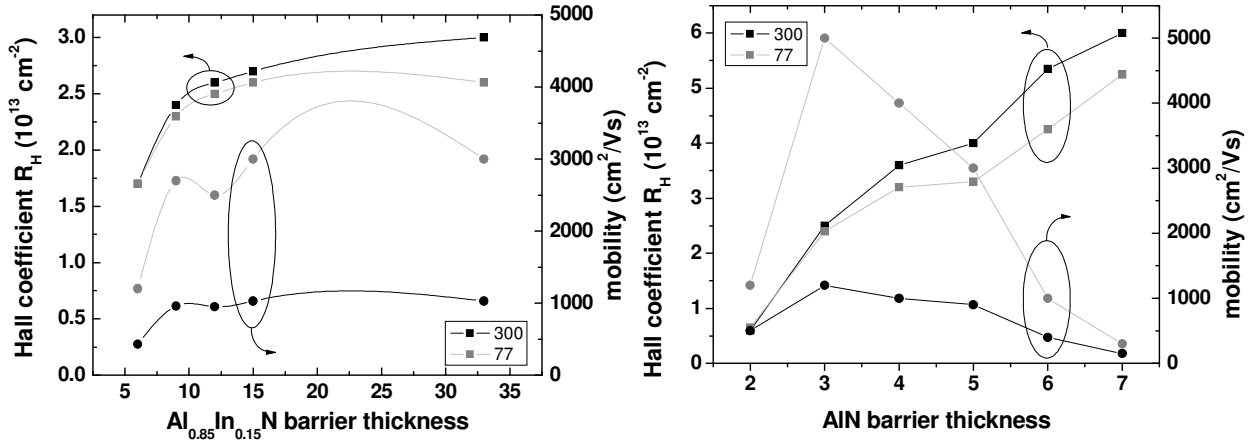


Figure 4.10 (a) Hall coefficient R_H and mobility for an $\text{Al}_{0.85}\text{In}_{0.15}\text{N}/\text{AlN}(1\text{nm})/\text{Ga}\text{N}$ heterostructure depending on the AlInN thickness at RT and 77 K. (b) Hall coefficient R_H and mobility for an $\text{AlN}/\text{Ga}\text{N}$ heterostructure as a function of the AlN thickness at RT and 77 K from Ref. [21]. High mobility window is observed for AlN thickness variation. For high 2DEG density samples R_H decreases strongly at low temperatures.

Temperature dependence of mobility Since the temperature dependence of the mobility will be crucial, especially for device characteristics, we will briefly summarize the relevant scattering mechanisms. A deeper insight into scattering rates can be found in Annex C and the references therein.

Usually the coupling of electron transport to acoustic phonon can be mediated through two modes namely the deformation potential or piezoelectric potential scattering. Since the acoustic branch of the dispersion has both longitudinal and transverse components one should ideally consider both. However, it has been shown that the transverse component is much weaker and is commonly neglected [2, 24]. In Figure 4.11 the temperature dependence of an $\text{Al}_{0.85}\text{In}_{0.15}\text{N}(13\text{nm})/\text{AlN}(1\text{nm})/\text{Ga}\text{N}$ heterostructure is displayed. Here the mobilities for deformation potential, piezoelectric scattering and optical phonon scattering are calculated using the expressions from Ref. [24] under the assumption of a single occupied subband. One can see that the contribution from the piezoelectric potential scattering is much weaker compared to the deformation potential scattering. For the scattering time on the dominant longitudinal-mode acoustic phonon one finds the following expression [2, 24]

$$\frac{1}{\tau_{ac}} = \frac{3 m^* b a_c^2 k_B T}{16 \rho v_s^2 \hbar^3} \quad (4.19)$$

where b is the parameter of the Fang-Howard wavefunction (for Figure 4.11 $b \sim 2.5 \times 10^9 \text{ m}^{-1}$), a_c is the deformation potential at the GaN Γ -valley ($\sim 9.1 \text{ eV}$), ρ is the density and v_s the sound velocity of GaN. This approximation is valid since acoustic phonon energy is very small [19].

Nevertheless, even more important is the scattering on optical phonon (black squares in Figure 4.11). If the phonon absorption process dominates, the scattering time is given by [25]

$$\frac{1}{\tau_{op}} = \frac{e^2 \omega_0 m^* N_B(T) G(q_0)}{2 \epsilon \epsilon_0 q_0 \hbar^2 F(y)} \quad (4.20)$$

Here, $q_0 = \sqrt{2m^*(\hbar\omega_{op})/\hbar^2}$ is the polar optical wavevector, N_B is the Bose-Einstein distribution function $N_B(T) = 1/(\exp(\hbar\omega_{op}/k_B T) - 1)$, and $F(y)$ is given by $F(y) = 1 + (1 - e^{-y})/y$ and y being a dimensionless variable $y = \pi\hbar^2 n_{2d} / m^* k_B T$. $G(q_0)$ is the form factor for the 2D wavefunction.

Over a wide range of temperatures the 2D mobility is mainly dominated by scattering on optical phonons. At low temperatures the mobility is limited by scattering mechanisms induced by interface roughness, interface roughness induced mechanisms, dislocation scattering, and scattering on ionized impurities. This will be subject of the following chapter. These mechanisms show only a very weak dependence on temperature [24]. The total mobility in Figure 4.11 is finally obtained using Matthiessen's rule.

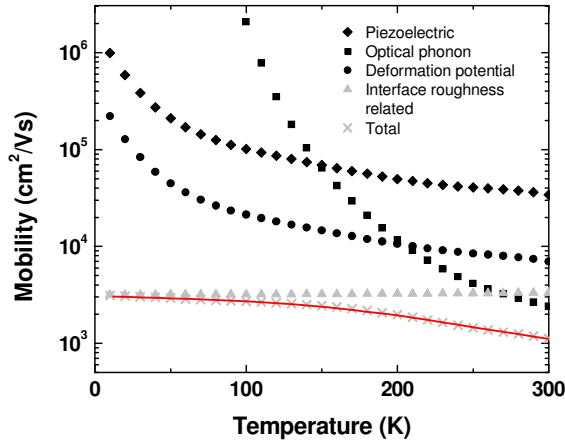


Figure 4.11 Temperature dependence of mobility of an $\text{Al}_{0.85}\text{In}_{0.15}\text{N}(13\text{nm})/\text{AlN}(1\text{nm})/\text{GaN}$ heterostructure. Scattering rates for potential, piezoelectric scattering and optical phonon are calculated following Ref. [24]. Total mobility is obtained by using Matthiessen's rule.

Bibliography

- [1] O. Ambacher, and V. Cimalla, *Polarization effects in semiconductors : from ab initio theory to device application* (Springer, New York, 2007).
- [2] D. Jena, *Polarization effects in semiconductors : from ab initio theory to device application* (Springer, New York, 2007).
- [3] P. Blood, *Capacitance-voltage profiling and the characterisation of III-V semiconductors using electrolyte barriers*, Semicond. Sci. Tech. **1**, 7 (1986).
- [4] D. K. Schroder, *Semiconductor material and device characterization* (Wiley, New York ; Chichester, 1990).
- [5] L. Zhou *et al.*, *Polarization field mapping of $\text{Al}_{0.85}\text{In}_{0.15}\text{N}/\text{AlN}/\text{GaN}$ heterostructure*, Appl. Phys. Lett. **94**, 121909 (2009).
- [6] C. L. Wu, C. H. Shen, and S. Gwo, *Valence band offset of wurtzite InN/AlN heterojunction determined by photoelectron spectroscopy*, Appl. Phys. Lett. **88**, 032105 (2006).

4 Electrical characterization of $\text{Al}_{1-x}\text{In}_x\text{N}$ (0001) ($0.07 \leq x \leq 0.21$)

- [7] P. D. C. King *et al.*, *Surface electronic properties of undoped InAlN alloys*, Appl. Phys. Lett. **92**, 172105 (2008).
- [8] E. Iliopoulos *et al.*, *Energy bandgap bowing of InAlN alloys studied by spectroscopic ellipsometry*, Appl. Phys. Lett. **92**, 191907 (2008).
- [9] P. D. C. King *et al.*, *InN/GaN valence band offset: High-resolution x-ray photoemission spectroscopy measurements*, Phys. Rev. B **78**, 033308 (2008).
- [10] F. Bernardini, and V. Fiorentini, *Nonlinear macroscopic polarization in III-V nitride alloys*, Phys. Rev. B **64**, 085207 (2001).
- [11] D. N. Quang *et al.*, *Roughness-induced piezoelectric charges in wurtzite group-III-nitride heterostructures*, Phys. Rev. B **72**, 115337 (2005).
- [12] D. N. Quang *et al.*, *Roughness-induced mechanisms for electron scattering in wurtzite group-III-nitride heterostructures*, Phys. Rev. B **72**, 245303 (2005).
- [13] J. M. Wagner, and F. Bechstedt, *Properties of strained wurtzite GaN and AlN: Ab initio studies*, Phys. Rev. B **66**, 115202 (2002).
- [14] V. Darakchieva *et al.*, *Lattice parameters, deviations from Vegard's rule, and E-2 phonons in InAlN*, Appl. Phys. Lett. **93**, 261908 (2008).
- [15] L. F. Jiang, W. Z. Shen, and Q. X. Guo, *Temperature dependence of the optical properties of AlInN*, J. Appl. Phys. **106**, 013515 (2009).
- [16] K. Lorenz *et al.*, *Relaxation of compressively strained AlInN on GaN*, J. Cryst. Growth **310**, 4058 (2008).
- [17] K. Lorenz *et al.*, *Anomalous ion channeling in AlInN/GaN bilayers: Determination of the strain state*, Phys. Rev. Lett. **97**, 085501 (2006).
- [18] C. Ostermaier *et al.*, *Ultrathin InAlN/AlN Barrier HEMT With High Performance in Normally Off Operation*, IEEE Electron Device Lett. **30**, 1030 (2009).
- [19] C. Hamaguchi, *Basic semiconductor physics* (Springer, Berlin ; New York, 2001).
- [20] M. Gonschorek *et al.*, *High electron mobility lattice-matched AlInN/GaN field-effect transistor heterostructures*, Appl. Phys. Lett. **89**, 062106 (2006).
- [21] Y. Cao, and D. Jena, *High-mobility window for two-dimensional electron gases at ultrathin AlN/GaN heterojunctions*, Appl. Phys. Lett. **90**, 182112 (2007).
- [22] L. Shen *et al.*, *AlGaIn/AlN/GaN high-power microwave HEMT*, IEEE Electron Device Lett. **22**, 457 (2001).
- [23] X. L. Wang *et al.*, *AlGaIn/AlN/GaN/SiC HEMT structure with high mobility GaN thin layer as channel grown by MOCVD*, J. Cryst. Growth **298**, 835 (2007).
- [24] M. N. Gurusinghe, S. K. Davidsson, and T. G. Andersson, *Two-dimensional electron mobility limitation mechanisms in $\text{Al}_x\text{Ga}_{1-x}\text{N}$ /GaN heterostructures*, Phys. Rev. B **72**, 045316 (2005).
- [25] B. L. Gelmont, M. Shur, and M. Strosio, *Polar Optical-Phonon Scattering in 3-Dimensional and 2-Dimensional Electron Gases*, J. Appl. Phys. **77**, 657 (1995).

Subband Structure and Transport

5.1 Introduction

This Chapter aims to describe electronic transport in AlInN/AlN/GaN heterostructures. Consequently, the first subchapter is dedicated to the structure of the electronic levels and its dependence on parameters such as barrier thickness and temperature. Since there are several hints for second subband population the transport properties are discussed in the framework of a multiband model. Then the morphology of the GaN/AlN interface is investigated more detailed because it is the main source of scattering for 2DEG. Afterwards, the strain induced in the GaN buffer by the monolayer fluctuations occurring at the AlN/GaN interface is discussed. This gives rise to local deformation of the conduction band and as a corollary to a strong local piezoelectric electric field. Besides the scattering on spatial fluctuations of the confining potential (*i.e.* interface roughness scattering), this is one of the main scattering sources in the high density regime. At the end of this Chapter it will be demonstrated that the transport property depending on barrier thickness agrees excellently with, if we take into account these scattering mechanisms.

5.2 Subband Structure

5.2.1 Generalities

In Chapter 4 the electronic properties of heterostructures were discussed in the framework of simple analytic models. However they do not allow to discuss the fine structure of electronic states. Therefore we start from one of the most fundamental equation in quantum mechanics, namely the *Schrödinger equation* which reads as

$$H_0 \Psi_n(\mathbf{r}) = \left(\frac{p^2}{2m} + V(\mathbf{r}) \right) \Psi_n(\mathbf{r}) = E_n \Psi_n(\mathbf{r}) \quad (5.1)$$

where p is the momentum operator, V the potential, m the mass of the particle, E energy of the particle and Ψ its wavefunction. If the particle is moving in a crystalline solid with a lattice periodicity Bloch has proven that the particles wavefunction can be written as the product of a plane wave and a function $u_{n,\mathbf{k}}(\mathbf{r})$ which has the same periodicity of the lattice. This is known as Bloch's theorem

$$\Psi_{n,\mathbf{k}}(\mathbf{r}) = u_{n,\mathbf{k}}(\mathbf{r}) e^{i\mathbf{k} \cdot \mathbf{r}} \quad (5.2)$$

where \mathbf{k} is referred to as the particles *wavevector*. The discrete index n labels the different states also called as *bands*. It is now of particular interest of knowing the particles energy E_n versus particles wavevector \mathbf{k} , which is referred to as *band dispersion relation*. This is the main motivation for the $k \cdot p$ perturbation theory sketched in the following briefly. Inserting now Equation (5.2) in Equation (5.1) yields

5 Subband Structure and Transport

$$H_{\mathbf{k}} u_{n,\mathbf{k}} = \left(\frac{p^2}{2m} + \frac{\hbar \mathbf{k} \cdot \mathbf{p}}{m} + \frac{\hbar^2 k^2}{2m} + V \right) u_{n,\mathbf{k}} = E_{n,\mathbf{k}} u_{n,\mathbf{k}} \quad (5.3)$$

The Hamiltonian can hence be written as sum of an unperturbed Hamiltonian H_0 and a perturbation $H_{\mathbf{k}}'$, *i.e.*

$$H_{\mathbf{k}} = H_0 + H_{\mathbf{k}}', \quad H_0 = \frac{p^2}{2m} + V, \quad H_{\mathbf{k}}' = \frac{\hbar \mathbf{k} \cdot \mathbf{p}}{m} + \frac{\hbar^2 k^2}{2m} \quad (5.4)$$

The approach is called the $k \cdot p$ perturbation theory due to the presence of the term $k \cdot p$ in Equation (5.3). At $\mathbf{k}=0$, *i.e.* at the Γ point of the Brillouin zone Equation (5.3) reduces to the unperturbed Hamiltonian H_0 , *i.e.* to Equation (5.1). The $k \cdot p$ perturbation approach exhibits an increase in accuracy towards small \mathbf{k} values and *vice versa*. According to the lowest non-trivial order perturbation theory $E_{n,\mathbf{k}}$ is given as [1]

$$E_{n,\mathbf{k}} = E_{n,0} + \frac{\hbar^2 k^2}{2m} + \frac{\hbar^2}{m^2} \sum_{n' \neq n} \frac{\left| \langle u_{n,0} | \mathbf{k} \cdot \mathbf{p} | u_{n',0} \rangle \right|^2}{E_{n,0} - E_{n',0}} \quad (5.5)$$

Note that several assumptions are made for these expressions, *i.e.* a degenerated band with an extremum at $\mathbf{k}=0$ (*i.e.* at the Γ point), spin-orbit coupling neglected. As a consequence bands become coupled and to increase the accuracy of the results especially for larger \mathbf{k} more bands have to be included. From Equation (5.5) an approximation for the conduction band dispersion $E_C(\mathbf{k})$ can be derived by, loosely speaking, replacing the denominator by the bandgap energy E_g . From $E_C(\mathbf{k})$ the effective mass, *i.e.* the curvature of the dispersion relation can be found by its second derivative

$$m^* = \hbar^2 \cdot \left[\frac{d^2 E(\mathbf{k})}{dk^2} \right]^{-1} \quad (5.6)$$

In general the effective mass is a tensor, *i.e.* its elements depend on the direction. Interestingly a very successful approximation for the conduction band effective mass m_C^* can be derived from Equation (5.5) with the help of Equation (5.6) yielding $m/m_C^* \approx 2P^2/mE_g$. With this approximation the m_C^* of most III-V and II-VI semiconductor can predicted correctly within 15% error assuming for the matrix element $E_P=2P^2/m$ a value of ~ 20 eV [1]. On the other hand if strongly confined carriers are present whose states lying energetically far above the bottom of the conduction band its effective mass becomes energy dependent and the dispersion relation hence is non-parabolic. This nonparabolicity can be described in the framework of Kane's model [2] which can be written, neglecting spin-orbit coupling, as

$$m/m^*(E) \approx 1 + 2F + E_P / (E + E_g) \quad (5.7)$$

where F is a parameter accounting for coupling to remote bands which amounts to $F=-0.9$ for GaN and E the subband [3] energy. Since the subband energy of confined 2DEGs can amount to several hundred meV in nitride heterostructures a strong increase of the corresponding in-plane effective mass is expected. An increase of 50% is found experimentally in InGaAs/InP QWs [4] and of 30% AlGaIn/GaN heterostructures [5] with respect to the bulk value. Nevertheless in the following the dispersion relation of the subbands are derived using numerical methods.

5.2.2 Application to AlInN/AlN/GaN heterostructures

Subband structure in heterostructures with high 2DEG densities The access to 2DEG densities above $2 \times 10^{13} \text{ cm}^{-2}$ was only achieved recently [6, 7]. For the AlGaIn/GaN system, where the 2DEG densities are restricted to $1.5 \times 10^{13} \text{ cm}^{-2}$ due to lower polarization charge across the interface, single band occupation is a sufficient approximation [8]. Therefore only scarce efforts have been undertaken to investigate multi-subband effects. For higher densities, however, this approximation does no longer hold. Experimentally subband occupation has been demonstrated with magnetoresistance experiments (Shubnikov-deHaas oscillations) indicating clearly the presence of higher occupied subbands [9-11].

To obtain the wavefunctions, subband densities and energies taking into account $k \cdot p$ corrections one has to solve Equation (5.3) together with the Poisson equation:

$$-\text{div}[\varepsilon(z) \nabla \varphi(z)] = -n(z) - \text{div} P_{pz}(z) - \text{div} P_{sp}(z) \quad (5.8)$$

where ε is the dielectric constant, φ the electrostatic potential, n the electron density and P the polarization charges, respectively. If the 2D subband energy dispersion relations are isotropic in the 2D Brillouin zone, *i.e.* $E(k_x, k_y) = E(k_{\parallel})$ with $k_{\parallel}^2 = k_x^2 + k_y^2$ (which is the case for wurtzite GaN), the integration reduces to a 1D integral and the subband densities are given by [12]

$$n(z) = \sum_{k_z} \frac{1}{2\pi} \int dk_{\parallel} k_{\parallel} \sum_i^8 |\chi_{in}|^2 f(E(k_{\parallel})) \quad (5.9)$$

with the $k \cdot p$ wave function χ and the Fermi-Dirac distribution function f . For the assumption of a parabolic 2D subband dispersion *i.e.* [13]

$$\Psi_n(\mathbf{r}) = \frac{e^{ik_{\parallel} \cdot \mathbf{r}_{\parallel}}}{\sqrt{A}} \Psi_n(z)$$

$$E(\mathbf{k}) = E_n + E(k_{\parallel}) = E_n + \frac{\hbar^2}{2m} (k_x^2 + k_y^2) \quad (5.10)$$

Equation (5.9) can be simplified to the expression

$$n(z) = \sum_n \left(\frac{mk_B T}{\pi \hbar^2} \right) \ln \left[1 + e^{(E_F - E_n)/k_B T} \right] |\Psi_n(z)|^2 \quad (5.11)$$

In the following, we compare the subband structure for an $\text{Al}_{0.85}\text{In}_{0.15}\text{N}(13 \text{ nm})/\text{AlN}(1 \text{ nm})/\text{GaN}$ heterostructure containing a total 2DEG density of $\sim 2.6 \times 10^{13} \text{ cm}^{-2}$ with parabolic subband dispersion (black) and with $k \cdot p$ corrections (red). Figure 5.1 shows a self-consistent calculation of electronic eigenstates of such a heterostructure for the first 3 subbands at $T=300 \text{ K}$. States are calculated with (red full lines) and without $k \cdot p$ corrections (black full lines), *i.e.* at $k=0$. The form of the wave function is not essentially altered. $k \cdot p$ states lie energetically higher than at $k=0$. Additionally, the single state variational solution is given (dashed line). It underestimates the position of the maximum because of not considering the piezoelectric charges [8].

5 Subband Structure and Transport

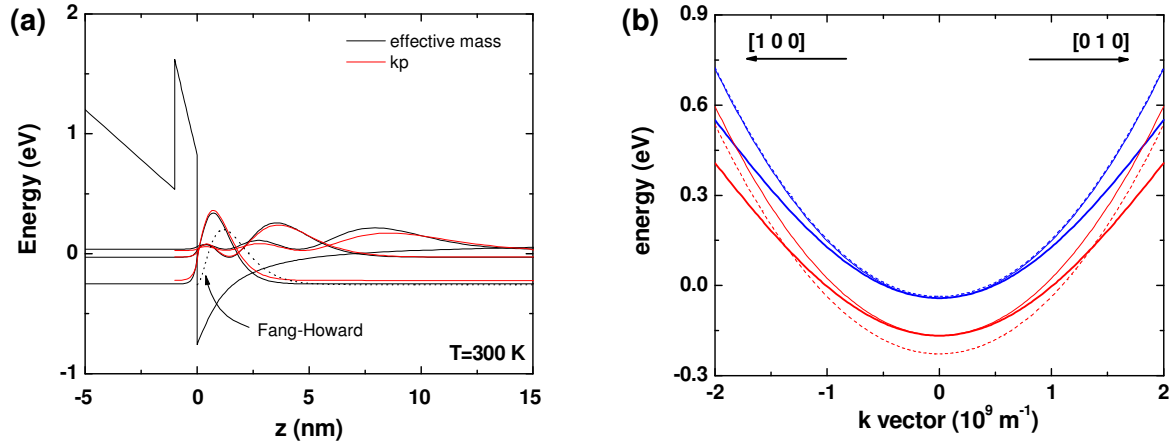


Figure 5.1 (a) Self-consistent calculation of electronic eigenstates in an $\text{Al}_{0.85}\text{In}_{0.15}\text{N}(13 \text{ nm})/\text{AlN}(1 \text{ nm})/\text{GaN}$ heterostructure for the first 3 subbands at $T=300 \text{ K}$. States are calculated with (red full lines) and without $k \cdot p$ corrections (black full lines), *i.e.* at $k=0$. Fermi level is at $E=0 \text{ eV}$. Variational solution for the ground state is given as dashed line. (b) In-plane dispersion relations for the first two subbands calculated in the framework of self-consistent single-band effective mass (dotted lines) and with self-consistent $k \cdot p$ (thick lines). The shaded full lines show the parabolic approximation. The Fermi level is always at $E=0 \text{ eV}$.

Neglecting $k \cdot p$ effects mainly affects the energy of the eigenstates. The ground state energy within the parabolic approximation is overestimated by $\sim 40 \text{ meV}$, the effect on the second subband is only one tenth, *i.e.* $\sim 4 \text{ meV}$. Note that the wavefunctions in parabolic approximation do not deviates significantly from $k \cdot p$ wavefunctions, as can be seen from Figure 5.1 (a). The main consequence for the in-plane transport is therefore the increase of the effective masses derived from the subband dispersion relations according to Equation (5.6) [4]. Since transport occurs at the Fermi circle the effective mass for the ground state should be strongly enhanced up to $m^* \sim 0.4 m_0$ for 2DEG densities $\geq 3 \times 10^{13} \text{ cm}^{-2}$ while the effective mass of the second subband is comparable to the effective mass in bulk GaN, *i.e.* $m^* \sim 0.2 m_0$. This increase of effective mass for the ground state has already been demonstrated experimentally for the AlGaN/GaN 2DEGs [14].

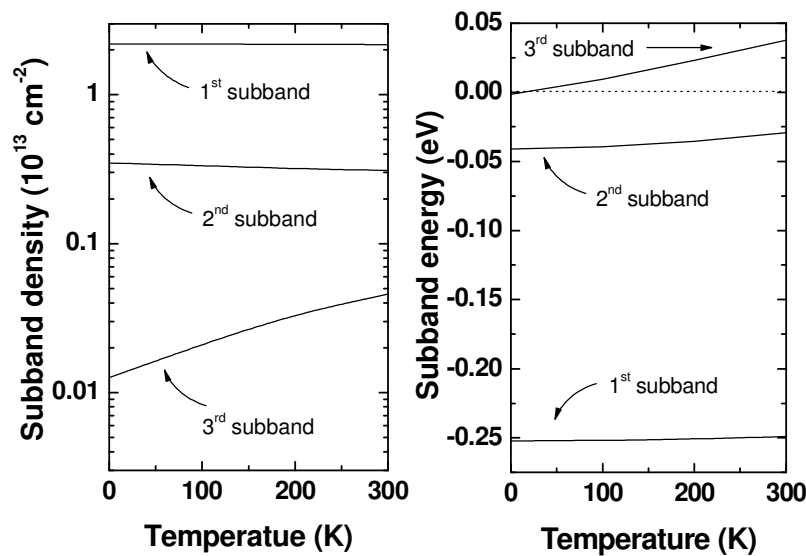


Figure 5.2 Self-consistent calculation of electronic eigenstates in an $\text{Al}_{0.85}\text{In}_{0.15}\text{N}(13 \text{ nm})/\text{AlN}(1 \text{ nm})/\text{GaN}$ heterostructure for the first 3 subbands in the temperature range 0 to 300 K. No temperature dependence on the lattice is assumed. Changes are only caused by the Fermi-Dirac statistics. Fermi level is located at $E=0 \text{ eV}$.

Another important issue is the stability of the subband occupancy *versus* temperature change. In Figure 5.2 the subband densities and energy levels are calculated for different temperatures in the 0 - 300 K range. Note that no temperature dependence was imposed on the piezoelectric charges, bandgap values, or surface potential in order to visualize the effect of the Fermi-Dirac statistics solely. It is found that only states close to the Fermi level are sensitive to the temperature. Far away from the Fermi level occupations are very inert towards temperature change. As a thumb rule one finds that the subband density drops by a factor 10 from the lower to the higher state, *e.g.* for this heterostructure $\sim 2.3 \times 10^{13} \text{ cm}^{-2}$ electrons are in the first state, $\sim 0.3 \times 10^{13} \text{ cm}^{-2}$ are in the second state and $\sim 0.04 \times 10^{13} \text{ cm}^{-2}$ are in the third state. Therefore, the high amount of carriers in the second state can affect the transport properties significantly.

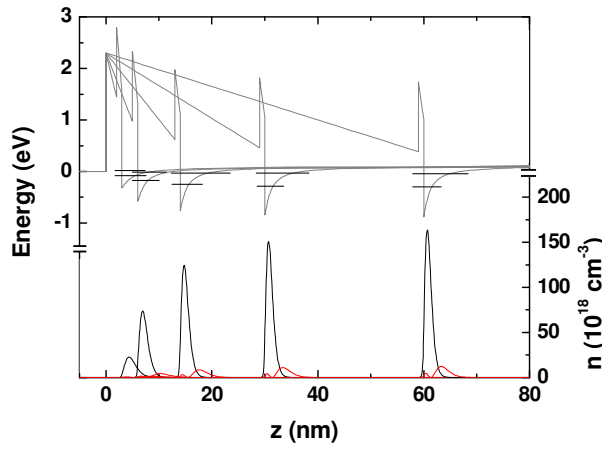


Figure 5.3 Self-consistent calculation of the electronic band structure, eigenstates and subband densities in a $\text{Al}_{0.85}\text{In}_{0.15}\text{N}/\text{AlN}(1\text{nm})/\text{GaN}$ heterostructure for the first 2 subbands at $T=300 \text{ K}$ as function of the AlInN barrier thickness.

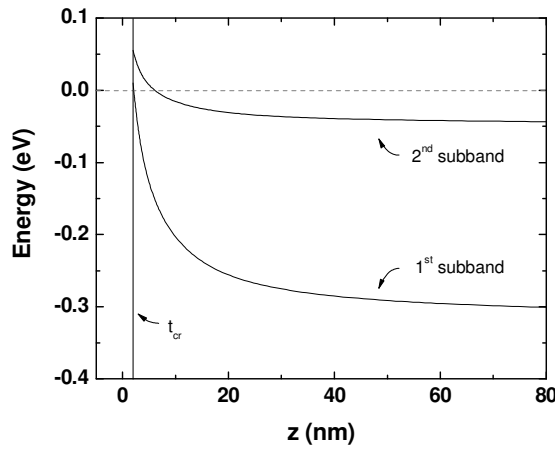


Figure 5.4 Self-consistent calculation of eigenstate energy in a $\text{Al}_{0.85}\text{In}_{0.15}\text{N}/\text{AlN}(1\text{nm})/\text{GaN}$ heterostructure for the first 2 subbands at $T=300 \text{ K}$ as function of the AlInN barrier thickness. Fermi level is located at $E=0 \text{ eV}$.

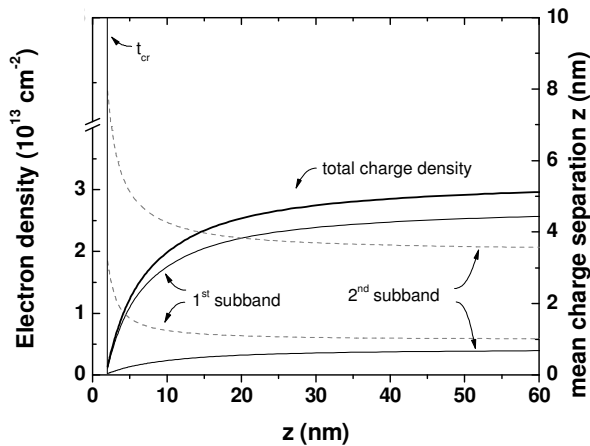


Figure 5.5 Self-consistent calculation of subband densities in an $\text{Al}_{0.85}\text{In}_{0.15}\text{N}/\text{AlN}(1\text{nm})/\text{GaN}$ heterostructure for the first 2 subbands at $T=300 \text{ K}$ as function of the AlInN barrier thickness. The dashed lines corresponds to the mean charge separation from the heterointerface in the presence of the piezoelectric charges according to relation $\bar{z} = \int z |\Psi|^2 dz / \int |\Psi|^2 dz$.

5 Subband Structure and Transport

Now we are focusing on the subband occupation as a function of the AlInN barrier thickness. The total 2DEG carrier density summed over all subbands should coincide with the findings from the simple charge balance model in chapter 4. This is depicted in Figure 5.5, where the 2DEG densities for the first two subbands and the sum of both as a function of the $\text{Al}_{0.85}\text{In}_{0.15}\text{N}$ barrier thickness are shown. Figure 5.3 displays the corresponding band structure and wavefunctions with the pinned surface. In Figure 5.4 the corresponding energies of the eigenstates are reported. For very thin barriers, and hence low 2DEG densities, the second subband lies energetically above the Fermi level at RT. From the wavefunctions, it is possible *via* the relation $\bar{z} = \int z |\Psi|^2 dz / \int |\Psi|^2 dz$ to calculate the mean charge separation from the heterointerface at $z=0$. These mean charge separations are also displayed in Figure 5.5 for the first two subbands. The mean charge separation is closely related to the transport properties: the larger the separation from $z=0$, the lower is the sensitivity to interface roughness and related scattering mechanisms. Especially, the second subband has a separation which is ~ 3 times larger than the ground state, thus it is expected to suffer less from scattering and thus possess higher mobility.

Now we are turning to the subband occupation under applied voltages. Figure 5.6 (a) shows the 2DEG subband and the total density for an $\text{Al}_{0.85}\text{In}_{0.15}\text{N}(13 \text{ nm})/\text{AlN}(1 \text{ nm})/\text{GaN}$ heterostructure under applied voltages calculated self-consistently. Additionally, the mean charge separation for the two subbands is given. The behaviour is similar to the case of barrier thickness variation. If the 2DEG is depleted the charge separation from the heterointerface is larger and consequently the scattering at the interface roughness is reduced. Hence the mobility increases. This manifests itself also in typical device characteristics and explains the observed transconductance peak which occurs at several volt reverse bias [15-17]. From the gradient of $n_{\text{total}}(V)$ the CV can directly be derived using Equation (4.15), which is depicted in subfigure 5.6 (b) and shown in the inset. Important is the conclusion that with CV methods no multi-subband occupation can be detected because they are depleted simultaneously. This differs from the behaviour in the GaAs system where occupied states are depleted subsequently [18] owing to the strong confinement and localizations of the wavefunctions and huge differences in subband densities in nitride heterostructures.

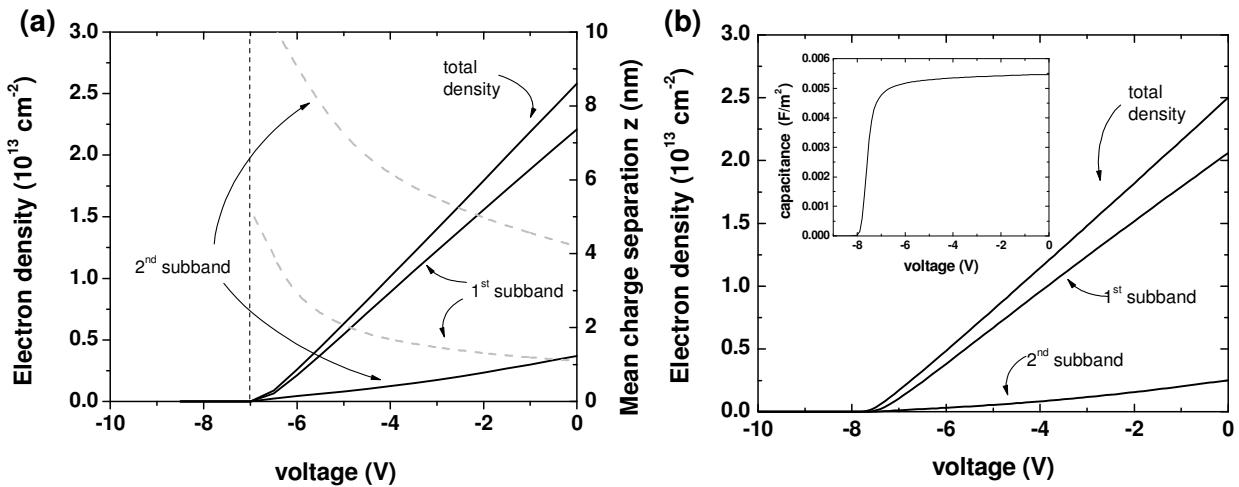


Figure 5.6 (a) 2DEG subband and total densities for an $\text{Al}_{0.85}\text{In}_{0.15}\text{N}(13 \text{ nm})/\text{AlN}(1 \text{ nm})/\text{GaN}$ heterostructure under applied voltages calculated self-consistently. Additionally, the mean charge separations for the two subbands are given. (b) According to Equation (4.15) the CV is given as the gradient of $n_{\text{total}}(V)$ and is shown in the inset. Temperature is 300 K.

5.3 Surface morphology, auto-correlation function, and power spectral density

Height distribution The height distribution function provides a complete specification of the random variable $h(r)$ at a position r . Although different rough surfaces may have different height distributions, the most generally used height distribution is the Gaussian height distribution

$$p(h) = \frac{1}{\sqrt{2\pi}w} \exp\left(-\frac{h^2}{2w^2}\right) \quad (5.12)$$

due to its mathematical simplicity and its place in the central limit theorem of the sum of large amount of random variables. Here w is the interface width. The n th order momentum is given as [19]

$$E\{(h-\bar{h})^n\} = \int_{-\infty}^{+\infty} (h-\bar{h})^n p(h) dh \quad (5.13)$$

where E is an average operator, which takes the ensemble average. \bar{h} is the average height and is usually assumed to be zero. The second order moment $n=2$ is one of the most important. Evaluating Equation (5.13) together with Equation (5.12) for $n=2$ gives:

$$E\{(h)^2\} = \int_{-\infty}^{+\infty} h^2 p(h) dh = w^2 \quad (5.14)$$

where w is called the root-mean-square (RMS) roughness or the interface width. Here it also equals to the standard deviation since $\bar{h}=0$. The w describes the fluctuations of the surface heights around an average surface height. Higher orders of Equation (5.13) define *e.g.* the skewness and kurtosis of the surface height.

Auto correlation function (ACF) The auto-covariance function is then defined as [19]

$$G(\mathbf{r}_1, \mathbf{r}_2) = E\{h(\mathbf{r}_1)h(\mathbf{r}_2)\} = \int_{-\infty}^{+\infty} \int_{-\infty}^{+\infty} h_1 h_2 p_j(h_1, h_2; \mathbf{r}_1, \mathbf{r}_2) dh_1 dh_2 \quad (5.15)$$

where p_j is the joint probability distribution which can be written as $p_j(h_1, h_2; \mathbf{r}_1, \mathbf{r}_2) = p(h_1)p(h_2)$ if h_1 and h_2 are independent of each other. Finally, the auto-correlation function is given as:

$$ACF(\mathbf{r}_1, \mathbf{r}_2) = \frac{G(\mathbf{r}_1, \mathbf{r}_2)}{w^2} \quad (5.16)$$

If $G(\mathbf{r}_1, \mathbf{r}_2)$ is isotropic one may write $r = |\mathbf{r}_1 - \mathbf{r}_2|$. It is obvious that $G(0) = w^2$, *i.e.*, the value of an auto-covariance function $G(r)$ at $r=0$, is equal to the variance of a surface height. An equivalent function to the ACF is the height-height correlation function $H(r)$, which is simply related to the $ACF(r)$ by $H(r) = 2w^2 [1 - ACF(r)]$.

So far, we have discussed only the statistical properties of a random field in real space. It is well known that there are two equivalent expressions for a field. One is in real space, as discussed above, and the other one is in Fourier space (reciprocal space). To

5 Subband Structure and Transport

consider the frequency properties of a field, an expression in reciprocal space is much more convenient. The most important statistical function in reciprocal space is the power spectrum $P(\mathbf{k})$, which can be simply defined as the Fourier transform of an auto-covariance function $G(\mathbf{r})$,

$$P(\mathbf{k}) = \frac{1}{2\pi} \int_{-\infty}^{+\infty} G(\mathbf{r}) e^{-i\mathbf{k} \cdot \mathbf{r}} d\mathbf{r} \quad (5.17)$$

Here \mathbf{k} is the wave vector in Fourier space. Thus $P(\mathbf{k})$ and $G(\mathbf{r})$ form a Fourier transform pair

$$G(\mathbf{r}) = \frac{1}{2\pi} \int_{-\infty}^{+\infty} P(\mathbf{k}) e^{i\mathbf{k} \cdot \mathbf{r}} d\mathbf{k}. \quad (5.18)$$

This is the famous Wiener-Khinchine relation. For a homogeneous, isotropic, random rough surface, $P(\mathbf{k}) = P(k)$, *i.e.* the power spectrum is also independent of the directions.

Typ	ACF	P(k)
Gaussian	$G(r) = w^2 e^{-r^2/a^2}$	$\frac{w^2 a}{2\sqrt{\pi}} e^{-k^2 a^2/4}$
Exponential	$G(r) = w^2 e^{- r /a}$	$\frac{w^2 a}{2\sqrt{\pi}} \frac{1}{1+k^2 a^2}$
Self-Affine	$G(r) = w^2 e^{-[r /a]^{2\alpha}}, 0 \leq \alpha \leq 1$	$\frac{4\pi\alpha w^2 a^2}{(1+k^2 a^2)^{1+\alpha}}$

Table 5.1 Auto covariance function and respective power spectrum for typical surface types. a is the correlation length, *i.e.* the length at which the correlation between two height distribution gets lost if they are shifted about a against each other.

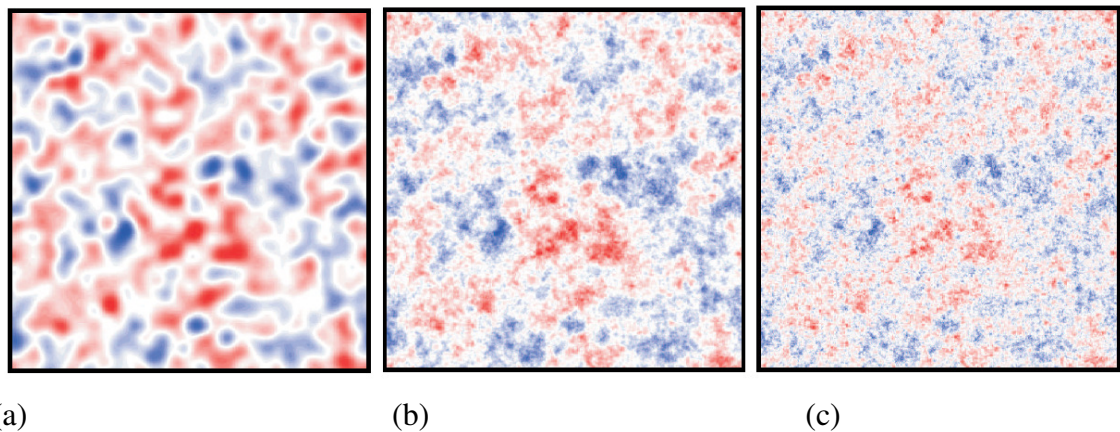


Figure 5.7 2D examples of random media realisations with (a) Gaussian, (b) exponential and (c) self-affine autocorrelation function. Images taken from Ref. [20].

Characterization of the GaN surface In Figure 5.8 (a) the AFM image of the optimized GaN buffer from chapter 3 is shown again. In the upper part of subfigure (b) the corresponding height distribution is reported. The distribution can be assumed in good approximation to be Gaussian (full red line). From Equation (5.12) the interface width w is related to the full width at half maximum (FWHM) via $FWHM = w \cdot 2 \cdot \sqrt{\ln(2) \cdot 2}$. The RMS value from the height distribution leads to $w \sim 0.47$ nm. The lower part of the subfigure (b) shows linescans along the x and y -axis of the 2D height distribution. Clearly the step like behavior can be seen. The discrete jumps are in very good agreement with one monolayer height $c/2 \sim 0.26$ nm.

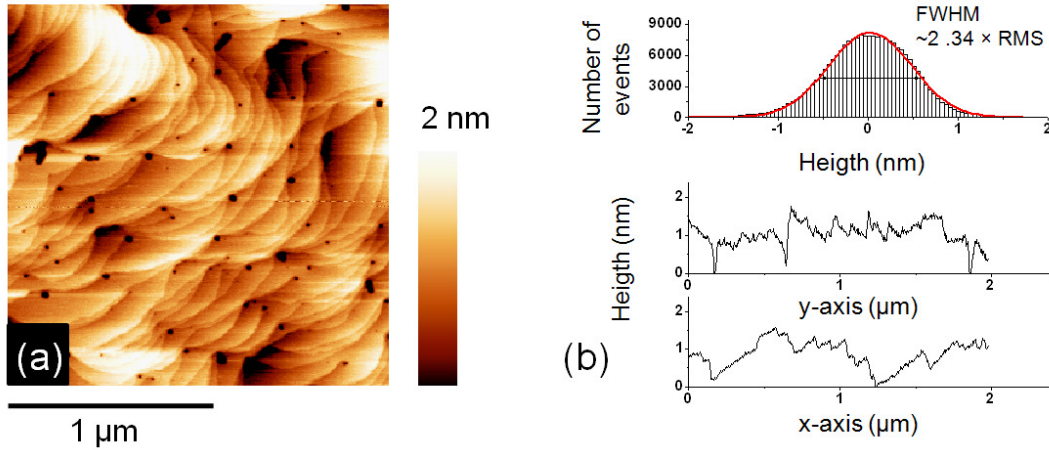


Figure 5.8 (a) AFM image of the optimized GaN buffer grown on sapphire and (b) respective height distribution. The RMS value from the height distribution leads to $w \sim 0.47$ nm. The lower part of the subfigure (b) shows linescans along the x and y -axis of the 2D height distribution. The discrete jumps are in very good agreement with one monolayer height $c/2 \sim 0.26$ nm.

However, the surface exhibits an asymmetric morphology. The plateaus have an average length of ~ 500 nm while the width is only ~ 90 nm. Consequently this results in an asymmetric auto covariance function shown in Figure 5.9. Subfigure (a) shows the 2D ACF obtained by numerical evaluation of Equation (5.15) with the 2D height distribution according to Figure 5.8 (a). The center of the image corresponds therefore to $G(0)$. The ACF exhibits two distinct principal directions indicated by the arrows in subfigure (a). In subfigure (b) the ACF along these directions are plotted *versus* the radial distance starting from $G(0)$. In the direction of the red arrow, the ACF shows an oscillatory behavior exhibiting a satellite peak, while in the perpendicular direction the ACF drops monotonically. Thus the surface can be characterized as an anisotropic mounded surface. The black ACF drops faster than the red ACF due to the anisotropy of the plateau length and width (width ~ 90 nm shorter correlation length, stronger decrease of the ACF, length ~ 500 nm larger correlation length, slower decrease of ACF).

Mounded surface For a mounded 2D surface the following auto correlation function was proposed [19] which will be used to describe the ACF in the direction with oscillatory behavior

$$G(r) = e^{-\left(\frac{r}{\xi}\right)^{2\alpha}} J_0\left(\frac{2\pi r}{\lambda}\right) \quad (5.19)$$

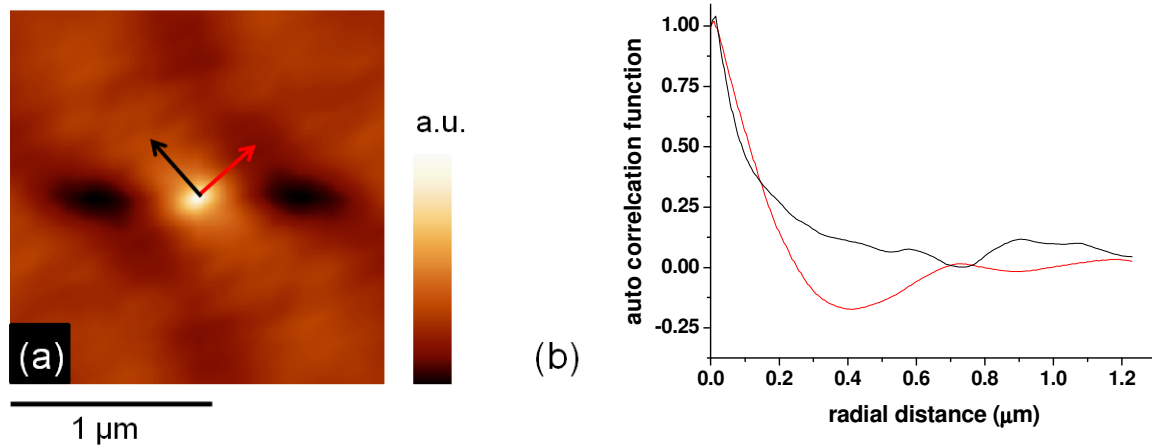


Figure 5.9 (a) 2D ACF obtained by numerical evaluation of Equation (4.15) with the 2D height distribution according to Figure 5.8 (a). The center of the image corresponds to $G(0)$. The ACF exhibits two distinct principal directions indicated by the 2 arrows. (b) The ACF along this 2 principal directions are plotted *versus* the radial distance starting from $G(0)$.

where $J_0(x)$ is the zeroth-order Bessel function. Four parameters are used to describe the surface: the interface width w , the system correlation length ζ , the roughness exponent α , and the average mound separation λ . For a mounded surface it is known that the local surface is quite flat. In Figure 5.10 the height-height correlation is plotted. From the slope near $G(0)$ one can extract $2\alpha \sim 1.25$. The lateral correlation length ξ can be defined through the ACF as $G(\xi)=1/e$ and is in this case a function of both ζ and λ . The length where G drops to $1/e$ is approximately $\xi \sim 0.17 \mu\text{m}$ as indicated in Figure 5.10. A fit with Equation (5.19) yields the 2 unknown parameters $\zeta = 0.385 \mu\text{m}$ and $\lambda = 0.67 \mu\text{m}$. Therefore it holds that $\xi = 0.27 \cdot \lambda$. The fit according to Equation (5.19) is shown in Figure 5.10 as dashed line.

In the perpendicular direction no pronounced oscillations can be observed. A similar analysis as that performed in Figure 5.10 yields $2\alpha \sim 1.33$ and $\zeta \sim 0.1 \mu\text{m}$. Since no oscillations are observed the mound separation length goes to infinity according to Equation (5.19) and $\lim_{\lambda \rightarrow \infty} J_0(1/\lambda) = 1$, *i.e.* only the exponential part contributes to the ACF.

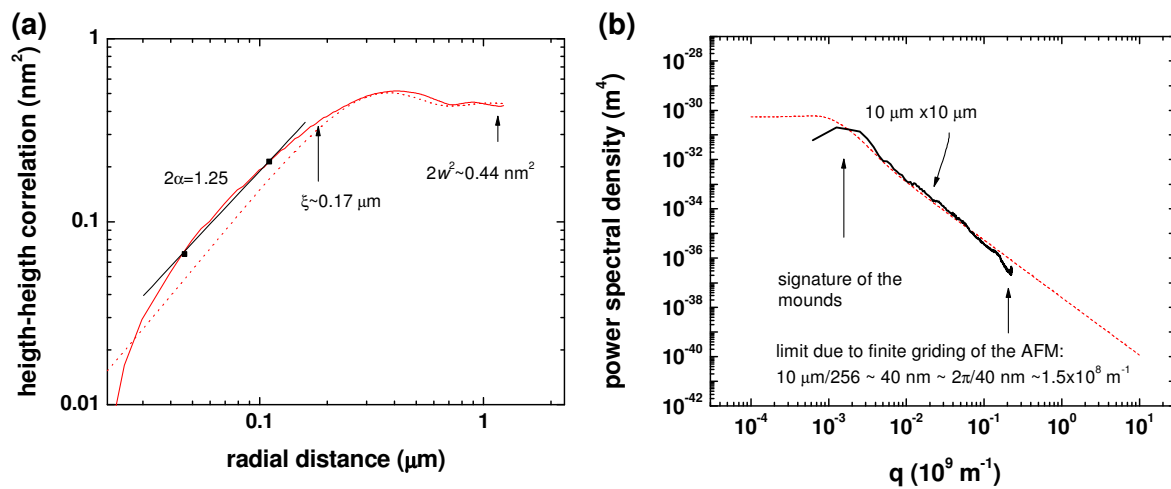


Figure 5.10 (a) Parameters of the mounded surface ACF model determined from the height-height correlation of the GaN surface. (b) Power spectral density directly obtained from the numerical Fourier transforms of the 2D ACF of the GaN surface. Every AFM image contains 256 points x 256 points. This sets an upper limit for accessible q vectors $\sim 1.5 \times 10^8 \text{ m}^{-1}$. Hillock-like signature of mounds clearly visible at $q \sim 1 \times 10^6 \text{ m}^{-1}$. Additionally, the PDS calculated numerically from Equations (5.19) and (5.17) is shown (red dashed line).

Figure 5.10 (b) displays then the PSD obtained from the Fourier transform of the 2D ACF. If the ACF is isotropic then $k = \sqrt{k_x^2 + k_y^2}$, *i.e.* the 2D dependence can be reduced to 1D and expressed in dependence on a radial wave vector [19]. Units are here q , where q is given as $q=k/2\pi$. From Equations (5.17) and (5.19) together with the obtained parameters the PSD can be computed numerically (analytical solution only for $\alpha=1$) and is indicated as red dashed line. The in practice accessible q values are limited by scan size and the number of points.

In this subchapter, it was found that the GaN surface can be classified as a mounded surface. Therefore, a description with simple models according to Table 5.1 will always fail. Since the relevant relations for transport are formulated in k -space the PSD of the given surface becomes crucial. Therefore we assume that the PSD in 5.10 (b) describes completely the surface/interface properties for our specific samples and will be used in the following for the estimation of scattering times for the specific interface related mechanisms. Note that beside also an analytical expression exists for the PSD of Equation (5.19) [19].

5.4 Roughness induced strain, deformation potential and piezoelectric fields

Strain minimization As demonstrated in the previous subsection the GaN surface exhibits a plateau-like structure with atomically flat terraces with a length of 100 nm and a plateau offset of monolayer step heights *i.e.* 0.26 or 0.52 nm. This subsection aims to illustrate the effect of the strain in the vicinity of these steps if an AlN layer is introduced. For comparison, we discuss the same situation without AlInN barrier, *i.e.* for a AlN/GaN heterostructure. Feenstra *et al.* [21, 22] first discussed this problem for Si/Ge channels in cubic elasticity approximation. Quang *et al.* [23, 24] adopted the formalisms for AlN/GaN wurtzite heterostructures also in cubic elasticity approximation and giving analytical solution for strain components in the vicinity of the fluctuation. This problem is highly non-trivial. A strain-minimization scheme is employed taking into account the full wurtzite structure of the unit cells. A strain free substrate material and appropriate boundary conditions have to be defined. Then the total strain energy is minimized in the heterostructure with respect to the unstrained substrate. For details see the nextnano code [25] and the references therein [12].

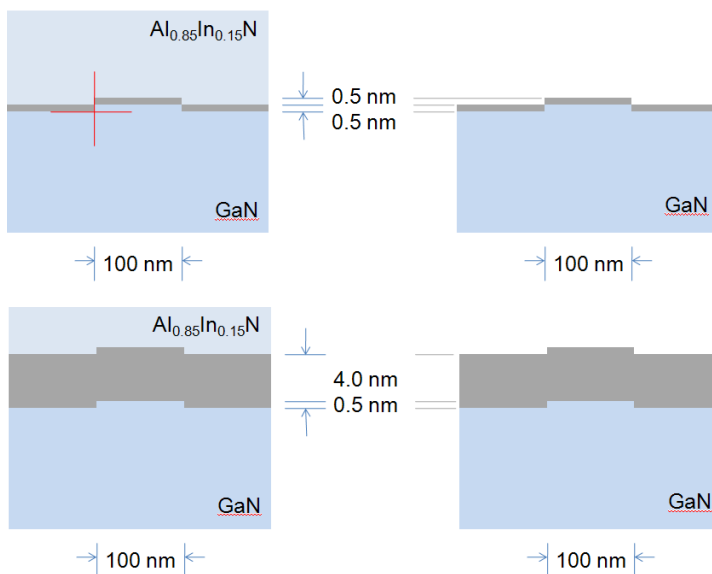


Figure 5.11 The strain calculations refer in the following to these sketches. Calculations will be performed for lattice matched AlInN/GaN heterostructure with AlN interlayers (grey area) (left part in the upper sketch) and AlN/GaN HS (right part in the upper sketch) for different AlN layer thicknesses, namely 0.5, 1, 2 and 4 nm. The step height offset in the GaN is assumed to be 0.52 nm, *i.e.* 2 monolayers. Roughness induced strain, conduction band fluctuations and electric field fluctuations are depicted in the following along the lines indicated by the red cross in the upper left figure.

5 Subband Structure and Transport

First we want to discuss the ε_{zz} component of the strain tensor. This is depicted in Figure 5.12. Black lines corresponds to a LM AlInN(20 nm)/AlN/GaN heterostructures. Red lines indicate a pure AlN/GaN heterostructure but with the same AlN thickness as the interlayer in the former case. Interestingly the strain induced by the AlN interlayer is accommodated by the GaN and the AlInN. In the case of AlN/GaN the strain is only accommodated by the GaN and consequently is higher in the GaN buffer, decreasing stronger the channel quality.

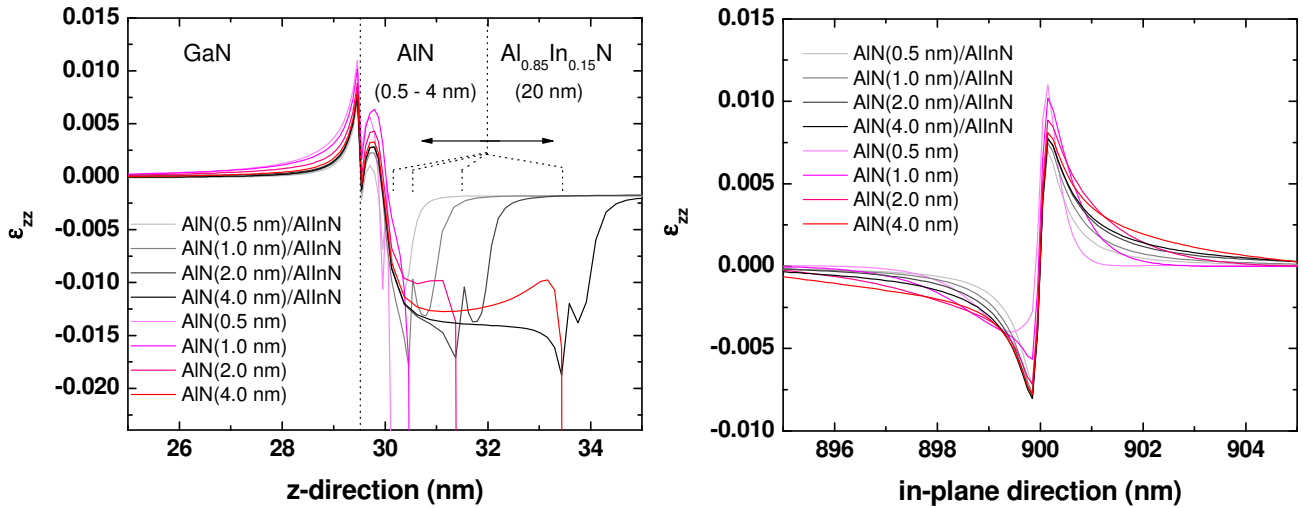


Figure 5.12 The ε_{zz} strain tensor component in the vicinity of a step fluctuation according to Figure 5.11 for different AlN layer thicknesses. Black lines corresponds to a LM AlInN(20 nm)/AlN/GaN heterostructure. Red lines indicate a pure AlN/GaN heterostructure with the same AlN thickness.

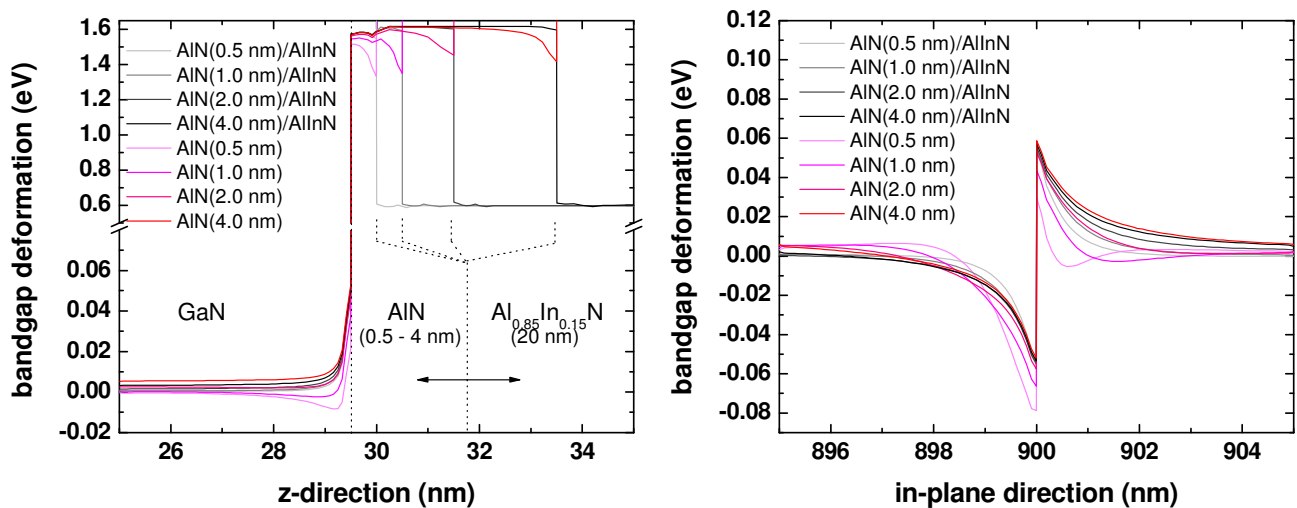


Figure 5.13 The conduction band deformation in the vicinity of a step fluctuation for different AlN (inter)layer thicknesses. Black lines corresponds to a LM AlInN(20 nm)/AlN/GaN heterostructure. Red lines indicate a pure AlN/GaN heterostructure with the same AlN thickness.

As pointed already out, the shift of the conduction band of the unit cell is given by the trace of the strain tensor and is proportional to the deformation potential [8]. In Figure 5.13 the conduction band deformation is shown along the same lines as in Figure 5.12. Especially the subfigure (b) in in-plane direction illustrates how the deformation of the conduction band can cause a serious obstacle for the electron transport in the channel. The height of the jump mounts up to 120 meV. For thin AlN interlayers ≤ 1 nm the magnitude of the conduction band deformation is lower and affects few unit cells laterally (~ 1 nm). For larger interlayer thickness > 1 nm the conduction band in the vicinity of the step is strongly affected and the width of affected in-plane unit cell increases. This correlates with the observed ‘high-mobility window’. For AlN interlayers ≤ 1 nm there might also be a high probability of quantum mechanical tunneling, consequently 2DEG electrons would only be slightly disturbed in their motion contrary to the situation of thicker interlayers. This issue is under investigation.

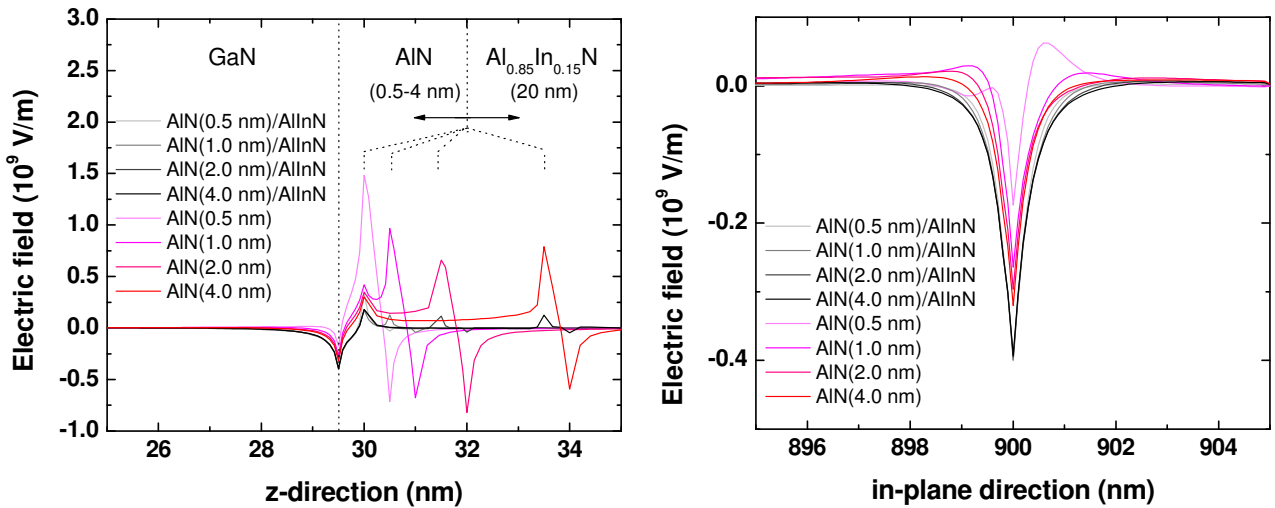


Figure 5.14 The electric field in the vicinity of a step fluctuation for different AlN (inter)layer thicknesses arising from the non-vanishing elements of the polarization tensor. Black lines corresponds to a LM AlInN(20 nm)/AlN/GaN heterostructure. Red lines indicate a pure AlN/GaN heterostructure with the same AlN thickness.

A last issue will be briefly discussed. The presence of steps and hence the deviation from atomically perfect interfaces, gives also rise to non-vanishing elements of the piezoelectric tensor, namely by the e_{15} component. This gives rise to non-vanishing electric fields. Note that they should not be confused with the barrier electric field in growth direction. These fields are purely located around the steps. Results are depicted in Figure 5.14. As it can be seen there is only a weak dependence on AlN (inter)layer thickness. These fields have also magnitudes where they act as relevant scattering sources for the electron motion, reducing therefore the mobility. As in the previous cases the electric field decays exponentially in the GaN buffer. Magnitude increases only very little for interlayer thickness > 1 nm. They are located in a small volume with a radius of ~ 3 nm around the step fluctuation.

5.5 Scattering mechanisms in nitride heterostructures

Two subband transport At this point, the transport involving two occupied subbands will be briefly sketched. A more detailed derivation starting from the Boltzmann transport equation (BTE) can be found in Ref. [26]. The main idea of multiband transport bases on the work of Ando, Siggia and co-workers [27-29]. The mobility for the n -th subband is given as

$$\mu_n = \frac{|e|}{m_n(E_F)} \tau_n(E_F) \quad (5.20)$$

where e is the electric charge, m_n the subband effective mass and τ_n the relaxation time per subband. Relaxation times τ_n have to satisfy the coupled linear equations

$$P_n(E_F) \tau_n(E_F) - \sum_{m \neq n} P_{nm}(E_F) \tau_m(E_F) = 1 \quad (5.21)$$

where $P_n(E_F)$ and $P_{nm}(E_F)$ are ($E_F > E_n$) and are given at $T=0$ as [30-32]

$$\begin{aligned} P_n(E_F) &= \frac{m_n(E_F)}{2\pi\hbar^3} \int_0^{2\pi} d\phi \left| V_{eff_{nn}}(q) \right|^2 (1 - \cos \phi) \\ &\quad + \sum_{m \neq n} \frac{m_m(E_F)}{2\pi\hbar^3} \int_0^{2\pi} d\phi \left| V_{eff_{nm}}(q') \right|^2 \theta(E_F - E_m) \\ P_{nm}(E_F) &= \frac{m_n(E_F)}{2\pi\hbar^3} \left[\frac{n_m(E_F)}{n_n(E_F)} \right]^{1/2} \int_0^{2\pi} d\phi \left| V_{eff_{nm}}(q') \right|^2 \cos \phi \end{aligned} \quad (5.22)$$

where $q' = (k_{F_n}^2 + k_{F_m}^2 - 2k_{F_n} k_{F_m} \cos \theta)^{1/2}$ and the k_F are the 2D Fermi vectors of the respective subband. The 2D Fermi vectors are given by $k_{F_{n,m}} = \sqrt{2\pi \cdot n_{n,m}(E_F)}$. For a further reading the attention is drawn to Refs. [27-29]. If the mobilities for the subbands are known the total drift and Hall mobility are given as

$$\begin{aligned} \mu_{drift} &= \frac{\sum_n n_n(E_F) \mu_n(E_F)}{\sum_n n_n(E_F)} \\ \mu_H &= \frac{\sum_n n_n(E_F) \mu_n^2(E_F)}{\sum_n n_n(E_F) \mu_n(E_F)} \end{aligned} \quad (5.23)$$

The Hall mobility μ_H is the mobility which will be measured by Hall effect while the drift mobility μ_{drift} is the true mean mobility of the coupled two subband system.

Scattering mechanisms In the following we briefly summarized the possible scattering mechanisms of the 2DEG channel electrons. We want to focus on the temperature independent scattering mechanisms.

Dislocation scattering We start with scattering on charged *dislocations*. The expression can be obtained by integrating a Coulomb potential along a line charge with a density $\lambda = e f / c_0$, where c_0 is the GaN lattice constant and f a filling factor lying between 0.1-0.5 [33, 34]. The areal density of dislocations is N_{dis} , then according to [8]

$$\begin{aligned} & \left| V_{eff_{nm}}(q) \right|^2 \\ &= N_{dis} \frac{e^4 f^2}{4 \epsilon_0^2 \epsilon^2 c_0^2 q^2} \int_{-\infty}^{\infty} dz_i \left| \sum_{n'm'} \epsilon_{nm,n'm'}^{-1}(q) P_{n'm'}(q, z_i) \right|^2 \end{aligned} \quad (5.24)$$

with

$$P_{n'm'}(q, z_i) = \int_{-\infty}^{\infty} dz \Psi_n(z) \Psi_{m'}(z) e^{-q|z-z_i|}$$

Remote impurity scattering Since the source for the 2DEG electrons are the surface states, the 2D electrons leave the same amount N_{2DEG} of positively charged centers at the surface behind when they are forming the 2DEG. The channel electrons are then scattered *via* the Coulomb force at this positive surface charge. It is clear that this will be more dominant for ultrathin layers. This sheet charge of density N_{2DEG} is located at a distance t_b from the heterointerface [8, 31]

$$\begin{aligned} & \left| V_{eff_{nm}}(q) \right|^2 \\ &= N_{2DEG} \frac{e^4}{4 \epsilon_0^2 \epsilon^2 q^2} \left| \sum_{n'm'} \epsilon_{nm,n'm'}^{-1}(q) P_{n'm'}(q, z_i = t_b) \right|^2 \end{aligned} \quad (5.25)$$

Alloy disorder scattering Since it cannot be excluded that a small residual amount of indium atoms is incorporated in the GaN buffer we have also to consider alloy disorder scattering [13, 32]

$$\begin{aligned} & \left| V_{eff_{nm}}(q) \right|^2 \\ &= x(1-x) \delta V^2 \Omega \int dz \left| \sum_{n'm'} \epsilon_{nm,n'm'}^{-1}(q) \Psi_n(z) \Psi_{m'}(z) \right|^2 \end{aligned} \quad (5.26)$$

where x is the alloy composition, δV the conduction band offset between binary compounds (*i.e.* in this case GaN and InN) and the volume of the hexagonal unit cell $\Omega = \sqrt{3} a^2 c / 2$.

5 Subband Structure and Transport

Interface roughness scattering The scattering of 2DEG electrons by potential fluctuation induced by a non-atomically perfect flat interface reads as

$$\begin{aligned} & \left| V_{eff_{nm}}(q) \right|^2 \\ &= C(q) \left| \sum_{n'm'} \epsilon_{nm,n'm'}^{-1}(q) F_{nm} \right|^2 \end{aligned} \quad (5.27)$$

where $C(q)$ is the 2D spectral density defined in section 5.2 and F_{nm} the effective electric field given by

$$F_{nm} = \begin{cases} \int_{-\infty}^{\infty} dz |\Psi_n(z)|^2 \frac{\partial \phi(z)}{\partial z} & \text{for } n = m \\ (F_n F_m)^{1/2} & \text{for } n \neq m \end{cases}$$

Scattering at the roughness induced piezoelectric charges The scattering at the roughness induced piezoelectric charges as introduced in section 4.3 can be expressed as:

$$\begin{aligned} & \left| V_{eff_{nm}}(q) \right|^2 \\ &= \left\{ \frac{\alpha \epsilon_{\parallel} e Q}{4 \epsilon_0 \epsilon} q \right\}^2 C(q) \left| \sum_{n'm'} \epsilon_{nm,n'm'}^{-1}(q) F_{n'm'}(q) \right|^2 \end{aligned} \quad (5.28)$$

where α accounts for the deviation from cubic elasticity and Q is an effective charge introduced by the analytical model in Refs. [23, 24].

$$F_{n'm'}(q) = \int_{-\infty}^{\infty} dz \Psi_{n'}(z) \Psi_{m'}(z) F_{PE}(q, z)$$

The F_{PE} are given by

$$F_{PE}(q, z) = \frac{1}{2q} \begin{cases} e^{qz} & \text{for } z < 0 \\ e^{-qz} (1 + 2qz), & \text{for } z > 0 \end{cases}$$

Note that these expressions are derived for a single barrier layer. The value of α should at least be as large as the anisotropy ratio of the zinc-blende phase to take into account the elastic isotropy approximation, *i.e.* $\alpha > 2.5$. Q evaluated for an AlN/GaN heterostructure in the framework of the discussion of Refs. [23, 24] yields ~ 3.5 .

Scattering at the roughness induced deformation potential The scattering at the screened potential of the roughness induced deformation potential reads as

$$\begin{aligned} & \left| V_{eff_{nm}}(q) \right|^2 \\ &= \left\{ \frac{\alpha \epsilon_{\parallel} \Xi_D}{2} Q_s q \right\}^2 C(q) \left| \sum_{n'm'} \epsilon_{nm,n'm'}^{-1}(q) F_{n'm'}(q) \right|^2 \end{aligned} \quad (5.29)$$

$$F_{n'm'}(q) = \int_{-\infty}^{\infty} dz \Psi_{n'}(z) \Psi_{m'}(z) e^{-q|z|}$$

Q_s evaluated for a AlN/GaN heterostructure in the framework of the discussion of Refs. [23, 24] yields ~ 1.7 . The Ξ_D is the GaN deformation potential and lies around ~ 9 eV [8].

Dielectric matrix In the above expression the $\epsilon_{nm,n'm'}^{-1}$ are the elements of the inverse matrix of the dielectric response function. The dielectric matrix in random phase approximation (RPA) can be written as [27, 31, 35]

$$\epsilon_{nm,n'm'}(q) = \delta_{nn'} \delta_{mm'} + (q_s / q) F_{nm,n'm'}(q) \chi_{n'm'}^0(q) \quad (5.30)$$

where

$$q_s = 2me^2 / 4\pi\epsilon_0\hbar^2 = 2 / a_B$$

is the 2D ‘Thomas-Fermi’ screening vector.

This has two implications: the 2D polarization functions $\chi^0(q)$ [27, 36] are only analytical for parabolic bands and no local field corrections are included which becomes more important for low 2DEG densities [37, 38]. The form factor $F_{nm,n'm'}$ taking into account for the z -extension of the 2DEG is defined as [27, 31]

$$\begin{aligned} F_{nm,n'm'}(q) &= \int_{-\infty}^{+\infty} \Psi_n(z) \Psi_m(z) dz \\ &\times \int_{-\infty}^{+\infty} \Psi_{n'}(z') \Psi_{m'}(z') e^{-q|z-z'|} dz' \end{aligned} \quad (5.31)$$

In Ref. [27] also the expression for the dielectric function for $T \neq 0$ is given. To treat this is out of the scope of this work.

5.6 Application to AlInN/AlN/GaN heterostructures

Now, we want to apply the above scattering mechanisms to the AlInN/AlN/GaN heterostructures. We focus on an interlayer thickness of ~ 1 nm. The wavefunctions are obtained by means of solving self-consistently the Schrödinger-Poisson Equations (5.8)-(5.11) including the polarization charges numerically. This resulted in Figure 5.3. To further process the solution for the transport model the numerical solution is fitted with the extended Fang-Howard wavefunctions

$$\Psi_0(z) = \begin{cases} A\kappa^{1/2} e^{\kappa z/2} & \text{for } z < 0 \\ Bk_0^{1/2} (k_0 z + c_0) e^{-k_0 z/2} & \text{for } z > 0 \end{cases}$$

$$\Psi_1(z) = \frac{\sqrt{2} (z - c_1 z^2) e^{-z k_1/2}}{\left(\frac{k_1^2 - 6c_1 k_1 + 12c_1^2}{k_1^5} \right)^{0.5}} \quad (5.32)$$

where Ψ_0 stands for the ground state and Ψ_1 for the first additional subband. Fits according to Equations (5.32) agree to more than 99% with the numerical solution. This allows evaluating the form factors *via* Equation (5.31). The form factors take into account the z -extension of the 2DEG, therefore it should more likely to be referred to as quasi 2DEG. The result is still analytic but yields a rather complex polynomial form. A Padé approximation [39] can be used to reduce further the complexity of the polynomial to speed up the 4×4 matrix inversion. For symmetry reasons the 16 elements of the matrix Equation (5.30) reduces to 6 independent form factors shown in Figure 5.15 (a). With the form factors the dielectric matrix Equation (5.30) can be setup. Figure 5.15 (b) shows the diagonal elements of the inverted matrix. As expected from the polarizability the $\epsilon_{00,00}$ element exhibits a kink at $2 k_{F0}$, the Fermi vector of the ground state while the $\epsilon_{11,11}$ element exhibits the kink at $2 k_{F1}$, the Fermi vector of the first state. For mixed elements it appears at $k_{F0} + k_{F1}$.

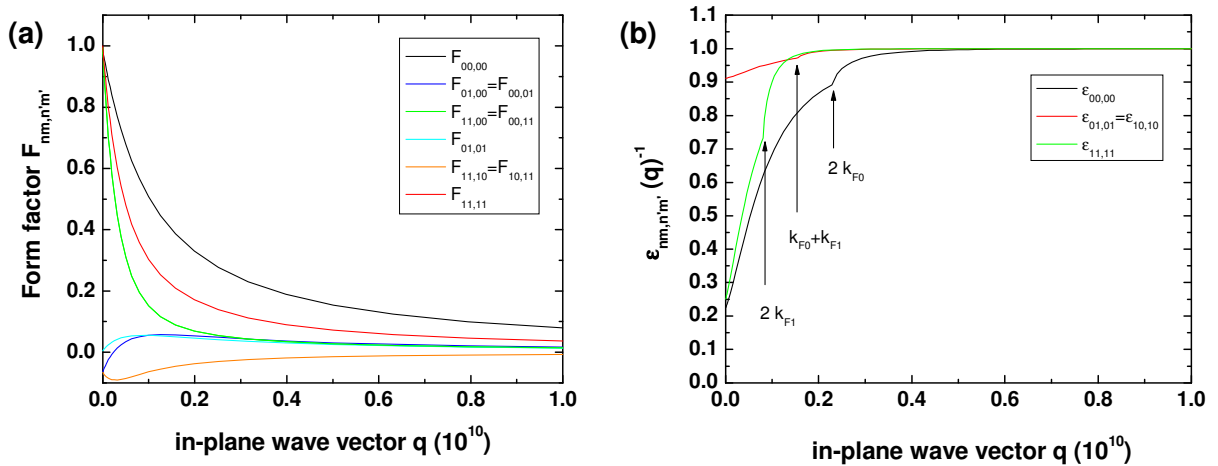


Figure 5.15 Form factors for an $\text{Al}_{0.85}\text{In}_{0.15}\text{N}(13\text{nm})/\text{AlN}(1\text{nm})/\text{GaN}$ heterostructure evaluated by Equation (5.31) using the wavefunctions determined by Equation (5.32) while their parameters are obtained self-consistently corresponding to section 5.1. The 4×4 matrix reduces due to symmetry reasons to the 6 form factors shown in subfigure (a). Subfigure (b) shows the diagonal elements of the inverse dielectric matrix.

Mobility In the following we will restrict ourselves to the case $T=0$. Then the $\chi^0(q)$ have an analytic form [27, 36]. Further we neglect any thermal dependent scattering mechanisms such as scattering on acoustic or optical phonons. Thus, the following discussion will reveal the maximum achievable mobility in those heterostructures as a function of the barrier properties for the given structural parameters. Figure 5.16 (a) shows the calculated mobilities of the 0th (ground state) and 1st subband for an $\text{Al}_{0.85}\text{In}_{0.15}\text{N}/\text{AlN}(1\text{nm})/\text{GaN}$ heterostructure as a function of total barrier thickness at $T=0$ calculated from the single scattering mechanisms using Matthiessen's rule. For barrier thickness up to 6 nm the mobility is mainly limited by remote impurity scattering, *i.e.* by Coulomb scattering since the separation of the 2DEG from the positive charges located at the surface is very low. For larger thicknesses and hence higher 2DEG density interface roughness and related mechanisms become more important since the ground state electrons will be localized closer to the heterointerface and will suffer more from scattering on the interface related mechanisms. Note that the interface roughness, piezoelectric scattering and deformation potential scattering yields scattering rates in the same order of magnitude. For $t \sim 15$ nm both electrons in both subbands exhibit the same mobility. For larger thickness and higher 2DEG density the 1st subband is sufficiently charged so it can have an effect on the total Hall mobility. The fact that the mobility of the 1st subband is larger than that of the ground state (0th subband) can also be seen from the scattering potentials: the effective field in Equation (5.27) for the 1st subband is typically only one fourth as those of the ground state. Piezoelectric potential in Equation (5.28) and deformation potential in Equation (5.29) scattering drops exponentially as roughly e^{-qz} from the heterointerface into the GaN buffer. This is also in agreement with the numerical simulations according to Figures 5.12 (a), 5.13 (a) and 5.14 (a).

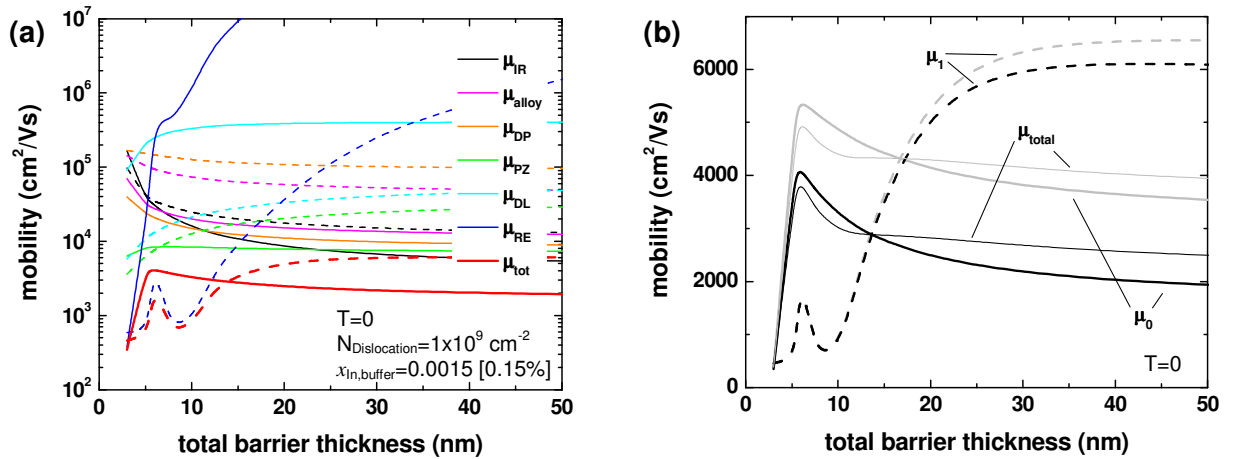


Figure 5.16 (a) Mobilities for the first two subbands (full colored lines: 0th subband, dashed colored lines: 1st subband) of an $\text{Al}_{0.85}\text{In}_{0.15}\text{N}/\text{AlN}/\text{GaN}$ heterostructure as a function of total barrier thickness at $T=0$. Various scattering mechanisms contribute to the total mobilities: interface roughness scattering (IR), alloy scattering (alloy), roughness induced deformation potential scattering (DP), roughness induced piezoelectric scattering (PZ), dislocation scattering (DL) and remote impurity scattering (RE). Total mobility of the respective subband according to Matthiessen's rule is given by red full and dashed line. (b) Subband mobilities and total drift mobility with (black lines) and without (grey lines) nonparabolic effects for an $\text{Al}_{0.85}\text{In}_{0.15}\text{N}/\text{AlN}/\text{GaN}$ heterostructure as a function of total barrier thickness at $T=0$.

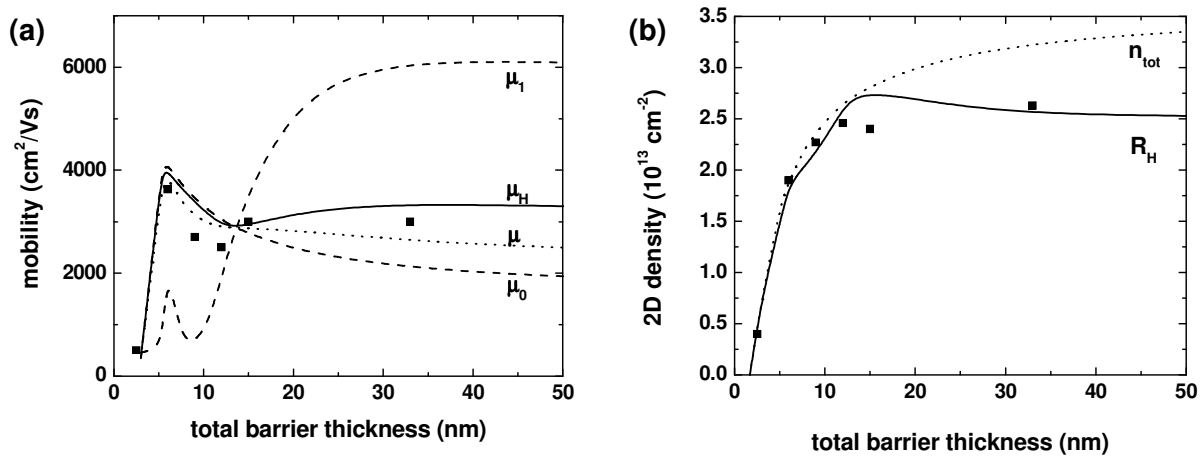


Figure 5.17 (a) Electrical and transport properties as function of the total barrier thickness for $\text{Al}_{0.85}\text{In}_{0.15}\text{N}/\text{AlN}/\text{GaN}$ heterostructures at $T=0 \text{ K}$. Additional 77 K Hall data is shown: subband, total drift and Hall mobilities. (b) True 2DEG density together with Hall coefficient R_H .

Since the mean charge separation from the heterointerface is $\sim 0.8 \text{ nm}$ for the ground state and $\sim 3.5 \text{ nm}$ for the first state for an $\text{Al}_{0.85}\text{In}_{0.15}\text{N}(14\text{nm})/\text{AlN}(1\text{nm})/\text{GaN}$ heterostructure the 1st subband should exhibit a mobility which is roughly $e^{-0.8} / e^{-3.3} \sim 10$ times larger than the ground state for each of those two scattering mechanisms. Assuming a similar contribution from the interface roughness scattering we find that $\mu_1 \approx 1/(1/10 + 1/10 + 1/10) \cdot \mu_0 \approx 3 \cdot \mu_0$ in the high 2DEG density limit (or correspondingly thick barriers $> 15 \text{ nm}$). Figure 5.16 (a) is obtained by deriving the effective masses from the in-plane dispersion relation of each state [4]. Nonparabolic effects are thus included. Subfigure (b) shows the same situation in comparison with neglecting these nonparabolic effects. Mainly the mobility of the ground state will be affected. Only for very thin barrier thicknesses corresponding to 2DEG densities below $1.5 \times 10^{13} \text{ cm}^{-2}$, the total drift mobility nearly coincides with the ground state mobility since only the ground state contributes significantly to the transport.

Figure 5.17 shows electrical and transport properties as function of the total barrier thickness for $\text{Al}_{0.85}\text{In}_{0.15}\text{N}/\text{AlN}/\text{GaN}$ heterostructures at $T=0 \text{ K}$ together with 77 K Hall. Subfigure (a) displays the corresponding subband mobilities together with the total drift mobility and the Hall mobility corresponding to Equation (5.23). Clearly, this bump like feature at 6 nm is reproduced. This high mobility peak arises mainly from the interplay between the remote impurity, interface roughness and deformation potential scattering for the ground state as can be seen from Figure 16 (a). The 2DEG needs a certain separation from the surface remote impurities $\sim 3 \text{ nm}$ and on the other hand the 2DEG density should not be too high otherwise electrons suffer from interface related scattering mechanisms. Subfigure (b) shows the Hall coefficient R_H together with the true 2DEG density. We want to point out that no further temperature dependence of the 2DEG density is imposed here, which certainly not holds since the temperature leads to an expansion or shrinking of the unit cells and consequently the piezoelectric polarization should be altered. Figure 5.18 shows the subband mobilities as function of the applied voltage for an $\text{Al}_{0.85}\text{In}_{0.15}\text{N}(13\text{nm})/\text{AlN}(1\text{nm})/\text{GaN}$ heterostructure. The respective 2DEG density as function of the applied voltage was shown in Figure 5.6. The behaviour is similar to the barrier thickness variation: for high 2DEG densities, the interface roughness related scattering dominates while in the low density regime the remote impurities and dislocation scattering is important. This mobility maximum at $V \sim 4 \text{ V}$ is also in agreement with the observed transconductance maximum [16].

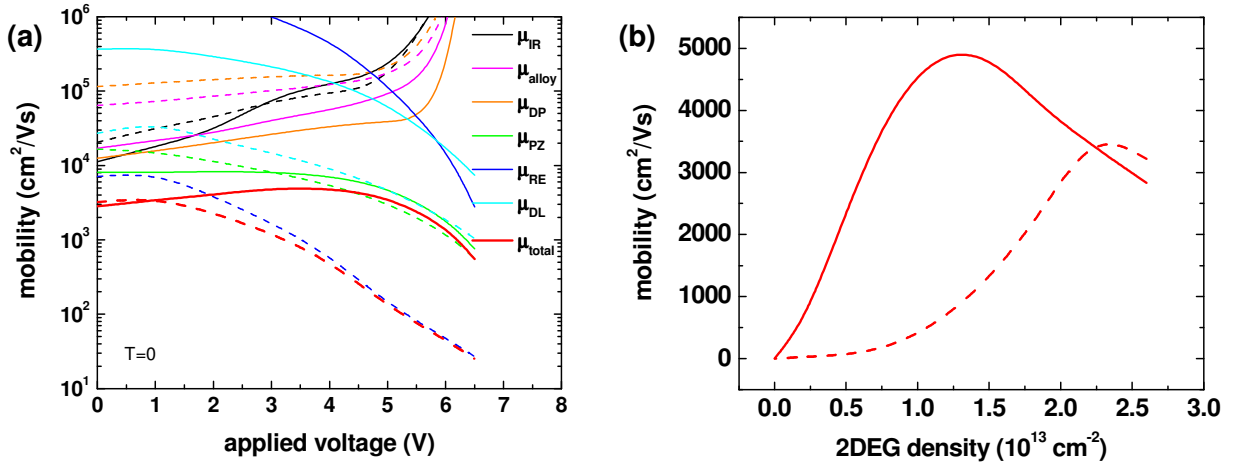


Figure 5.18 (a) Subband mobilities as function of the applied gate voltage for an Al_{0.85}In_{0.15}N(13nm)/AlN(1nm)/GaN heterostructure. The respective 2DEG density as function of the applied voltage was shown in Figure 5.6. A maximum mobility of 5500 cm²/Vs is found at ~4 V (full colored lines: 0th subband, dashed colored lines: 1st subband). (b) Subband mobilities from Fig. 13 (a) as a function of the total 2DEG density at T=0.

5.7 Conclusions

We demonstrated that for (AlInN)/(AlN)/GaN heterostructures containing 2DEG densities with more than $1.5 \times 10^{13} \text{ cm}^{-2}$ the second subband is always occupied. As a rule of thumb the density of the second subband is 10% of the ground state density but can significantly influence transport at low temperature when the phonon scattering can be excluded. These subband occupation can only be observed in transport measurements since during a CV measurement subbands are always depleted simultaneously.

The influence of strain arising from monolayer fluctuation at the AlN/GaN interface was studied in detail. It turned out that the AlN interlayer induces significant distortion on the GaN conduction band at the position where the 2DEG is located with amplitude of up to 100 meV and a lateral extension in the order of 1-2 nm. Additionally, strong piezoelectric fields in the order of few MV/cm arise due to the coupling of the ϵ_{xx} and ϵ_{yy} elements of the strain tensor to the e_{15} component of the piezoelectric tensor. This is consistent with the discussion conducted in Ref. [40]. Note that these two mechanisms plus the interface roughness scattering yield scattering times in the same order of magnitude for the ground state. The second subband however has a larger separation from the heterointerface and since the interface related distortions drop quickly within a few nm towards the buffer second subband electrons experience less scattering and exhibit a larger mobility. This is therefore sufficient to decrease the Hall coefficient significantly. These findings are consistent with the ‘high mobility windows’. Thicker interlayer or AlN barrier induce more strain decreasing the channel mobility. Another benefit of the LM AlInN barrier is that it can partly accommodate the strain induced by the interlayer, *i.e.* strain found in the GaN is lower than for an AlN/GaN heterostructure with the same AlN thickness. Along these lines also the mobility in AlN/GaN heterostructures could potentially be calculated.

Bibliography

- [1] P. Yu, and M. Cardona, *Fundamentals of semiconductors: physics and materials properties* (Springer Verlag, 2010).
- [2] H. Nalwa, *Nanostructured materials and nanotechnology* (Academic Pr, 2002).
- [3] S. Shokhovets, G. Gobsch, and O. Ambacher, *Momentum matrix element and conduction band nonparabolicity in wurtzite GaN*, Appl. Phys. Lett. **86**, 161908 (2005).
- [4] C. Wetzel *et al.*, *Electron effective mass and nonparabolicity in $Ga_{0.47}In_{0.53}As/InP$ quantum wells*, Phys. Rev. B **53**, 1038 (1996).
- [5] W. Knap *et al.*, *Effective g factor of two-dimensional electrons in GaN/AlGaN heterojunctions*, Appl. Phys. Lett. **75**, 3156 (1999).
- [6] Y. Cao, and D. Jena, *High-mobility window for two-dimensional electron gases at ultrathin AlN/GaN heterojunctions*, Appl. Phys. Lett. **90**, 182112 (2007).
- [7] M. Gonschorek *et al.*, *Two-dimensional electron gas density in $Al_{1-x}In_xN/AlN/GaN$ heterostructures ($0.03 \leq x \leq 0.23$)*, J. Appl. Phys. **103**, 093714 (2008).
- [8] D. Jena, *Polarization effects in semiconductors : from ab initio theory to device application* (Springer, New York, 2007).
- [9] Y. Cao *et al.*, *Very low sheet resistance and Shubnikov-de-Haas oscillations in two-dimensional electron gases at ultrathin binary AlN/GaN heterojunctions*, Appl. Phys. Lett. **92**, 152112 (2008).
- [10] C. P. Jiang *et al.*, *Subband electron properties of modulation-doped $Al_xGa_{1-x}N/GaN$ heterostructures with different barrier thicknesses*, Appl. Phys. Lett. **79**, 374 (2001).
- [11] T. W. Kim *et al.*, *Magnetotransport, optical, and electronic subband properties in $Al_xGa_{1-x}N/AlN/GaN$ heterostructures*, Solid State Commun. **132**, 67 (2004).
- [12] S. Hackenbuchner, *Elektronische Struktur von Halbleiter-Nanobau-elementen im thermodynamischen Nichtgleichgewicht* München, 2002), Vol. 48.
- [13] C. Hamaguchi, *Basic semiconductor physics* (Springer, Berlin ; New York, 2001).
- [14] N. Tang *et al.*, *Effective mass of the two-dimensional electron gas and band nonparabolicity in $Al_xGa_{1-x}N/GaN$ heterostructures*, Appl. Phys. Lett. **88**, 172115 (2006).
- [15] M. A. Khan *et al.*, *Microwave Performance of a $0.25 \mu m$ Gate AlGaIn/GaN Heterostructure Field-Effect Transistor*, Appl. Phys. Lett. **65**, 1121 (1994).
- [16] F. Medjdoub *et al.*, *Barrier-layer scaling of InAlN/GaN HEMTs*, IEEE Electron Device Lett. **29**, 422 (2008).
- [17] T. Zimmermann *et al.*, *AlN/GaN insulated-gate HEMTs with 2.3 A/mm output current and 480 mS/mm transconductance*, IEEE Electron Device Lett. **29**, 661 (2008).

-
- [18] J. Jo *et al.*, *Probing the Subband Structure of a Wide Electron-System in a Parabolic Quantum-Well Via Capacitance-Voltage Measurements*, Phys. Rev. B **47**, 4056 (1993).
 - [19] Y. Zhao, G. C. Wang, and T. M. Lu, *Characterization of amorphous and crystalline rough surface : principles and application* (Academic Press, San Diego, 2001).
 - [20] C. Sick, *Analysis and numerical modeling of seismic wave fields in random media*, Master thesis, FR Geowissenschaften, Freie Universität Berlin (2002).
 - [21] R. M. Feenstra, and M. A. Lutz, *Scattering from Strain Variations in High-Mobility Si/SiGe Heterostructures*, J. Appl. Phys. **78**, 6091 (1995).
 - [22] R. M. Feenstra *et al.*, *Roughness Analysis of Si/SiGe Heterostructures*, J. Vac. Sci. Technol. B **13**, 1608 (1995).
 - [23] D. N. Quang *et al.*, *Roughness-induced piezoelectric charges in wurtzite group-III-nitride heterostructures*, Phys. Rev. B **72**, 115337 (2005).
 - [24] D. N. Quang *et al.*, *Roughness-induced mechanisms for electron scattering in wurtzite group-III-nitride heterostructures*, Phys. Rev. B **72**, 245303 (2005).
 - [25] NEXTNANO³ device simulation package, see <http://www.nextnano.de> and <http://wsi.tum.de/nextnano.de>
 - [26] G. Bastard, *Wave mechanics applied to semiconductor heterostructures* (Editions de Physique, Les Ulis, 1990).
 - [27] T. Ando, A. B. Fowler, and F. Stern, *Electronic-Properties of Two-Dimensional Systems*, Rev. Mod. Phys. **54**, 437 (1982).
 - [28] S. Mori, and T. Ando, *Intersubband Scattering Effect on the Mobility of a Si (100) Inversion Layer at Low-Temperatures*, Phys. Rev. B **19**, 6433 (1979).
 - [29] E. D. Siggia, and P. C. Kwok, *Properties of Electrons in Semiconductor Inversion Layers with Many Occupied Electric Subbands .1. Screening and Impurity Scattering*, Phys. Rev. B **2**, 1024 (1970).
 - [30] L. R. Gonzalez *et al.*, *Effect of band nonparabolicity on mobility in a δ -doped semiconductor*, Phys. Rev. B **60**, 7768 (1999).
 - [31] T. Sahu, *Intersubband-coupling and screening effects on the electron subband mobility in a GaAs/In_xGa_{1-x}As delta-doped double quantum well system*, J. Appl. Phys. **96**, 5576 (2004).
 - [32] T. Sahu, and J. Patnaik, *Electron transport mobility in a δ -doped double quantum well structure*, J. Appl. Phys. **88**, 2658 (2000).
 - [33] K. Leung, A. F. Wright, and E. B. Stechel, *Charge accumulation at a threading edge dislocation in gallium nitride*, Appl. Phys. Lett. **74**, 2495 (1999).
 - [34] D. M. Schaadt *et al.*, *Lateral variations in threshold voltage of an Al_xGa_{1-x}N/GaN heterostructure field-effect transistor measured by scanning capacitance spectroscopy*, Appl. Phys. Lett. **78**, 88 (2001).
 - [35] G. D. Mahan, *Many-particle physics* (Kluwer Academic/Plenum Publishers, New York ; London, 2000).
 - [36] R. Fletcher *et al.*, *Persistent Photoconductivity and 2-Band Effects in GaAs/Al_xGa_{1-x}As Heterojunctions*, Phys. Rev. B **41**, 10649 (1990).

5 Subband Structure and Transport

- [37] C. Bulutay, and M. Tomak, *Dielectric properties of the quasi-two-dimensional electron liquid in heterojunctions*, Phys. Rev. B **54**, 14643 (1996).
- [38] C. Bulutay, and M. Tomak, *Dielectric function of the two-dimensional electron liquid: An analytical fitting*, Phys. Rev. B **53**, 7317 (1996).
- [39] Padé approximation: http://en.wikipedia.org/wiki/Pad%C3%A9_approximant.
- [40] C. J. Humphreys *et al.*, in *EMC 2008 14th European Microscopy Congress 1-5 September 2008, Aachen, Germany, The atomic structure of GaN-based quantum wells and interfaces*, edited by Springer(2008), pp. 41.

Optical properties of $\text{Al}_{1-x}\text{In}_x\text{N}/\text{AlN}/\text{GaN}$ (0001) ($0.03 \leq x \leq 0.23$)

6.1 Introduction

This Chapter aims to discuss optical properties of $\text{AlInN}/(\text{AlN})/\text{GaN}$ heterostructures. It will be demonstrated that the luminescence spectra of AlInN alloy are in agreement with the common model for alloy broadening. Additionally, there is a strong effect of the built-in electric field across the barrier on the spectra. Understanding the optical properties allows drawing conclusion on the film quality. Besides, the bandgap of the AlInN alloy in the composition regime under investigation mediates between those of GaN and AlN , *i.e.* the spectral range which is interesting for UV optoelectronic devices.

6.2 Absorption and luminescence, origin of the stokes shift

Optical properties of the AlInN alloy are interesting not only for device application such as UV emitters or sensor, but also for fundamental questions around carrier recombination mechanisms. In addition, optical characterization is also a powerful tool in order to investigate structural quality and homogeneity of the samples.

Several authors reported a strong difference between the absorption and recombination (*i.e.* Stokes shift) within the AlInN alloy of several hundred meV [1-3].

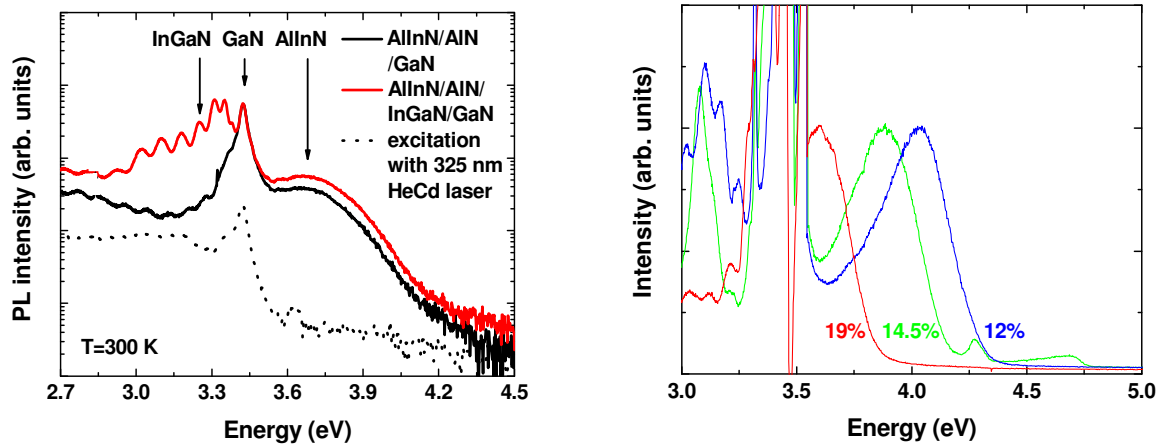


Figure 6.1 (a) RT PL spectra of an $\text{Al}_{0.85}\text{In}_{0.15}\text{N}(13 \text{ nm})/\text{AlN}(1\text{nm})/\text{GaN}$ heterostructure (black line) and a heterostructure where a 3 nm thick $\text{In}_{0.03}\text{Ga}_{0.97}\text{N}$ quantum well was inserted between the AlN interlayer and the GaN buffer (red line) indicating a direct recombination in the AlInN alloy at $\sim 3.7 \text{ eV}$. The dashed black line shows the PL spectrum when the sample is excited below the AlInN band gap with a 325 nm HeCd laser, for comparison. (b) PL-spectra of $\text{Al}_{1-x}\text{In}_x\text{N}(14\text{nm})/\text{AlN}(1\text{nm})/\text{GaN}$ heterostructures excited with a 244 nm Ar^+ CW laser at 8 K for different barrier indium contents.

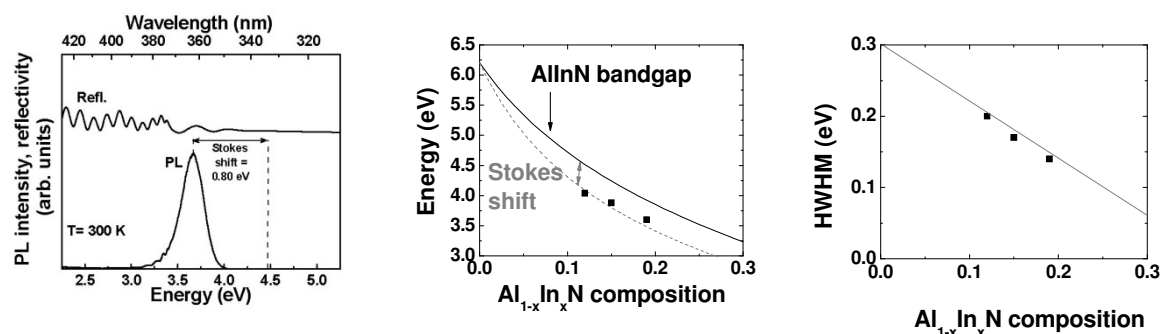


Figure 6.2 (a) Stokes shift, *i.e.* difference between absorption and PL for a 100 nm LM AlInN/GaN heterostructure taken from Ref. [1]. (b) Energy at PL maximum in comparison with bandgap values obtained from absorption measurement in Ref. [4] for thin layer with different indium composition. (c) Half width at half maximum of AlInN related PL peaks from Figure 6.1 (b) *versus* its indium content.

To ensure that the carrier recombination occurs within the AlInN, *i.e.* is of spatially direct nature we grew samples with an additional pseudomorphic $\text{In}_{0.03}\text{Ga}_{0.97}\text{N}$ quantum well (QW) of 3 nm thickness between the 1 nm AlN interlayer and the GaN buffer. For the samples with QW an additional PL intensity arises energetically below the GaN. Since there is no shift of the AlInN-related peak for samples with and without QW it can be concluded that no spatially indirect transition across the interfaces are involved in the luminescence line at 3.7 eV. Results are displayed in Figure 6.1 (a). In subfigure (b) the photoluminescence (PL) spectra for the $\text{Al}_{1-x}\text{In}_x\text{N}(14\text{nm})/\text{AlN}(1\text{nm})/\text{GaN}$ heterostructures are shown for several compositions. Clearly, it shifts with decreasing indium content to higher energies. For indium contents higher than 20% it becomes difficult to resolve the AlInN related peak for those thin layers. In Figure 6.2 (a) therefore the PL is shown together with the absorption measurements for a 100 nm LM AlInN/GaN heterostructure. Clearly, a large Stokes shift of ~ 0.6 eV is present (from Ref. [1]).

In subfigure (b) the energies at PL intensity maximum for different indium compositions are shown together with the bandgap obtained by composition dependent absorption measurements from Ref. [4]. Note that absorption measurements directly on these very thin films are not possible. In subfigure (c) the half widths at half maximum (HWHM) for AlInN related PL peaks from Figure 6.1 (b) are shown. Interestingly, they are very large compared to literature values found for AlGaIn or InGaIn alloys. Additionally, they increase for lower indium contents. This behaviour will be discussed in the following. Concerning the Stokes shift, a wide range of origins have been proposed in literature: defect related recombination [2], a localization due to nanoclustering [3] or hole localization at In-N-In chains which occurs even in perfect random alloys [5].

Another important consequence of alloy disorder is the following. A disordered system is no longer invariant with respect to translations. As a consequence, the wave vector is no longer a good quantum number and the dispersion relation $E(\mathbf{k})$ loses, strictly speaking, its meaning. A disordered system is in principle characterized only by its density of states. In three dimensions a potential well must have a certain width R and depth V to localize or bind a particle of mass m with [6]

$$VR^2 \geq \frac{\hbar^2}{m_{e,h}} \quad (6.1)$$

This is the reason why holes are more easily localized than electrons. Assuming a localization radius of $R \sim 0.4$ nm as obtained for In-N-In chains in InGaN [5], V is assumed to correspond to the difference in valence bands offset for AlN and InN (~ 1.3 eV) and GaN and InN (~ 0.6 eV). Together with the extreme difference in heavy hole effective masses (AlN ~ 10 and GaN ~ 2) one would indeed expect a ~ 10 times stronger localization in the AlInN alloy compared to InGaN. This is sketched in Figure 6.3 where for values ≥ 1 holes are localized. Again it should be pointed out that this is an intrinsic effect. The In-N-In chains are formed purely statistically and appear also in perfect homogeneous random alloy. The density of those chains is $d_{\text{In-N-In}} = 2x/ca^2 3^{0.5}$, where x is the indium content (no longer chains are considered which are also forms besides). Then the mean distance between two chains is given as $d_{\text{In-N-In}}^{-1/3}$. For the LM AlInN alloy therefore the mean distance between two chains is ~ 0.7 nm *i.e.* below its exciton Bohr radius of ~ 2 nm. If the thermal velocity is $v_{th} = \sqrt{k_B T / m_{e,h}}$, then the time for a heavy hole to travel the distance of 0.7 nm is given as $0.7 \text{ nm} / \sqrt{k_B T / m_{e,h}}$, *i.e.* in the order of sub-ps even for ultralow temperatures whereas the exciton lifetime is of the order of ns (or sub-ns) according to the relation for the radiative lifetime of the optical transition which is given as $\tau_{rad} = 2\pi \epsilon_0 m_e c^3 / n e^2 \omega^2 f_{osc}$. Here m_e is the electron effective mass, c is the speed of light, n is the refractive index, and f_{osc} the oscillator strength. That means that holes even if they are created away from the chain will practically instantaneously condensate there and recombine after some ns but with a reduced energy. More extended discussions about electrons and holes in disordered systems can be found in Ref. [7].

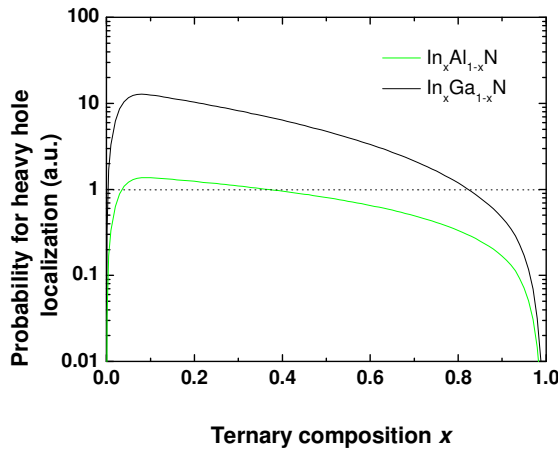


Figure 6.3 Probability of heavy hole localization in InGaN and AlInN according to Equation (6.1). A value above 1 means that localization is very likely. Of course, in the case of binaries, *i.e.* $x=0$ and $x=1$ there is no localization at all.

6.3 Alloy broadening in nitrides – a metastudy

Alloy broadening was already discussed intensively for III-arsenides. Corresponding to Ref. [8] the HWHM for alloy broadening is given as

$$\Gamma_{alloy} = \sqrt{2 \ln 2} \frac{dE_{gap}}{dx} \sqrt{\frac{x(1-x)}{KV_{ex}}} \quad (6.2)$$

with dE_g/dx the derivative of the bandgap, V_{ex} the excitonic volume and K the cation density. V_{ex} is given as $4/3 \pi a_{ex}^3$, where $a_{ex} = \epsilon \hbar^2 / \mu e^2$ and $\mu^{-1} = m_e^{-1} + m_h^{-1}$. The cation density is given by two times the inverse of the unit cell volume. This model describes successfully the broadening mechanisms in the AlGaN alloy [9, 10]. Figure 6.4 (b) shows the exciton Bohr radius a_{ex} evaluated for different nitride alloys as a function of the composition. The a_{ex} ranges from ~ 1.5 nm for AlN to ~ 3 nm for GaN and ~ 12 nm for InN. Effective masses and relative dielectric constants are interpolated linearly between binary compounds. Subfigure (a) shows the calculated HWHM according to Equation (6.2). For the excitonic volume the exciton Bohr radius from subfigure (b) is taken. For the alloys bandgap *versus* composition dependence we took the values already discussed in Chapter 1.4. Cation density is assumed to be constant (coherent material). The calculated curves are displayed together with experimental data from Ref. [9, 10] for AlGaN/GaN heterostructures and from Ref. [11] for InGaN/GaN heterostructures. In general, one finds a good agreement with Equation (6.2). Especially, for indium containing alloys (InAlN and InGaN) the HWHM are larger than the values the model predicts. This is partially caused by not considering electric field effects as discussed in the next subsection.

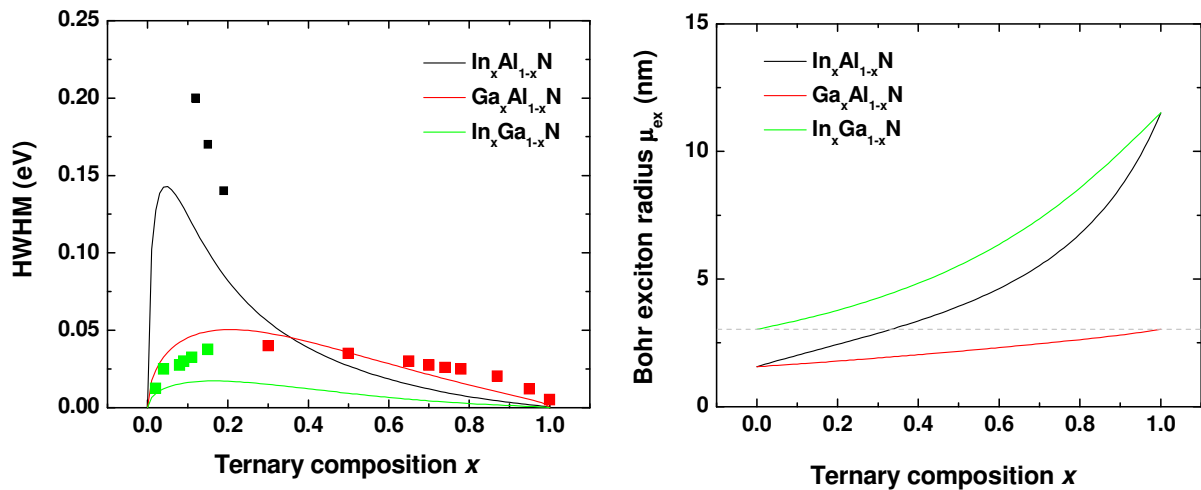


Figure 6.4 (a) Calculated HWHM Γ_{alloy} from Equation (6.2) for nitride ternary alloys assuming bandgap bowing but linear interpolation of effective masses. Experimental data are added for AlGaN [9, 10], for InGaN [11], and for AlInN (our data). (b) Corresponding exciton Bohr radius a_{ex} for ternary alloys.

6.4 Field broadening in $\text{Al}_{1-x}\text{In}_x\text{N}/\text{AlN}/\text{GaN}$ (0001) heterostructures

In Figure 6.5 (a) PL spectra for an $\text{Al}_{0.85}\text{In}_{0.15}\text{N}/\text{AlN}(1\text{nm})/\text{GaN}$ heterostructure with different AlInN barrier thicknesses are shown. Clearly, an increase in the HWHM values for thinner samples of the same composition is observed together with a loss of AlInN related PL intensity. The HWHM is shown again in subfigure (b). This is caused by field broadening effect. As we saw in Figure 4.6 (b) the electric field across the AlInN barrier depends strongly on the 2DEG density but is *a priori* known from the charge balance model.

The derivation of the relation between the electric field and the broadening is non-trivial and is discussed in Ref. [12] basing on the solution of the equation $(-\Delta - 2/r + f z)\Psi(\mathbf{r}) = E\Psi(\mathbf{r})$, where f represents the 1D electric field in z -direction (in excitonic units). Electron-hole interaction is taken into account via the term $2/r$.

According to Ref. [12] the broadening is *nothing but the immediate consequence of a complete continuous spectrum. The physical interpretation of this effect is, however, more appealing. Considering the effective potential, we see that we have to distinguish between three regions for $z \leq 0$. Whereas for small $|z|$ the potential is dominated by the Coulomb potential, for large $|z|$ it approaches the potential due to the field. These regions are separated by a potential barrier, which increases with increasing field. Owing to the finite tunnelling probability, any excitonic bound state has an admixture of continuum states. This makes the spectrum continuous and as a remnant of the true bound states, we have broadened resonances only. In the time domain this may be interpreted as a finite lifetime of bound excitonic states due to their ionization, resulting from the finite tunnelling probability.*

The frequency dependent contribution due to field broadening to the spectrum is given as $\Gamma_{\text{field}}(\Omega) = 16f^3 \exp(-4|\Omega|^{3/2}/3f)$, whose HWHM amounts to

$$\Gamma_{\text{field}} = 0.647 E_r (F a_{\text{ex}} / E_r)^{2/3} \quad (6.3)$$

with a_{ex} the exciton radius, E_r the exciton Rydberg energy given as $E_r = e^2 / 2 \epsilon a_{\text{ex}}$ and F the electric field [V/m]. In Figure 6.5 (b) the electric field across the AlInN barrier for different thicknesses (Figure 4.6 (b)) is redrawn. For large thicknesses (>100 nm) the field effect is weak and broadening is dominated by alloy broadening. In Refs. [13, 14] it was argued that the total broadening is simply the sum over the individual broadening mechanisms *i.e.*

$$\Gamma_{\text{total}} = \Gamma_{\text{alloy}} + \Gamma_{\text{field}} \quad (6.4)$$

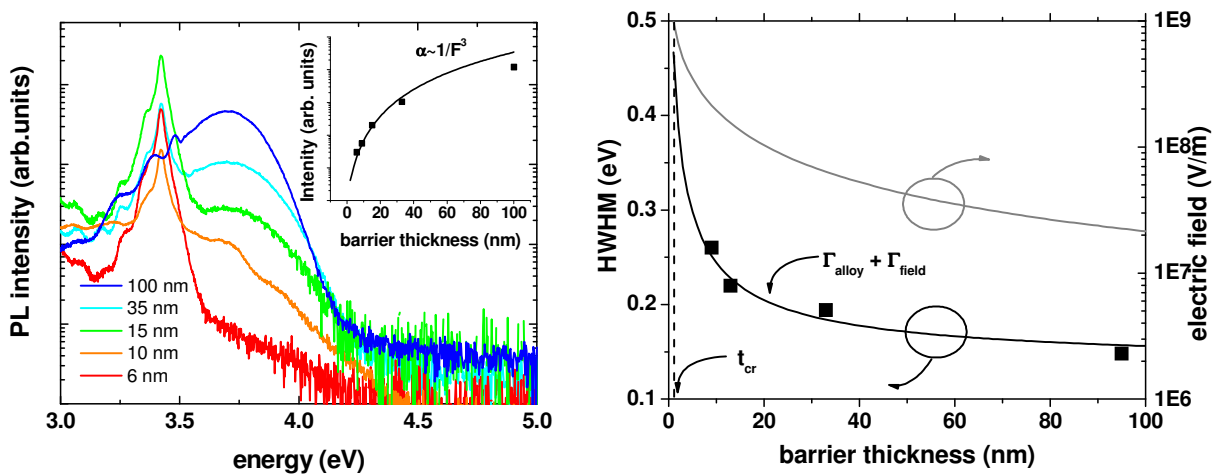


Figure 6.5 (a) PL spectra for $\text{Al}_{0.85}\text{In}_{0.15}\text{N}/\text{AlN}(1\text{nm})/\text{GaN}$ heterostructures versus AlInN barrier thickness. Inset shows intensity dependence of the AlInN related peak on the barrier thickness (b) HWHM of AlInN related PL peak versus barrier thickness. Additionally, the electric field across the AlInN barrier for different thicknesses is shown. For large thicknesses (>100 nm) the field effect is weak and broadening is dominated by alloy broadening. The alloy broadening is of the order of $\Gamma_{\text{alloy}} \sim 140$ meV.

Therefore, neglecting the field induced broadening for thin layers, where the electric field is extremely high, can cause a significant increase of the total broadening. Another interesting aspect is that Equations (6.2) and Equation (6.3) can be used to estimate the reduced effective mass of the LM alloy. The black curve in Figure 6.5 (b) yields a reduced effective mass of $\sim 0.3m_0$ and reproduces very well the experimental data. This also hints towards a recombination process involving a localized hole rather than a localized electron since the reduced effective mass is mainly dominated by m_e ($m_e \ll m_h$). Therefore m_e for the LM AlInN alloy is $0.3m_0$ in good agreement with the value obtained when interpolating between the two binaries.

Interestingly is also the AlInN related PL intensity *versus* barrier thickness dependence. By tuning the barrier thickness from 6 to 100 nm a strong increase of intensity over few decades can be observed, which is not expected from a Lambert-Beer-like behavior for absorption. Also here this behavior can be explained with the strong electric fields. From Equations (8.35) and (8.40) in Ref. [12] it is found that the absorption in the presence of an electric field scales roughly as $\alpha \sim 1/F^3$. Therefore in the inset of Figure 6.5 (a) one can see that $1/F^3$ emission intensity dependence (with the electric field F taken from Figure 6.5 (b)) well accounts for AlInN related PL intensity trend with the barrier thickness.

6.5 Spatial and thermal aspects of LM AlInN related luminescence

At the end of this Chapter we want to use the so-called micro-Photoluminescence (μPL) to probe the luminescence spectra spatially resolved. Usually, the setup works with a spot exhibiting an excitation diameter of $0.5 \mu\text{m}$. Excitation was carried out as in the previous cases with the 244 nm line of an Ar^+ CW laser. Details on the setup can be found in Refs. [15, 16] and Chapter 6.3. Figure 6.6 (a) shows the wavelength fluctuation at the AlInN related PL intensity maximum of a 13 nm $\text{Al}_{0.85}\text{In}_{0.15}\text{N}$ barrier recorded *via* μPL on a $60 \times 60 \mu\text{m}^2$ scan. Fluctuations are in the order of ± 0.1 nm. This is notably low, taking the slope bandgap *versus* composition from Figure 6.2 (b) yields a fluctuation of the composition lower than 0.1% on this scan. Subfigure (b) shows the corresponding intensity variation in percent.

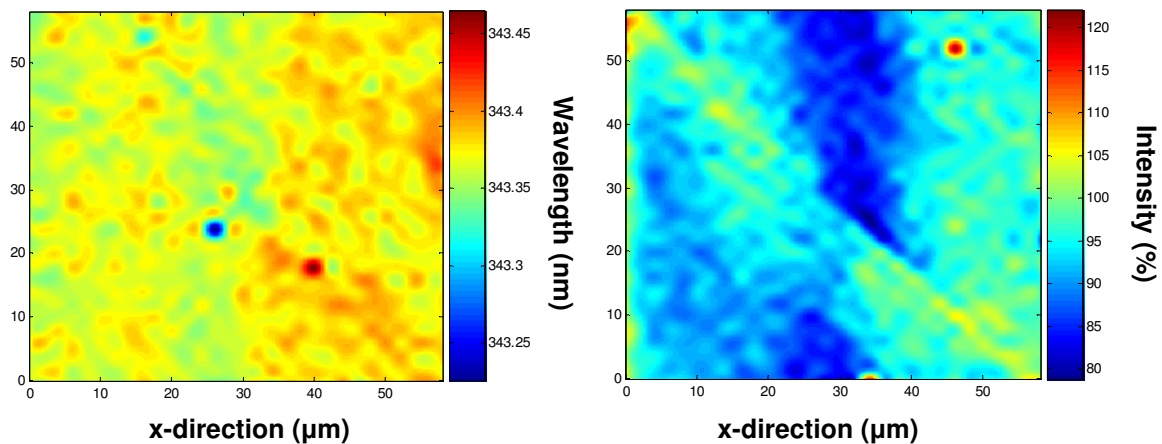


Figure 6.6 (a) Wavelength fluctuation at the AlInN related PL intensity maximum of a 13 nm $\text{Al}_{0.85}\text{In}_{0.15}\text{N}$ barrier recorded *via* μPL on a $60 \times 60 \mu\text{m}^2$ area. Subfigure (b) shows the corresponding intensity variation in percent.

However, it is difficult to claim any quantitative accuracy on this technique since other effects such as exciton migration could play a role and also the peaks are very broad.

Figure 6.7 show the temperature dependence of the PL of an $\text{Al}_{0.85}\text{In}_{0.15}\text{N}(14\text{nm})/\text{AlN}(1\text{nm})/\text{GaN}$ heterostructure grown on sapphire. The AlInN related intensity maximum shift as a function of temperature is in good agreement with Varshni's formula. On the other hand the HWHM is very stable over this temperature range, owing to the fact that the AlInN related luminescence is dominated by alloy broadening, which is a temperature independent process and where phonon effects, as found in bulk GaN [14], are negligible.

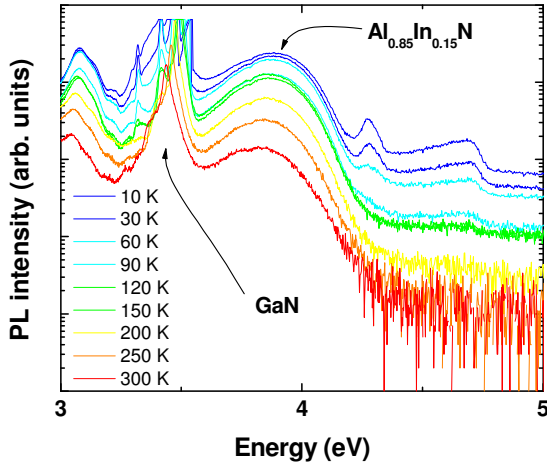


Figure 6.7 Temperature dependence of the PL spectra for an $\text{Al}_{0.85}\text{In}_{0.15}\text{N}(14\text{nm})/\text{AlN}(1\text{nm})/\text{GaN}$ heterostructure grown on sapphire.

6.6 Conclusions

It was demonstrated that the optical properties of AlInN barriers in heterostructures are strongly affected by built-in electric field decreasing the luminescence intensity as $\sim 1/F^3$. The broadening of the AlInN related luminescence peak can be attributed to one part to the alloy disorder effect, which exhibits the greatest magnitude among the nitride alloy due to the strong bandgap bowing and change in excitonic volume *versus* indium content. And secondly to a field effect which becomes important for thicknesses lower than 100 nm and which broadens the spectra significantly. Using analytical expressions allows us extracting the reduced effective mass from the HWHM *versus* barrier thickness dependence which yields $\sim 0.3 m_0$ for the LM alloy. Since $m_e \ll m_h$ it follows that $m_e \approx \mu$. Since this effective electron mass is close to the expected value one might conclude that the Stokes shift originates from hole localization process. Indeed, the hole localization has the largest probability to occur in AlInN among the nitride alloy due to the large hole effective mass. A possible origin of the localization is the randomly formed In-N-In chains, with distances lower than the exciton Bohr radius. Hole would practically instantaneously be localized at these chains and recombination would then occur at a reduced energy. Moreover, spatial resolved μPL reveal low indium fluctuation in average for LM AlInN heterostructures, which is also consistent with findings from simulated XRD spectra.

Bibliography

- [1] R. Butté *et al.*, *Current status of AlInN layers lattice-matched to GaN for photonics and electronics*, J. Phys. D Appl. Phys. **40**, 6328 (2007).
- [2] S. F. Chichibu *et al.*, *Origin of defect-insensitive emission probability in In-containing (Al, In, Ga) N alloy semiconductors*, Nat. Mater. **5**, 810 (2006).
- [3] T. Onuma *et al.*, *Recombination dynamics of localized excitons in $\text{Al}_{1-x}\text{In}_x\text{N}$ epitaxial films on GaN templates grown by metalorganic vapor phase epitaxy*, J. Appl. Phys. **94**, 2449 (2003).
- [4] E. Iliopoulos *et al.*, *Energy bandgap bowing of InAlN alloys studied by spectroscopic ellipsometry*, Appl. Phys. Lett. **92**, 191907 (2008).
- [5] L. W. Wang, *Calculations of carrier localization in $\text{In}_x\text{Ga}_{1-x}\text{N}$* , Phys. Rev. B **63**, 245107 (2001).
- [6] C. F. Klingshirn, *Semiconductor optics* (Springer, Berlin ; New York, 2007).
- [7] M. Mostovoy, F. Antonsen, and J. Knoester, *Optical excitation of electron-hole pairs in disordered one-dimensional semiconductors*, Phys. Rev. B **65**, 155210 (2002).
- [8] E. F. Schubert *et al.*, *Alloy Broadening in Photoluminescence Spectra of $\text{Al}_x\text{Ga}_{1-x}\text{As}$* , Phys. Rev. B **30**, 813 (1984).
- [9] G. Coli *et al.*, *Linewidths of excitonic luminescence transitions in AlGaIn alloys*, Appl. Phys. Lett. **78**, 1829 (2001).
- [10] G. Coli *et al.*, *Excitonic luminescence linewidths in AlGaIn alloys with high aluminum concentrations*, Appl. Phys. Lett. **80**, 2907 (2002).
- [11] W. Shan *et al.*, *Optical properties of $\text{In}_x\text{Ga}_{1-x}\text{N}$ alloys grown by metalorganic chemical vapor deposition*, J. Appl. Phys. **84**, 4452 (1998).
- [12] W. Schäfer, and M. Wegener, *Semiconductor optics and transport phenomena* (Springer, Berlin ; New York, 2002).
- [13] J. Lee, E. S. Koteles, and M. O. Vassell, *Luminescence Linewidths of Excitons in GaAs Quantum-Wells Below 150-K*, Phys. Rev. B **33**, 5512 (1986).
- [14] W. Liu *et al.*, *Phonon-assisted photoluminescence in wurtzite GaN epilayer*, Semicond. Sci. Tech. **13**, 769 (1998).
- [15] G. Christmann, *III-nitride based microcavities towards polariton condensation at room temperature* (PhD Thesis, EPFL, Lausanne, 2009).
- [16] D. Simeonov, *Synthesis and optical investigation of single polar GaN/AlN quantum dots* (PhD Thesis, EPFL, Lausanne, 2009).

Devices based on $\text{Al}_{1-x}\text{In}_x\text{N}/\text{AlN}/\text{GaN}$ (0001) heterostructures ($0.03 \leq x \leq 0.23$)

7.1 Introduction

In 2005 the number of transistors per head of world population exceeded one billion. In 2007 more than one billion cell phones were sold. Obviously there is a huge global digital revolution in process. For this demand the appropriate technology has to be provided. For communication purposes radio frequency (RF) applications cover already a large range of wavelengths as depicted in Figure 7.0 (a). Transistors based on semiconductor materials have then the capability to act as power amplifiers where the limits arising from the semiconductor intrinsic properties. The physical power-frequency limit is estimated from the argument that carriers move with the saturation velocity v_{sat} near the breakdown field E_B along the channel with a length l needing the transit time τ , *i.e.* $2\pi \cdot f = 1/\tau = v_{sat}/l = v_{sat} \cdot E_B/V$, yielding the relation $V \cdot f \leq v_{sat} \cdot E_B/2\pi$. A similar consideration for the current leads to a relation for the dependence of the power $I \cdot V$ on frequency, namely $P \cdot f^2 \leq 1/X_C \cdot (v_{sat} \cdot E_b/2\pi)^2$. Using appropriate material parameters this results in the so-called Figure of Merit (Figure 7.0 (b)) [1]. Obviously GaN is an interesting candidate for high power high frequency operation. Therefore in this chapter properties and limits of AlInN/AlN/GaN HEMTs will be discussed.

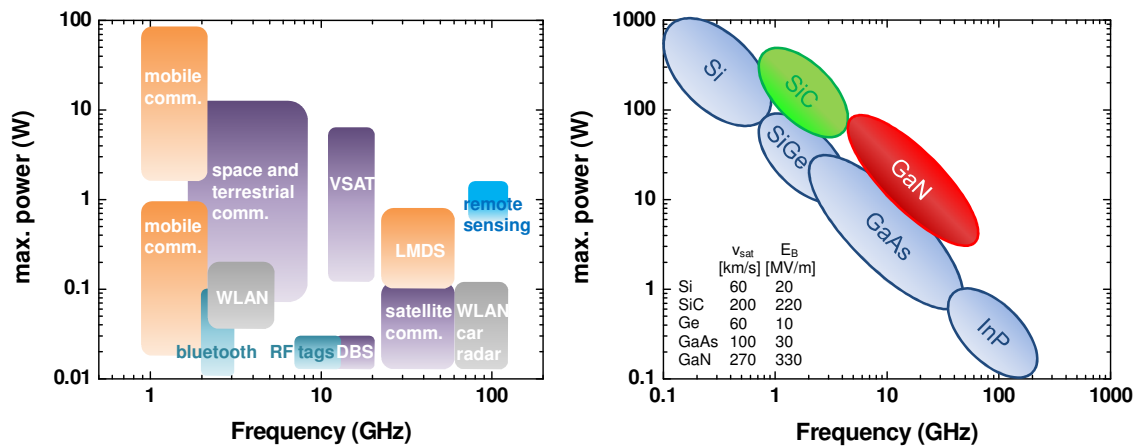


Figure 7.0 (a) Maximum emitting power *versus* operating frequency for different radio frequency (RF) power applications. (b) Physical power-frequency limits: relation between high frequency parameters and semiconductor properties. Figures adapted from Ref. [2].

7.2 High electron mobility transistors (HEMT)

7.2.1 Principles of HEMT devices

HEMT generalities There are basically two main types of semiconductor transistors, namely *bipolar* and *unipolar* devices. For the former two types of carriers, *i.e.* electrons and holes, are involved in the current transport while in the operation of the latter one only one carrier type is involved, despite they may contain *pn*-junctions. The *unipolar* transistor is also referred to as *field-effect transistor* (FET) and is divided in mainly to families: *junction FET* (JFET) and *insulated gate FET* (IGFET). The latter is also commonly referred to as *metal-oxide-semiconductor FET* (MOSFET). *Metal-semiconductor FETs* (MESFETs) are JFETs where the *pn*-junction is replaced by a Schottky contact. High electron mobility transistors (HEMTs) are a specific type of MESFETs where a 2DEG located at a suitably designed heterostructure interface is used for current transport which is able to achieve very high frequencies due to its superior carrier mobility. Beside benefiting from the ‘polarization doping’ in nitride heterostructures, HEMTs are successfully fabricated from InGaAs/InP /AlInAs and Si/SiGe heterostructures, where the high mobility is obtained by the spatial separation of the 2DEG in the triangular well from the donors in the barrier. Today mainly pseudomorphic pHEMTs (AlGaAs/InGaAs/GaAs) and metamorphic HEMTs (InAlAs/InGaAs on GaAs) dominate the RF market.

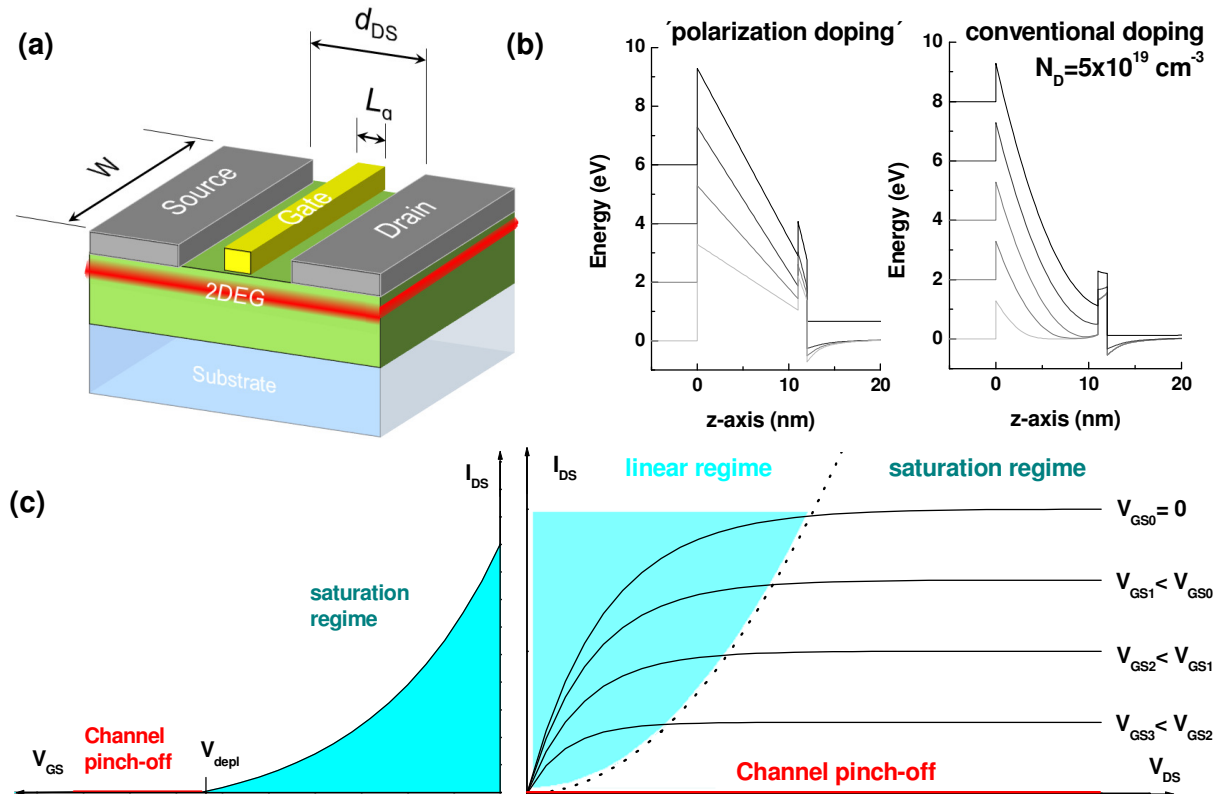


Figure 7.1 (a) Schematic sketch of a HEMT device. Main parameters are indicated. (b) Band diagrams for an AlInN/AlN/GaN HEMT under the gate contact for different applied gate voltages. Left panel shows the situation with purely ‘polarization doping’, while right panel sketches the situation if the same 2DEG density of $2 \times 10^{13} \text{ cm}^{-2}$ is obtained by conventional impurity doping without the presence of polarization charges. (c) Schematic sketch of the I_{DS} curves versus V_{DS} for different applied gate voltages V_{GS} . Adapted from Ref. [3] .

In Figure 1.1 (a) a schematic sketch of a HEMT device is shown. The important dimensions are the gate width W , the gate length L_g and the drain-source distance d_{DS} . Since the current flowing through the device is proportional to W it is conventionally given in (A/mm). The HEMT can be driven as a four terminal device with source, drain, gate and substrate contact, but usually source and substrate are connected. The impact of an applied gate (=Schottky) voltage on the band diagrams of an $\text{AlInN}/\text{AlN}/\text{GaN}$ HEMT heterostructure is shown in Figure 1.1 (b). Left panel shows the situation with purely ‘polarization doping’ as discussed in Chapter 4, while right panel sketches the situation if the same 2DEG density of $2 \times 10^{13} \text{ cm}^{-2}$ is obtained by conventional impurity doping solely without the presence of polarization charges. To achieve this one would require a shallow donor with a density of $N_D \sim 5 \times 10^{19} \text{ cm}^{-3}$ in the barrier. As a consequence the band profile is no longer linear as it is the case for ‘polarization doping’. According to the Poisson equation this non-linearity corresponds to free carriers within the barrier. This is clearly a drawback since it would lead to an increase in leakage current, *i.e.* a large current flow when applying V_{GS} . The lowest, light gray band profile corresponds to the situation at $V_{\text{GS}}=0 \text{ V}$. Applying now a voltage V_{GS} means lifting the electrons over the Fermi level, *i.e.* depleting the 2DEG. The carrier density under the gate can hence be modulated by applying V_{GS} . In the case of a highly doped barrier a voltage $\Delta V = w^2 q N_D / 2 \epsilon \epsilon_0$ has to be added to the reverse bias to overcome the space charge region w within the barrier. In such highly doped structures ΔV can amount to several volts. The conducting layer (*i.e.* for HEMTs the 2DEG) underneath the contacts is called the *channel*. Applying now a voltage V_{DS} to the drain for a $V_{\text{GS}}=0 \text{ V}$ causes a potential gradient along the channel forcing the electrons in the 2DEG to move. For small V_{DS} , the drain-source current I_{DS} is proportional to V_{DS} (ohmic behavior), while for large V_{DS} the electrons of the 2DEG interact with the lattice and I_{DS} becomes saturated. The corresponding IV characteristic is depicted in Figure 1.1 (c). If now additionally a gate voltage is applied, *i.e.* $V_{\text{GS}} < 0 \text{ V}$ and the channel becomes depleted, the maximum amount of current which can be transported underneath the gate is reduced with respect to the situation with $V_{\text{GS}}=0 \text{ V}$. Consequently, IV curves in Figure 1.1 (c) shift to lower values.

Frequency operation So far the behavior of the HEMT under DC conditions was discussed. Now the question arises how the device behaves under AC conditions. If one considers a HEMT as a 3-terminal device with S, D, and G and additionally one signal entering and one signal leaving the device it is hence possible to realize 3 different types circuits. The terminal where no signal enters or leaves the device is referred to as ‘common’. Consequently, the 3 circuits are labeled as ‘common source’ (CS), ‘common gate’ (CG) and ‘common drain’ (CD). We are in the following interested in the situation of a signal entering *via* G and leaving *via* D, *i.e.* a common source circuit which is depicted in Figure 7.2 (a). In electrical engineering and for circuit design purposes it is useful to regard such devices as ‘black boxes’, *i.e.* the device or a group of devices is described by its entering and leaving electrical signals at the ports. The FET or the HEMT can therefore be described by a two-port network or quadripole (four terminals). In general the conversion between the outgoing and incoming complex AC signal at each port is mediated *via* a 2×2 matrix giving rise to the so-called z (impedance), y (admittance), h (hybrid) and g (inverse hybrid) parameters. However the z , y , h , and g parameters only applies at low frequencies. At very high frequencies the concept of voltage and current loses its meaning and it is more favorable to operate with the terms power and energy. This is ensured by the so-called s or scattering parameters.

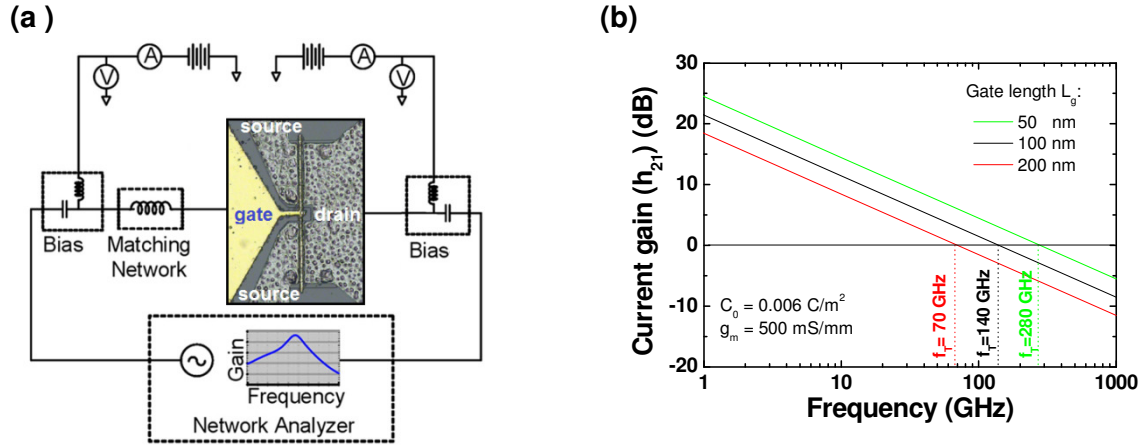


Figure 7.2 (a) HEMT in a common source amplification circuit with input signal connected to gate-source and output signal connected to drain-source. Adapted from Ref. [4]. (b) Hypothetic current gain h_{21} according to Equation (7.6) as function of the gate length L_g for a fixed barrier capacity C_0 and channel transconductance g_m as indicated in the inset.

The scattering parameters can directly be measured using a network analyzer. For the two-port network S_{11} is referred to as the input port reflection coefficient, S_{12} as the reverse gain, S_{21} as the forward gain, and S_{22} as the output port reflection coefficient. If the scattering parameters are known several important frequency dependent quantities can be obtained. For the measurement of HEMT devices the 'gate-source' signals refers to port 1 while the 'drain-source' signals refers to port 2.

Current gain The scattering parameters can directly be converted in any of the z , y , h , and g parameters [5]. Especially if current gain is desired it is convenient to chose the hybrid parameters where h_{21} is defined as the ratio between input and output current, *i.e.*

$$h_{21} \equiv \left. \frac{I_2}{I_1} \right|_{V_2=0} \quad (7.1)$$

If h_{21} is expressed in terms of scattering parameters it reads as [5] for identical input and output impedances

$$h_{21} = \frac{-2S_{21}}{(1-S_{11}) \cdot (1+S_{22}) + S_{12} \cdot S_{21}} \quad (7.2)$$

Maximum Available Power Gain (MAG) The maximum available power gain is defined as the ratio of power being output to the load impedance and the power being input to the transistor if both input and output impedances match. This leads to the relation [6]

$$\text{MAG} = \left| \frac{S_{21}}{S_{12}} \right| \cdot \left(K - \sqrt{K^2 - 1} \right) \quad (7.3)$$

where K is called stability factor and is a measure for stability of the transistor in the frequency range. It is given as $K = \left(1 + |S_{11} \cdot S_{22} - S_{12} \cdot S_{21}|^2 - |S_{11}|^2 - |S_{22}|^2 \right) / \left(2|S_{12}| \cdot |S_{21}| \right)$. The transistor is stable for $K > 1$. At $K=1$ Equation (7.3) reduces to $\text{MSG} = |S_{21}/S_{12}|$, the maximum stable gain (MSG).

Unilateral Power Gain (U) The gain if a lossless feedback is used to cancel the transmission of power from the output to the input is referred to as unilateral (*i.e.* $S_{12}=0$). It is given by [6]

$$U = \left| \frac{S_{21}}{S_{12}} - 1 \right|^2 / 2 \left(K \cdot \left| \frac{S_{21}}{S_{12}} \right| - \text{Re} \left[\frac{S_{21}}{S_{12}} \right] \right) \quad (7.4)$$

Note that $S_{12}=0$ is only valid for the feedback amplifier the value S_{12} of the transistor in Equation (7.4) is non-zero. The unilateral power gain is also referred to as Mason's gain.

Current Gain Cutoff Frequency The cut-off frequency f_T is the frequency at which the magnitude of the transistor short-circuit current gain h_{21} drops to unity, *i.e.* $h_{21}(f_T)=1$. To estimate f_T for an intrinsic FET it is convenient to introduce the following quantities

$$g_m = \left. \frac{\partial I_D}{\partial V_{GS}} \right|_{V_{DS}=\text{const.}} \quad g_d = \left. \frac{\partial I_D}{\partial V_{DS}} \right|_{V_{GS}=\text{const.}} \quad (7.5)$$

where g_m is referred to as transconductance and g_d as output conductance with the unit (S/m). The evolution of the transconductance *versus* V_{GS} for an AlInN HEMT is shown in Figure (7.6). Then Equation (7.1) together with Equation (7.5) and the gate (input) impedance $Z_{GS} = 1/j\omega C_{GS}$ yields

$$h_{21} = \frac{\partial I_D}{\partial I_{GS}} = \frac{g_m \partial V_{GS}}{(j\omega C_{GS}) \partial V_{GS}} = \frac{g_m}{(j\omega C_{GS})} \quad (7.6)$$

imposing that $h_{21}=1$ and using $\omega = 2\pi \cdot f_T$ the cut-off frequency becomes

$$f_T = \frac{g_m}{2\pi C_{GS}} \quad (7.7)$$

where C_{GS} is the gate capacitance. To achieve a high f_T the g_m should be large as possible, *i.e.* a high I_{DS} and the C_{GS} as small as possible, *i.e.* small gate lengths. This is illustrated in Figure 7.2 (b), where the hypothetic current gain h_{21} according to Equation (7.6) is shown as a function of the gate length L_g for a fixed barrier capacity C_0 of 0.006 F/m^2 and a channel transconductance g_m of 500 mS/mm .

Maximum Oscillation Frequency The maximum oscillation frequency f_{max} is defined as the frequency at which U drops to the unity, *i.e.* $U(f_{max})=1$. f_{max} is for FETs typically larger than f_T , since it takes additionally into account possible voltage gain. To estimate f_T practically s -parameters are converted into the h -parameters and current gain is plotted *versus* frequency. f_{max} is estimated by extrapolation of the measured unilateral power gain *versus* frequency. For further reading on analytic models for f_{max} see Refs [7, 8].

Output power By adjusting the gate voltage the amplifier can operate in different modes or classes by adjusting the bias point with respect to the voltage axis as sketched in Figure (7.3). This effects the efficiency of the device significantly. The *drain efficiency* η is defined as the ratio of RF output power and the supplied DC power at the quiescent point, *i.e.* $\eta = P_{out}/P_{DC}$. The important classes are A, B and C. In class A the quiescent point (also Q - or operating point) is located at the centre of the load line causing a maximum efficiency η of 50% but has the advantage that the signal is not distorted. In class B the Q -point is located on the voltage

axis resulting in an η of $\pi/4=78\%$ but signal distortion is increased. In class C operation the Q-point is below the voltage axis causing even higher η but signal distortion is further increased and the available output power drops strongly. We will restrict here only to class A operation. The situation is sketched in Figure (7.3). The slope of the load line (red) is given as $-R_L = (V_{br} - V_{knee}) / I_{DS,sat}$, with the breakdown voltage V_{br} and the voltage V_{knee} at $I_{DS,sat}(\text{max})$. The Q-point is located at $I_{DS,sat} / 2$ and $(V_{br} + V_{knee}) / 2$. The AC signal and the voltage amplitude swings around this point. The RF output power that can be delivered from the transistor to the load is given as $P_{out} = \frac{1}{T} \int_0^T R_L \cdot i_L^2$. Assuming for the AC signal $i_L = I_{DS,sat} / 2 \cdot \sin(T)$ for class A operation, the integration yields [9]

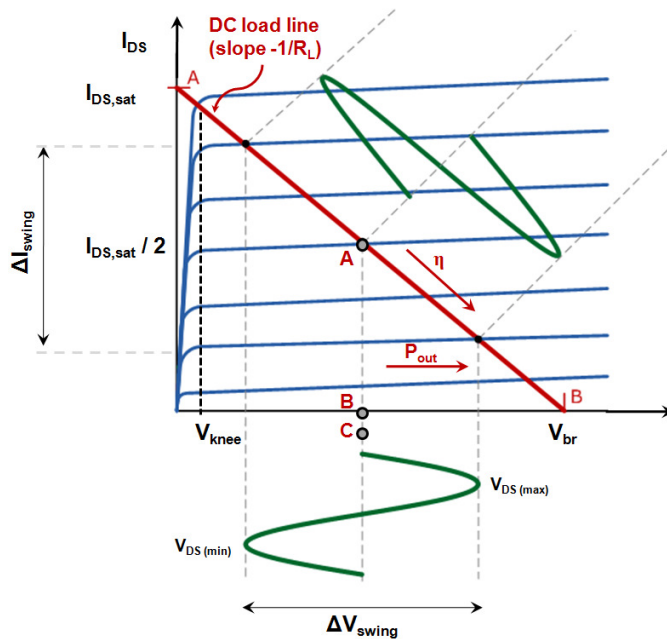
$$P_{out} = \frac{I_{DS,sat} (V_{br} - V_{knee})}{8} \quad (7.8)$$

this differs from the total DC power of the quiescent point which is given as $P_{DC} = I_{DS,Q} \cdot V_{DS,Q}$, with the current and voltage of the quiescent point.

Additionally a measure is defined called the *power added efficiency (PAE)* which takes into the account RF input power

$$PAE = \left[P_{out,RF} - P_{in,RF} \right] / P_{DC} = \eta \times \left[1 - \frac{1}{G} \right] \quad (7.9)$$

PAE will be very similar to η when the RF gain $G = P_{out,RF} / P_{in,RF}$ of the amplifier is sufficiently high. But if the amplifier gain is low the amount of power $P_{in,RF}$ that is needed to drive the input of the amplifier should be considered. As a very simplified example one could consider a transistor with $V_{br}=30$ V, $V_{knee}=10$ V, and $I_{DS,sat}=1$ A/mm. Then Equation (7.8) results in $P_{out}=2.5$ W/mm, while P_{DC} amounts with $I_{DS,Q}=0.5$ A/mm and $V_{DS,Q}=20$ V to 10 W/mm yielding an $\eta=25\%$. If V_{knee} would be zero the maximum η that can be expected in class A operation amounts to 50%.



An important parameter to increase the device performance is hence the improvement of DC device capabilities of the maximum drain current, the breakdown voltage and the knee voltage. Moreover the use of other operation classes (AB, B, C, F, etc.) is necessary to improve the PAE. All of them are requiring high RF gains to allow advanced wave forming by microwave designers. AlInN/GaN HEMTs are devices that could offer both lower knee voltages and higher RF gains, and those support the current active research activities on these devices.

Figure 7.3 Loadline of output power for class A operation imposed on an idealized FET characteristics. Additionally quiescent point Q for class B and C are indicated. Direction for increased P_{out} and η are indicated as function of Q. Voltage and current swings around Q are also sketched. Adapted from Ref. [10].

7.2.2 A survey of $\text{AlInN}/\text{AlN}/\text{GaN}$ HEMT characteristics

$\text{Al}_{0.85}\text{In}_{0.15}\text{N}(13\text{nm})/\text{AlN}(1\text{nm})/\text{GaN}/\text{sapphire}$ heterostructures In this subsection, we summarize the results obtained for HEMT devices processed from $\text{AlInN}/\text{AlN}/\text{GaN}$ heterostructures used throughout this work. At this point we spare to explain details on processing steps. A good overview over recent processing techniques can be found in Ref. [3] or especially for nitrides in Ref. [11]. It is clear that if one wishes to stick with Moore's law [12] one has to shrink the device size. The minimum feature size (MFS) [13] using a UV light source is ~ 1 micron using standard photolithography techniques. This limit concerns mainly the processing of the gate contacts. To go beyond this MFS one has to engage other technologies such as e-beam lithography. With such technologies state of the art gate length down to 30 nm can be obtained also on nitride HEMT devices [14].

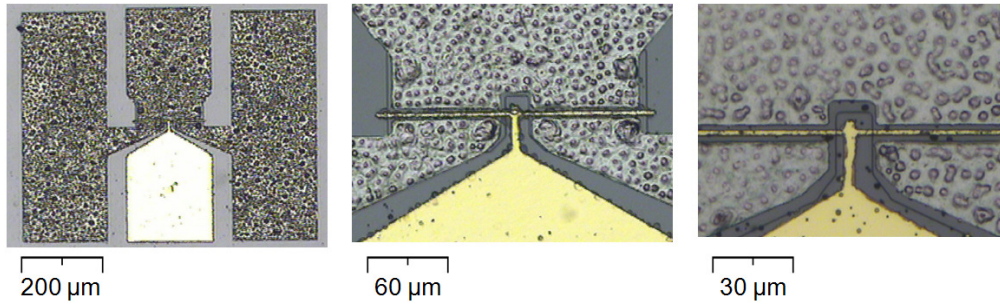


Figure 7.4 Typical HEMT device processed from $\text{AlInN}/\text{AlN}/\text{GaN}$ heterostructures with different magnifications (optical microscopy). In subfigures (b) and (c) the $\text{AlInN}/\text{AlN}/\text{GaN}$ MESA is visible close to the end of the gate contact. In this example, $L_g = 1.5 \mu\text{m}$ and drain-source distance $d_{DS} = 5 \mu\text{m}$. Typically MESA height is $0.4 \mu\text{m}$ (Process from EPFL).

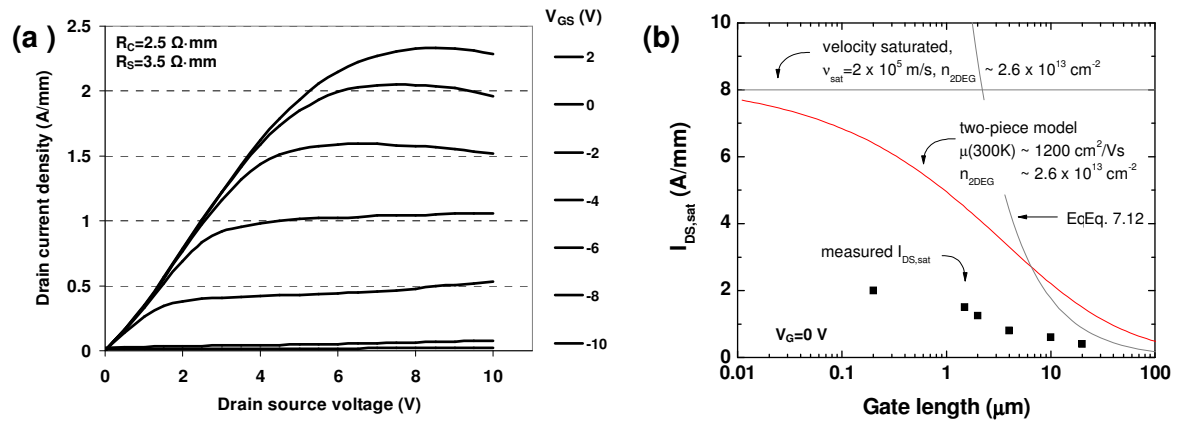


Figure 7.5 (a) I_{DS} versus V_{DS} for different gate voltages for a HEMT processed from an $\text{Al}_{0.85}\text{In}_{0.15}\text{N}(13\text{nm})/\text{AlN}(1\text{nm})/\text{GaN}/\text{sapphire}$ heterostructure with $L_g = 0.25 \mu\text{m}$ and $W = 50 \mu\text{m}$. Current densities up to 2 A/mm are achieved for the first time. Typical contact resistance R_C and source resistance R_S are indicated. (b) $I_{DS,sat}$ versus gate length obtained for gated TLMs on the same wafer as subfigure (a). Additionally, the red curve shows the prediction within a two-piece model assuming $n_{2DEG} = 2.6 \times 10^{13} \text{ cm}^{-2}$ and $\mu = 1200 \text{ cm}^2/\text{Vs}$ and the black line the velocity saturated limit (*i.e.* if all 2DEG carriers move with v_{sat}). Apparently, there is a huge difference (factor 4) in expected and measured values which will be clarified in the following (Processing at Ulm University).

7 Devices based on $\text{Al}_{1-x}\text{In}_x\text{N}/\text{AlN}/\text{GaN}$ heterostructures ($0.03 \leq x \leq 0.23$)

Some typical pictures of processed HEMTs are shown in Figure 7.4 at different magnifications. The contact processing has been carried out under the following conditions: mesa isolation has been performed with dry etching in chloride based plasma. For the Ohmic contacts, a standard Ti/Al/Ti/Au metal stack (40 nm/150 nm/40 nm/40 nm) was deposited *via* *e*-beam. Gate contacts consist of 20 nm/170 nm Ni/Au stacks.

Now we are turning on to the electrical characterization of such devices. Figure 7.5 (a) shows the I_{DS} versus V_{DS} for different gate voltages for a HEMT processed from a $\text{Al}_{0.85}\text{In}_{0.15}(13\text{nm})/\text{AlN}(1\text{nm})/\text{GaN}/\text{sapphire}$ heterostructure with $L_g=0.25 \mu\text{m}$ and $W=50 \mu\text{m}$. Current densities up to 2 A/mm are achieved for the first time [15, 16]. In subfigure (b) $I_{DS,sat}$ obtained for HEMTs with different gate lengths and drain source distances are depicted as black squares, where V_{GS} is always 0 V. Measurements subfigure (a) and (b) are carried out on the same wafer. At this point we want to introduce the two-piece model taking into account a transition between the velocity saturated regime (near the gate edge) and the mobility limited regime (between source and gate and gate and drain see also Figure 7.14). The transition is non-abrupt using the phenomenological relation $v = \mu F(x) / (1 + \mu F(x) / v_{sat})$ [17]. Here, we spare out the exact deviation of the relation, it can be found in Ref. [18]. Then the current at the saturation point $I_{DS,sat}$ is given as [17, 18]

$$I_{DS,sat} = \frac{2(V_G - V_{off})^2 W \epsilon \epsilon_0 \mu}{Ld} \left[1 + \left\{ 1 + \frac{2\mu(V_G - V_{off})}{v_{sat} L} \right\}^{1/2} \right]^{-2} \quad (7.10)$$

where V_G and V_{off} are the gate and the pinch-off voltages, respectively, W is the gate width, ϵ and ϵ_0 are the relative dielectric constant and the dielectric permittivity of the vacuum, respectively, μ is the electron mobility, v_{sat} is the saturation velocity, L is the gate length and d is the barrier thickness. Note that $n_{2DEG} = \epsilon \epsilon_0 V_{off} / ed \sim$ of $2.6 \times 10^{13} \text{ cm}^{-2}$, where e is the electron charge. Typical pinch-off voltages of these heterostructures are $\sim -7 \text{ V}$. $\epsilon \epsilon_0 / d$ corresponds to the gate capacitance C_0 ($\sim 0.006 \text{ F/m}^2$ for this heterostructure). This relation has two limiting cases, namely

$$\lim_{L \rightarrow 0} \frac{c_1}{L} \left[1 + \left\{ 1 + \frac{c_2}{L} \right\}^{1/2} \right]^{-2} = \frac{c_1}{c_2} \equiv \frac{2(V_G - V_{off})^2 W C_0 \mu}{2\mu(V_G - V_{off}) / v_{sat}} = (V_G - V_{off}) W C_0 v_{sat}$$

$$I_{DS,sat} = e n_{2DEG} W v_{sat} \quad (7.11)$$

i.e. all carriers in the channel move with the saturation velocity. This is the ultimate limit for ultra-narrow gate lengths and is indicated as horizontal line with 8 A/mm in Figure 7.5 (b). The other limiting case is when v_{sat} goes to infinity, then

$$\lim_{v_{sat} \rightarrow \infty} \frac{2(V_G - V_{off})^2 W \epsilon \epsilon_0 \mu}{Ld} \left[1 + \left\{ 1 + \frac{2\mu(V_G - V_{off})}{v_{sat} L} \right\}^{1/2} \right]^{-2}$$

$$= \frac{2(V_G - V_{off})^2 W \epsilon \epsilon_0 \mu}{Ld} \left[\frac{1}{4} \right]$$

$$I_{DS,sat} = \frac{(V_G - V_{off})^2 WC_0 \mu}{2L} \quad (7.12)$$

This result successfully describes the behavior of the saturation currents in GaAs based HEMT heterostructures [3], but fails by far for nitride HEMTs. In Figure 7.5 (b) therefore the behavior according Equation (7.10) assuming $V_G=0$ V, $V_{off}=-7$ V, $d=15$ nm, $v_{sat} \sim 2 \times 10^5$ m/s and a mobility of $1200 \text{ cm}^2/\text{Vs}$ at RT is shown as a function of the gate length L_g . The measured densities are a factor 4 lower than the values the model predicts.

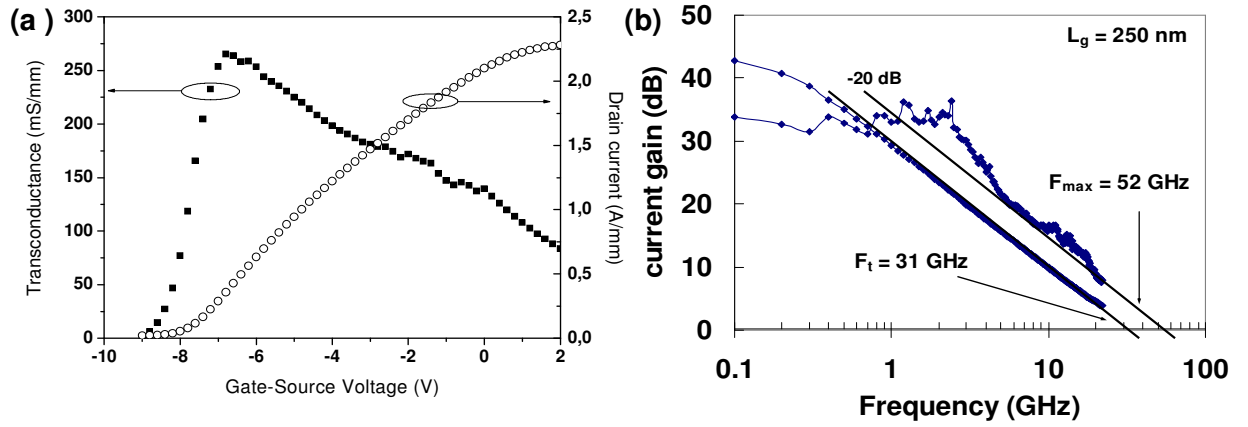


Figure 7.6 (a) I_{DS} versus V_{GS} at $V_{DS}=10$ V for a HEMT processed from an $\text{Al}_{0.85}\text{In}_{0.15}\text{N}(13\text{nm})/\text{AlN}(1\text{nm})/\text{GaN}/\text{sapphire}$ heterostructure with $L_g=0.25 \mu\text{m}$ and $W=50 \mu\text{m}$. As the V_{GS} increases electrons in the channel are depleted and current decreases consequently until a complete depletion under the gate. The transconductance according Equation (7.5) is also shown. The transconductance exhibits a peak-like feature at ~ -6 V. Subfigure (b) shows the respective current gain versus frequency for this device (Processing at Ulm University and measurements at IEMN).

Figure 7.6 (a) shows the drain-source current I_{DS} for a fixed drain-source voltage $V_{DS}=10$ V while gate voltage V_{GS} is varied between zero and the depletion voltage. The HEMT device is processed from an $\text{Al}_{0.85}\text{In}_{0.15}\text{N}(13\text{nm})/\text{AlN}(1\text{nm})/\text{GaN}/\text{sapphire}$ heterostructure with $L_g=0.25 \mu\text{m}$ and $W=50 \mu\text{m}$. As the V_{GS} increases electrons in the channel are depleted and current decreases consequently until a complete depletion under the gate. The transconductance according to Equation (7.5) is also shown. The transconductance exhibits a peak-like feature at ~ -6 V. This peak is related, as explained in Chapter 4, to the fact that the mobility for $V_{GS}=0$ V is strongly reduced by interface roughness related mechanisms. If the 2DEG is depleted the carriers are less confined at the interface (see Figure 5.6) and suffer less from these mechanisms resulting in a peak on the transconductance. At low 2DEG density, mobility decreases again due to scattering at ionized impurities, dislocation, etc. These strong scattering effects, which are related to the interface quality, are more pronounced than in other material systems [19] where interfaces are closer to atomic perfection.

Figure 7.6 (b) reports the respective current gain *versus* frequency for this device indicating a high F_{max} and F_t [15]. Figure 7.7 shows now the cut-off frequency f_T *versus* gate length L_g for the HEMT heterostructure discussed above. Measured values are taken from Ref. [15]. Full line shows behavior according to Equation (7.7) assuming a peak

7 Devices based on $\text{Al}_{1-x}\text{In}_x\text{N}/\text{AlN}/\text{GaN}$ heterostructures ($0.03 \leq x \leq 0.23$)

transconductance g_m of 265 mS/mm and a gate capacitance C_0 of 0.006 F/m². Small deviations might originate from neglecting any parasitic capacitances but describe the behavior correctly. All current-gain *versus* frequency curves were recorded under $V_{DS}=10$ V and $V_{GS}=-6.5$ V. We want to mention that recently the 100 GHz threshold was exceeded on this heterostructures grown on Si substrate with a L_g of 0.1 μm [20]. These heterostructures exhibited slightly higher transconductance g_m of 350 mS/mm with an only 10 nm thin $\text{Al}_{0.86}\text{In}_{0.14}\text{N}$ barrier.

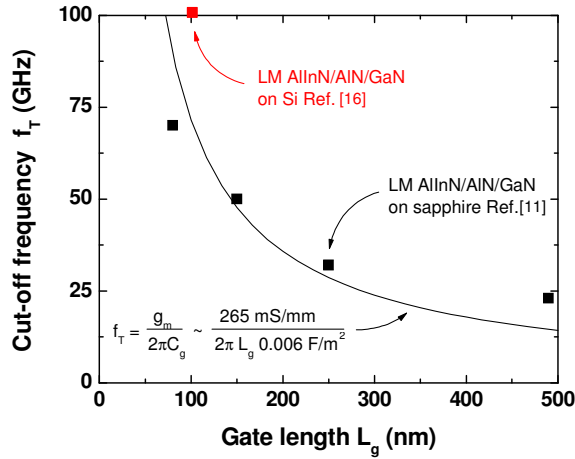


Figure 7.7 Cut-off frequency f_T versus gate length L_g for a HEMT processed from an $\text{Al}_{0.85}\text{In}_{0.15}$ (13 nm)/AlN(1 nm)/GaN/sapphire heterostructure. Measured values are taken from Ref. [15]. Full line shows behavior according to Equation (7.7) assuming a peak transconductance g_m of 265 mS/mm and a gate capacitance C_0 of 0.006 F/m². Small deviations might originate from neglecting any parasitic capacitances in the analysis. All current-gain *versus* frequency curves were recorded under $V_{DS}=10$ V and $V_{GS}=-6.5$ V. Additionally, record f_T obtained on Si substrates from Ref. [20] is indicated.

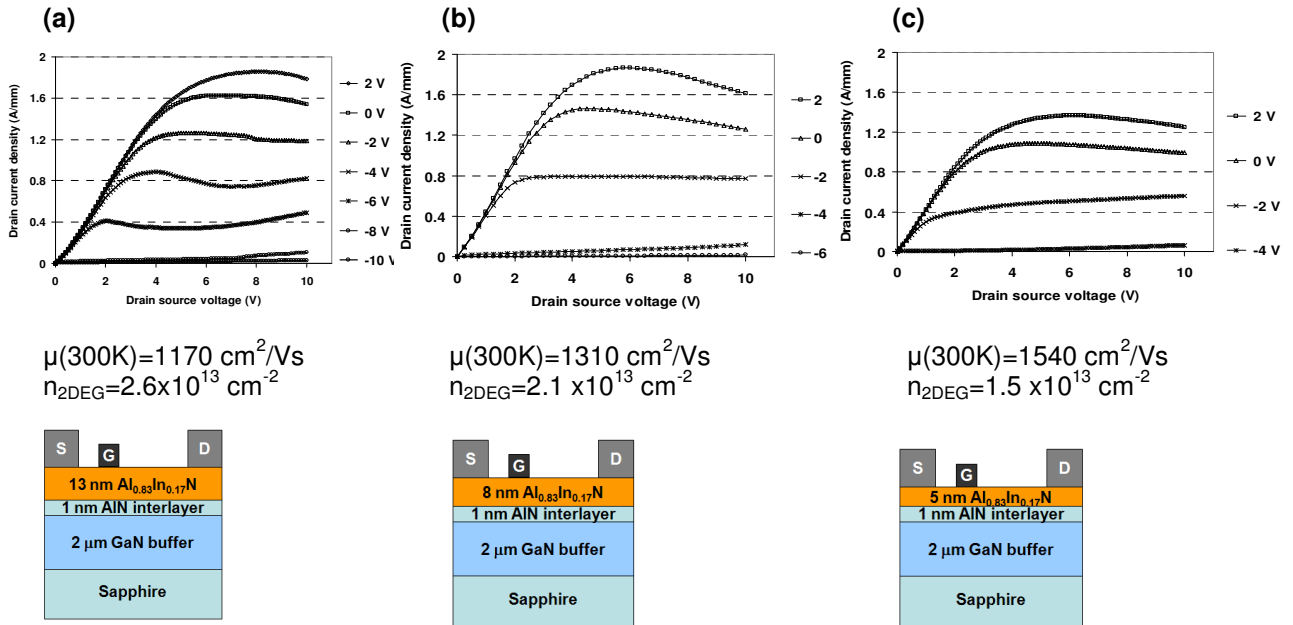


Figure 7.8 IV-characteristics of HEMT devices processed from $\text{Al}_{0.85}\text{In}_{0.15}\text{N}/\text{AlN}(1\text{ nm})/\text{GaN}/\text{sapphire}$ heterostructures for (a) 13 nm (b) 8 nm and (c) 5 nm AlInN thickness. RT electric properties are additionally given. $I_{DS,sat}$ decreases for $V_{GS}=0$ V towards thinner AlInN thickness. IV characteristics are taken from Ref. [21].

$\text{Al}_{0.85}\text{In}_{0.15}\text{N}/\text{AlN}(1\text{nm})/\text{GaN}/\text{sapphire}$ with different barrier thicknesses Now we focus on the dependence of the $I_{DS}(V)$ curves on the $\text{Al}_{0.85}\text{In}_{0.15}\text{N}$ barrier thickness for (a) 13 nm, (b) 8 nm and (c) 5 nm thick AlInN layer as depicted in Figure 7.8. The IV characteristics are taken from Ref. [21]. RT electrical properties are also given. 2DEG density and in-plane transport behave according to the discussion developed in chapters 4 and 5. All HEMT devices were processed with $W=50\text{ }\mu\text{m}$ and $L_g=0.25\text{ }\mu\text{m}$. The $I_{DS,sat}$ decreases for $V_{GS}=0\text{ V}$ towards thinner AlInN thickness. This behavior will be discussed in the next section.

Influence of the substrate In Figure 7.9 IV-characteristics of HEMT devices processed from $\text{Al}_{0.85}\text{In}_{0.15}\text{N}(10\text{nm})/\text{AlN}(1\text{nm})/\text{GaN}$ heterostructures grown on (a) sapphire (b) Si and (c) SiC substrates are given. RT electrical properties are also given. On all substrates CV curves are nearly perfectly identical (not shown here) and consequently the 2DEG densities are equal. Interestingly, similar transport properties are achieved for heterostructures grown on sapphire and on SiC. Structure on Si exhibits a lower mobility. This correlates also with the measured rms roughness displayed in Figure 3.5, *i.e.* heterostructures on SiC and sapphire exhibit similar rms of $\sim 0.2\text{ nm}$ while the rms of AlInN grown on Si is $\sim 0.3\text{ nm}$. Roughness values are consistent with literature values *e.g.* in Ref. [22]. This higher rms will therefore induce more interface roughness related scattering and will reduce therefore the mobility. According to Ref. [22] the rms can be improved by optimizing AlN layer growth conditions. Interestingly, the structure on SiC does not exhibit higher $I_{DS,sat}$ as one might expect from higher thermal conductivity. This will be revealed in the next section. On the other hand, the saturation current seems to be approximately proportional to the channel mobility as seen from the comparison of subfigure (a), (b) and (c).

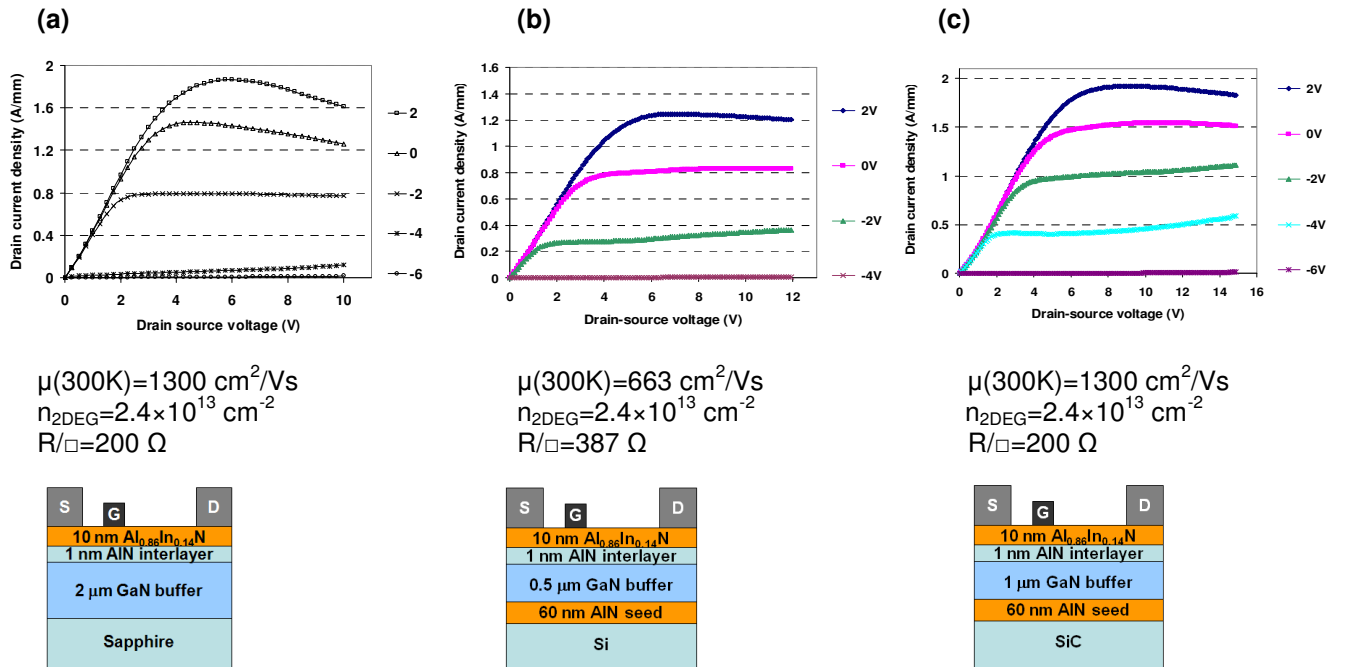


Figure 7.9 IV-characteristics of HEMT devices processed from $\text{Al}_{0.85}\text{In}_{0.15}\text{N}(10\text{nm})/\text{AlN}(1\text{nm})/\text{GaN}$ heterostructures grown on (a) sapphire (b) Si and (c) SiC substrates. RT electrical properties are additionally given. HEMT devices were processed with $W=50\text{ }\mu\text{m}$ and $L_g=0.25\text{ }\mu\text{m}$. (Processing at Ulm University)

7.2.2 Spatially resolved temperature profiling in $\text{AlInN}/\text{AlN}/\text{GaN}$ HEMT devices using $\mu\text{Photoluminescence}$

$\mu\text{Photoluminescence}$ (μPL) setup Many temperature analysis techniques in (nitride) HEMT devices rely on the well established Raman spectroscopy [23-25]. However, there is a severe drawback with this technique, namely the depth resolution. *e.g.* 1.5 micron is reported by the group of Kuball *et al.* [24]. Other groups report on the excitation with the 514.5 nm line of an Argon-ion laser [23]. Such large excitation wavelength results only in a poor depth resolution. This motivated us to probe a HEMT device under applied voltages by means of Micro-Photoluminescence (μPL). We spare here to discuss on the setup in detail. More information on this issue can be found in Refs. [26, 27]. Some key specifications are the spatial resolution, which is $\sim 0.25 \mu\text{m}$ (limited by the step width of the piezo actuator moving in the sample plane), the diameter of the exciting spot around $0.5 \mu\text{m}$ (depending on exciting wavelength and objective) and a spectral resolution of $\sim 0.01 \text{ nm}$. The μPL setup is schematically sketched in Figure 7.10. The advantage of this technique is the use of a short excitation wavelength, namely a 244 nm line of a continuous wave Ar⁺ laser frequency doubling unit.

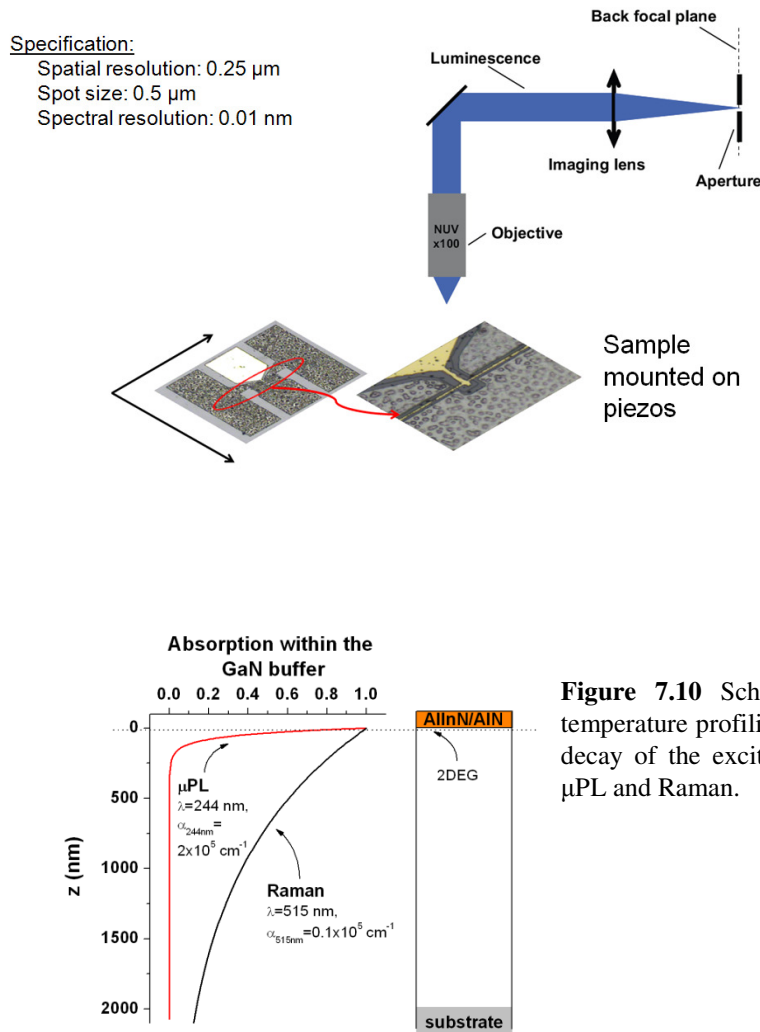


Figure 7.10 Schematic sketch of the μPL setup for temperature profiling of a HEMT device. Additionally, the decay of the exciting light within the GaN is shown for μPL and Raman.

The absorption coefficient of GaN at 244 nm is around $2 \times 10^5 \text{ cm}^{-1}$ [28], *i.e.* the length where the absorption drops to $1/e$ is ~ 50 nm. This makes the luminescence probe quite sensitive to the channel region compared to the low depth resolution of the Raman technique.

Spectra at a fixed position under non-equilibrium condition To increase the μPL signal from the AlInN layer, measurements displayed in Figure 7.11 were performed on a 100 nm thick AlInN barrier sample processed in an ungated TLM contact configuration with a drain-source distance of 6.5 μm . As can be seen from Figure 7.11 there is only a marginal peak shift of ~ 50 meV of the AlInN alloy luminescence when the drain-source voltage varies from 0 to 20 V. On the other hand, the GaN exciton energy emission decreases by ~ 350 meV for the same voltage range. It is of course straightforward to ascribe this red-shift to heating of the device. Using the empirical Varshni formula $E_g(T) = E_g(0) - \alpha T^2/(\beta + T)$ (as already introduced in Chapter 1) with the parameters $\alpha = 0.94$ meV/K, $\beta = 791$ K and $E_g(0) = 3.492$ eV for GaN [29] the heating of the channel can be estimated to be as high as 600 K at 20 V. The GaN exciton peak is also strongly broadened due to the larger phonon occupation probability at higher temperatures. It is worth mentioning that the empirical Varshni formula includes several mechanisms which contribute to the bandgap decrease such as phonon occupation and lattice constant expansion [30]. Further, spatially resolved μPL spectra clearly exhibit two longitudinal-optical (LO) phonon replicas with an energy separation ~ 92 meV for low drain source voltages < 5 V (not shown here). The ratio of the 1LO and 2LO phonon replica intensities is known to give a measure of the temperature [31]. Unfortunately, for higher voltages these replicas are too low in intensity and cannot be distinguished anymore. Notice that strong electric fields are always present throughout the heterostructure: under unbiased conditions in the growth direction mainly at the position where the 2DEG is located and under applied voltages additionally in-plane across the channel.

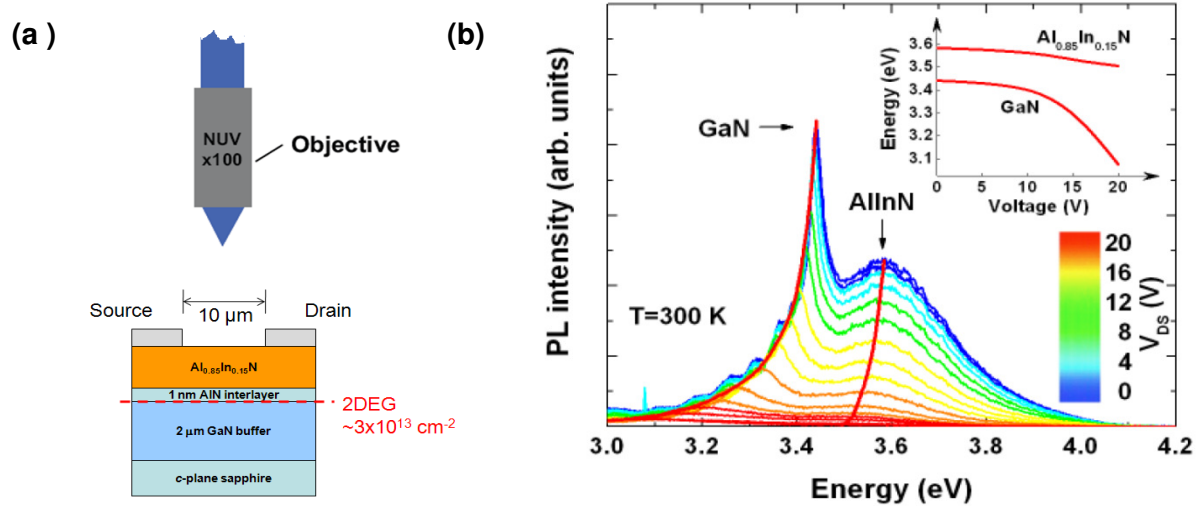


Figure 7.11 (a) Schematically sketched situation for a fixed position of the excitation spot within a non-gated TLM device with a drain-source distance of 6.5 μm processed from an $\text{Al}_{0.85}\text{In}_{0.15}\text{N}(100\text{nm})/\text{AlN}(1\text{nm})/\text{GaN}/\text{sapphire}$ heterostructure. (b) A barrier thickness of 100 nm AlInN was chosen in order to get a high AlInN-related μPL intensity. Under high applied voltages the GaN related exciton energy shift is ~ 7 times larger than that of the AlInN barrier. Lines are guides to the eyes (see also inset).

Since the GaN exciton is not confined within the bulk-like buffer layer the field related red-shift of the exciton energy should not exceed 10% of the exciton binding energy [32]. Thus, if

the Varshni parameters are known, the accuracy of the temperature determination is limited by electric field effects (± 8 K) and the spectral resolution (± 0.3 K) according to Equation (1.2). For temperatures above RT, the thermal energy $k_B T$ is larger than the bulk GaN exciton binding energy (~ 27 meV). Furthermore, the electric field is larger than 10 kV/cm under biased conditions. Such high electric fields significantly broaden or even destroy the excitonic resonance due to field ionization. These effects can therefore lead to a dissociation of GaN excitons. However, even in situations where excitons are dissociated to form an electron-hole plasma, this would only induce a minor correction to the transition energies in the order of a few meV whereas the thermally induced band gap reduction amounts up to ~ 500 meV.

Line scans across gated TLMs under non-equilibrium condition Figure 7.12 (a) exhibits an optical microscope image of the HEMT-like gated TLM structure investigated using μPL . The drain-source distance varies from 80 down to 5 μm while the gate length decreases from 20 down to 1.5 μm . The gate width is constant 200 μm . Figure 7.12 (b) shows the respective drain-source current I_{DS} characteristics as a function of applied drain-source voltage V_{DS} . Further details on the electrical performance and characteristics of those devices can be found in Refs. [15, 16]. Self-heating is already obvious from the strong non-linear behaviour of I_{DS} for high V_{DS} values. However, it is not straightforward to estimate the temperature from the I_{DS} curve as some authors attempt (e.g. Simms et al. [24]). For the sake of clarity, we restrict ourselves to line scans across the channel. Figure 7.13 (b) displays the temperature profiles obtained from the μPL line scans across the channel for the different channel and gate lengths according to Figure 7.12 (a) as a function of the applied drain-source voltages in the range 0 to 20 V. In nitride 2DEG channels, the emission of longitudinal optical (LO) phonons is the main energy dissipation mechanism for high-energy electrons [33]. Since the LO-phonon decay time exceeds by far the LO-phonon emission time by hot electrons, an accumulation of nonequilibrium phonons takes place. Thus, the number of excited nonequilibrium phonons depends on the 2DEG density in the channel and the mean free path length between phonon excitations [34]. Furthermore, the temperature profiles are asymmetric with a higher temperature observed on the gate-drain side which is expected from the electric field distribution and is also found using micro Raman spectroscopy [24]. The highest temperature we measured on this sample was 1130 K for the 1.5 μm gate length device operating at 20 V. Since the melting point of the gold gate metallization is at 1337 K degradation effects might occur at higher voltages or shorter gate lengths.

According to Ref. [30] the band gap variation above RT is mainly due to the LO phonon term. Therefore, the estimated temperature might reflect the LO phonon temperature. Nevertheless, this is the relevant parameter for 2DEG electron scattering and hence the strong decrease of $I_{DS,sat}$. Besides, the LO phonons are also known to quickly decay, in a reversible manner, into acoustic phonons according to $\text{LO} \leftrightarrow \text{TO} + \text{LA}_1$ and $\text{TO} \leftrightarrow \text{LA}_2 + \text{LA}_3$ with lifetimes of LO and TO phonons of a few ps [35]. Acoustic phonons have a large group velocity and are thus assumed to be in thermodynamic equilibrium so that they are used to define the lattice temperature [36]. Therefore the classical temperature of the lattice defined by the acoustic phonons might be slightly lower than the LO phonon temperature.

Let us comment on the lowest GaN μPL energy of 2.94 eV found in the drain-gate region of the 5 μm device at 20 V that would correspond to a very high temperature of 1130 K not found in AlGaIn/GaN HEMT device [24]. We must keep in mind that the extremely high 2DEG density of $2.6 \times 10^{13} \text{ cm}^{-2}$ which is twice the amount of standard AlGaIn/GaN HEMTs, will significantly affect the rate of created hot phonons. Together with the poor

thermal conductivity of 26 W/mK of the sapphire substrate, which is only one tenth the thermal conductivity of SiC usually used for high power devices. This will thus lead to larger temperatures within the GaN buffer compared to AlGaN/GaN devices.

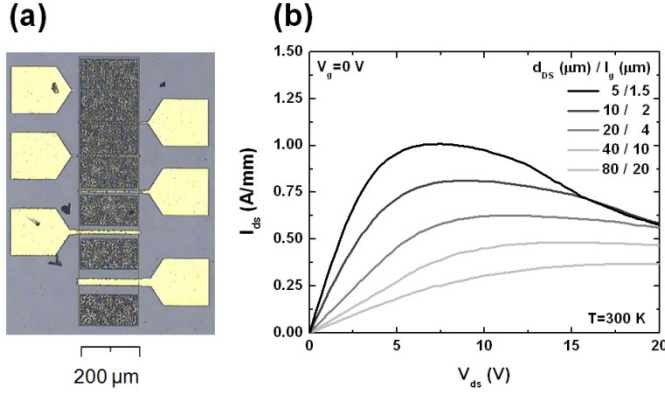


Figure 7.12 (a) Gated TLM pattern processed from an $\text{Al}_{0.85}\text{In}_{0.15}\text{N}(13 \text{ nm})/\text{AlN}(1 \text{ nm})/\text{GaN}$ heterostructure grown on *c*-plane sapphire. (b) Corresponding I-V characteristics. Note that the 2DEG density at 300 K is $2.6 \times 10^{13} \text{ cm}^{-2}$ while the RT mobility of this specific sample is only $900 \text{ cm}^2/\text{Vs}$. Consequently the $I_{DS,\text{sat}}$ is lower compared to the record samples.

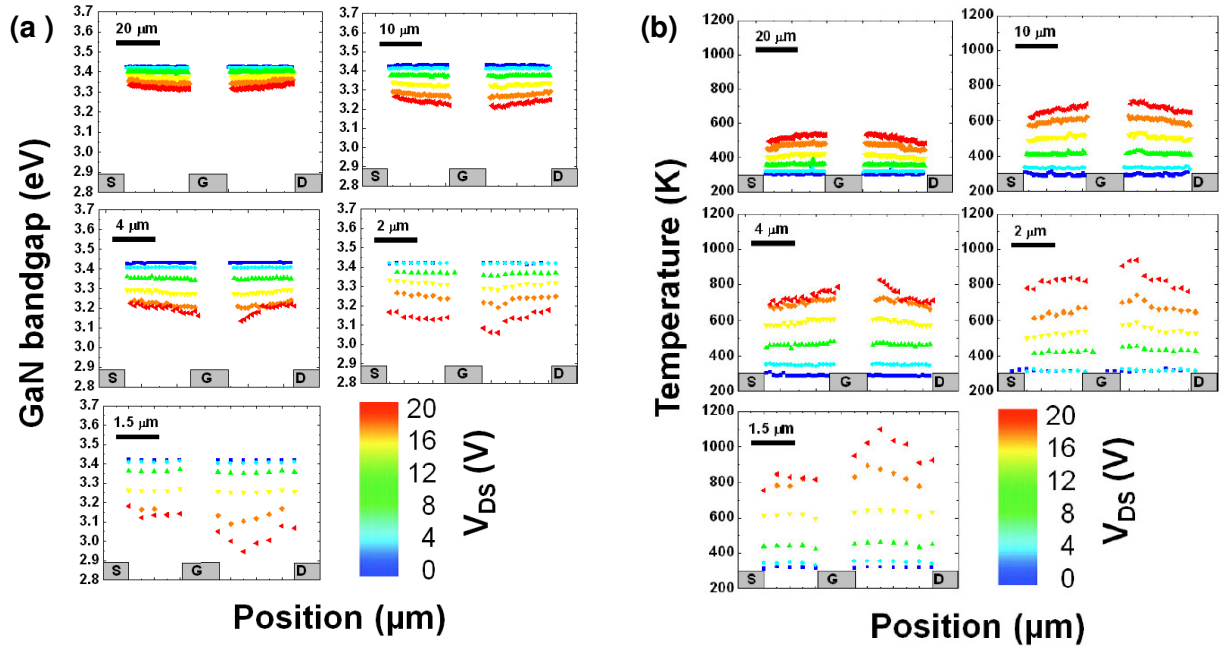


Figure 7.13 (a) Local transition energy within the GaN across the channel deduced from μPL line scans for a gated TLM processed from an $\text{Al}_{0.85}\text{In}_{0.15}\text{N}(13 \text{ nm})/\text{AlN}(1 \text{ nm})/\text{GaN}$ heterostructure with a 2DEG density of $2.6 \times 10^{13} \text{ cm}^{-2}$. Profiles are shown for a gate length varying between 20 and 1.5 μm and for applied drain-source voltages I_{DS} in the 0-20 V range. (b) Temperature profiles deduced from subfigure (a) using Varshni's relation.

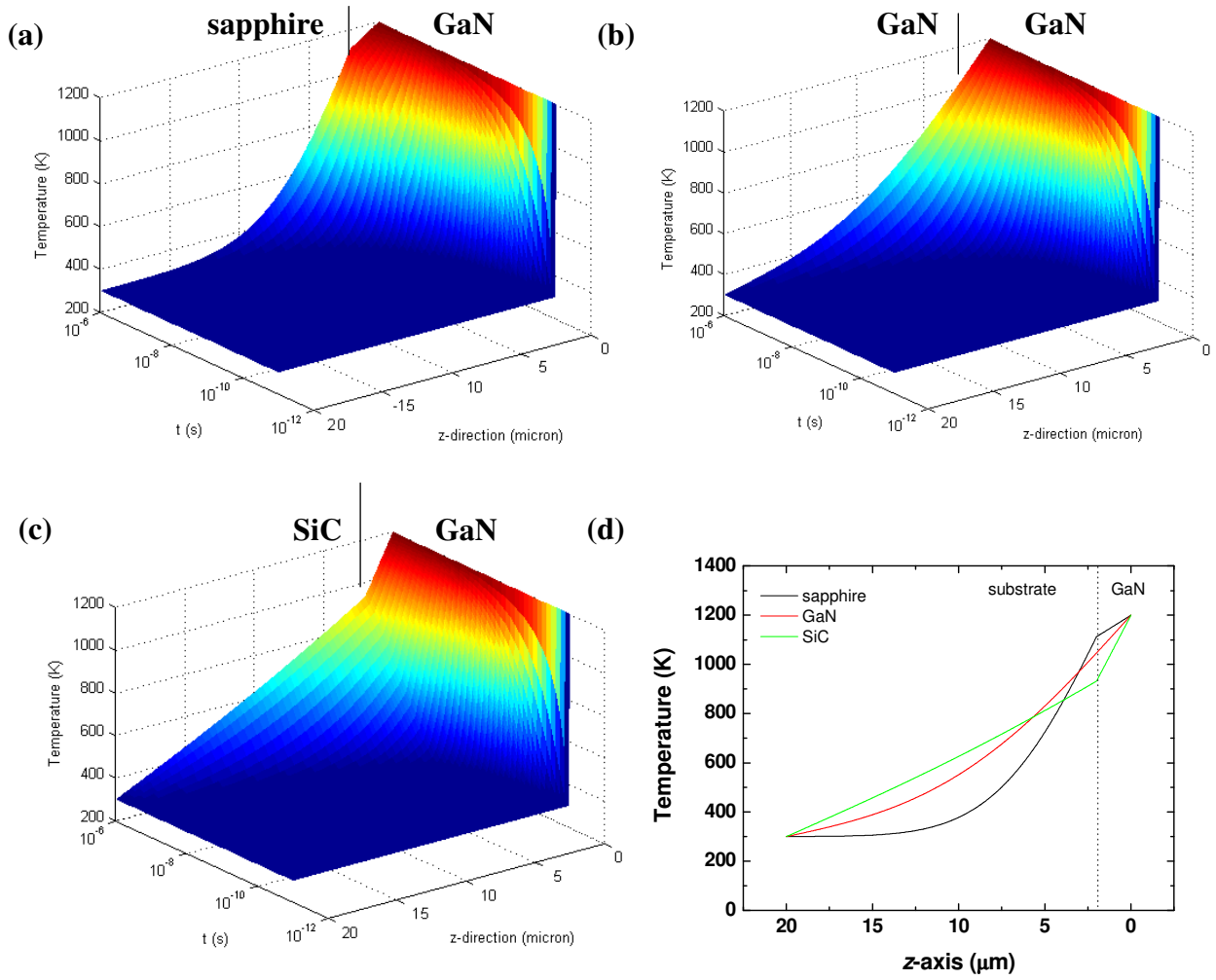


Figure 7.14 Solution of the time dependent 1D anisotropic heat equation with Neumann boundary conditions (*i.e.* vanishing flux over boundaries) for (a) 2 μm GaN on sapphire, (b) 2 μm GaN on GaN and (c) 2 μm GaN on SiC. Initial temperature profile is assumed to be Gaussian located near the surface with a maximum of 1200 K. Time scale ranges from 1 ps to 1 μs . Subfigure (d) shows the cross-section of (a)-(c) at $t = 1 \mu\text{s}$.

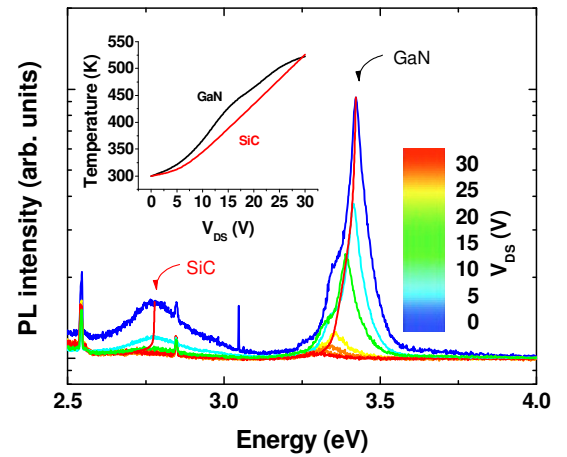
Choice of substrate However, the question arises how the choice of the substrate influences this measurement technique and in fact all techniques relying on optical excitation. On the other hand, if there would be a strong temperature gradient in the GaN buffer this would also have a strong influence on the measured optical properties, since then, the bandgap, the refractive index and the absorption become dependent on the depth. The question of temperature distribution can be treated under the simplest assumptions by solving the 1D heat equation which is given as $u_t(x, t) = k(x) u_{xx}(x, t)$, where u is the unknown spatial and time dependent temperature dependence and k is the thermal diffusivity which is defined as $k = \kappa / c_p \rho$ with κ the thermal conductivity, c_p the heat capacity and ρ the material density. The thermal diffusivities are $k_{\text{GaN}} = 0.43 \text{ cm}^2/\text{s}$, $k_{\text{sapphire}} = 0.13 \text{ cm}^2/\text{s}$, $k_{\text{SiC}} = 1.4 \text{ cm}^2/\text{s}$ and $k_{\text{Si}} = 0.8 \text{ cm}^2/\text{s}$ [37]. Then the 1D anisotropic heat equation has to be solved *i.e.* including the spatial dependence of the thermal diffusivity and together with appropriate boundary conditions which are in the simplest case of the Neumann type (vanishing flux over the boundaries), *i.e.*

$u_x(L,t)=0$, $u_x(R,t)=0$, $u(L,t)=T_L$ and $u(R,t)=T_R$, where L , T denotes the coordinate for the left and the right boundary, respectively and T_L , T_R the temperature at the left and the right boundary, respectively. However, the real situation is livelier since there is definitely heat flux propagating through the heterostructure down to the bottom of the substrate for samples grown on SiC resulting in a temperature above RT. However such effects require a treatment with non-local boundary condition resulting in integral equations. Additionally, other effects including heat generation terms or air-convection could be considered in a future work. Figure 7.14 shows the solution of the time dependent 1D anisotropic heat equation with Neumann boundary conditions for (a) 2 μm GaN on sapphire, (b) 2 μm GaN on GaN and (c) 2 μm GaN on SiC. Initial temperature $u(L,t=0)$ profile is assumed to be a constant, namely 300 K over the length of the 1D simulation domain. Boundary conditions during time evolution are constant as mentioned above, namely $T_L=300$ K and $T_R=1200$ K. Time scale ranges from 1 ps to 1 μs . In subfigure (a) there is only a low temperature gradient from the surface to the interface with the sapphire, with a difference of $\Delta T \sim 100$ K. It quickly drops within the sapphire, *i.e.* the heat is as expected not dissipated in the substrate but trapped in the GaN epilayer. For structures grown on SiC (c) the temperature difference between surface and GaN/substrate interface is much larger $\Delta T \sim 300$ K and much more heat is dissipated in the substrate. Consequently, as expected from the thermal diffusivities, a pure GaN bulk layer in subfigure (b) mediates between these two cases. Subfigure (d) shows the cross-section of $u(x,t)$ for (a)-(c) at $t=1$ μs .

Now we briefly want to summarize a similar measurement as in Figure 7.13 but this time the identical structure is grown on SiC. Therefore Figure 7.15 shows the μPL spectra in the vicinity of the drain-sided gate contact with $L_g=10$ μm in dependence on V_{DS} for a $\text{Al}_{0.85}\text{In}_{0.15}\text{N}(13\text{nm})/\text{AlN}(1\text{nm})/\text{GaN}/\text{SiC}$ heterostructure. Contrary to the sapphire substrate the SiC substrate is also excited. This is likely a secondary effect stimulated by the radiative recombination in the GaN. Inset shows the temperature calculated from Varshni's formula from the thermally induced bandgap shift for GaN and SiC. Varshni parameters for 6H-SiC are $\alpha_{\text{SiC}}=0.65$ meV and $\beta_{\text{SiC}}=1200$ K [37]. The absorption coefficient for SiC at 244 nm is $\sim 0.6 \times 10^5 \text{ cm}^{-1}$, *i.e.* the intensity of absorbed light should drop to 50% at ~ 200 nm depth within the SiC substrate.

Figure 7.15 (a) μPL spectra in the vicinity of the drain-sided gate contact with $L_g=10$ μm and $d_{DS}=40$ μm in dependence on V_{DS} for an $\text{Al}_{0.85}\text{In}_{0.15}\text{N}(13\text{nm})/\text{AlN}(1\text{nm})/\text{GaN}/\text{SiC}$ heterostructure. Contrary to heterostructures grown on sapphire or Si also a luminescence response from the SiC substrate can be observed at 2.78 eV. The SiC is likely excited from the GaN related recombination. Inset shows the temperature calculated from Varshni's formula from the thermally induced bandgap shift.

The results for the measurements on the TLMs processed from the $\text{Al}_{0.85}\text{In}_{0.15}\text{N}(13\text{nm})/\text{AlN}(1\text{nm})/\text{GaN}$ heterostructures on sapphire and SiC are summarized in Figure 7.16. Mean GaN temperatures *versus* V_{DS} and the respective normalized GaN related μPL intensities are shown for the 5 different d_{DS} ranging from 5 μm to 80 μm for sapphire substrate in subfigure (a) and SiC substrate in subfigure (b).



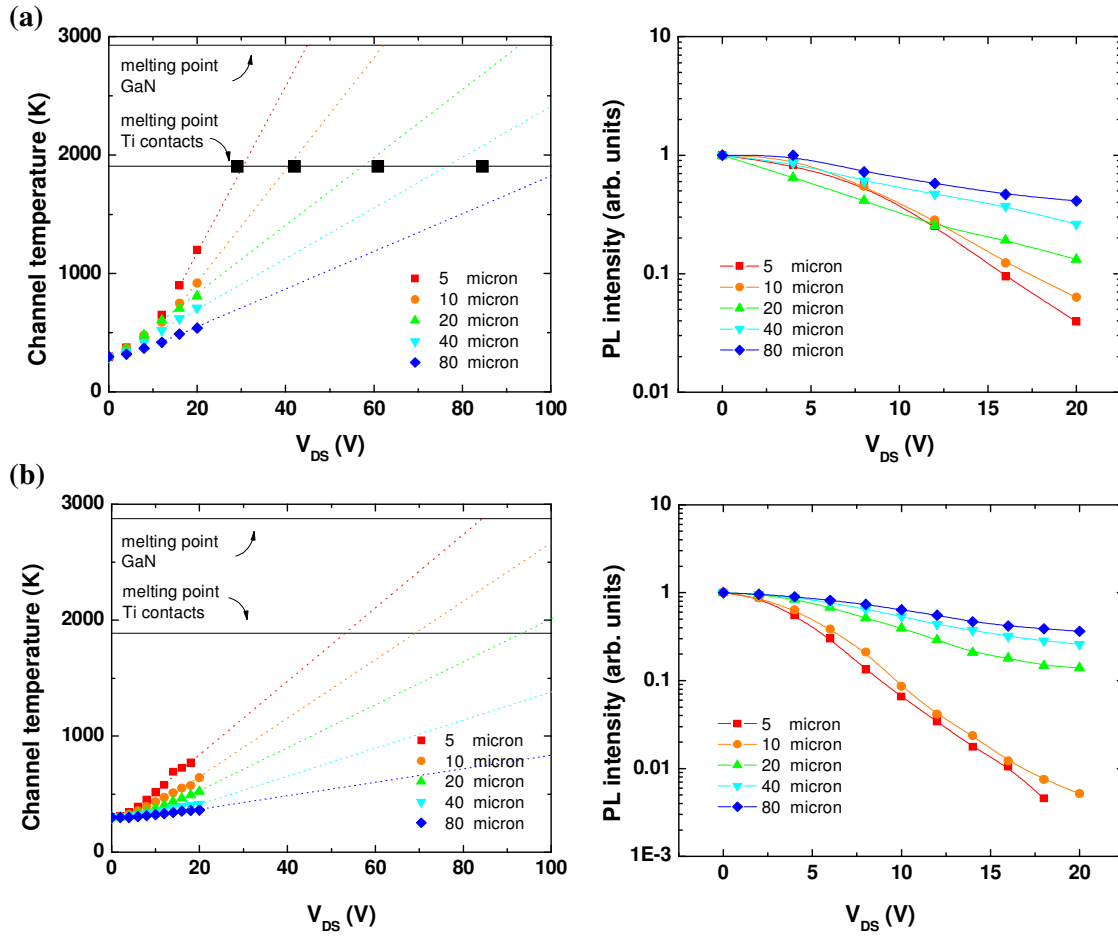


Figure 7.16 Mean GaN temperatures *versus* V_{DS} and the respective normalized GaN related μPL intensities for the 5 different d_{DS} for $\text{Al}_{0.85}\text{In}_{0.15}\text{N}(13\text{nm})/\text{AlN}(1\text{nm})/\text{GaN}$ heterostructures on sapphire substrate in subfigure (a) and SiC substrate in subfigure (b). Experimental contact breakdown voltage is indicates as black square.

From the comparison of the μPL measurement in Figure 7.16 four important points can be highlighted:

i) The mean temperature of 1 μm GaN on SiC is only 2/3 that of GaN on sapphire for a given V_{DS} (*e.g.* ~ 750 K in the former and ~ 1150 K in the latter case for a $d_{DS}=5$ μm and at $V_{DS}=20$ V).

ii) The temperature in the SiC is $\sim 30\%$ lower than that in 2 μm GaN (*e.g.* ~ 125 $^{\circ}\text{C}$ in the former and $\sim 175^{\circ}\text{C}$ in the latter case for a $L_g=10$ μm and at $V_{DS}=20$ V according to Figure 7.15).

iii) Results are in good agreement with general trends obtained from the 1D heat equation.

iv) For GaN on sapphire, heat is mainly trapped in GaN layer resulting in a very low gradient. Therefore the estimated temperature will be close to the true channel temperature even if the luminescence response would originate from a certain depth within the GaN away from the channel. The situation for GaN on SiC is opposite. A strong temperature gradient in growth direction should be present under applied voltages. If the luminescence response is

averaged over a large depth range then it will consequently lead to an averaged and lower temperature.

Thermally induced breakdown However this strong heating has a serious impact on the device performance and can even provoke phase transition of the device constituent materials. Therefore beside the breakdown due to the formation of avalanche electrons at a critical field according to Equation (2.3) there should exist also a breakdown mechanism due to achieving a critical electric field for creating sufficient heat to melt contacts or even the GaN. Contrary to the avalanche process [38], the thermally induced breakdown is caused only by the 2DEG electrons. Table 7.1 summarizes the melting points of different materials used in HEMT devices. Au diffusion after long-term operation has already been demonstrated [39]. On the other hand, the current flow should occur mainly in the channel not under contacts. Additionally they are separated by the barrier which might have similar thermal diffusivity as the SiC substrate, namely $k_{\text{AlN}} = 1.47 \text{ cm}^2/\text{s}$, *i.e.* temperature of contacts is probably lower than that of the channel. Nevertheless, beside the gate contact it is the weakest spot of the device. Therefore we assume as the ultimate criterion of thermally induced breakdown the melting point of the Ti, which forms the junction with the semiconductor barrier, although Al and Ni exhibit a lower melting point. We want to point out the breakdown also occurs in ungated TLMs. However, since the highest temperatures occur near the gate its metallization will be affected first, but since the drain and source contacts are crucial for maintaining current flow they should be optimized with priority.

Going back to Figure 7.16 one finds that the mean temperature in the channel scales approximately linear for large V_{DS} . This behavior will be discussed in the next section. Unfortunately, the GaN related μPL intensity drops quickly as can be seen from the right column in Figure 7.16 for both substrates. Therefore it is very difficult to resolve the spectra for large V_{DS} . We extrapolate linearly the V_{DS} indicated by the dotted colored lines in Figure 7.16. The intercept with the horizontal line at $\sim 1900 \text{ K}$ marks therefore the breakdown of the device due to contact destruction. An example of a $5 \mu\text{m}$ device after breakdown is shown in Figure 7.17 which is indeed achieved at a $V_{DS} \sim 30 \text{ V}$ on sapphire in good agreement with the prediction. On SiC however this breakdown is shifted to higher V_{DS} due to the superior thermal dissipation through the substrate. For the $5 \mu\text{m}$ device the breakdown should occur at $V_{DS} \sim 50 \text{ V}$ on SiC.

Material	Melting point (°C)
GaN	2500
Ni	1450
Al	660
Ti	1660
Au	1065

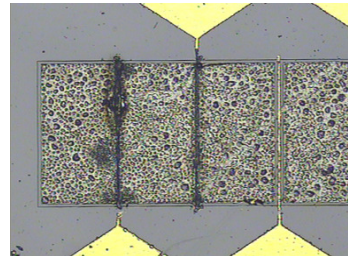


Table 7.1 Melting point of $\text{AlInN}/\text{AlN}/\text{GaN}$ HEMT constituent materials.

Figure 7.17 Thermal induced breakdown of a $5 \mu\text{m}$ gated TLM device on sapphire after applying drain-source voltages $V_{DS} > 30 \text{ V}$. This is in good agreement with the prediction according to Figure 7.16.

7.2.3 Field *versus* phonon limited current saturation mechanisms

As we demonstrated in the last subsection there are strong heating effects. The aim of this subsection is to discuss the origin and consequences of the heating which explains the large difference in expected and measured saturation currents. It will be shown that an increase of the carrier density will not necessarily result in an increase of the saturation currents. Beside it will be demonstrated that the influence of the substrate is less than many authors believe.

Figure 7.18 (a) illustrates again the electric field distribution within the 2D channel. Note that according to the model Equation (7.10) it is distinguished between a region where the current is mobility limited and a region where the electrons reach the saturation velocity near the drain-handled edge of the gate contact. In subfigure (b) expected saturation currents in dependence on 2DEG density are given. Black lines are obtained according to Equation (7.11) (all 2D electrons move with the saturation velocity) and red lines according to Equation (7.10) (two-piece model for 0.1 and 1 micron gate lengths and a RT mobility of $1200 \text{ cm}^2/\text{Vs}$) *versus* 2DEG density. Additionally, experimental saturation currents are given: blue squares for AlGaIn/GaN [14], green for $\text{AlInN}/\text{AlN}/\text{GaN}$ [21] and red for AlN/GaN [40]. Apparently, measured saturation currents are far below the expected values from the two-piece model.

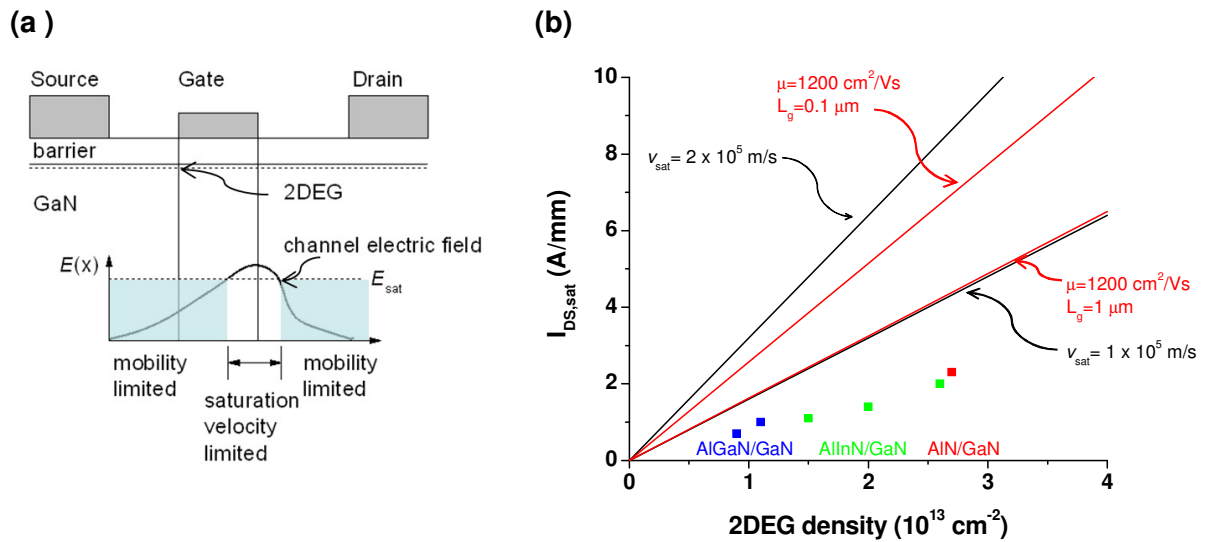


Figure 7.18 (a) Schematic sketch of the electric field distribution within the 2D channel. Note that according to the model Equation (7.10) it is distinguished between a region where the current is mobility limited and a region where the electrons reach the saturation velocity near the drain-handled edge of the gate contact. (b) Saturation currents according to Equation (7.11) (all 2D electrons move with the saturation velocity=black lines) and according to Equation (7.10) (two-piece model for 0.1 and 1 micron gate length and a RT mobility of $1200 \text{ cm}^2/\text{Vs}$ =red lines) *versus* 2DEG density.

At this point we will give a brief deviation for a qualitative estimation of the heat developed in the channel region. The crucial point for understanding the heat effect is to relate the number of created phonons (=number of electrons reaching the phonon energy at a given electric field in a fixed volume) by the 2D electrons with the volume covered by this electrons and the number of available phonons in this volume.

$$V_{2DEG} = FWHM_{\Psi_{2DEG}(z)} \times W \times d \quad (7.13)$$

where V_{2DEG} is the volume covered by the 2DEG. W is the width of the volume in the direction parallel to the contacts, d is the length of the volume in the direction of the electric field and for the z -extension the FWHM of the 2D wavefunction Ψ_{2DEG} is assumed, which behaves according to Figure 5.6 as $FWHM_{\Psi_{2DEG}(z)} = 0.9 / \sqrt{n_{2DEG}}$. This is an important fact because at higher 2DEG densities the 2DEG is stronger localized, *i.e.* covers less GaN unit cells, therefore one expects stronger heating effects.

$$\langle n_{LO, \max} \rangle = 2 \times \frac{V_{2DEG}}{V_{unitcell}} \quad (7.14)$$

$\langle n_{LO, \max} \rangle$ gives the maximum number of available phonons in the volume covered by the 2D electrons. The factor 2 arises from the fact that 2 LO phonons are available per unit cell [41]. The unit cell volume $V_{unitcell}$ is given as

$$V_{unitcell} = \frac{\sqrt{3}}{2} a^2 c \quad (7.15)$$

The Bose-Einstein distribution function as introduced above reads as

$$\langle n_{LO}(T) \rangle = \frac{\langle n_{LO, \max} \rangle}{\exp\left(\frac{\omega_{LO} \hbar}{k_B T}\right) - 1} \quad (7.16)$$

The creation of phonons *via* electron-phonon interaction was already discussed by Shockley in 1951 for Silicon [34]. The mean free path l_{MFP} for a given electric field E depends in such a condition only on the energy of the LO phonon. The number of how often a single electron gains this LO energy when travelling through a length d (in field and current direction) and with constant electric field E is $\sim 11 \cdot d \cdot E$.

$$\begin{aligned} a &= \frac{e}{m^*} \cdot E \\ a &= \left(v_{final}^2 - v_{initial}^2 \right) / 2 \cdot l_{MFP} \\ v_{final} &\approx \sqrt{(\omega_{LO} \cdot \hbar) \cdot 2 / m^*} & v_{initial} &\approx 0 \\ l_{MFP} &= \frac{\omega_{LO} \cdot \hbar}{e \cdot E} \\ \langle n(E) \rangle &= \frac{d}{l_{MFP}} = \frac{d \cdot e \cdot E}{\omega_{LO} \cdot \hbar} \approx 11 \cdot d \cdot E \end{aligned} \quad (7.17)$$

7 Devices based on $\text{Al}_{1-x}\text{In}_x\text{N}/\text{AlN}/\text{GaN}$ heterostructures ($0.03 \leq x \leq 0.23$)

This has to be multiplied according to Equation (7.18) with all available electrons in the volume. Equation (7.19) defines then the actual temperature as the sum of excited phonons at 300 K plus the excited phonons due to the acceleration in the electric field.

$$\langle n(E) \rangle_{V_{2DEG}} = n_{2DEG} \times W \times d \times \langle n(E) \rangle = n_{2DEG} \times W \times d^2 \times 11 \cdot E \quad (7.18)$$

$$\langle n_{LO}(T) \rangle = \langle n(E) \rangle_{V_{2DEG}} + \langle n_{LO}(300K) \rangle \quad (7.19)$$

Then the above Equation (7.19) can be resolved for the temperature yielding

$$T = \frac{\omega_{LO} \hbar / k_B}{\ln \left[\frac{11 \cdot n_{2DEG} \cdot d \cdot E + \langle n_{LO, \max} \rangle \cdot FWHM \Psi_{2DEG}(z)}{11 \cdot n_{2DEG} \cdot d \cdot E + \langle n_{LO}(300K) \rangle \cdot FWHM \Psi_{2DEG}(z)} \right]} \quad (7.20)$$

Note that d in the above derivation was introduced as an arbitrary scaling parameter which can be fixed with data from Figure 7.13 and Equation (7.20) yielding a characteristic length which can be roughly estimated to be ~1 micron. A deeper understanding beyond this simple model requires than the consideration of the electron-phonon interaction and a detailed analysis of the spatial distribution of the phonon population and related decay processes. The evaluation of the LO limited mobility $\mu(T) = \mu_0 \cdot [\exp(\omega_{LO} \hbar / k_B T) - 1]$ at the true local temperature yields the actual reduced mobility

$$\mu(E, n_{2DEG}) = \mu_0 \cdot \left[\frac{\langle n_{LO, \max} \rangle \cdot FWHM \Psi_{2DEG}(z)}{11 \cdot n_{2DEG} \cdot d \cdot E + \langle n_{LO}(300K) \rangle \cdot FWHM \Psi_{2DEG}(z)} \right] \quad (7.21)$$

where μ_0 is a constant which is defined as $\mu_0 = \mu_{300K} / (\exp(\omega_{LO} \hbar / k_B \cdot 300K) - 1)$. As μ_{300K} is the mobility at RT, e.g. $\mu_{300K} = 1200 \text{ cm}^2/\text{Vs}$ then $\mu_0 = 40$. This expression can now be plugged back in Equation (7.10) to replace the static RT mobility by the mobility Equation (7.21) which includes field and 2DEG density dependent mobility decrease.

Consequences At this point we want to demonstrate the consequences of phonon induced channel heating. Since the effect is of course more pronounced for small gate length we assume for instance a gate length of $d_{DS} = 5 \text{ } \mu\text{m}$ and $L_g = 1.5 \text{ } \mu\text{m}$. Then Equation (7.20) evaluates the temperature as a function of the local 2DEG density and the lateral electric field E . E is roughly estimated by V_{DS}/d_{DS} , which however seems to be a good approximation at least for ungated devices as can be seen from self-consistent calculations (Figure 7.27). The result is shown in Figure 7.19. For a given 2DEG density, e.g. $n_{2DEG} = 2.6 \times 10^{13} \text{ cm}^{-2}$, the calculated temperatures match nicely the experimental ones if compared with Figure 7.13. Typical AlGaIn/GaN 2DEGs exhibit 2DEG densities in the order $1.0 - 1.5 \times 10^{13} \text{ cm}^{-2}$, leading therefore to temperatures in the range from 600 to 800 K. These values are indeed found with Raman spectroscopic methods [23].

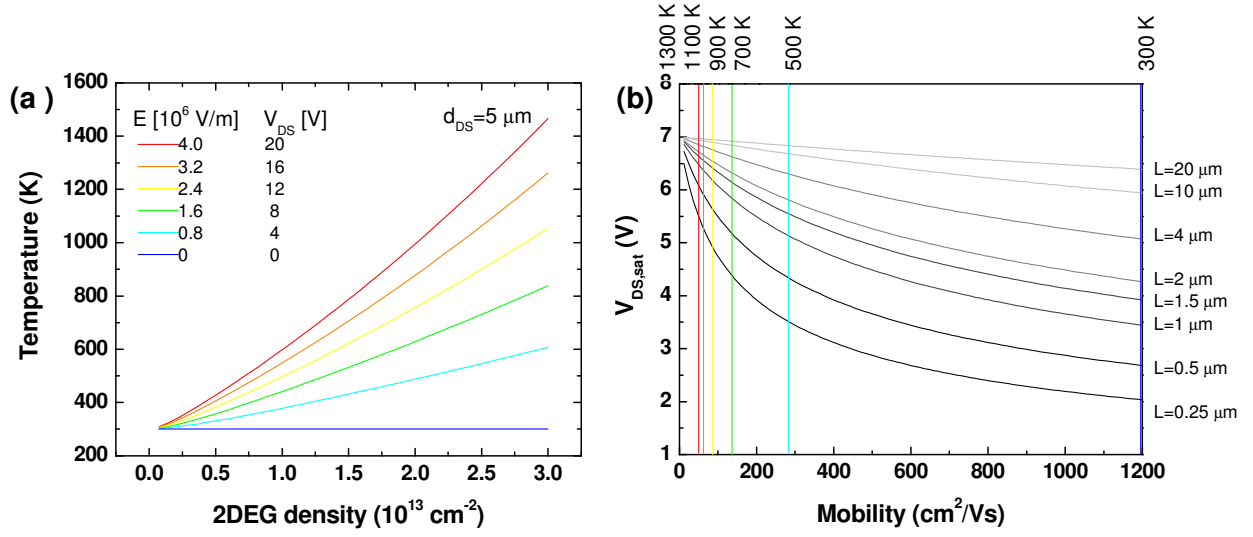


Figure 7.19 (a) Temperature *versus* the local 2DEG density and the lateral electric field E . E is approximated by a V_{DS}/d_{DS} where d_{DS} is the drain-source distance $\sim 5 \mu\text{m}$. For a given 2DEG density, *e.g.* $n_{2DEG} = 2.6 \times 10^{13} \text{ cm}^{-2}$, the calculated temperatures matches the experimental ones compared with Figure 7.13. (b) The voltage point where the I_{DS} curve becomes saturated, *i.e.* $V_{DS,sat}$ in dependence on gate length L_g and mobility for an $\text{Al}_{0.85}\text{In}_{0.15}\text{N}(13\text{nm})/\text{AlN}(1\text{nm})/\text{GaN}$ heterostructure with a 2DEG density of $2.6 \times 10^{13} \text{ cm}^{-2}$. The temperatures are assigned to the mobilities according to $\mu(T) = \mu_0 \cdot [\exp(\omega_{LO}\hbar/k_B T) - 1]$.

Another important consequence of the channel heating is that the voltage point where the I_{DS} curve becomes saturated, *i.e.* $V_{DS,sat}$ shifts to higher voltages. Figure 7.19 (b) exhibits dependence of $V_{DS,sat}$ on gate length L_g and mobility for an $\text{Al}_{0.85}\text{In}_{0.15}\text{N}(13\text{nm})/\text{AlN}(1\text{nm})/\text{GaN}$ heterostructure with a 2DEG density of $2.6 \times 10^{13} \text{ cm}^{-2}$. In addition, the channel temperature is assigned to the mobilities according to $\mu(T) = \mu_0 \cdot [\exp(\omega_{LO}\hbar/k_B T) - 1]$. The shift of the $V_{DS,sat}$ is more pronounced for small L_g . If there would be no heating at all *e.g.* $\mu_{300K} = 1200 \text{ cm}^2/\text{Vs}$ for $L_g = 0.25 \mu\text{m}$ one would expect a $V_{DS,sat}$ of $\sim 2 \text{ V}$. Since we find strong heating in these structures the actual mobility is strongly reduced to $\mu(1200\text{K}) = 50 \text{ cm}^2/\text{Vs}$. Therefore $V_{DS,sat}$ is increased to 5.5 V . This is in good agreement with Figures 7.8 and 7.12. Note that this has also a serious impact on the power density that can be extracted. Effectively, $(V_{knee} - V_{br})$ is reduced.

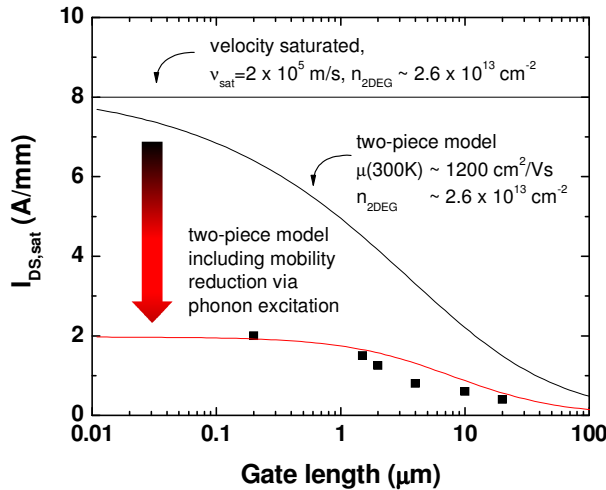


Figure 7.20 Re-evaluation of Figure 7.5 including the reduction of the RT mobility *via* phonon creation. The strong heating causes therefore a strong reduction of the saturation currents $I_{DS,sat}$ at the saturation voltage $V_{DS,sat}$.

7 Devices based on $\text{Al}_{1-x}\text{In}_x\text{N}/\text{AlN}/\text{GaN}$ heterostructures ($0.03 \leq x \leq 0.23$)

Now we want to use Equation (7.21) to re-evaluate Equation (7.10). Effectively, the static μ at 300K is replaced by $\mu(T_{LO})$ as a function of E and n_{2DEG} . We have to use therefore the lateral electric field taken at the saturation voltage $V_{DS,sat}$. As discussed in Figure 7.19 (b) the $V_{DS,sat}$ is in the case of heating ~ 6 V with a negligible dependence on L_g . The gate-drain distance is assume to be $1.5 \times L_g$ (see *e.g.* TLM Figure 7.12), then Equation (7.21) can be evaluated if the field is approximated to $E = 6 \text{ V} / (1.5 \times L_g)$. The resulting curve *versus* L_g looks like a downshift of the curve without heating and fits nicely the measured saturation currents. This is shown in Figure 7.20. From evaluating Equation (7.10) with Equation (7.21) and taking the limits L_g yields the maximum $I_{DS,sat}$ in these heterostructures

$$I_{DS,sat} \bigg|_{L \rightarrow 0} \bigg|_{\mu=\mu(E,n_{2DEG})} = n (V_g - V_{off})^2 C_0 \langle n_{LO,max} \rangle \mu_0 FWHM_{\Psi_{2DEG}(z)} v_{sat} \bigg/ \left\{ \begin{aligned} & 11 v_{sat} n_{2DEG} d V_{DS,sat} \\ & + \sqrt{11} v_{sat} n_{2DEG} d V_{DS,sat} \sqrt{\frac{11 v_{sat} n_{2DEG} d V_{DS,sat} + 2 \langle n_{LO,max} \rangle \mu_0 FWHM_{\Psi_{2DEG}(z)} n (V_g - V_{off})}{n_{2DEG} d V_{DS,sat} v_{sat}}} \\ & + \langle n_{LO,max} \rangle \mu_0 FWHM_{\Psi_{2DEG}(z)} n (V_g - V_{off}) \end{aligned} \right\} \quad (7.22)$$

where n stands for the ratio between drain-source distance and gate length *i.e.* $n = d_{DS}/L_g$. The above relation is obviously not very practicable compared to Equation (7.11) or (7.12) but allows to give the ultimate limit for $I_{DS,sat}$ and hence the power density in such heterostructures. A rough estimation can be given by assuming that the first two terms in the denominator are equal (strictly valid only for $\mu_0=0$) and both terms are much larger than the contribution from the last term. Then Equation (7.22) reduces to

$$I_{DS,LO-sat} \approx e \cdot \frac{(\omega_{LO} \hbar) \langle n_{LO,max} \rangle \mu_0 \sqrt{n_{2DEG}}}{2 \cdot d \cdot V_{DS,sat} \cdot C_0} \quad (7.23)$$

Again, $\mu_0 = \mu_{300K} / (\exp(\omega_{LO} \hbar / k_B \cdot 300K) - 1)$. Interestingly, the saturation current does not scale anymore with n_{2DEG} but its square root. Also the RT mobility is still important. On the other hand $I_{DS,sat}$ is proportional to the LO phonon energy and the phonon density.

One may ask now whether an improvement of the interface morphology towards an atomically perfect interface would lead to an increase of $I_{DS,sat}$ *e.g.* for an $\text{Al}_{0.85}\text{In}_{0.15}\text{N}(13\text{nm})/\text{AlN}(1\text{nm})/\text{GaN}$ heterostructure with a 2DEG density of $2.6 \times 10^{13} \text{ cm}^{-2}$. The mobility at RT is given by

$$\mu_{total}(300K) = \left(\mu_{op}^{-1} + \mu_{ac}^{-1} + \mu_{IR}^{-1} \right)^{-1} \approx \left(\mu_{op}^{-1} + 5000^{-1} + 3500^{-1} \right)^{-1} = 1200 \text{ cm}^2 / \text{Vs} \quad (7.24)$$

This yields a mobility μ_{op} of $\sim 2500 \text{ cm}^2/\text{Vs}$. For a perfect interface μ_{IR} is zero but the other thermal dependent components are still present giving a maximum mobility of μ_{tot} of $\sim 1850 \text{ cm}^2/\text{Vs}$. The situation is shown in Figure 7.21 (a) for different barrier thickness or respectively 2DEG density in the channel. Experimental values are nicely reproduced by the

theory. Now, we re-evaluate Equation (7.22) for the 14 nm barrier and varying the mobility while all other parameters are kept constant. The present state of the art mobility and the limit are indicated as vertical lines. Therefore for an atomically flat interface, which could be maintained over hundreds of microns, one would expect an improvement of the $I_{DSS,sat}$ proportional to the difference between the state-of-the art and the phonon limited mobility of $\sim 33\%$, *i.e.* one could potentially increase $I_{DSS,sat}$ to 2.5 A/mm.

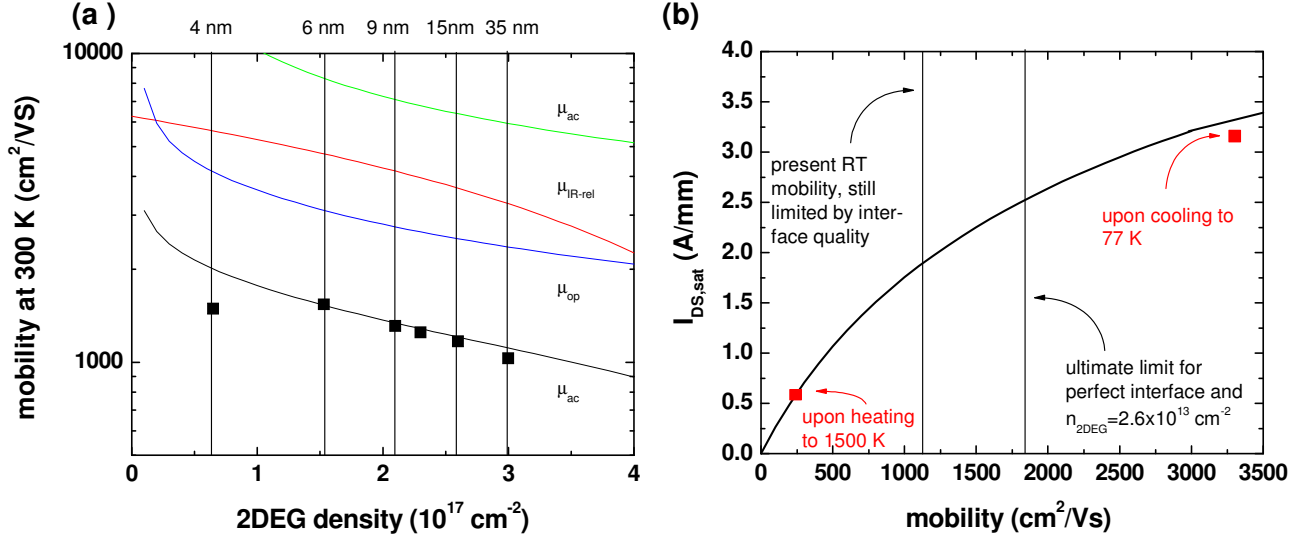


Figure 7.21 (a) RT mobility for $\text{Al}_{0.85}\text{In}_{0.15}\text{N}/\text{AlN}(1\text{nm})/\text{GaN}$ heterostructure as a function of the channel 2DEG density or respectively barrier thickness. Measured data together with mobility calculated from temperature dependent scattering mechanisms according to Equation (7.24). (b) Equation (7.22) evaluated for an $\text{Al}_{0.85}\text{In}_{0.15}\text{N}(13\text{nm})/\text{AlN}(1\text{nm})/\text{GaN}$ heterostructure versus 300 K mobility. By growing atomically flat interfaces one could increase $I_{DSS,sat}$ up to 2.5 A/mm. Data for cooling and heating of the device are also indicated.

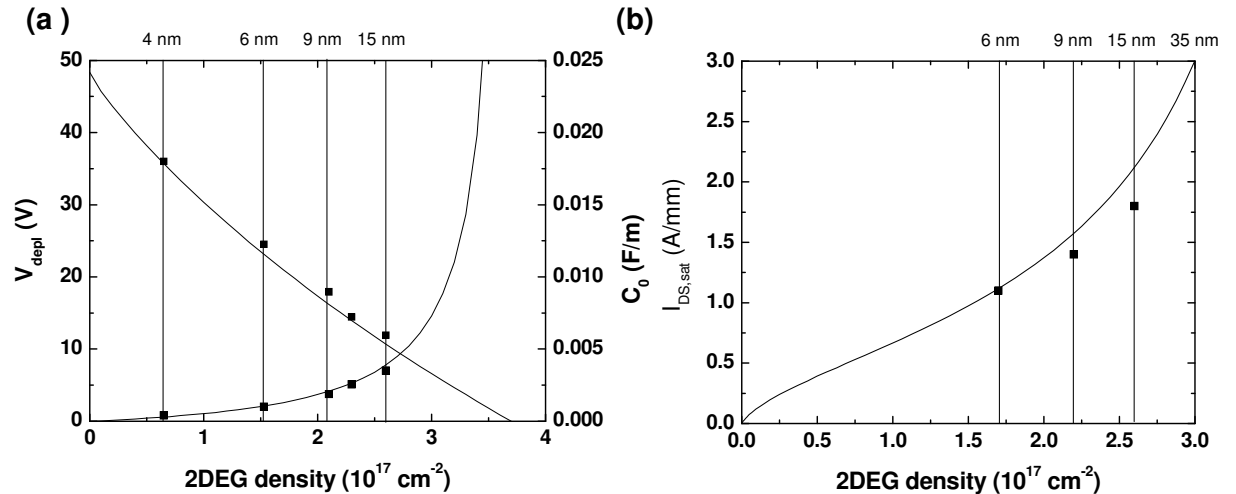


Figure 7.22 (a) Capacitance C_0 and depletion voltage V_{depl} as a function of 2DEG density and respectively on barrier thickness for an $\text{Al}_{0.85}\text{In}_{0.15}\text{N}/\text{AlN}(1\text{nm})/\text{GaN}$ heterostructure. Squares indicate measured data. (b) expected maximum $I_{DSS,sat}$ according to Equation (7.22) for different $\text{Al}_{0.85}\text{In}_{0.15}\text{N}$ barrier thickness. For C_0 , V_{depl} and μ the dependencies on 2DEG densities according to Figure 7.21 (a) and Figure 7.22 (a) are used. Measured $I_{DSS,sat}$ are also in good agreement with the calculated trend.

7 Devices based on $\text{Al}_{1-x}\text{In}_x\text{N}/\text{AlN}/\text{GaN}$ heterostructures ($0.03 \leq x \leq 0.23$)

Figure 7.21 (b) explains further the behaviour on external cooling or heating. Indeed if the sample is cooled down externally to 77 K the mobility is increased due to the reduced number of excited phonons to $\sim 3100 \text{ cm}^2/\text{Vs}$. Therefore one can go “artificially” along the curve 7.21 (b) beyond the RT limit up to $\sim 3100 \text{ cm}^2/\text{Vs}$ yielding a $I_{DS,sat}$ of 3 A/mm since the pool of unexcited phonons is larger than at RT. This is also found experimentally. *Vice versa* for external heating we move along the line to lower mobilities and consequently lower saturation currents because at higher higher temperature already a lot of phonons are excited. e.g. for external heating of $\sim 1500 \text{ K}$ one gets experimentally an $I_{DS,sat}$ of 0.6 A/mm (all for the same device).

Turning now to the case of varying the AlInN barrier thickness and consequently the 2DEG density. The behaviour of the capacitance C_0 and the depletion voltage V_{depl} on the barrier thickness are depicted in Figure 7.22 (a) together with measured data. The depletion voltage *versus* barrier thickness was already discussed in chapter 4. Keeping in mind that high densities $> 3.0 \times 10^{13} \text{ cm}^{-2}$ will not be achieved since layers relax if they are thicker than 50 nm when LM condition is not exactly fulfilled. On the other hand, too thick layers are not interesting since the depletion voltages are too high and exceed easily 10 V for 30 nm barriers. Figure 7.22 (b) shows expected maximum $I_{DSS,sat}$ according to Equation (7.22) as a function of AlInN barrier thickness. For C_0 , V_{depl} and μ the dependencies on 2DEG densities according to Figure 7.21 (a) and Figure 7.22 (a) are used. Measured $I_{DSS,sat}$ from Ref. [21] are also shown following nicely the calculated trend.

Substrate difference / alternative heterostructures As can be seen from data for AlInN/AlN/GaN heterostructures grown on different substrates in the subsection 7.2 the $I_{DSS,sat}$ scales also in good agreement with the RT mobility. *i.e.* for equal 2DEG densities (sapphire, Si, SiC) SiC exhibits the highest $I_{DSS,sat}$ because it has the highest RT mobility and consequently the best interface quality. That means that the influence of the substrate is much lower than widely believed. Even if one has higher thermal conductivity which allows an effective transport of the heat (mainly LA phonons) the $I_{DSS,sat}$ is limited by excited LO phonons in the channel. They are created permanently if a voltage is applied to the contacts and reducing therefore permanently the transport of electrons through the channel. However, it has been shown that the $I_{DSS,sat}$ can be increased by $\sim 50\%$ *via* pulsed measurements using pulse length of $\sim 500 \text{ ns}$. The model describe above is static and does not takes into account any time dependence. The description of such a time dependence coupled with detailed balance equations for LA and LO phonons could be a subject for a further work and is here out of the scope.

We can use Equation (7.22) to apply it to AlN/GaN heterostructures which are the record-holder in terms of $I_{DSS,sat}$ which is 2.3 A/mm [40] obtained with L_g of $0.25 \mu\text{m}$. The other parameters are the following: $\mu_{300\text{K}} \sim 1370 \text{ cm}^2/\text{Vs}$, $n_{2\text{DEG}} \sim 2.75 \times 10^{13} \text{ cm}^{-2}$, $C_0 \sim 0.005 \text{ F/m}^2$, $V_{DS,sat} \sim 8 \text{ V}$. These parameters inserted in Equation (7.22) yields $\sim 2.4 \text{ A/mm}$ close to the measured value. Also in this heterostructures, strong heating is found [42-44].

Delocalization of the 2DEG We aim now to discuss if the saturation currents might be increased despite the conclusions drawn from the discussion in section 7.4. This could only be realized by a delocalization of the 2DEG either by shifting the maximum of the wavefunction away from the interface or by increasing the extension towards the buffer, *i.e.* the FWHM of the 2DEG wavefunction. To this aim we consider first the case of a delta like doping in the vicinity of the 2DEG. Figure 7.23 (a) shows self-consistent calculation of this structure for two different doping levels. To significantly create additional electrons, doping level has to be higher than 10^{19} cm^{-3} . As it can be seen in Figure 7.23 (a) the additional electrons are located at $z=10 \text{ nm}$ and do not merge into the 2DEG which gives rise to a second conducting layer additional to the 2DEG. Also the maximum of the 2DEG wavefunction is not affected. Experimentally, delta doping in GaN gives only poor mobility of the order of $300 \text{ cm}^2/\text{Vs}$ due to scattering at ionized impurities [45]. Consequently the main benefit for saturation currents would come from the large extension of the charge distribution towards the GaN buffer. Hence heat could be distributed over a larger effective volume. According to Equation (7.23) $I_{DS,sat}$ might be increased by $\sim 0.5 \text{ A/mm}$.

Subfigure (b) shows the situation in the presence of an additional 3 nm thick $\text{In}_{0.1}\text{Ga}_{0.9}\text{N}$ quantum well (QW) directly grown between GaN and AlN interlayer (red curve) leading obviously to a even stronger confinement of the 2DEG where the location of the maximum of the charge density is decreased from 0.75 nm for a standard structure down to 0.6 nm . This is accompanied by an increase of the 2DEG density due to the increased polarization charge density at the AlN/ $\text{In}_{0.1}\text{Ga}_{0.9}\text{N}$ interface. Experimentally, we found for a 3 nm $\text{In}_{0.03}\text{Ga}_{0.97}\text{N}$ QW a 2DEG density of $2.9 \times 10^{13} \text{ cm}^{-2}$ (compared to $2.6 \times 10^{13} \text{ cm}^{-2}$ in standard structures) with mobilities of $300 \text{ cm}^2/\text{Vs}$. On the other hand if the QW is inserted a few nm away from the AlN/GaN interface (in our example $\sim 10 \text{ nm}$) the 2DEG is not affected. The QW is not occupied with electrons and has not effect on the confinement. These additional QW in the GaN buffer is also referred to as back-barrier and it was found helping to reduce buffer leakage [46].

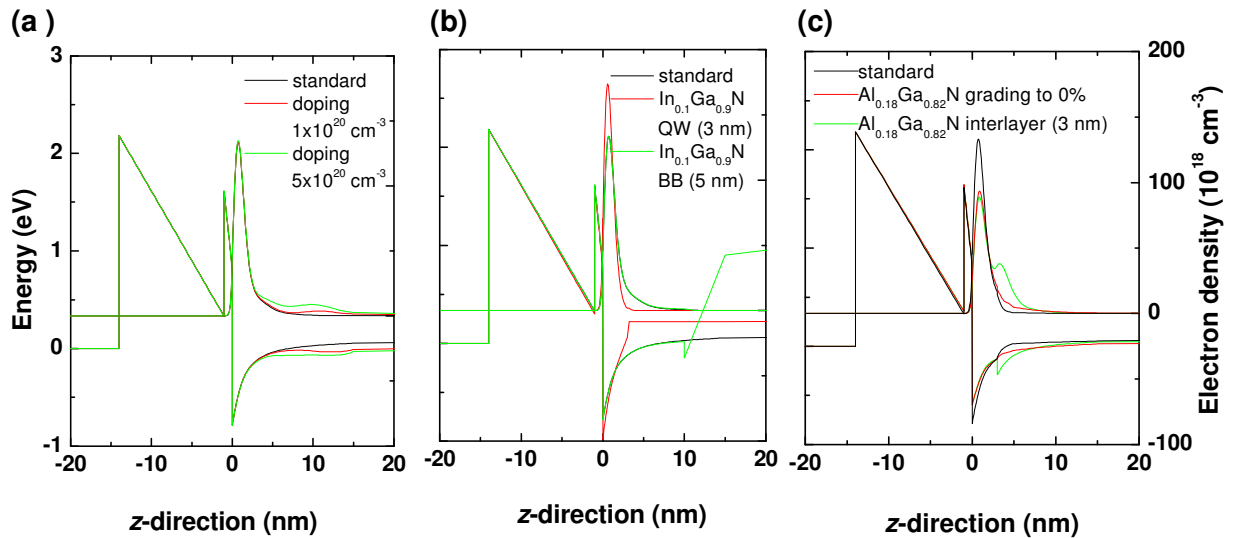


Figure 7.23 1D conduction band and charge density in the vicinity of the 2DEG channel for (a) additional delta doping for two different doping levels. (b) additional $\text{In}_{0.1}\text{Ga}_{0.9}\text{N}$ QW, inserted directly between AlN interlayer and GaN buffer (red) and at a distance of $\sim 10 \text{ nm}$ from the AlN/GaN interface (green). (c) additional $\text{Al}_{0.18}\text{Ga}_{0.82}\text{N}$ interlayer (3 nm) between AlN and GaN (green) and a grading (red) from the AlN/GaN interface towards the buffer with a depth of grading of 10 nm down to 0%.

7 Devices based on $\text{Al}_{1-x}\text{In}_x\text{N}/\text{AlN}/\text{GaN}$ heterostructures ($0.03 \leq x \leq 0.23$)

There is a medium range where the QW can have an influence on the 2DEG, namely if it is located at 1 nm away from the AlN interlayer. Then the maximum of the 2DEG wavefunction is located at ~ 0.84 nm. This would result in an increase of mobility thanks to reduced phonon scattering of $\sim 2100 \text{ cm}^2/\text{Vs}$ instead of $1800 \text{ cm}^2/\text{Vs}$ for the standard structure. However, the altered strain conditions might degrade the channel structural properties, and thereby the mobility.

Subfigure (c) displays the situation in presence of an additional AlGaN layer. The benefit from such a layer would arise from redistributing the 2DEG and hence achieving a larger extension into the buffer by modulating the bandgap at the position of the 2DEG. Green curve shows the situation if a 3 nm thick $\text{Al}_{0.18}\text{Ga}_{0.82}\text{N}$ is directly inserted between the AlN interlayer and the GaN, leading obviously to a strong delocalization of the 2DEG with a shift of the maximum to 0.85 nm and a smeared out tails of the charge density distribution. The same effect would be obtained with a gradient starting from $\text{Al}_{0.18}\text{Ga}_{0.82}\text{N}$ at the AlN/GaN interface down to GaN at $z=10$ nm. Obviously this would lead to a delocalization. But unfortunately mobility is expected to be very low due to alloy scattering. For a 2 nm $\text{Al}_x\text{Ga}_{1-x}\text{N}$ interlayer one would expect mobilities as low as $\sim 1400 \text{ cm}^2/\text{Vs}$ for $x \sim 0.05$, $\sim 750 \text{ cm}^2/\text{Vs}$ for $x \sim 0.1$ and $\sim 420 \text{ cm}^2/\text{Vs}$ for $x \sim 0.2$.

7.2.5 Modelling AlInN/AlN/GaN HEMT devices using 2D Current-Poisson calculations

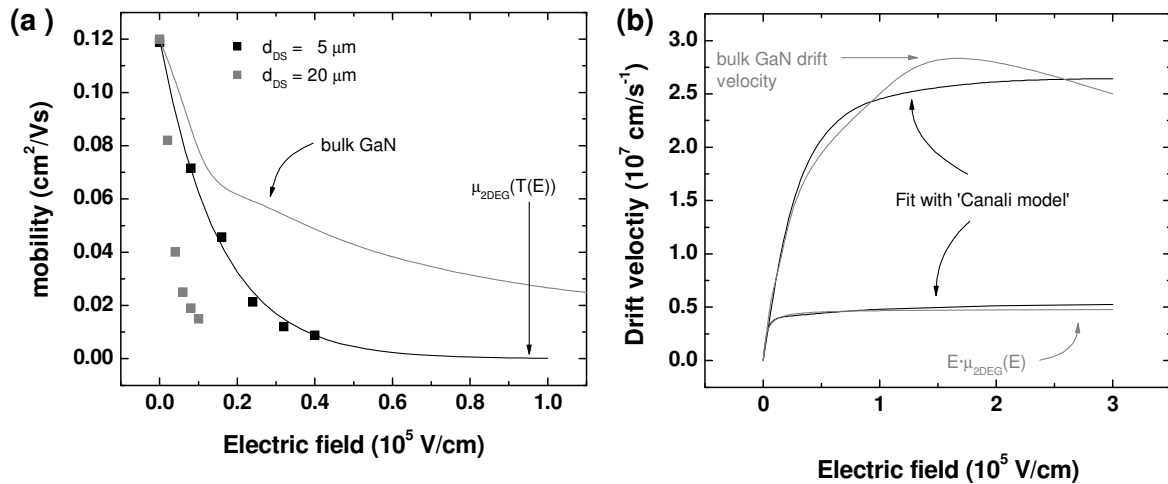


Figure 7.24 (a) Mobility decrease of the 2DEG in an AlInN/AlN/GaN/sapphire heterostructure due to channel heating as a function of mean lateral electric field. Squares indicate data according to heating from Figure 7.13 (b) and fit via Equation (7.21). For comparison the drift velocity for an electron moving in GaN bulk is given (grey line) [28]. (b) Drift velocity for an electron moving in GaN bulk [28] and fit via Canali model Equation (7.28). Drift velocity of the 2DEG is reduced due to heating.

To study the electric field across the 2D channel it is useful to perform self-consistent 2D current-Poisson calculations. To be more accurate one has to solve the 2D current-Poisson-Schrödinger which has been done *e.g.* in Ref. [47]. But in the present context we will be satisfied by treating the charge density classically. The main difference is the Schrödinger equation takes into account the exact electron distribution on a nm scale (see chapter 5) while here we will be dealing with the classic solution, *e.g.* the electron density is not longer given by the Fang-Howard wavefunction but by an exponential decay from the heterointerface into

the GaN. The total amount of charges is conserved, of course. This has the advantage of speed up calculations but might be compared to refined results later on. Literature on solving the current-Poisson-Schrödinger system on a finite grid may be found in Refs. [47, 48]. It will be briefly sketched in the following. The Poisson equation in 2D is given as

$$\begin{aligned} \nabla[\epsilon(x, y)\nabla\Phi(x, y)] &= -\rho(x, y) \\ \rho(x, y) &= q[-n(x, y) - \nabla \cdot P_{pz}(x, y) - \nabla \cdot P_{sp}(x, y)] \end{aligned} \quad (7.25)$$

As already introduced, Φ is the electrostatic potential, ρ is the charge density, q is the electron charge, n is the electron density and $P_{pyro/piezo}$ are the density of the spontaneous and piezoelectric polarizations. The electron density is obtained by

$$n(x, y) = 2 \left(\frac{2\pi k_B T m^*(x, y)}{h^2} \right)^{3/2} F_{1/2} \left[\frac{-E_{c0}(x, y) + e\Phi(x, y) + E_{Fn}(x, y)}{k_B T} \right] \quad (7.26)$$

where $F_{1/2}$ is the Fermi integral of order 1/2. E_{c0} is the band edge without electrostatic potential and E_{Fn} is the quasi Fermi level for the electrons (holes will be neglected in this context). Therefore contrary to Equation (5.11), the density obtained here is purely classical. The current is then given by

$$J_n = \mu_n(x, y) n(x, y) \nabla E_{Fn}(x, y) \quad (7.27)$$

There are a lot of semi-empirical transport models. We will employ here the so-called Canali model [49] where the mobility dependence on the electric field E is given as

$$\mu_n(\vec{E}) = \frac{\mu_{n,E0}}{\left[1 + \left(\mu_{n,E0} \frac{|\vec{E}|}{v_{sat}} \right)^{k_n} \right]^{1/k_n}} \quad (7.28)$$

Solving Equations (7.25)-(7.28) together with suitable boundary conditions and the current continuity Equation $\nabla \cdot J_n = 0$ gives the electron densities, 2D band edge and electric fields for equilibrium and biased condition for arbitrary device geometry.

In the following we compare again a HEMT device with a short drain-source distance (~1 micron) for the two transport models discussed in Figure 7.20. Namely the velocity saturated model Equation (7.11) and the mobility model from Equation (7.21).

Figure 7.24 displays the mobility decrease of the 2DEG in the $\text{AlInN}/\text{AlN}/\text{GaN}/\text{sapphire}$ heterostructure due to channel heating depending on mean lateral electric field. Black squares indicate data according to heating from Figure 7.13 (b) and a fit *via* Equation (7.21). For comparison the drift velocity for an electron moving in GaN bulk is given (grey line) [28], which is assumed to be at RT. In addition, the grey squares show the mobility expected from the mean electric field across the channel for a device with a drain source distance of 20 μm . Since weaker fields are achieved for the same applied voltage range, the heating is expected to be lower and hence higher mobility are obtained (the grey squares are consequently shifted to the upper left with respect to the black squares).

7 Devices based on $\text{Al}_{1-x}\text{In}_x\text{N}/\text{AlN}/\text{GaN}$ heterostructures ($0.03 \leq x \leq 0.23$)

In the following we refer to the device geometry as given in Figure 7.25. Computations are performed on a 150×50 grid. Computation time is of the order of 10^5 s with a 3 GHz Intel Pentium 4 processor. For a voltage increment of 0.05 V this corresponds to a computation time of 1000 s per increment. All calculations are carried out with the NextNano³ code [50].

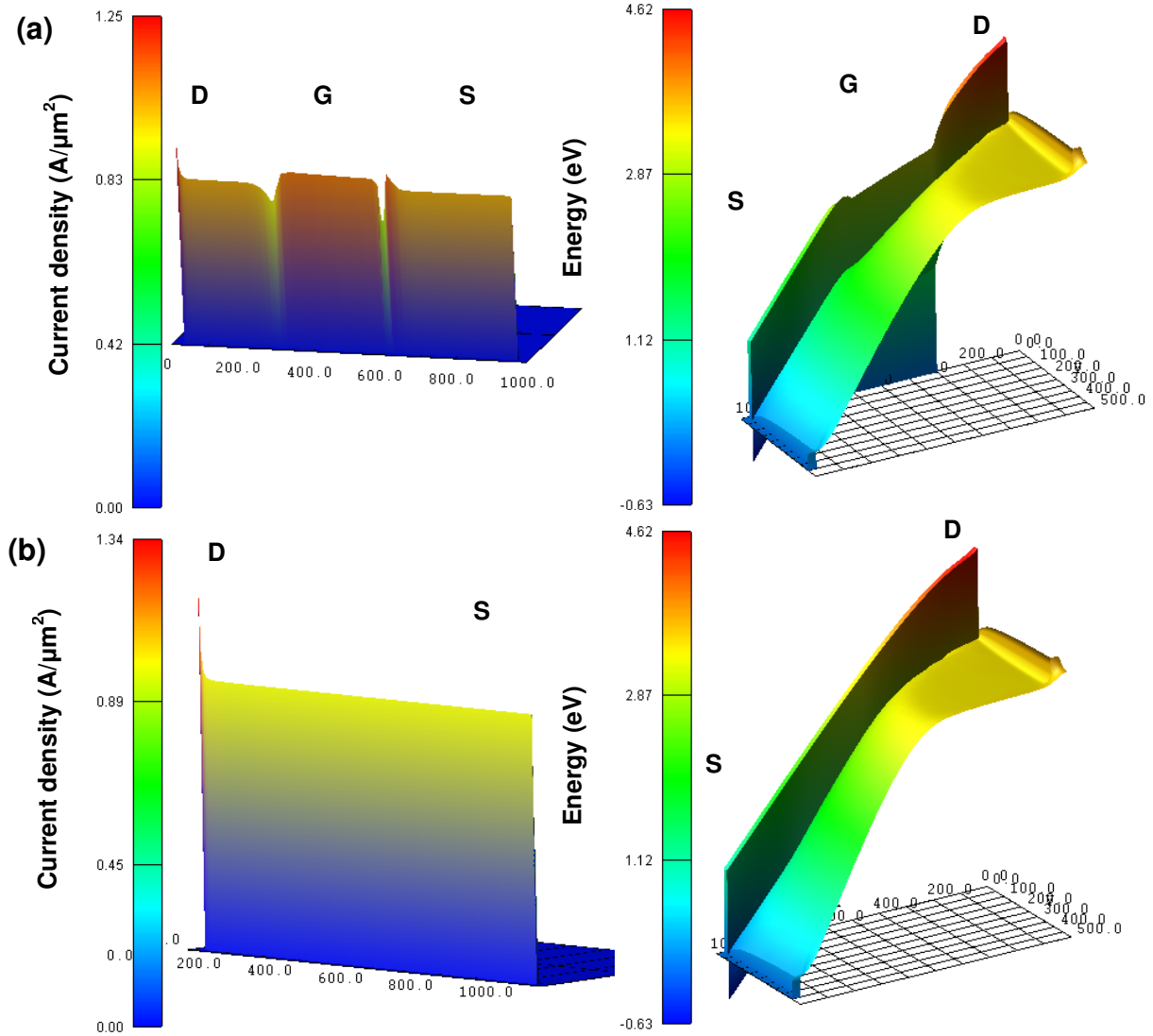


Figure 7.26 2D Current density and 2D conduction band for a gated (a) and ungated (b) $\text{Al}_{0.85}\text{In}_{0.15}\text{N}(13\text{nm})/\text{AlN}(1\text{nm})/\text{GaN}$ HEMT at $V_{\text{DS}}=3.5$ V and $V_{\text{g}}=0$ V calculated with the phonon-limited current saturation model. Note that the current density is only the x-component of the 2D current vector.

Figure 7.25 Geometry of the simulated HEMT device. S, G, and D denote source (S), gate (G) and drain (D) contacts. Drain-source distance d_{DS} is $1 \mu\text{m}$ and gate length $L_{\text{g}}=0.3 \mu\text{m}$.

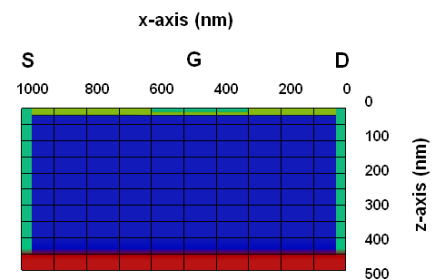


Figure 7.26 shows the 2D current density and 2D conduction band for a gated (a) and ungated (b) $\text{Al}_{0.85}\text{In}_{0.15}\text{N}(13\text{nm})/\text{AlN}(1\text{nm})/\text{GaN}$ HEMT at $V_{DS}=3.5$ V and $V_g=0$ V calculated with the phonon-limited current saturation model (Figure 7.24 (b)). Note that the current density is only the x -component of the 2D current vector. Interestingly, for the ungated device the current distribution is nearly constant throughout the channel and the conduction band scales linearly in contrast to the presence of the gate contact which causes a bump on the drain hand side giving rise to a strong local electric field. This is similar to results found by other authors [36]. This behaviour is plotted in Figure 7.27 which shows the 1D conduction band profile and electric field deduced from the 2D solution at the heterointerface with the GaN buffer for different applied voltages for the gated (thick colored lines) and ungated (thin colored lines) case calculated with the saturated current model (a) and with the phonon-limited current saturation model (b). The gate voltage V_g is always zero.

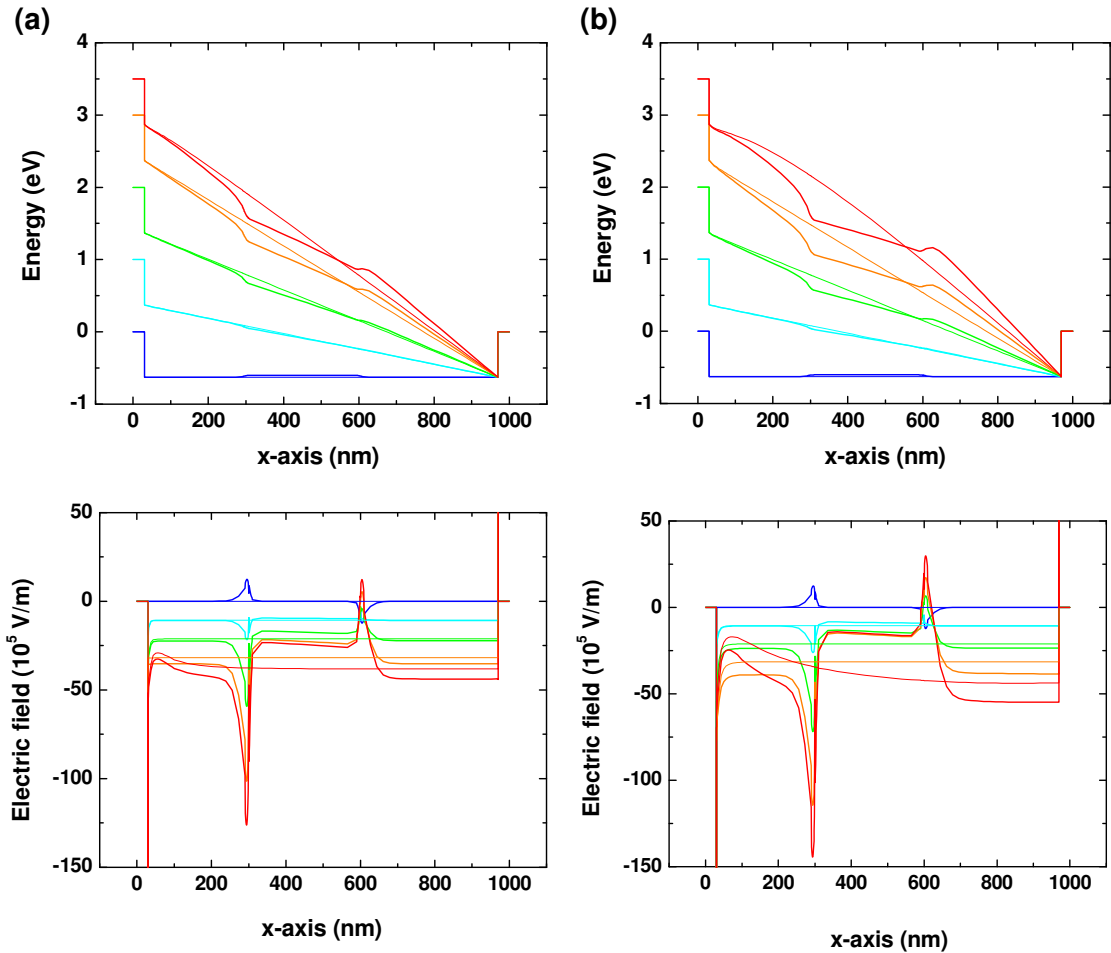


Figure 7.27 1D Cross-section of the 2D conduction band energy at the AlN/GaN heterointerface (*i.e.* bottom of the triangular potential well) and electric field in dependence on applied drain-source voltage V_{DS} and keeping $V_g=0$ V. Subfigure (a) shows the situation using the velocity saturated current model while subfigure (b) uses the phonon-limited current saturation model. Thick lines for all four subfigures indicate the situation when the gate contact is present while thin lines indicate the ungated case. The V_{DS} can be deduced from the potential at $z=0$ in the upper row. In all four subfigures same colour means same applied V_{DS} .

7 Devices based on $\text{Al}_{1-x}\text{In}_x\text{N}/\text{AlN}/\text{GaN}$ heterostructures ($0.03 \leq x \leq 0.23$)

Interestingly, the conduction band looks similar for both mobility models. For ungated devices the electric field throughout the channel is approximately given by $E = d_{DS}/V_{DS}$, while the situation in the presence of the gate is more lively. One might speak in terms of a mean lateral electric field. However, the drain handed peak of the electric field is more than twice the amount of the mean lateral electric field at a given V_{DS} and located in a small ~ 100 nm region. Since the electric field is the derivative of the conduction band it holds that $V_{DS} = \int_D^S E(x) dx$. On the other hand the resulting IV_{DS} characteristics are shown in Figure 7.28 for both mobility models. Correspondingly to Figure 7.20 subfigure (a) gives the current density for the velocity saturation model yielding $I_{DS,sat}$ of ~ 10 A/mm while the phonon-limited model gives a $I_{DS,sat}$ of ~ 2.3 A/mm as depicted in subfigure (b). Gated devices also exhibit a slightly higher current. This originates from the fact that under the gate the carrier density is slightly increased under these specific bias conditions. The slope of Figure 7.28 (b) near $V_{DS}=0$ V deviate from measured curves. This simply results from the effect that $\mu(T)$ was taken from $5 \mu\text{m}$ device while simulation domain is only $1 \mu\text{m}$ to save computation time.

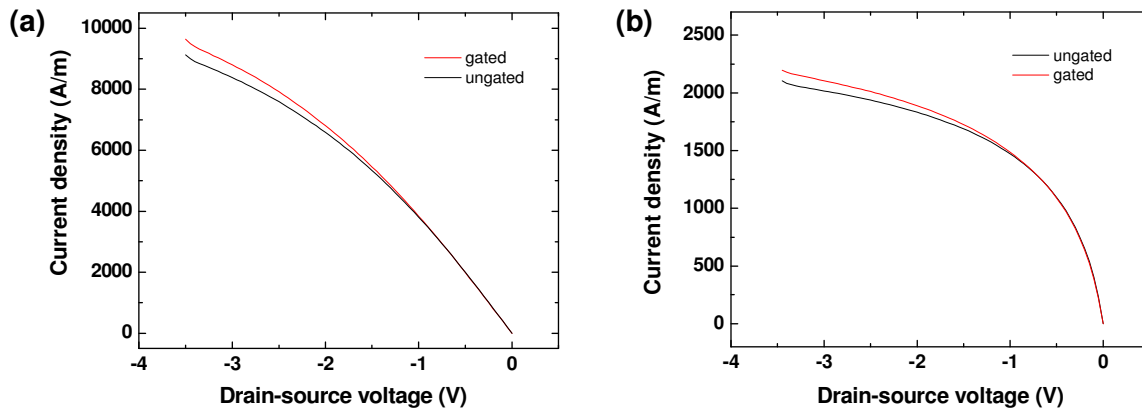


Figure 7.28 Simulated IV characteristics for a gated and ungated $\text{Al}_{0.85}\text{In}_{0.15}\text{N}(13\text{nm})/\text{AlN}(1\text{nm})/\text{GaN}$ HEMT at $V_g=0$ V calculated with (a) the velocity saturated current model and (b) the phonon-limited current saturation model.

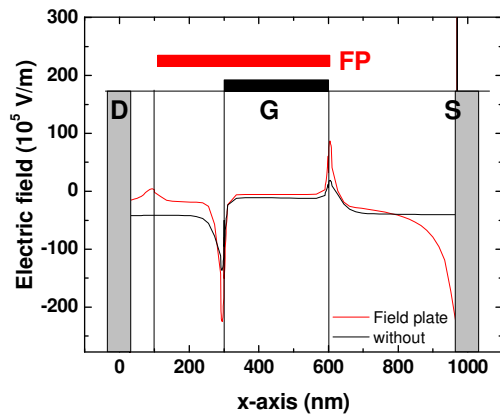


Figure 7.29 Redistribution of the electric field due to the presence of a field plate according to the geometry in the inset. Especially the field on the drain handed side becomes lower. $V_g=0$ V and $V_{DS}=3.5$ V.

Field plate As we will see in the next subchapter the presence of a so-called field plate will improve HEMT characteristics such as leakage current or increase the output power. Therefore Figure 7.29 shows the redistribution of the electric field due to the presence of a field plate according to the geometry in the inset. Especially the field on the drain handed side becomes lower. Since $V_{DS} = \int_D^S E(x)dx$ holds the electric field has to increase on the source handed side.

7.2.6 Advanced concepts

Thermal oxidation At this point we want to mention some concepts to improve HEMT operation. A serious problem is still the far too high gate leakage current which easily reaches the magnitude of mA. We want to point out that until now a consistent model of currents in nitride heterostructure Schottky diodes is still missing. Usually, the current in Schottky diodes is described in the framework of thermionic emission [38]. A reason why this approach fails *e.g.* is the strong heating even in Schottky diodes processed from the AlInN/GaN heterostructures which is found to be 500 K near the depletion voltage of the 2DEG detected with μPL . It was also demonstrated that dislocations in the barrier act as enhanced current paths [51]. AlInN possesses now the possibility of being oxidized electrically [52] or thermally, *i.e.* transforming the AlInN mainly into Al_2O_3 . The thermal oxidation can be performed in a rapid thermal annealing (RTA) system under oxygen supply. Figure 7.30 shows the gate current *versus* gate source voltage for a $\text{Al}_{0.85}\text{In}_{0.15}\text{N}(13\text{nm})/\text{AlN}(1\text{nm})/\text{GaN}$ HEMT device with and without thermal oxidation. The oxidation was performed for 30 min at 800°C after processing of the ohmic contacts. As it can be seen it reduces the leakage current by about five orders of magnitude. The drawback of this method is that it is difficult to control the homogeneity and the thickness of the oxide. Therefore attempts were made to directly deposit Al_2O_3 as gate dielectric and build metal oxide semiconductor (MOS) structures or using a thin GaN cap layer. This work on wafers grown at EPFL was mainly done in the framework of the European UltraGaN project at the University of Vienna (by G. Pozzovivo and J. Kuzmik) and at the University of Ulm (F. Medjdoub and E. Kohn).

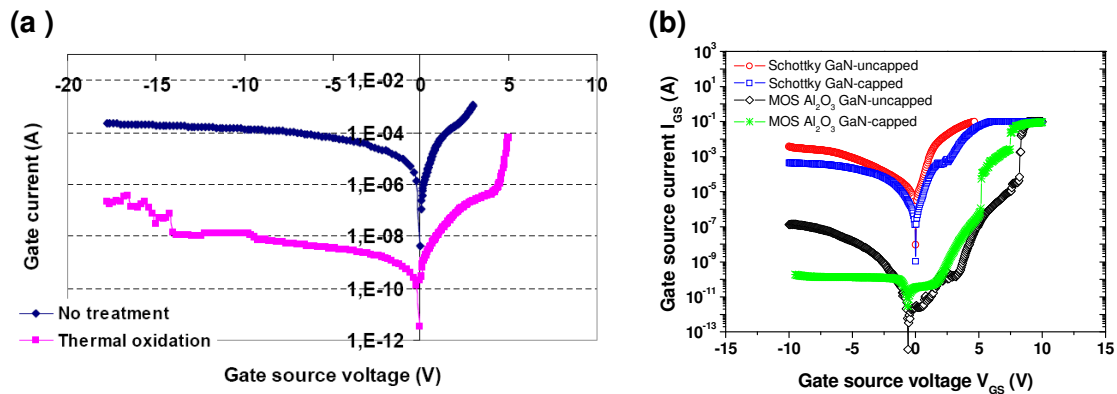


Figure 7.30 (a) $I_{GS}(V_{GS})$ for an $\text{Al}_{0.85}\text{In}_{0.15}\text{N}(13\text{nm})/\text{AlN}(1\text{nm})/\text{GaN}$ HEMT device with and without thermal oxidation of the AlInN . Courtesy of F. Medjdoub (b) $I_{GS}(V_{GS})$ for a $\text{Al}_{0.85}\text{In}_{0.15}\text{N}(13\text{nm})/\text{AlN}(1\text{nm})/\text{GaN}$ HEMT device with and without GaN cap (2 nm) and Al_2O_3 (10 nm) deposited with PLD. Subfigure (b) is taken from Ref. [53]. Courtesy of G. Pozzovivo.

7 Devices based on $\text{Al}_{1-x}\text{In}_x\text{N}/\text{AlN}/\text{GaN}$ heterostructures ($0.03 \leq x \leq 0.23$)

Figure 7.30 (b) shows the $I_{GS}(V_{GS})$ for an $\text{Al}_{0.85}\text{In}_{0.15}\text{N}(13\text{nm})/\text{AlN}(1\text{nm})/\text{GaN}$ HEMT device with and without GaN cap (2 nm) and Al_2O_3 (10 nm). Results are taken from Ref. [53]. One can see that Al_2O_3 has a huge impact on the leakage current which can be reduced by several orders of magnitude.

Field plate It has been shown that field plate technology has a significant effect on HEMT performance. *e.g.* it allowed to generate ~ 30 W/mm in $\text{AlGaIn}/\text{GaN}/\text{SiC}$ HEMTs [54]. Therefore this attempt has also been made to investigate its influence on $\text{Al}_{0.85}\text{In}_{0.15}\text{N}(13\text{nm})/\text{AlN}(1\text{nm})/\text{GaN}/\text{sapphire}$ HEMT device. Results are shown in Figure 7.31 which is a courtesy from Ref. [55]. It shows the reverse characteristic of the Schottky gate contact without field plate and with the different field plate extension (FP1=0.7 μm , FP2=1.2 μm and FP3=1.7 μm). Drain-source distance is $d_{DS}=2.5$ μm and gate length $L_g=0.25$ μm . Subfigure (b) shows the corresponding device geometry. Since the HEMT device here is driven as a Schottky contact with low reverse current density the breakdown is of electrical nature. The field plate reduces the leakage current by two orders of magnitude and increases the breakdown voltage of the gate Schottky from -35 V up to ~ -100 V, *i.e.* nearly a factor three.

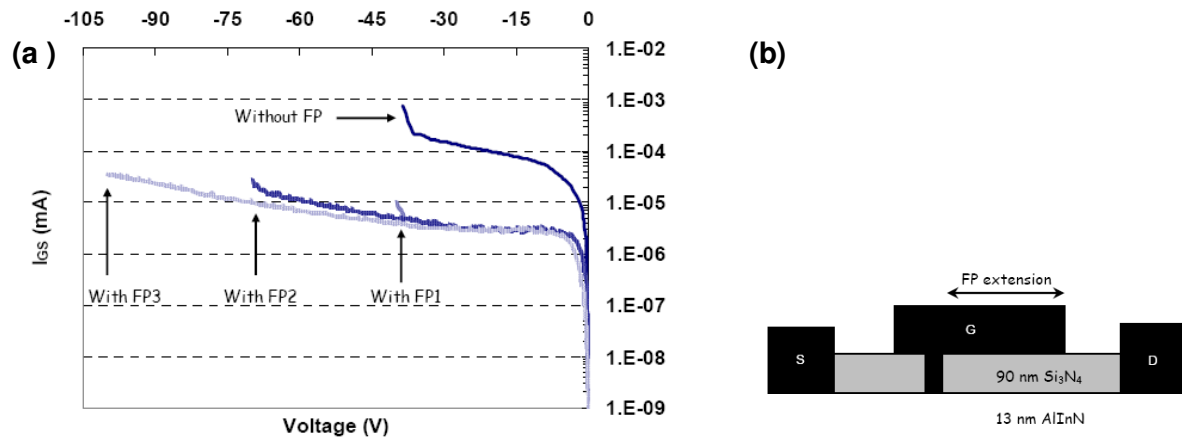


Figure 7.31 (a) Reverse characteristics of the Schottky-like gate contact without field plate and with the different field plate extension (FP1=0.7 μm , FP2=1.2 μm and FP3=1.7 μm). Drain-source distance is $d_{DS}=2.5$ μm and gate length $L_g=0.25$ μm . The gate width is 25 μm . Graph are taken from Ref. [55]. Courtesy of F. Medjdoub. (b) Corresponding device geometry.

7.3 Chemical, thermal and UV sensing

In this section the possibility of using the 2DEG $\text{AlInN}/\text{AlN}/\text{GaN}$ heterostructures for sensing applications will be investigated. However a lot of work was already done for AlGaN/GaN system proving the high potential of nitride based sensing applications for harsh environments [56]. At this point we will briefly present some results how the 2DEG in the $\text{AlInN}/(\text{AlN})/\text{GaN}$ heterostructure reacts on different external stimuli, *i.e.* radiation, heat, or in contact with polar liquids.

Chemical sensing If the device surface is exposed to liquids characterized by a strong dipole moment these molecules are adsorbed. These dipoles superimpose to the electrostatic fields in the barrier, increasing therefore the field in the semiconductor and consequently the surface potential. Hence the 2DEG in the channel gets more depleted and the resistivity increases according to $\rho_{\square} = 1/e \cdot n_{2\text{DEG}} \cdot \mu(n_{2\text{DEG}})$. Note in this context the dependence of the mobility on the 2DEG density, which causes a significant effect on the sheet resistivity even for a small amount of depleted 2DEG electrons. According to 7.21 (a) it might be approximated as $\mu(n_{2\text{DEG}}) \approx 1676 - 1.1 \times 10^{-12} \cdot n_{2\text{DEG}} - 7.1 \times 10^{-25} \cdot n_{2\text{DEG}}^2$ [cm^2/Vs] in high 2DEG density regime at RT. Figure 7.32 displays the sheet resistivity depending on time for an $\text{AlInN}(13\text{nm})/\text{AlN}/\text{GaN}$ heterostructure in Van der Pauw geometry under the exposition of the surface to different polar liquids, namely methanol, acetone and iso-propanol. After the droplet deposition the 2DEG is depleted and consequently resistivity increases. After evaporation initial resistivity is recovered. Interestingly, for methanol and acetone the resistivity decreases with respect to the steady state at the moment when the liquid is evaporated completely. This might be related to a cooling effect due to the enthalpy of vaporization of the liquid. Consequently the mobility would increase due to the decrease in 2DEG sheet resistivity. The exponential recovering of the steady state resistivity could be interpreted in terms of recovering to ambient temperature due to air convection. Interesting is further the amplitude of the resistivity change, which is biggest for methanol. In Table 7.2 properties of the liquids are listed.

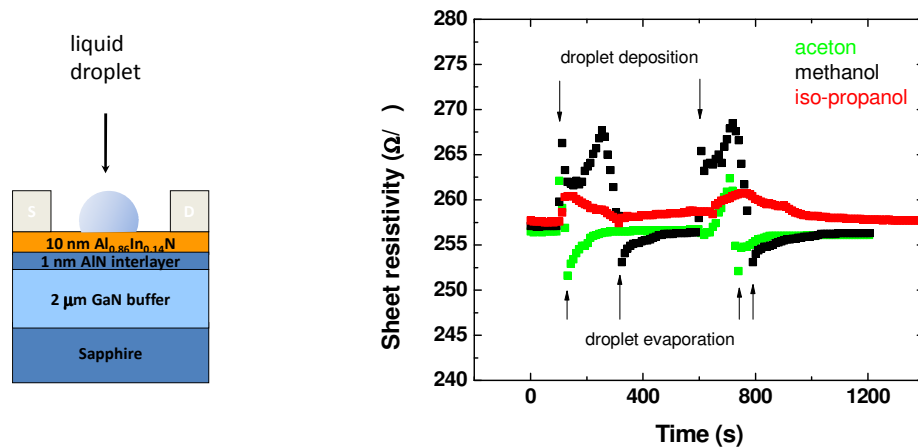


Figure 7.32 Sheet resistivity of an $\text{AlInN}(13\text{nm})/\text{AlN}(1\text{nm})/\text{GaN}$ heterostructure in Van der Pauw geometry and exposition of the surface to different polar liquids. After the droplet deposition the 2DEG is depleted and consequently resistivity increases. After evaporation initial resistivity is recovered. Measurement performed at EPFL.

7 Devices based on $\text{Al}_{1-x}\text{In}_x\text{N}/\text{AlN}/\text{GaN}$ heterostructures ($0.03 \leq x \leq 0.23$)

Liquid	Molar mass (g/mol)	Dipole Moment (liquid phase) (D) [57]	Dipole Concentration ($1/\text{nm}^3$)	Static Dielectric constant ϵ_s	High Frequency Dielectric Constant ϵ_∞	Polarization of the liquid film (C/m^2)
Methanol	32	2.87	14.8	32.6	1.77	0.011
Aceton	58	2.86	8.2	20.7	1.85	0.008
Iso-propanol	60	1.65	7.8	18.3	1.9	0.0034

Table 7.2 Molar mass, molecule dipole moment, dipole concentration, dielectric constants and macroscopic polarization for the polar liquid films deposited on the $\text{AlInN}/\text{AlN}/\text{GaN}$ heterostructure at RT.

Liquid	$\Delta\rho_\square$ (Ω/\square)	$\Delta n_{2\text{DEG}}$ (10^{17}m^{-2})	$\Delta\Phi_B$ (eV)	$P/2\epsilon_0\epsilon_{\text{AlInN}} \cdot d_{\text{AlInN}}$ (eV)
Methanol	+8	-0.33	+0.75	+0.72
Aceton	+6	-0.27	+0.64	+0.52
Iso-propanol	+2	-0.12	+0.25	+0.22

Table 7.3 Resistivity change, amount of depleted 2DEG electrons, surface potential change according to Equation (4.7) and surface potential change according to Equation (7.29) for the polar liquid films deposited on the $\text{AlInN}/\text{AlN}/\text{GaN}$ heterostructure at RT.

Interestingly, the resistivity change seems to be proportional to the dipole concentration. However, even if we neglect for instance surface charge density, one still has to consider a field inside the liquid since the normal component across hetero-boundary behaves as $\epsilon_1 \cdot E_{1,z} = \epsilon_2 \cdot E_{2,z}$. This will induce an electric field in the liquid at least close to the heterointerface which is by a factor $\epsilon_{S,\text{AlInN}} / \epsilon_{S,\text{liquid}}$ lower than the field in the AlInN barrier. This field will polarize the dipoles in the liquid according to the Onsager Equation for strong polar liquids [58]

$$\bar{P} = N \left[\frac{\mu^2}{3k_B T} \frac{3\epsilon_S}{(2\epsilon_S + 1)} + \frac{\epsilon_S [\epsilon_\infty - 2]}{[2\epsilon_S + \epsilon_\infty]} \alpha \right] \bar{E} \quad (7.29)$$

where P is the macroscopic polarization, μ the dipole moment per molecule and N is the number of dipoles per volume. This relation holds for $\mu E \ll kT$, *i.e.* moderate electric fields. Calculating then the macroscopic polarization from Equation (7.29) by neglecting field induced dipoles and assuming RT and taking parameters from Table 7.2 one arrives at

polarizations given in the last column of Table 7.2. From Gauss law follows that the field imposed on the barrier built-in field is proportional to the macroscopic polarization of the liquid film, *i.e.* $E = \sigma / 2\epsilon_0\epsilon_{\text{AlInN}}$ (for an infinite extended dipole sheet), where σ is the polarization sheet density from Table 7.2 (*i.e.* $\sigma = P$). Consequently the amount of depleted electrons is proportional to the last column of Table 7.2 in excellent agreement with the experiments. These results might be compared with the common Helmholtz model describing the potential increase at a polar liquid/solid heterointerface [59]. Finally the surface potential increase from experimental resistivities can be estimated from Equation to be $\Delta V_{\text{methanol}} = 0.72$ eV, $\Delta V_{\text{acetone}} = 0.52$ eV and $\Delta V_{\text{iso-propanol}} = 0.22$ eV. These findings are in excellent agreement with calculated potential increase from Equation (4.7). Results are summarized in Table 7.3.

Thermal sensing Nitride semiconductors have an extremely high melting point compared to other conventional semiconductors (GaAs : 1538 K, Si : 1687 K). This fact makes them very attractive for temperature sensing application. Especially heterostructures with a degenerated 2DEG are interesting since the change of the 2DEG density with temperature is very low compared to the thermal activation of carriers from doped 3D bulk material. As widely discussed in this work the temperature dependence of the 2DEG mobility is given from Equation (4.20). This can directly be related to the sheet resistivity of those $\text{AlInN}(13\text{nm})/\text{AlN}(1\text{nm})/\text{GaN}$ heterostructures *via* the formula given as inset in Figure 7.33 (b) if no major temperature dependence of the 2DEG density is assumed. Most critical point would be the melting of the contacts as already discussed for the subsection of thermally induced breakdown of HEMT devices. However, the resistivity behaves strongly non-linearly and especially in the high temperature range where the gradient is low.

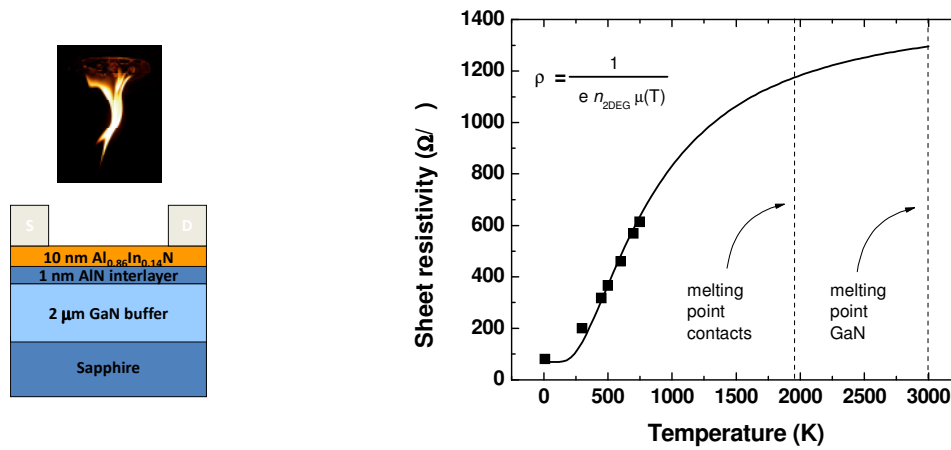


Figure 7.33 Thermal sensing *via* the sheet resistivity of the 2DEG in $\text{AlInN}(13\text{nm})/\text{AlN}(1\text{nm})/\text{GaN}$ heterostructures. The sheet resistivity is given by the inset formula. Melting point of contacts and GaN are indicated as well. Squares indicated measured resistivity in the accessible temperature range. Measurement performed at EPFL.

7 Devices based on $\text{Al}_{1-x}\text{In}_x\text{N}/\text{AlN}/\text{GaN}$ heterostructures ($0.03 \leq x \leq 0.23$)

UV sensing In Ref. [60] the possibility of the use of AlInN epitaxial layers for UV sensing was discussed. This motivated us to briefly investigate the electrical response on the excitation with UV light. This section is more of qualitative nature. Figure 3.34 shows the resistivity of $\text{AlInN}/\text{AlN}/\text{GaN}$ heterostructure exposed to the sun spectrum and under dark conditions. Under exposed conditions high energy photons create carriers in the barrier and screen therefore partially the electric field in the barrier. This would lead to a reduced depletion of the 2DEG and hence to a lower resistivity. Under dark conditions the electric field in the barrier is not longer screened, and consequently higher leading to and increased 2DEG depletion and consequently to an increase of the resistivity.

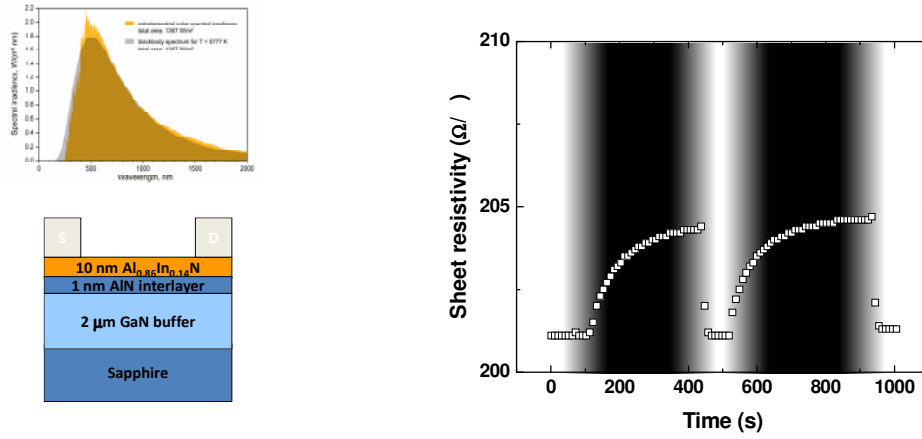


Figure 7.34 2DEG sheet resistivity for an $\text{AlInN}(13\text{nm})/\text{AlN}(1\text{nm})/\text{GaN}$ heterostructure under exposition to sun spectrum (white areas) and dark conditions (black areas) as a function of time.

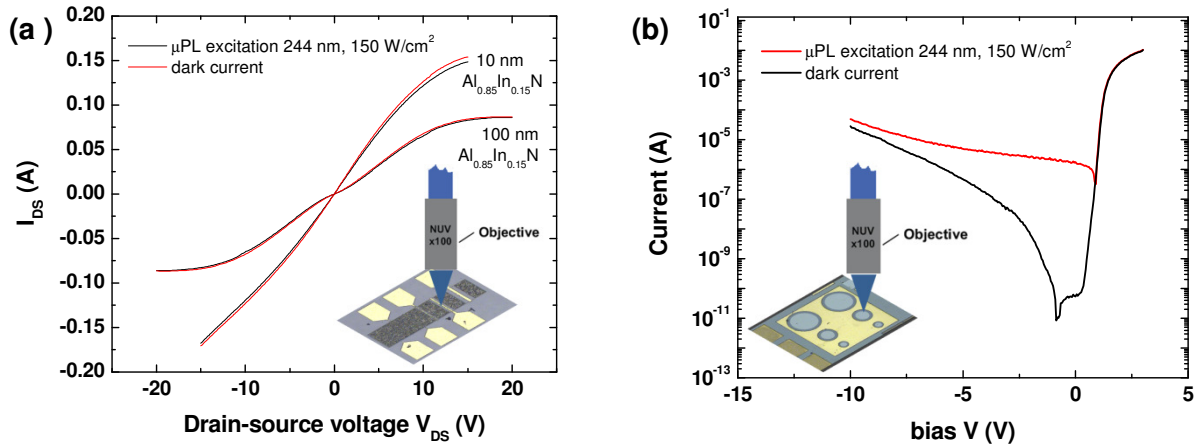


Figure 7.35 (a) Dark current and current under μPL excitation with $\sim 150 \text{ W/cm}^2$ in the channel of an $\text{Al}_{0.85}\text{In}_{0.15}\text{N}/\text{AlN}(1\text{nm})/\text{GaN}$ HEMT device with 10 nm and 100 nm barrier with an $d_{DS}=40 \mu\text{m}$. (b) The same situation as (a) but for a Schottky device processed from a 100 nm barrier with semitransparent $\text{Ni}(5\text{nm})/\text{Au}(5\text{nm})$ contact. Diameter of the Schottky contact is 200 μm .

Now we are turning to an intentional excitation with a 244 nm laser beam. Figure 7.35 (a) shows the dark current and current under μPL excitation with $\sim 150 \text{ W/cm}^2$ in the channel of an $\text{Al}_{0.85}\text{In}_{0.15}\text{N}/\text{AlN}(1\text{nm})/\text{GaN}$ HEMT device with 10 nm and 100 nm barrier with and $d_{DS}=40 \mu\text{m}$. Note that the spot diameter of $\sim 1 \mu\text{m}$ covers only a small fraction of the channel surface and consequently a homogenous excitation is not guaranteed. But interestingly the effect on the IV curve under excited conditions is larger for the 10 nm ($\Delta I_{DS} \sim 6 \text{ mA}$) rather than for the 100 nm ($\Delta I_{DS} \sim 0.7 \text{ mA}$) barrier. If the source of the current increase would be directly caused by the excited carriers within the barrier which contributed to the conduction one would expect an opposite behaviour. *i.e.* more carriers would be created in the thicker layer causing larger currents. But here the effect is similar as for the resistivity discussed above. For thinner barriers the effect of the electric field screening on the 2DEG depletion is much more pronounced for thinner barriers. Consequently, if the field is screened the mean field across the barrier is lowered and the amount of 2DEG density increases and hence the I_{DS} increases.

Figure 7.35 (b) shows the same experiment as (a) but for a Schottky diode processed from a 100 nm barrier with semitransparent $\text{Ni}(5\text{nm})/\text{Au}(5\text{nm})$ contact. Here, the current increases significantly at larger reverse bias after excitation compared to the dark current, *e.g.* the difference arises at -10 V as $I_{\text{excited}}(-10\text{V}) - I_{\text{dark}}(-10\text{V}) \sim 2 \times 10^{-5} \text{ A}$. With the excitation power of $\sim 150 \text{ W/cm}^2$ this yields a responsivity $\Delta I/P_{\text{excitation}} \sim 2 \times 10^{-5} \text{ A} / 150 \text{ W/cm}^2 \sim 0.5 \times 10^{-3}$ for the 200 μm diameter diode. This magnitude is in agreement with Ref. [60]. One might also estimate the amount of the current assuming an excited carrier density as $\Delta n = \Delta p = G\tau$, with the generation rate G and the excess carrier lifetime τ . Then $\Delta n = G \cdot \tau = P_{\text{excitation}} / [e \cdot 1239.84 \text{ nm} / \lambda_{\text{excitation}}] \cdot \tau \approx 150 \times 10^4 [W/m^2] \cdot 1 / (5 \cdot 1.6 \times 10^{-19}) [J^{-1}] \cdot 50 \times 10^{-12} [s]$ which gives $\Delta n \approx 1 \times 10^{15} [m^{-2}]$. Using then the relation $I = e \cdot F \cdot \mu \cdot \Delta n / d$, where F is the electric field, μ the mobility and d the thickness where photons are absorbed. With some reasonable assumptions one arrives, assuming 10 V reverse bias, at $I = e \cdot 10 [V] / 100 \times 10^{-9} [m^{-1}] \cdot 0.01 [m^2/Vs] \cdot 1 \times 10^{15} [m^2] / 100 \times 10^{-9} [m] \approx 1.5 \times 10^9 [1/m^2s]$. Assuming now that the current increase results mainly from the region under the exciting spot one gets for the current increase $\Delta I \sim 1.5 \times 10^9 [1/m^2s] \cdot (0.25 \times 10^{-6} [m])^2 \cdot \pi \approx 2 \times 10^{-4} [A]$, which gives nearly the correct order of magnitude compared with the experiments.

7.4 Conclusions

HEMT devices HEMT devices processed from the $\text{AlInN}/\text{AlN}/\text{GaN}$ heterostructures grown on different substrates show excellent device performance. Remarkable records were achieved: above 2 A/mm saturation currents, above 100 GHz cut-off frequency on Si substrate. Continuous-wave power measurements in class-A operation at 10 GHz with $V_{DS} = 15 \text{ V}$ revealed a 19-dB linear gain, a maximum output power density of 2.5 W/mm with an $\sim 23\%$ power-added efficiency, and a 9-dB large-signal gain.

Further we investigated HEMT devices grown on sapphire and SiC by means of spatial resolved μPL revealing strong heating effects under biased conditions up to $\sim 1200 \text{ K}$ for devices grown on sapphire. The heat dissipation depends crucially on the substrate. The thermal breakdown can directly be observed and related to the temperature. By knowing the

actual channel temperature the discrepancy between a pure velocity saturated current and a phonon excited process can be understood. The 2DEG electrons accelerated in the high electric fields under applied V_{DS} change therefore the local phonon occupation in the channel as soon as they gained enough energy which is comparable to $\hbar\omega_{LO}$. The excited optical phonons on the other hand give rise to a drastically increased scattering reducing the electron mobility and consequently the currents which can be transported laterally decrease. The local occupation of optical phonons in the vicinity of the 2DEG channel is therefore independent of the choice of the substrate. Consequently IV characteristics exhibit similar saturation currents. A simple model based on phonon statistics is proposed, allowing to predict correctly the behavior of saturation currents and lift the discrepancy. It reveals that a drastic increase in 2DEG electrons will not lead to a significant increase of saturation currents. This mechanism together with the thermal induced shift of $V_{DS,sat}$ to higher voltages will have a negative impact on device output power.

Sensing devices As we demonstrated in the corresponding subsection the electric response of the heterostructures can be manipulated by applying various stimuli. But nevertheless it is crucial to understand the physical properties of the sample. The resistivity, *i.e.* the 2DEG, is very sensitive to the manipulation of the surface potential. It is therefore possible to distinguish different polar liquid by means of their influence on the heterostructure barrier. Further the nitride semiconductors are stable on a wide temperature range that allowing to use them for ultra-high temperature sensors above the melting point of most common semiconductors. Another relevant application is the UV sensing. It was demonstrated that in the presence of an UV excitation source currents can be manipulated laterally and parallel to the growth direction. One especially can benefit from the fact that the AlInN has a bandgap of ~ 4.3 eV. In a future work measurements could be performed spectrally resolved and compared to common results obtained for AlGaN UV devices [61].

Bibliography

- [1] B. J. Baliga, *Power Semiconductor-Device Figure of Merit for High-Frequency Applications*, IEEE Electron Device Lett. **10**, 455 (1989).
- [2] K. Takahashi, A. Yoshikawa, and A. Sandhu, *Wide bandgap semiconductors: fundamental properties and modern photonic and electronic devices* (Springer Verlag, 2007).
- [3] R. Waser, *Nanoelectronics and information technology : advanced electronic materials and novel devices* (Wiley-VCH, Weinheim, 2005).
- [4] C. Kocabas *et al.*, *Radio frequency analog electronics based on carbon nanotube transistors*, Proceedings of the National Academy of Sciences **105**, 1405 (2008).
- [5] D. A. Frickey, *Conversion between S, Z, Y, H, ABCD, and T parameters which are valid for complex source and load impedances*, Microwave Theory and Technique, IEEE Transaction on **42**, 205 (1994).
- [6] G. Meinke, *Taschenbuch der Hochfrequenztechnik*, (1987).

- [7] F. Ren, and J. Zolper, *Wide energy bandgap electronic devices* (World Scientific Pub. Co. Inc., 2003).
- [8] A. Singh *et al.*, *Admittance parameter and unilateral power-gain evaluation of GaN MESFET for microwave circuit applications*, *Microw. Opt. Techn. Lett.* **31**, 387 (2001).
- [9] I. J. Bahl, *Fundamentals of RF and Microwave Transistor Amplifier* (John Wiley & Sons, Inc., 2008).
- [10] B. Kumar, and S. B. Jain, *Electronic devices and circuits* (PHI Learning Pvt. Ltd., 2007).
- [11] J. Dorsaz, *Lattice-matched AlInN alloys for nitride-based optoelectronic devices* (PhD Thesis, EPFL, Lausanne, 2006).
- [12] http://en.wikipedia.org/wiki/Moore%27s_law.
- [13] <http://en.wikipedia.org/wiki/Photolithography>.
- [14] M. Higashiwaki, T. Mimura, and T. Matsui, *30-nm-gate AlGaIn/GaN heterostructure field-effect transistors with a current-gain cutoff frequency of 181 GHz*, *Jpn. J. Appl. Phys. Part 2-Letters & Express Letters* **45**, L1111 (2006).
- [15] C. Gaquière *et al.*, *AlInN/GaN a suitable HEMT device for extremely high power high frequency applications*, 2007 IEEE International Microwave Symposium Digest, Vols 1-6, 2136 (2007).
- [16] F. Medjdoub *et al.*, *Small-signal characteristics of AlInN/GaN HEMTs*, *Electron. Lett.* **42**, 779 (2006).
- [17] H. Morkoc, and J. Leach, *Polarization effects in semiconductors : from ab initio theory to device application* (Springer, New York, 2007).
- [18] K. Lehovec, and R. Zuleeg, *Volgate-Current Characteristics of GaAs J-Fets in Hot Electron Range*, *Solid State Electron* **13**, 1415 (1970).
- [19] K. Ismail *et al.*, *High-Transconductance n-Type Si/SiGe Modulation-Doped Field-Effect Transistors*, *IEEE Electron Device Lett.* **13**, 229 (1992).
- [20] H. F. Sun *et al.*, *102-GHz AlInN/GaN HEMTs on Silicon With 2.5-W/mm Output Power at 10 GHz*, *IEEE Electron Device Lett.* **30**, 796 (2009).
- [21] F. Medjdoub *et al.*, *Barrier-layer scaling of InAlN/GaN HEMTs*, *IEEE Electron Device Lett.* **29**, 422 (2008).
- [22] H. Lahreche *et al.*, *Optimisation of AlN and GaN growth by metalorganic vapour-phase epitaxy (MOVPE) on Si(111)*, *J. Cryst. Growth* **217**, 13 (2000).
- [23] E. Pichonat *et al.*, *Temperature analysis of AlGaIn/GaN high-electron-mobility transistors using micro-raman scattering spectroscopy and transient interferometric mapping*, *Eur. Microw. Integrat.*, **54** (2006).
- [24] R. J. I. Simms *et al.*, *Channel temperature determination in high-power AlGaIn/GaN HFETs using electrical methods and Raman spectroscopy*, *IEEE Trans. Electron Dev.* **55**, 478 (2008).
- [25] R. J. T. Simms *et al.*, *Current collapse in AlGaIn/GaN transistors studied using time-resolved Raman thermography*, *Appl. Phys. Lett.* **93**, 203510 (2008).

- [26] G. Christmann, *III-nitride based microcavities towards polariton condensation at room temperature* (PhD Thesis, EPFL, Lausanne, 2009).
- [27] D. Simeonov, *Synthesis and optical investigation of single polar GaN/AlN quantum dots* (PhD Thesis, EPFL, Lausanne, 2009).
- [28] <http://www.ioffe.rssi.ru/SVA/NSM/Semicond/GaN/index.html>.
- [29] K. B. Nam *et al.*, *Optical properties of AlN and GaN in elevated temperatures*, Appl. Phys. Lett. **85**, 3489 (2004).
- [30] I. A. Vainshtein, A. F. Zatsépin, and V. S. Kortov, *Applicability of the empirical Varshni relation for the temperature dependence of the width of the band gap*, Phys. Solid State **41**, 905 (1999).
- [31] M. G. Tkachman *et al.*, *Phonon-assisted exciton luminescence in GaN layers grown by MBE and chloride-hydride VPE*, Semiconductor **37**, 532 (2003).
- [32] J. D. Dow, and D. Redfield, *Electroabsorption in Semiconductors - Excitonic Absorption Edge*, Phys. Rev. B **1**, 3358 (1970).
- [33] M. Ramonas *et al.*, *Hot-phonon effect on power dissipation in a biased $\text{Al}_x\text{Ga}_{1-x}\text{N}/\text{AlN}/\text{GaN}$ channel*, Phys. Rev. B **71**, 075324 (2005).
- [34] W. Shockley, *Hot Electrons in Germanium and Ohms Law*, At&T Tech. J. **30**, 990 (1951).
- [35] C. Y. Tsai *et al.*, *Theoretical modeling of nonequilibrium optical phonons and electron energy relaxation in GaN*, J. Appl. Phys. **85**, 1475 (1999).
- [36] S. Sridharan, A. Venkatachalam, and P. Yoder, *Electrothermal analysis of AlGaIn/GaN high electron mobility transistors*, Journal of Computational Electronics **7**, 236 (2008).
- [37] <http://www.ioffe.rssi.ru/SVA/NSM/Semicond/>.
- [38] S. M. Sze, *High-speed semiconductor devices* (Wiley, New York, 1990).
- [39] H. Jung *et al.*, *Reliability behavior of GaN HEMTs related to Au diffusion at the Schottky interface*, physica status solidi (c) **6**, S976 (2009).
- [40] T. Zimmermann *et al.*, *AlN/GaN insulated-gate HEMTs with 2.3 A/mm output current and 480 mS/mm transconductance*, IEEE Electron Device Lett. **29**, 661 (2008).
- [41] H. Siegle *et al.*, *Zone-boundary phonons in hexagonal and cubic GaN*, Phys. Rev. B **55**, 7000 (1997).
- [42] S. K. Tripathy *et al.*, *Evidence of hot electrons generated from an AlN/GaN high electron mobility transistor*, Appl. Phys. Lett. **92**, 013513 (2008).
- [43] S. K. Tripathy *et al.*, *Investigation of hot electrons generated from AlN/GaN-based high electron mobility transistor* - art. no. 689208, Ultrafast Phenomena in Semiconductors and Nanostructure Materials **6892**, 89208 (2008).
- [44] G. Xu *et al.*, *Investigation of hot electrons and hot phonons generated within an AlN/GaN high electron mobility transistor*, Laser Phys. **19**, 745 (2009).
- [45] J. S. Flynn *et al.*, *Delta doped AlGaIn and AlGaIn/GaN HEMTs: Pathway to improved performance?*, 5th International Conference on Nitride Semiconductors (ICNS-5), Proceedings, 2327 (2003).

- [46] T. Palacios *et al.*, *AlGaN/GaN high electron mobility transistors with InGaN back-barriers*, IEEE Electron Device Lett. **27**, 13 (2006).
- [47] K. Kim *et al.*, *Nanoscale device modeling and simulation: Fin field-effect transistor (FinFET)*, Jpn. J. Appl. Phys. Part 1-Regular Papers Short Notes & Review Papers **43**, 3784 (2004).
- [48] S. Hackenbuchner, *Elektronische Struktur von Halbleiter-Nanobaulementen im thermodynamischen Nichtgleichgewicht* München, 2002), Vol. 48.
- [49] C. Canali *et al.*, *Electron and Hole Drift Velocity-Measurements in Silicon and Their Empirical Relation to Electric-Field and Temperature*, IEEE Trans. on Electron Devices **22**, 1045 (1975).
- [50] NEXTNANO³ device simulation package, see <http://www.nextnano.de> and <http://wsi.tum.de/nextnano.de>
- [51] E. G. Brazel, M. A. Chin, and V. Narayanamurti, *Direct observation of localized high current densities in GaN films*, Appl. Phys. Lett. **74**, 2367 (1999).
- [52] J. Dorsaz *et al.*, *Selective oxidation of AlInN layers for current confinement in III-nitride devices*, Appl. Phys. Lett. **87**, 072102 (2005).
- [53] G. Pozzovivo *et al.*, *Gate insulation and drain current saturation mechanism in InAlN/GaN metal-oxide-semiconductor high-electron-mobility transistors*, Appl. Phys. Lett. **91**, 043509 (2007).
- [54] Y. F. Wu *et al.*, *30-W/mm GaNHEMTs by field plate optimization*, IEEE Electron Device Lett. **25**, 117 (2004).
- [55] F. Medjdoub *et al.*, *Impact of Field Plate technology on the Schottky diode characteristic of InAlN/GaN HEMTs*, 15th European Workshop on Heterostructure Technology, Manchester UK (2006).
- [56] O. Ambacher, and V. Cimalla, *Polarization effects in semiconductors : from ab initio theory to device application* (Springer, New York, 2007).
- [57] A. L. McClellan, *Tables of experimental dipole moments* (W.H. Freeman, San Francisco,, 1963).
- [58] R. Bartnikas, *Electrical insulating liquids* (ASTM, Philadelphia, PA, 1994).
- [59] T. Kokawa *et al.*, *Liquid-phase sensors using open-gate AlGaIn/GaN high electron mobility transistor structure*, J. Vac. Sci. Technol. B **24**, 1972 (2006).
- [60] W. Y. Weng *et al.*, *GaN MSM Photodetectors with a Semi-Insulating AlInN Cap Layer and Sputtered ITO Transparent Electrodes*, Electrochem. Solid St. **12**, H369 (2009).
- [61] M. Razeghi, and A. Rogalski, *Semiconductor ultraviolet detectors*, Photodetectors: Materials and Devices **2685**, 114 (1996).

Conclusion

Summary of experimental results The growth of $\text{Al}_{1-x}\text{In}_x\text{N}$ ternary compound epilayers with indium mole fractions around the lattice-matched condition $x \sim 16.5\%$ on 2-inch GaN templates previously deposited on different substrates, namely sapphire, SiC and Si(111), was successfully demonstrated. Similar to other polar heterostructures, electrons originate from the sample surface and accumulate at the $\text{AlInN}/(\text{AlN})/\text{GaN}$ heterointerface forming a 2DEG without any additional doping. The 2DEG density is as high as $2.6 \times 10^{13} \text{ cm}^{-2}$ for a 14 nm $\text{Al}_{0.85}\text{In}_{0.15}\text{N}$ barrier. Note that the 2DEG density is a crucial indicator for the crystalline quality. Note that in some recent publications on such heterostructures substantially lower densities have been reported that could be due to Ga incorporation in the barrier [1]. Especially, the insertion of an additional ultrathin AlN interlayer between LM AlInN and GaN gives rise to a ‘high-mobility’ window [2] with an optimum of $\sim 1200 \text{ cm}^2/\text{Vs}$ for a 2DEG density of $2.6 \times 10^{13} \text{ cm}^{-2}$ at RT and an interlayer thickness of $\sim 1.1 \text{ nm}$.

The structural properties of the AlInN epilayers were probed by various measurements methods such as XRD, AFM, SNMS, RBS, μPL indicating an overall very good crystalline quality in terms of rms roughness, homogeneity and strain state [3]. It should be pointed out that these AlInN epilayers can be grown with an outstanding quality at least for the LM case on all substrates mentioned above.

HEMT devices processed from these heterostructures exhibited outstanding device properties with several records among the nitride compound heterostructures: above 2 A/mm saturation currents [4], above 100 GHz cut-off frequency on Si substrate [5]. On the latter substrates, continuous-wave power measurements in class-A operation at 10 GHz with $V_{DS} = 15 \text{ V}$ revealed a 19-dB linear gain, a maximum output power density of 2.5 W/mm with an $\sim 23\%$ power-added efficiency, and a 9-dB large-signal gain.

Further we investigated HEMT devices grown on sapphire and SiC by means of spatial resolved μPL which might be a competitive technique to the well-established Raman method revealing strong heating effects under biased conditions up to $\sim 1200 \text{ K}$ for devices grown on sapphire at a drain-source voltage $V_{DS} = 20 \text{ V}$ and a drain-source distance $d_{DS} = 5 \mu\text{m}$ [6]. The heat dissipation depends crucially on the choice of the substrate. The thermal induced breakdown at high V_{DS} can directly be observed and related to the temperature when the melting of the contacts is achieved.

As we demonstrated, the electric response of the $\text{AlInN}/(\text{AlN})/\text{GaN}$ heterostructures can be manipulated by various stimuli. The resistivity of the 2DEG is very sensitive to the modification of the surface potential. It is therefore possible to distinguish different polar liquid through their influence on the heterostructure barrier electric field. Further the nitride semiconductors are stable on a wide temperature range, which allows one to use them for ultra-high temperature sensors above the melting point of most common semiconductors. Another relevant application is the UV sensing. It was demonstrated that for 244 nm excitation currents can be manipulated laterally and parallel to the growth direction.

Conclusion

Conclusion It was demonstrated that a simple charge balance model can describe adequately the electrical properties. Especially for LM $\text{Al}_{0.85}\text{In}_{0.15}\text{N}/\text{AlN}(1\text{nm})/\text{GaN}$ the polarization charges were found to be as high as $\sigma_{\text{AlInN/GaN}}(0.15) \sim 3.7 \times 10^{17} \text{ m}^{-2}$, the dielectric constant $\epsilon_{\text{AlInN}}(0.15) \sim 11.2$, the surface potential $e\Phi_s \sim 3 \text{ eV}$ and the critical thickness for the formation of the 2DEG $t_{cr} = 2.3 \text{ nm}$. The latter is especially important for normally-off HEMT devices, *i.e.* devices where a voltage has to be applied in order to have carriers in the channel [7]. These results were confirmed with potential mapping measurements *via* electron holography [8]. This description holds in the tensile strain regime.

In the compressive regime, 2DEG density and consequently the polarization charges are too high compared with the theoretical calculation. It has been shown in the literature that compressive AlInN relaxes favourably by building a compositional gradient ending with the LM composition at the surface [9]. We calculated the polarization charge in such a heterostructure and it was found that any deviation from the homogenous case will give a background polarization additional to the polarization discontinuities at the heterointerfaces. This would indeed lead to an increase of the total polarization and consequently to an increase of the 2DEG density.

From experimental and theoretical findings it can be concluded that for nitride heterostructures containing 2DEG densities more than $1.5 \times 10^{13} \text{ cm}^{-2}$ the second subband is always occupied, even at RT. As a rule of thumb the density of the second subband is 10% of the ground state density but can significantly influence transport at low temperature when the phonon scattering can be excluded. These subband occupations can only be observed in transport measurements since during a CV measurement occupied subbands are always depleted simultaneously.

The influence of strain arising from monolayer fluctuation at the AlN/GaN interface was studied in detail. It turned out that the AlN interlayer induces significant distortion on the GaN conduction band at the position where the 2DEG is located with amplitude up to 100 meV and a lateral extension in the order of 1-2 nm. Additionally, strong piezoelectric fields in the order of MV/cm arising from the coupling of ϵ_{xx} and ϵ_{yy} elements of the strain tensor to the e_{15} component of the piezoelectric tensor. This is consistent with the discussion conducted in Ref. [10]. Note that these two mechanisms and the interface roughness scattering yield scattering times in the same order of magnitude for the ground state. The second subband, however, has a larger separation from the heterointerface and since the interface related distortions drop quickly within a few nm towards the buffer, the second subband experiences less scattering and exhibits a larger mobility. This can therefore in a significant decrease of the Hall coefficient. These findings are consistent with the ‘high mobility windows’. Thicker interlayer or AlN barrier induce larger strain, which decreases thereby the channel mobility. Another benefit of the LM AlInN barrier is that it can partly accommodate the strain induced by the interlayer, *i.e.* strain found in the GaN is lower than for a AlN/GaN heterostructure with the same AlN thickness.

As discussed above the μPL is an appropriate tool to explore the actual temperature in the HEMT channel. By knowing the actual channel temperature, the discrepancy between a pure velocity saturated current and a phonon excited process can be understood. The 2DEG electrons accelerated in the high electric fields under applied V_{DS} change therefore the local phonon occupation in the channel as soon as they gained energy comparable to $\hbar\omega_{LO}$. The excited optical phonons on the other hand give rise to a drastic increase of scattering process reducing thereby the electron mobility and consequently the current which can be transported laterally. The local occupation of optical phonons in the vicinity of the 2DEG channel is

therefore independent of the substrate. Consequently IV characteristics exhibit similar saturation currents. A simple model based on phonon statistics is proposed allowing to predict correctly the behavior of saturation currents. It reveals that a significant increase in 2DEG density, as found for AlInN/GaN heterostructures compared to AlGaIn/GaN ones, will not lead to a drastic increase of saturation currents. This mechanism together with the thermal induced shift of $V_{DS,sat}$ to higher voltages, will have a negative impact on device output power.

To conclude, it is likely that AlInN based transistors, and more generally devices, will gain even more interest from the community owing to key assets like a very large electron sheet charge density, a high temperature stability, and strain-free heterostructures. In addition, AlInN/GaN heterostructures exhibit peculiar properties that could also be of large interest for fundamental studies related to quantum Hall effect.

Outlook Throughout this work many problems from the material until the device aspects were touched. At this last point some of the import issues are summarized which might serve as starting point for a more profound analyze, research and reflection

- 1) In Chapter 5 a contrast was revealed in evaluating micro-strains with numerical methods and the analytical expression from the literature (Quang *et al.*) which relied on a quasi-cubic approximation, which is certainly not true for wurtzite nitrides. This discrepancy should be lifted in a future work to unambiguously determine the prefactors in Equations (5.28) and (5.29).
- 2) Reviewing the in-plane potential profile Figure 5.13, it takes the form of a double exponential decaying form the center but possess different sign at the origin causing therefore a step-like behavior. For such a potential the transmission and tunneling probability should be evaluated in function on the energy of the incident electron. Results should be compared to the simple step-like behavior in Equation (5.28).
- 3) Development of a finite grid model taking into account time dependent rate equations for spatial LO/TA phonon population and related decay and conversion processes to study the actual buffer temperature distribution in dependence on substrate
- 4) Solving the 2D heat equation for the exact device geometry.
- 5) Study of the electron-phonon interaction on an atomic scale.
- 6) The study of exciton or plasma migration in GaN under extreme conditions, *i.e.* high temperature and high electric fields (might be realized with PL studies using GaN/Al_xGa_{1-x}N buffers with low x content).
- 7) The development of a physical model for the contact resistance (should explain the alignment of metals and their work function if they are deposited on wide-bandgap nitride heterostructures, then the mechanisms of transferring electrons from the triangular potential well to the metallization should be studied).
- 8) Instead of ‘overcharging’ a single triangular potential well with electrons which leads under high field conditions to an excitation of nearly all LO phonons in the accessible

volume one might think in terms of distribution of the electrons along the z -axis. For example a double $\text{Al}_{0.85}\text{In}_{0.15}\text{N}(13\text{nm})/\text{AlN}(1\text{nm})/\text{GaN}(6\text{nm})/\text{Al}_{0.85}\text{In}_{0.15}\text{N}(6\text{nm})/\text{GaN}(\text{buffer})$ heterostructures would lead to two 2DEGs with approximately the same density but spatially separated and still confined within the GaN. This would lead to higher saturation currents since the number of available phonon states is increased

Bibliography

- [1] L. Ardaravicius *et al.*, *Electron drift velocity in lattice-matched AlInN/AlN/GaN channel at high electric fields*, J. Appl. Phys. **106**, 073708 (2009).
- [2] M. Gonschorek *et al.*, *High electron mobility lattice-matched AlInN/GaN field-effect transistor heterostructures*, Appl. Phys. Lett. **89**, 062106 (2006).
- [3] M. Gonschorek *et al.*, *Two-dimensional electron gas density in $\text{Al}_{1-x}\text{In}_x\text{N}/\text{AlN}/\text{GaN}$ heterostructures ($0.03 \leq x \leq 0.23$)*, J. Appl. Phys. **103**, 093714 (2008).
- [4] F. Medjdoub *et al.*, *Small-signal characteristics of AlInN/GaN HEMTs*, Electron. Lett. **42**, 779 (2006).
- [5] H. F. Sun *et al.*, *102-GHz AlInN/GaN HEMTs on Silicon With 2.5-W/mm Output Power at 10 GHz*, IEEE Electron Device Lett. **30**, 796 (2009).
- [6] M. Gonschorek *et al.*, *Temperature mapping of $\text{Al}_{0.85}\text{In}_{0.15}\text{N}/\text{AlN}/\text{GaN}$ high electron mobility transistors through micro-photoluminescence studies*, Eur. Phys. J.-Appl. Phys. **47**, 30301 (2009).
- [7] C. Ostermaier *et al.*, *Ultrathin InAlN/AlN Barrier HEMT With High Performance in Normally Off Operation*, IEEE Electron Device Lett. **30**, 1030 (2009).
- [8] L. Zhou *et al.*, *Polarization field mapping of $\text{Al}_{0.85}\text{In}_{0.15}\text{N}/\text{AlN}/\text{GaN}$ heterostructure*, Appl. Phys. Lett. **94**, 121909 (2009).
- [9] K. Lorenz *et al.*, *Relaxation of compressively strained AlInN on GaN*, J. Cryst. Growth **310**, 4058 (2008).
- [10] C. J. Humphreys *et al.*, in *EMC 2008 14th European Microscopy Congress 1-5 September 2008, Aachen, Germany, The atomic structure of GaN-based quantum wells and interfaces*, edited by Springer(2008), pp. 41.

Acknowledgement

First of all I would like to acknowledge Prof. Nicolas Grandjean. He gave me the opportunity to write this thesis in this outstanding research group at this exceptional place. His strong mental, professional and financial support made this work possible.

Then I would like to acknowledge Dr. Jean-François Carlin and Dr. Eric Feltin for the growth of the samples, intense discussions and for the uncouneted shared conference experiences.

Further, I want to mention the outstanding collaboration in the framework of the European UltraGaN project. This made it possible to rapidly share ideas, concepts, approaches and methods on a high scientific level throughout Europe. Especially I would like to thank Dr. Gianmauro Pozzovivo and Jan Kuzmik for sapphire deposition and Mohammed Alomari for the processing of HEMT structures grown on SiC.

In particular I am grateful to Dr. Vanya Darakchieva who helped me a lot with structural characterization of nitride heterostructures and the organization of a research visit at the Linköping University. I really appreciated her hospitality.

Special thanks deserve Dr. Rapphaël Butté who successfully turned into red most of my manuscripts. But nevertheless, this helped much to improve the quality, despite needing a lot of endurance to revise the fifth or higher versions. I appreciated a lot his patience in helping me with optical characterization and scientific discussion.

I am also grateful to Dr. Dobri Simeonov who installed the μ PL setup allowing performing all the interesting measurements. In this context I would also like to mention Jacques Levrat who took his place after he left from EPFL.

For the introduction into the field of processing nitride heterostructures I would like to thank Dr. Julien Dorsaz and Dr. Antonino Castiglia. They always have been helpful in the last year whenever there was something to etch, or to anneal. We shared the office as well which was very pleasant throughout the last four years.

Thanks also to Dr. Marcel Py for the introduction and maintenance of the setups for the electrical characterization, Nils Kaufmann for supporting me taking AFM images and Hansjörg Buehlmann for his amazing technical skills *e.g.* wire bonding and the fabrication of special designed sample supports etc.

I would also like to thank all the others who make the research group of LASPE to a lively, agreeable and creative working environment. Namely Aline Gruaz who organized our conference journeys, my other colleagues in the office Alexei Althoukov and Tiankai Zhu. Thanks also to all other colleagues or former colleagues not mentioned so far, namely Dr. Amélie Dussaigne, Dr. Sylvain Nicolay and Dr. Gabriel Christmann for all the great evenings spent in the Satellite.

Acknowledgement

I want also not forget to thank Stefan Birner who helped me patiently with all the problems and question occurred during the work with the NextNano³ code. I also want to mention Patrick Waltereit who supplied me generously with the MadMax code for X-ray simulations.

Last but not least if there remains a life besides time-consuming work I want to acknowledge Dr. Ulf Richter and Jan Kerschgens for the uncounted philosophical and scientific discussions.

Finally I would like to thank my family who was always patient with me, especially my parents, my companion and my son. To them this thesis is dedicated.

Personal details

Name : GONSCHOREK Marcus
Nationality : german
Date of Birth : 11.07.1979
Adress : Avenue de Ruchonnet 2b, CH-1003 Lausanne
Telephone : +41 765420711
E-Mail : marcus.gonschorek@gmx.de

Doctoral studies

08/2005 - 08/ 2009 Researcher at the Ecole Polytechnique Fédérale de Lausanne (EPFL),
Lausanne, Switzerland (<http://laspe.epfl.ch>)

Conception, fabrication and characterization of nitride heterostructures for high-power high electron mobility transistor (HEMT) and optoelectronic devices

02/2007 Collaboration with the University of Linköping (Sweden), Laboratory of Prof. B. Monemar: Characterization of nitride heterostructures

08/2005 - 08/2009	Collaborator in the UltraGaN european project to replace AlGaIn/GaN based transistors by Al(In)N/(In)GaN (www.ultragan.eu)
-------------------	---

Graduate studies

04/2005 «Diplom-Physiker» (M.S. in physics), (grade:good)

05/2004 – 05/2005 Researcher at the University of Leipzig, Leipzig, Germany (www.uni-leipzig.de/~hlp)

Characterization of InGaAs quantum dots for non-volatile memory devices

09/2002 – 07/2003 studies of physics at « Université de Provence »
in Marseille, France (2nd cycle, maîtrise)

10/1999 – 04/2005 studies of physics at University of Leipzig, Germany

Education

09/1998 – 05/1999 military service, Weißenfels, Germany

06/1998 « Abitur », Goethe-Gymnasium Weißenfels, Germany, (grade:excellent)

Competences and Experiences

Development

Epitaxial growth of III-nitrides by Metal-Organic Vapor Phase Epitaxy (MOVPE)
Plasma-enhanced chemical-vapor deposition (PECVD) for device passivation

Processing

Optical lithography, plasma and reactive-ion etching, thermal oxidation
Electron-beam evaporator and contact annealing

Semiconductor characterization

Structural: x-ray diffraction (XRD), mass spectroscopy (SIMS)
Electrical: capacitance-voltage (CV), deep level transient spectroscopy (DLTS), IV, magnetotransport
Microscopy: atomic force microscopy (AFM), transmission electron microscopy (TEM)
Spectroscopy: Reflectivity, Electro- and photoluminescence (PL), spatial resolved μ PL

Solid state physics

Simulation of XRD spectra in heterostructures
Simulation of electronic states and strain in heterostructures and low dimensional systems (1D,2D,3D)
Non-equilibrium systems, transport, standard device physics (diodes, HEMTs, laser)

Computing

Standard office application (Word, PowerPoint, Excel)
Scientific (MatLab, LabView, LaTeX, Maple, Mathematica, Origin, C++)

Teaching&Referee activity

Supervision of students in the framework of doctoral candidates teaching duties
Referee for 2 international scientific journals and 1 conference proceedings

Languages

German (native)
English (fluent)
French (fluent)
Spanish (basic)

Personal interests

reading (daily press, classical literature), piano playing, travelling (backpacking, long-distance bike trips), art&culture, history, sociology, sports (biking, jogging)

Publications list

M.Gonschorek, J-F.Carlin, D. Simeonov, E.Feltin, M.Py, and N.Grandjean
Temperature mapping of $Al_{0.85}In_{0.15}N/AlN/GaN$ high electron mobility transistors through micro-photoluminescence studies
Eur. Phys. J. Appl. Phys. **47**, (2009).

M.Gonschorek, J-F.Carlin, E.Feltin, M.Py, and N.Grandjean
Two-dimensional electron gas density in $Al_{1-x}In_xN/AlN/GaN$ heterostructures
J.Appl.Phys. **103**, (2008).

M.Gonschorek, J-F.Carlin, E.Feltin, M.Py, and N.Grandjean
High electron mobility lattice-matched $AlInN/GaN$ field-effect transistor heterostructures
Appl.Phys.Lett. **89**, (2006).

M.Gonschorek, H.Schmidt, J.Bauer, G.Benndorf, G.Wagner, and M.Grundmann
Thermally-assisted tunneling processes in $InGaAs/GaAs$ quantum dot structures
Phys.Rev.B **74**, (2006).

Co-author:

R. Butté, J.-F. Carlin, E. Feltin, M. Gonschorek, S. Nicolay, G. Christmann, D. Simeonov, A. Castiglia, J. Dorsaz, H. J. Buehlmann, S. Christopoulos, G. Baldassarri Höger von Högersthal, A. J. D. Grundy, M. Mosca, C. Piquier, M. A. Py, F. Demangeot, J. Frandon, P. G. Lagoudakis, J. J. Baumberg, and N. Grandjean
Current status of $AlInN$ layers lattice-matched to GaN for photonics and electronics
J. Phys. D: Appl. Phys. **40**, (2007).

G. Pozzovivo, J. Kuzmik, S. Golka, W. Schrenk, G. Strasser, D. Pogany, K. Cico, M. Tapajna, K. Froehlich, J.-F. Carlin, M. Gonschorek, E. Feltin, and N. Grandjean
Gate insulation and drain current saturation mechanism in $InAlN/GaN$ metal-oxide-semiconductor high-electron-mobility transistors
Appl. Phys. Lett. **91**, (2007).

F. Medjdoub, D. Ducatteau, C. Gaquière, J.-F. Carlin, M. Gonschorek, E. Feltin, M. A. Py, N. Grandjean, and E. Kohn
Evaluation of $AlInN/GaN$ HEMTs on sapphire substrate in microwave, time and temperature domains
Electron. Lett. **43**, (2007).

F. Medjdoub, J.-F. Carlin, M. Gonschorek, M. A. Py, N. Grandjean, S. Vandenbrouck, C. Gaquiere, J. C. Dejaeger, and E. Kohn
Small-signal characteristics of $AlInN/GaN$ HEMTs
Electron. Lett. **42**, (2006).